PHOTONICS

CMDITR Review of Undergraduate Research

Contributions from undergraduate research experiences within the
NSF Center on Materials and Devices for Information Technology Research

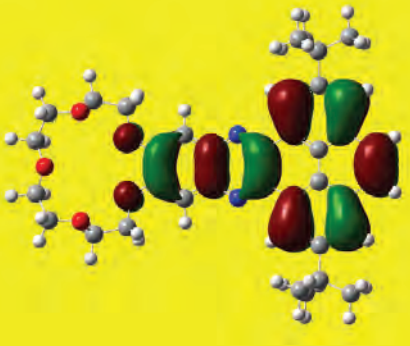

Volume 7, Number 1

This material is based upon work supported by the STC Program of the
National Science Foundation No. DMR 0120967.

Any opinions, findings, and conclusions or recommendations expressed in this material are those of the authors and do not necessarily reflect the views of the National Science Foundation.

Printed in the United States at the University of Washington, Seattle, WA

Inquires should be addressed to:

Center on Materials and Devices for Information Technology Research
University of Washington
Department of Chemistry
Box 351700
Seattle, WA 98195-1700

reu@stc-mditr.org

http://stc-mditr.org

Volume 7, Number 1

Table of Contents

Table of Contents continued...

Welcome to the Seventh Edition of CMDITR's Review of Undergraduate Research

This volume features extended abstracts written by student participants in the National Science Foundation (NSF) Center on Materials and Devices for Information Technology Research (CMDITR) Summer 2010 Research Experiences for Undergraduates (REU) program: Hooked on Photonics.

The REU experience is intended to serve as a catalyst for undergraduates to enter into careers involving science, technology, engineering, and mathematics. Hooked on Photonics provides a rich learning opportunity not only for the undergraduate participants who experience hands-on research prior to committing to graduate study, but also for the student's mentors, be they faculty members, research scientists, post-doctoral fellows or graduate students. While working with REU students, mentors develop teaching and mentoring skills, and benefit from reflecting on the excitement of the cutting-edge research upon which their careers have been built.

The CMDITR REU Program placed undergraduate students from across the United States in research laboratories at the University of Washington, the University of Arizona, and Georgia Institute of Technology. All of the participants worked on interdisciplinary research projects that contributed to advancements in information technology encompassing activities in chemistry, physics, optics, materials science and engineering. The program emphasized the teamwork nature of scientific research, and was supplemented by a collection of activities including ethics training and workshops in scientific communication.

This publication offers a forum for participants to share their research with their REU peers, future students, CMDITR graduate students and faculty, and others interested in the research activities of CMDITR. To learn more about Hooked on Photonics please visit *www.stc-mditr.org/reu*.

A special thanks to all of the students for their hard work, to their mentors for their time and patience, and to the REU program coordinators Denise Bale-Mushatt, Olanda Bryant, April Wilkinson, and Kimberly Sierra-Cajas, for their organizational efforts. A final, but important thanks goes to Ly Pham and Suzy Hunter for their work on the production of this volume.

The extended abstracts included here are presented in alphabetical order by the participant's last name.

Philip Reid, CMDITR Director

Effects of Dissolved Oxygen in Solvents on the Performance of Solution Processed Organic Field Effect Transistors

DANIEL E. ACEVEDO, University of Puerto Rico
Avishek Aiyar, Elsa Reichmanis, Georgia Institute of Technology

Introduction

Fabricated by Koezuka and coworkers, in 1986, the first organic field effect transistor (OFET) was introduced.[1] This device is capable of modulating the density of charge carriers in the channel between the source and drain electrodes, through a voltage applied to the gate contact. By employing an organic, cost efficient semiconductor, OFETs represent a viable option to amorphous silicon thin film transistors. Even though their performance does not consistently rival that of their inorganic counterparts, primarily due to the relatively lower mobility and instability in air, they are suitable for use in display applications that require low-cost, large-area coverage, structural flexibility and low-temperature processing.[2] Efforts have been made to improve the field effect mobility of OFETs, in addition to lowering operating voltages, although much progress is still required.[3,4]

Oxygen is believed to play an important role in the performance characteristics of solution processed OFETs, especially those based on poly(alkylthiophenes) (PATs), through the formation of a charge transfer complex.[5] Since the polymer of interest, poly(3-hexylthiophene) (P3HT) needs to be dissolved, for instance in chloroform, it is exposed to a certain amount of dissolved oxygen (or water) contained in the solvent, in addition to the oxygen in the atmosphere. Although it is believed that much of the impact of oxygen/moisture is to be attributed to the environment, the possibility of the solvent as a source has not been studied and thus should also be considered, especially since oxygen is known to cause large threshold voltage shifts.[6]

In this work, we intend to investigate the effects of dissolved gases in the solvent on P3HT based OFETs characteristics by degassing the solvent using conventional techniques such as freeze-pump-thaw and ultrasonic degassing. Results from the different degassing techniques will also be compared to study how the efficiency of degassing, and thus the final dissolved gas content, impacts device performance. Moreover, this new method of eliminating dissolved gases in solvents could prove to be a facile and cost-effective approach to reducing operating voltages in OFETs.

Experimental Methods

The OFETs are prepared by spin coating solutions of P3HT in anhydrous chloroform ($CHCl_3$) on substrates with bottom contact architecture, using gold as the source and drain electrodes and highly doped silicon as the gate contact, Figure 1.

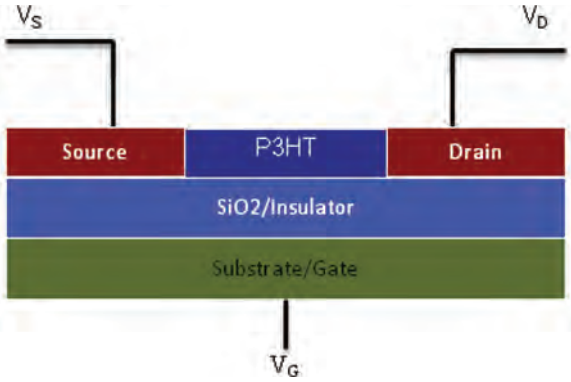

Figure 1. Bottom-contact device, with the organic semiconductor deposited onto prefabricated source and drain electrodes.

Thermally grown silicon dioxide acts as the gate dielectric material. Top contact is an additional architecture, fabricated by depositing first the organic film, which is the opposite sequence of the first configuration. The current study is split into modules that cover all aspects OFET fabrication and testing.

Microfabrication of substrates with bottom contact architecture by photolithography

Photolithography is a technique that uses a master pattern in a mask to transfer micron scale patterns into a light sensitive material, ensuring high precision. Generally, organic semiconductors exhibit low conductivity. Consequently the channel length (e.g. gap between drain and source) must be on the order of few microns or tens of microns to measure any appreciable drain current. A channel length ranging from 40 µm to 80 µm is chosen for the current purposes, while the width was fixed at 2 mm. A series of steps are involved in the microfabrication of the bottom contact devices and will be discussed, following the diagram in Figure 2.

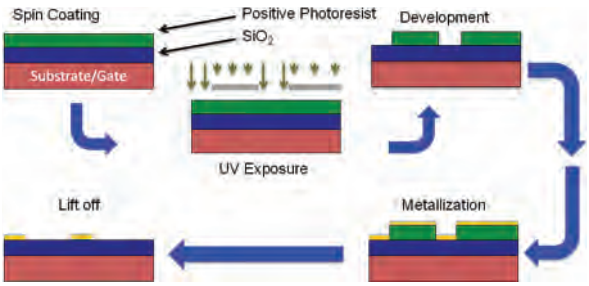

Figure 2. Diagram of the fundamental steps of photolithography with a lift off step included.

The assembly starts with a highly doped silicon wafer containing a 200 nm layer of thermally grown SiO_2. The application via spin coating of a primer, hexamethyldisilazane (HMDS), ensures good adhesion of the Shipley 1827 photoresist layer, of about 2 µm thick, on the substrate. The resist exposure is performed in the Karl Suss MA-6 Mask Aligner. The mask is aligned with the substrate and exposed to UV light of 405 nm wavelength and the resist is subsequently developed in a basic developer, followed by an analysis of the resist profile using the Tencor P15 Profilometer.

Metallization is the mechanism where, by metal vaporization in this case, a film of metal is deposited over the wafer surface. A CVC E-Beam Evaporator applies the gold coating (50 nm in this case) while the excess (not in contact with the SiO_2 surface) is removed afterward during the resist lift-off. This equipment is chosen over a sputtering since the former will only coat the top surface while the latter does it over the entire wafer surface. This is detrimental because a successful lift-off of the unwanted metal patterns relies on the differential metal deposition between planes perpendicular and parallel to the wafer substrate. The lift off is achieved by submerging the wafer in acetone. The thickness of the deposited metal after lift-off is then verified with the profilometer and it is ready for the fabrication of the gate contact. These sequences complete the fabrication of the bottom contact substrates that are now ready for fabrication of OFETs.

Testing and analyzing the device performance using different degassing techniques

The fabrication of the device is completed by spin coating P3HT. Once the dissolved P3HT is deposited, oxygen effects on the device performance will be closely analyzed. The dissolved oxygen levels within the solvent can be reduced employing different degassing techniques such as freeze-pump-thaw and ultrasonic degassing. Four and ten cycles were applied for freeze-pump-thaw and ultrasonic degassing, respectively. These cycle steps are illustrated in Figure 3.

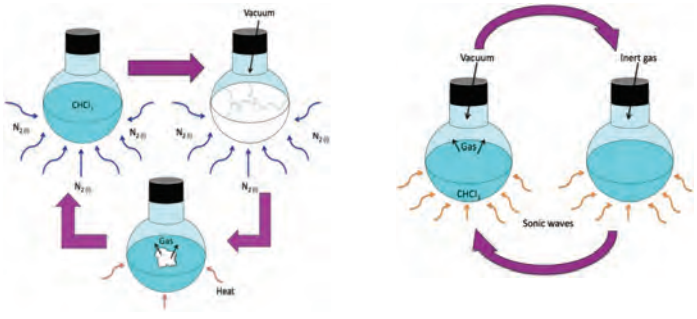

(a) (b)

Figure 3. (a) Freeze-pump-thaw basic steps; (b) Ultrasonic degassing process flow.

Figure 3a illustrates the freeze-pump-thaw degassing technique - the solvent is kept in liquid nitrogen (first step) in order to freeze the solvent followed by a vacuum application (second step) for ten minutes. Afterwards, the frozen chloroform is allowed to melt (third step). Dissolved gases escaping from the melting solvent can be clearly seen while it is maintained at room temperature. After no gas is observed escaping from the solvent throughout the melting process, the container is back-filled with argon and the solvent is ready for use. On the other hand, ultrasonic degassing is conducted applying sonic waves through the water into solvent, while maintaining a mild vacuum in a sealed container. The anhydrous degassed chloroform is used to dissolve the P3HT to be deposited onto the wafer and finalize the OFETs.

The testing process is conducted under ambient conditions intentionally, desiring to prove that consistent measurements can be obtained without a controlled environment. These types of environments, such as glove-box, require relative high costs to maintain an inert atmosphere; in addition they make the process even more difficult. Measurements of drain current (I_D) are plotted against gate voltage (V_G) at constant drain voltage (V_D); this way the device performance can be characterized. This study is mainly focused in the linear region described by equation 1:

$$I_D = \frac{\mu W C_i}{L}(V_G - V_T)V_D \qquad (1)$$

Where *L* and *W* are the length and width of the channel, respectively; while µ is the mobility, V_T is the threshold voltage and C_i is the gate insulator capacitance per unit area. Consequently, the relation with the oxygen concentration can be successfully understood as well as to determine the most efficient way to control the levels of oxygen in the solvent. This would enable us to understand the impact of dissolved oxygen (or other gases) on the device characteristics in OFETs, potentially leading to a new method of reducing the threshold and thus operating voltages in devices.

Results

Threshold voltage in this study would be the parameter to improve for obtaining better operation properties for OFETs since it is closely related to the operational voltage. Recent experiments have shown a significant threshold voltage decrease by 26.15 V. The difference was achieved by degassing the solvent with freeze-pump-thaw. These results are summarized in Table 1.

Degassing Technique	Mobility (cm^2/Vs)	Threshold Voltage (V)
No degassing	3.5E-04	33
Ultrasonic	1.50E-04	15
Freeze-pump-thaw	1.51E-04	7.85

Table 1. Results for degassed solvent obtained in recent experiments

In order to compare the results achieved with the degassing techniques, two control devices were developed under specific conditions. The first control sample consisted of P3HT/$CHCl_3$ solutions prepared under ambient conditions (Control #1), whereas for the second control sample, the vial containing the P3HT was degassed under vacuum and backfilled with argon, before adding the $CHCl_3$ and making the solution (Control #2); 8 mg of P3HT

were dissolved in 2 mL of anhydrous chloroform and finally spin coated into the bottom contact substrates to complete the transistor fabrication. The results are highlighted in Table 2 where an average of three measurements were taken.

Control Device	Mobility (cm^2/Vs)	Threshold Voltage (V)
1	2.73E-04	22.4
2	2.13E-04	15.1

Table 2. Control devices average results.

Our main interest is to study the transistor's transport properties via gate voltage sweeping, while maintaining the drain voltage constant, as visualized in Figure 4. This information permits the evaluation of the device performance by calculating the threshold voltage and mobility.

Freeze-pump-thaw and ultrasonic degassing techniques were employed to reduce the oxygen concentration which results are included in Table 3.

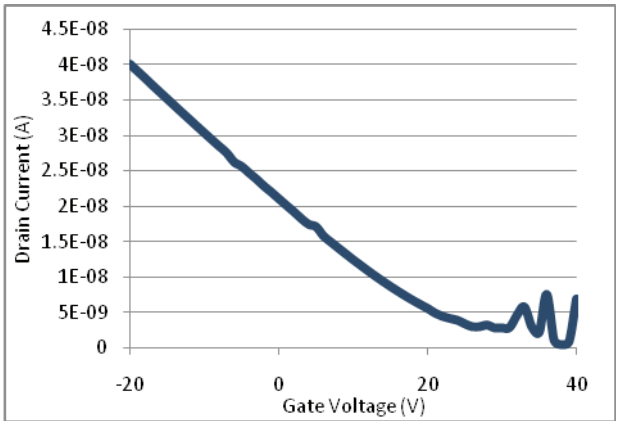

(a)

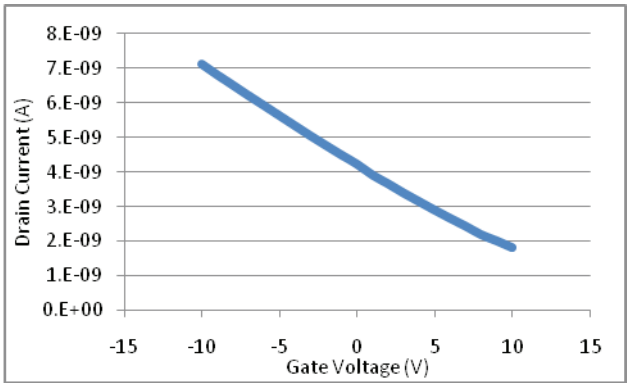

(b)

Figure 4: (a) Rieke P3HT in Non Degassed Anhydrous $CHCl_3$-Control Device #1 (air), transport characteristics; (b) Rieke P3HT in Non Degassed Anhydrous $CHCl_3$-Control #2 (inert gas), transport characteristics. Both measured at constant drain voltage of -3 V.

Degassing Technique	Mobility (cm^2/Vs)	Threshold Voltage (V)
Ultrasonic	3.03E-04	30.2
Freeze-pump-thaw	7.54E-04	28.7

Table 3. Current results after degassing the solvent

It came across that the devices had high leakage currents through the gate during the measurements, thus the gate voltage range was limited in most experiments. The most common sources were verified. Although the polymer film was completely patterned and the dielectric was tested, the inconsistent fluctuation of current leakage persisted. This also introduced an uncertain margin of error. Mainly because this leakage needed to be avoided, different gate voltage ranges were employed fluctuating between ±10 V and ±50 V.

Before the polymer deposition, in order to passivate the interface charge traps and maintain its properties between devices, an Octadecyltricholorosilane (OTS) monolayer was grown in the wafer by dip coating. This process was carried out in an inert atmosphere inside a glove-box that minimized atmospheric air and moisture effects. The devices were submerged in a well-diluted OTS solution for 1 to 2 hours, employing toluene as a solvent. After cleaning, the polymer deposition procedure was repeated to obtain two control devices. These results are summarized in Table 4.

Consequently, this step leads to a reduction on the dielectric-polymer interface variation between different devices as shown in Table 5, where the mobility stayed similar between each run.

Control Device	Mobility (cm^2/Vs)	Threshold Voltage (V)
Air	1.85E-03	24.6
Inert Atmosphere	6.58E-04	27.4

Table 4. Control devices average results using OTS monolayer, conducted at ±40 gate voltage range.

Discussion

In this study, freeze-pump-thaw demonstrated to be more effective than ultrasonic degassing. Without an analytical method to determinate the gasses' concentration in the solvent, freeze-pump-thaw permitted a visual approximation of how much gas was remaining in the solvent by observing the reducing gas flow escaping out of the solvent each cycle. Moreover, threshold voltage measurements coincided in a reduction of this property when applying freeze-pump-thaw degassing. Ultrasonic method does not offer a basic quantification of remaining dissolved gases in the solvent. It has been found that the concentration of oxygen depends on the physical properties of solvents that modify the propagation of ultrasound waves in ultrasonic degassing; which causes ultrasonic degassing to have no effects on chloroform. Concluding that this technique is not as convenient as freeze-pump-thaw to remove oxygen from most organic solvent.[7]

Placing in inert atmosphere after a vacuum reduced the threshold voltage obtained in both control devices. On the other hand, in the

second set of degassing experiments it was increased after the solvent was degassed. This could be due mostly to leakage fluctuation through the gate especially in the devices using degassed solvent. Another explanation is based on the existence of charge traps on the silicon dioxide interface that can cause threshold voltage shifts. Still the results are not adequate to determine the cause.

Interestingly, the mobility was almost invariable in the control devices as well as that from previous studies using the same degassing techniques. The current study without OTS showed the mobility was more than doubled using freeze-pump-thaw compared to ultrasonic degassing. This could be an indication of inconsistent interface conditions in the measurements in the current study. Also, both degassing methods increased threshold voltage, as opposed to the previous results. As well, this might be due to current leakage and oxygen presence during the tests, although the main cause remains unknown.

Finally the experiments utilizing OTS layer point to a trend where the threshold voltage increases as the gate voltage range gets wider. As seen in Table 5 the range increment doubled the threshold voltage, introducing another parameter to control in order to compare results. Moreover, the control devices maintained a similar gate voltage range showed a similar threshold voltage.

Conclusion

Freeze-pump-thaw represented the best degassing technique in this study. Nevertheless, more data is required to corroborate the threshold voltage behavior, since solvent degassing and current leaking represent uncertain values that may lead to misinterpretations. Further experiments should be conducted in a control environment such as a glove box to reduce the effects of oxygen coming from the environment during the testing. More important, experiments at fixed gate voltage ranges would reduce the undesired fluctuation, seen in this study, in order to reproduce the necessary data to achieve a conclusive explanation.

References

1. Horowitz, G. “Organic Field-Effect Transistors.” Advance Materials, 10 (1998): 365-377.
2. Tsumura, A., Koezuka, H., and Ando, T. “Macromolecular electronic device: Field-Effect Transistor with a polythiophene thin film.” Applied Physics Letter.49 (1986): 1210-1212.
3. Dimitrakopoulos, C., and D. Mascaro. "Organic Thin-film Transistors: A Review of Recent Advances." IBM Journal of Research & Development, 45 (2001): 11-27.
4. Sun,Y., Y. Liu, and D. Zhu.“Advances in Organic Field-effect Transistors.” Journal of Material Chemistry, 15 (2005): 53-65.
5. Abdou, MSA., F.P. Orfino, Y. Son, and S. Holdcroft. "Interaction of Oxygen with Conjugated Polymers: Charge Transfer Complex Formation with Poly(3-alkylthiophenes)." Journal of the American Chemical Society, 119 (1997): 4518-4524.
6. Sirringhaus, H. “Device Physics of Solution-Processed Organic Field-Effect Transistors.” Advance Materials, 17 (2005): 2411-2425.
7. Vencel, T., J. Donovalova, A. Gaplovsky, C. Kimura, and S. Toma. "Oxygen Exclusion from the Organic Solvents Using Ultrasound and Comparison with Other Common Techniques Used in Photochemical Experiments." Chemical Papers-chemickeZvesti, 59 (2005): 271-274.

Acknowledgments

The authors gratefully acknowledge financial support from the Center on Materials and Devices for Information Technology Research (CMDITR), an NSF Science and Technology Center No. DMR 0120967. Special thanks to everyone that was part of this great research group; their contributions are gratefully appreciated. It has been a pleasure to work during this outstanding summer opportunity.

DANIEL E. ACEVEDO is currently a senior student at the University of Puerto Rico, Mayagüez Campus where he is completing his bachelor’s degree in Chemical Engineering. He aspires to acquire a PhD in engineering to become a research scientist and contribute to enhance renewable energy efficiency and viability.

Qualitative Evaluation of Polymer Barrier Performance Using a P3HT Thin Film Optical Transmission Test

MANUEL AHUMADA, San Jose State University
Samuel Graham, Jimmy E. Granstrom, Georgia Institute of Technology

Introduction

Organic electronics, such as organic light emitting diodes (OLEDs) and organic photovoltaics (OPVs), have received high interest in the scientific community due to their potential to create low cost high performance energy efficient or energy conversion devices. A problem, which is common to both devices, is their susceptibility to water vapor and oxygen, which causes the performance of the device to degrade. To address this, vacuum deposited barrier layers have been developed to encapsulate the devices, which lower water vapor and oxygen exposure of the devices to acceptable levels. However, there is still a desire to develop solution processed barrier films in order to simplify the manufacturing process. Thus, techniques that involve the modification of polymer films, which can enable medium to high performance barriers, will have great technological and practical importance, given the low cost and the capability of high-speed fabrication with flexible electronics, in the creation of barrier systems for organic electronics. A problem that arises when dealing with polymer films is the fact that the polymer itself has a large free volume, which leaves it susceptible to rapid permeation of oxygen and water. In this work we will explore a perfluorinated polymer, Cytop™, which has been shown to improve barrier performance[1], as a potential polymer barrier and work to modify its properties to improve its barrier performance.

The evaluation of the Cytop™ barrier will be done qualitatively by using poly (3-hexythiophen) (P3HT) as an indicator of barrier performance. P3HT will be used in this study as opposed to the more commonly used calcium test. A 100 nm thick calcium film degrades in less than one minute if exposed to air. Thus, it must be deposited in a glovebox using a thermal evaporator. P3HT also degrades if exposed to air (primarily O_2), but the reactions are much slower. P3HT also requires a light source with a fairly high intensity (regular indoor lighting is not sufficient). Thus, the degradation rates for P3HT during the deposition and testing processes can therefore vary substantially. P3HT can be applied on a glass substrate in a few minutes in ambient conditions by spin coating a glass substrate with P3HT solution and curing the sample for 15 min. This process is considerably faster when compared to calcium, which needs to be handled in a glove box with low oxygen and water vapor levels, and the full process can take several hours in some cases (depending on the available deposition system). Also, given the fact that calcium films encapsulated with Cytop™ degrade in a few hours, the ultra sensitive calcium test is not needed for this qualitative study.

Experimental

In order to evaluate the barrier films, P3HT was deposited on glass substrates by a spin-coating deposition method. Unless otherwise noted, 1.5 cm x 1.5 cm square glass samples were cleaned using an acetone, methanol, and isopropanol wash. Once the samples were cleaned, a P3HT solution was made by mixing solid P3HT with a toluene solvent. The solution was then deposited on the glass substrate and spun at a rate of 1000 rpm for 60s, leaving a thin P3HT film. This sample was then transferred to a hot plate set to 100 °C for 15 min, in order to cure the P3HT film.

Then, in certain cases, a polymer barrier was deposited on top of the P3HT film, which followed the same procedure guidelines. A polymer solution was deposited on top of the P3HT film and spun at 1000 rpm for 60s then transferred to a hot plate set at 100 °C for 15 min. Figure 1 shows a schematic of the finished P3HT and Cytop™ deposition process product. Once the deposition was finished, initial light transmission tests were done.

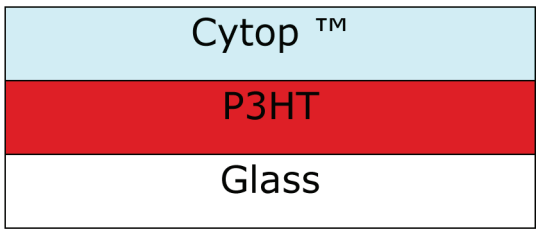

Figure 1. Schematic showing the application process of P3HT and Cytop™.

The transmission of light through the sample is then measured, followed by an exposure to a light source. The transmission of light is measured by screening the films with a light source and measuring the transmission of light through the sample with a photo-detector. The change in transmission vs. time gives relative barrier performance. Once this sample has been screened, it is exposed to a light source, which in this study is a commercial desk lamp, for a given amount of time. This process is repeated until the P3HT film is fully transparent; Figure 2 shows a comparison of a P3HT film with a fully degraded P3HT film.

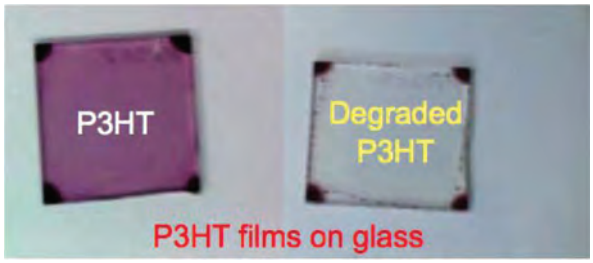

Figure 2. Comparison showing a P3HT film with no degradation and a fully degraded P3HT film.

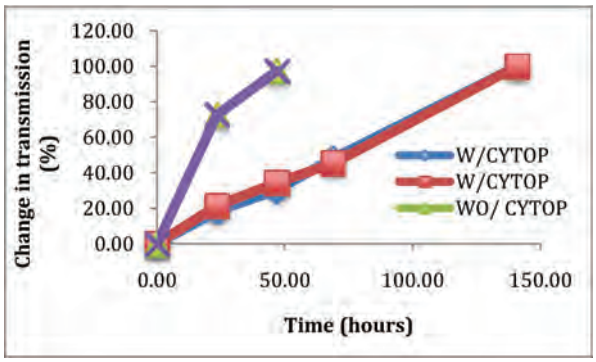

Figure 3. Relative P3HT transmission vs. time comparing a pure Cytop™ barrier with a P3HT sample with no barrier. This graph shows that, due to the fluorinated structure of Cytop™, the polymer serves as a good barrier against water and oxygen.

Results and Discussion

In order to have a baseline comparison, a pure Cytop™ barrier was spin-coated on P3HT. Based off of the results gathered from this experiment, Cytop™ increased the lifetime of P3HT by about 300% when compared to P3HT without any sort of barrier. Figure 3 shows the relative degradation of P3HT comparing P3HT samples without a barrier, and with a barrier.

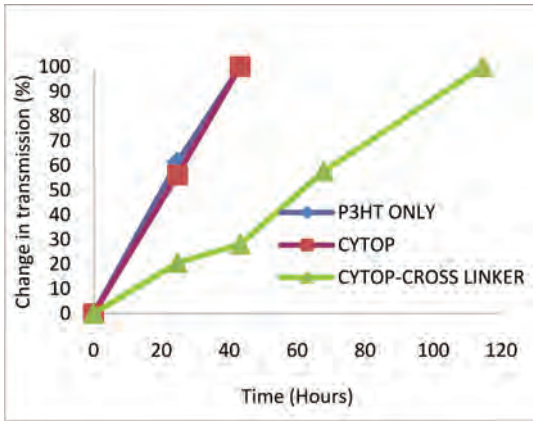

Figure 4. Relative P3HT transmission vs. time comparing pure Cytop™ with a Cytop™ cross linker mixture. It is apparent that the cross linker improved the P3HT lifetime 265%, when compared to un-modified Cytop™. It should be noted that the barrier performance of the thin Cytop™ film may be related to the poor film quality of Cytop™ on top of P3HT.

To address the problem of the free volume of Cytop™, cross linkers were introduced into the Cytop™ solution in a glove box. The cross linker used in this study, C_6-Si, has been used as a dielectric for organic field-effect transistors (OFETs)[3] C_6-Si has been used to improve the dielectric performance of thin (<100nm) Cytop™ dielectric films. Three different Cytop™ solutions were prepared with concentrations of 0.1, 0.5, and 1 vol-% cross linker, respectively. These solutions were then spin coated on top of the P3HT film and cured on a hot plate at 100 degrees Celsius for 15 minutes. The results of this experiment can be seen in Figure 4. Based off of the results gathered from this experiment it is apparent that the cross linker served as an additive which improved the barrier performance of a thin Cytop™ by 265%. Although there was not a clear difference in performance between the different concentrations of cross linker, a higher percentage of cross linker could be used in future work and cross-referenced with this data. It should also be noted that the cross-linker might segregate the Cytop™ polymer host over time, given the difference in surface energy of Cytop™ and the C_6-Si cross linker. Although no evidence of this phase segregation is available, e.g. cross-section scanning electron microscopy, it should be taken into consideration.

Given the significant improvement in barrier performance with the Cytop™ cross linker, tests were done by applying the Cytop™/ cross-linker solution on a polyethylene terephthalate (PET) substrate rather than a glass substrate given the flexible nature of PET. The Cytop™ solution was applied in the same fashion as in other tests, the Cytop™ solution was spin coated on top of the PET substrate at a rate of 1000 rpm for 60 seconds, then cured on a hot plate at 100 °C for 15 minutes. The PET/Cytop™ film was placed on top of a P3HT film, which was on a glass substrate, and sealed with a proprietary sealant. Figure 5 shows the schematic of this application. This experiment was done with control samples: one was a reference sample of P3HT encapsulated with glass; the other was a P3HT sample without any barrier.

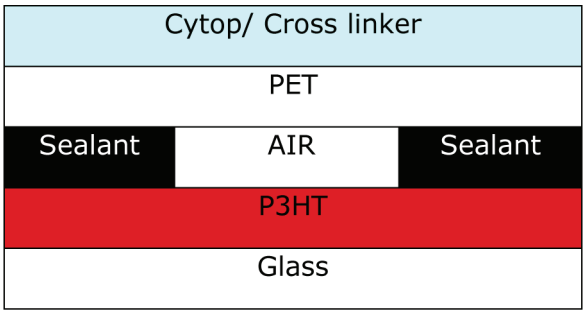

Figure 5. Schematic showing the application process.

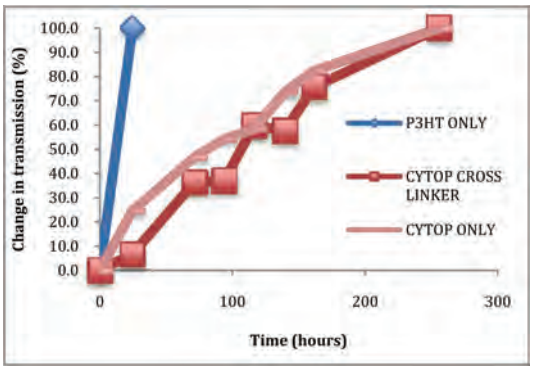

Figure 6. Relative P3HT transmission vs time for PET/ Cytop cross-linker barrier film.

The results of this experiment were as follows: the P3HT reference sample fully degraded within 24 h. The glass control sample showed the best barrier performance which shows as an indicator that the air (primarily O_2) trapped in the sample did not contribute significantly to the overall degradation of the P3HT film. The P3HT sample which had the Cytop™ barrier with the largest cross-linker amount exhibited the slowest degradation, which can be seen in

Figure 6, and the lowest amount of cross-linker degraded at the fastest rate. It is apparent that the additives had an effect on the Cytop™ barrier, possibly by filling the free volume of the Cytop™ polymer itself. More work still needs to be done to obtain more significant and consistent performance improvements for cross linked Cytop™ barrier layers. A qualitative wetting comparison on P3HT and PET was done by comparing the contact area of different solvents, since other solution-deposited barrier layers might also be interesting for future evaluation with the P3HT thin film optical transmission test. The solvents, water, methanol, propylene carbonate, CTSOLV-180, and dimethylformamide (DMF) were used in this study, since all of these solvents do not dissolve P3HT due to the solvent polarity (or perfluorinated structure of the polymer in the case of the commercial Cytop™ solvent CTSOLV-180). Figures 7-11 show the respective solvent droplets on the P3HT films. As a result of this experiment it is clear that out of the five solvents tested, CTSOLV-180, which is used in Cytop™, properly wets P3HT the best, resulting in a more uniform film.

Figure 7. CTSOLV-180 droplet on a P3HT film. This image shows that, when compared to the four other solvents tested, CTSOLV-180 properly wets P3HT, resulting in a more uniform film.

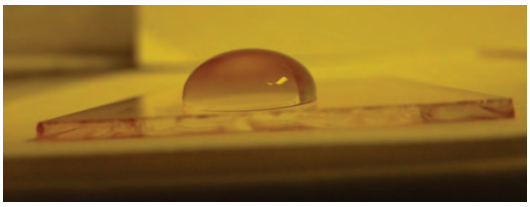

Figure 8. H_2O droplet on a P3HT film.

Figure 9. DMF droplet on a P3HT film.

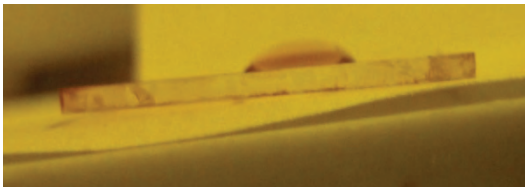

Figure 10. Methanol droplet on a P3HT film.

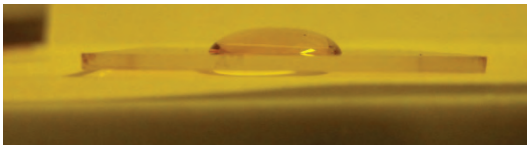

Figure 11. Propylene carbonate droplet on a P3HT film.

Summary

The P3HT thin film optical transmission test has been used as a cost-efficient method of qualitatively screening the barrier performance of (modified) polymer barrier layers. P3HT films encapsulated with the perfluorinated, hydrophobic polymer Cytop™ exhibited significantly longer P3HT lifetimes compared with equivalent films which had not been encapsulated. The cross-linker used in this experiment showed promising results. The fact that the solution cross-linked in air could have affected its barrier performance against water and oxygen, although the details of the mechanism are not clear at this time.

References

1. J. Granstrom, J. S. Swensen, J. S. Moon, G. Rowell, J. Yuen, and A. J. Heeger, Appl. Phys. Lett. 93, 193304 (2008).
2. J. S. Lewis and M. S. Weaver, IEEE J. Sel. Top. Quantum Electron. 10, 45 (2004).
3. X. Cheng, M. Caironi, Y. Noh, J. Wang, C. Newman, H. Yan, A. Facchetti, H. Sirringhaus Chemistry of Materials. 22, 1559 (2010).

Acknowledgments

This research was done in conjunction with the National Science Foundation (NSF), Grant # 0120967, Materials and Devices for Information Technology Research (MDITR).

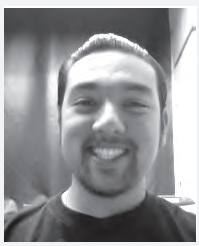

MANUEL AHUMADA is a mechanical engineering student attending San Jose State University entering his junior year. His goal is to obtain a PhD degree and apply what he has learned in school to a job in industry.

Durability Testing of Barrier Films for Flexible Electronics

GERARDO AVITIA, Arizona State University
Yongjin Kim, Samuel Graham, Georgia Institute Of Technology

Introduction

Flexible organic electronic devices have the potential to revolutionize applications in displays, lighting, integrated circuits, photovoltaic devices, electrochromic devices, and transistors. A broad range of viewing angles, lower energy requirements, and brighter displays are some of the many advantages that can be possible with flexible organic electronic devices. In spite of many attractive features, many issues arise preventing this technology from expanding wider into the commercial market. Degradation due to reactions with oxygen and moisture molecules is a primary concern, causing most organic devices to require barrier layers to prevent environmental exposure. Each application has its own barrier needs, with Organic Light Emitting Diodes (OLEDs) requiring the most stringent values of Water Vapor Transmission Rate (WVTR) and Oxygen Transmission Rate (OTR) at 1 x 10^{-6} g/m^2•day and 1 x 10^{-3} cm^3/m^2•day.[1] In general, many of the high performance barrier layers contain brittle inorganic layers and polymer films which have limited flexibility and mechanical reliability. These films must be coated onto polymer substrates to enable flexible applications. Coating the substrates with thin films has shown to lower the WVTR and OTR to acceptable levels while their durability has not been completely determined. Damage can be imposed to the organic layers and barriers by bending of the device. Once the barrier layers are damaged, moisture and oxygen molecules readily penetrate and degrade the device. Durability testing can determine the stresses and failure mechanisms and can lead to a better understanding of the material requirements for these devices.

Experimental Methods

A calcium degradation test was employed to test the effectiveness of the barriers. PET lids of dimension 1 in. x 15.4 µm x 125 µm were coated with different configurations of SiO_x and SiN_x with the use of the Unaxis PECVD. These configurations include: a single layer of SiN_x, single layer of SiO_x, four layers of SiN_x, alternating layers of SiN_x and SiO_x with SiN_x deposited first, alternating layers with SiO_x deposited first, and five layers of SiO_x and SiN_x in an alternating layer structure. All of the barrier films are a total of 100 nm thick. A thermal deposition system was used to deposit aluminum electrodes and calcium sensors of dimension 4 mm x 7 mm onto glass substrates of 1x1 in^2. The calcium was encapsulated with the coated PET lids with the use of sealing material inside a glovebox system. The encapsulated calcium sample was mounted onto a 1 in. x 3 in. glass and copper tape was fixed onto the Al electrodes with Silver Epoxy. The configuration can be seen in Figure 1. The four points probe method was used to measure the resistance every three minutes via the Agilent 34970A Data Acquisition/Switch Unit until the calcium degraded.

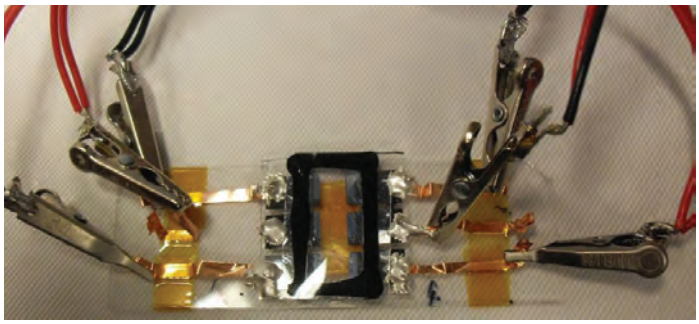

Figure 1. Demonstrates the calcium encapsulated between a glass substrate and barrier coated PET lid with the use of a sealing material.

The bending radius test was employed to test the durability of the inorganic thin film barriers. The configurations of barrier films described for the calcium degradation test were used for the bending radius test. The barrier films were deposited via Unaxis PECVD onto PET strips of dimension 75 mm x 15 x 125 µm. The PET strips were clamped to the instrument and bent to various radii (Figure 2). Inspection of films for cracks was done via the Nikon Eclipse ME600 microscope. The images were captured along a line perpendicular to the length, where the minimum radius (R_{min}) and thus maximum strain (ε_{max}) is located. The bending radius was calculated using the relationship $R=L_p/(2 \times 1.198)$, where L_p is the plate separation.[2] The strain values were calculated by $\varepsilon=y/R$, where y is half of the thickness of the PET substrate and R is the bending radius.[2]

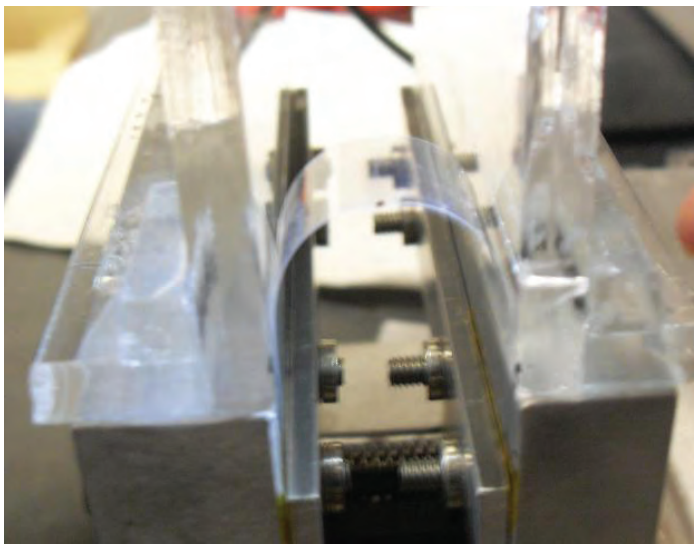

Figure 2. Bending radius test set-up. The bending radius can be calculated from the plate separation seen above.

Results

Values for the effective WVTR were calculated with the use of the following equation:

$$WVTR[g/m^2/day] = 2\delta_{Ca} \times \rho_{Ca} \times \frac{dG_S}{dt} \times \frac{M(H_2O)}{M(Ca)} \times \frac{Ca\_Area}{Window\_Area}$$

The value dG_s/dt is the slope of the linear portion of the conductance over time plot.[3] A linear fit of this portion for the different barriers was created to obtain the value dG_s/dt. The calculated effective WVTR values for all of the barrier structures can be seen in Table 1. Cracks in the barrier films were at first not apparent under the Nikon Eclipse ME600 microscope. A black permanent marker was used to draw a line across the width of the PET coated strips at the midpoint of the length, which resulted in better crack imaging. Table 2 shows the resulting strain ε corresponding to the values of bending radii for which the films experienced the onset of cracking.

Film structure/composition	WVTR [g/m^2/day]
SiO_x (100nm)	3.26×10^{-2}
SiN_x (100nm)	2.03×10^{-3}
SiN_x (25nm)/SiO_x (25nm)_Total(100nm)	1.94×10^{-3}
SiO_x (25nm)/SiN_x (25nm)_Total(100nm)	1.04×10^{-3}
SiN_x (10nm)/SiO_x (10nm)_Total(100nm)	1.94×10^{-3}
SiN_x (25nm)/SiN_x (25nm)_Total(100nm)	2.27×10^{-3}

Table 1. Shows the effective WVTR values for the different barrier films.

Film structure/composition	R (mm)	ε (%)
SiO_x (100nm)	5.829	2.14
SiN_x (100nm)	6.664	1.88
SiN_x (25nm)/SiO_x_100nmTotal	<6.664	<1.88

Table 2. Shows the bending radius (R) and associated strain (ε) at the onset of cracking.

Discussion

The SiN_x barrier layer and barriers containing SiN_x in their structure demonstrated superior WVTR values over SiO_x by an order of magnitude. Analysis of the surface morphology of the barrier films on PET by Atomic Force Microscopy indicate that SiN_x provides a smoother surface when compared to SiO_x, Figure 4. This indicates that the SiN_x is a denser film, which helps explain why it performed as the more efficient barrier. Due to its denser configuration, there are less nanoscale defects, such as pinholes, through which atmospheric gases permeate. Another explanation for this phenomenon can be the presence of nitride chemical reactions when permeation of moisture occurs. These reactions have been shown to dissociate a fraction of the moisture molecules and effectively trap the oxygen species, thus lowering the permeation rate.[4]

Multi barrier structures were hypothesized to create noticeable improvements in the WVTR values. As can be seen from Table 1, this is not the case. All of the alternating layer barriers are in the 10^{-3} g/m^2/day range. It is believed that the interfaces have no effect on the WVTR performance because the process of permeation is defect driven. The reason for these results could be due to the deposition method that was utilized. Literature in which multi barrier structures have been shown to improve the WVTR cite Atomic Layer Deposition (ALD) as the deposition process. It is likely that the method used here, PECVD, does not produce uniform layers to the level of those produced by ALD, thus allowing defects to be the means of permeation. In order to determine if the SiN_x and SiO_x multi layer barriers are effective, deposition by ALD is necessary.

From the bending radius test, SiO_x was found to be the more rugged barrier layer with crack initiation at a radius of 5.829 mm and strain of 2.14% (Table 2). As can be seen, the SiNx is slightly more brittle as cracks appear at a strain of 1.88%, while the more brittle films are the multilayer barriers. Due to the possibility of damage to the barrier films when the sample was taken out of the bending radius test and placed under the microscope, the strain values may not be correct. Since all of the films underwent the same conditions, it is safe to state that the test can identify the better barrier. Large area rollable sheets are the goal when it comes to manufacturing organic flexible electronics. As such, it has been stated that the barrier films be tested for bending radii of values ranging from 3 to 20 mm.[1] Currently, it is inconclusive if the films tested here would be able to perform under such conditions. The oxide and nitride layers are not appropriate if a 3 mm radius is necessary for flexible electronics.

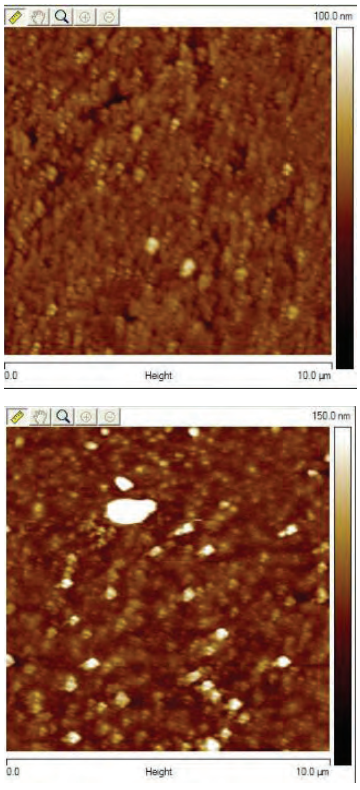

Figure 3. AFM images of SiN_x (100 nm) on PET (top) and SiO_x (100 nm) on PET (bottom). The former has a roughness of 5.72, thus it is more dense than SiO_x with a value of 19.3 nm.

Conclusion

Six configurations of barrier films composed of SiN_x and/or SiO_x were deposited onto PET and tested via the Calcium Corrosion Test. Barrier films containing SiN_x performed in the 10^{-3} g/m^2•day WVTR range. A single layer SiO_x barrier had a WVTR of 3.26×10^{-2} g/m^2•day. The multi layer barriers were hypothesized to show dramatic improvements in WVTR values. However this was not the case and it is probable that the method of deposition, PECVD, is the reason why improvements did not occur.

Barriers that were tested mechanically include: SiO_x (100 nm), SiN_x (100 nm), and SiO_x/SiN_x (2 layers, 25 nm each). The last barrier film was of an alternating layer configuration with SiN_x deposited first. SiO_x performed the best as it initiated cracking at a radius of 5.829 mm and strain of 2.14%. SiN_x initiated cracking at a radius of 6.624 and strain of 1.88% while the alternating layer structure at a slightly lower strain. Further research is required to determine if these films can be used for some flexible electronic device applications.

Future Work

In order to determine if the barrier films presented can be used in flexible applications, more durability testing is required. As such, the Fragmentation Test can be used to more accurately determine the initiation of cracking. This test can also be used to determine the mid-point cracking stage as well as the delimitation stage. More information about the cohesive strength of the barriers and adhesion to the PET substrate is required. The DTS Delaminator Test can be employed to determine these values. Cyclic Testing and corrosion testing after the barriers have been bent can determine a lot about the durability of the films.

References

1. Lewis, J.S.; Weaver, M. S. J. Sel. Top. Quant. 2004, 10, 45-57.
2. Grego, S., et al., J. Soc. Info. Display 2005, 13, 575-581.
3. Paetzold, R.; Winnacker, A.; Henseler, D.; Cesari, V.; Heuser, K. Rev. Sci. Instrum. 2003, 74, 5147-5150.
4. Erlat, E. G.; Henry, B. M.; Grovenor, C. R. M; Briggs, A. G. D. J. Phys. Chem. B 2004, 108, 883-890.

Acknowledgements

Funds for this research were provided by the Center on Materials and Devices for Information Technology Research (CMDITR), an NSF Science and Technology Center No. DMR 0120967. I would like to give special thanks to Yongjin Kim, Hyungchul Kim, Samuel Graham, and Jimmy Granstrom for all of their help. Thanks to the Kippelen Research Group for allowing us to use their labs.

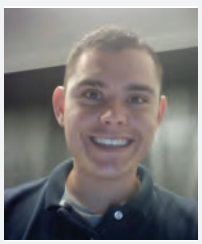

GERARDO AVITIA currently attends Arizona State University and plans on obtaining a Master's Degree in Mechanical Engineering.

Solution-Processable Squaraines as Donors for Organic Photovoltaics

VASHTI M. CAMPBELL, Norfolk State University
Seth Marder, Yanrong Shi, Georgia Institute of Technology

Introduction

Squaraines (Figure 1) are organic dyes that are distinguished by their aromatic four membered ring that is derived from squaric acid. These dyes are typically the condensation products of electron-rich aromatic or heterocyclic compounds.[1] With wide structural diversity, squaraines have been intensely studied for various applications, including photodynamic therapy,[2, 3] biologic labeling,[4] optical imaging,[5] ion sensing,[6, 7] photovoltaics, and light- emitting field-effect transistors.

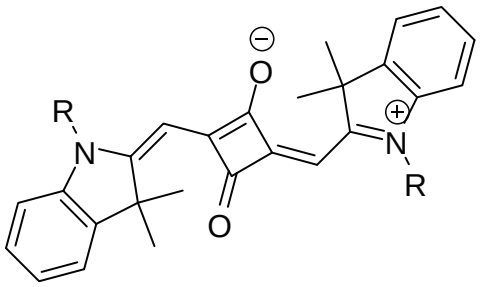

Figure 1. Squaraine.

One of the characteristic properties of squaraine is its high molar extinction coefficients ($\varepsilon > 10^5$ M^{-1} cm^{-1}) in the visible and near infrared region of the spectrum. In solid states, as a consequence of strong intermolecular charge transfer interactions and tendency to aggregate, squaraine absorption bands generally become rather broad. Structure modification, by extending conjugation or incorporating a variety of substituents, could effectively tune the energy level of squaraines to meet specific requirements for particular applications.

Photovoltaic science and technology is related to the processes of converting solar energy directly into electricity, which is believed to be one of the clean alternative energy sources to fossil fuels in the near future.

Squaraines are useful as donor molecules in OPV systems. Our goal is to incorporate squaraine moieties into polymers to improve the processability and morphology of the materials. Also squaraines can be copolymerized with other acceptor units like perylene diimde and naphthalene diimde to form donor-acceptor type copolymers as active layer for OPVs. Branched alkyl chains will be used to increase the solubility while oligo-ethylene glycol chain may help the intermolecular packing to control film morphology in the solid states. Making squaraines with dibromo or diacetylene functionality is the target of our research as shown in Figure 2, with preluding synthesis procedures shown in Figure 3.

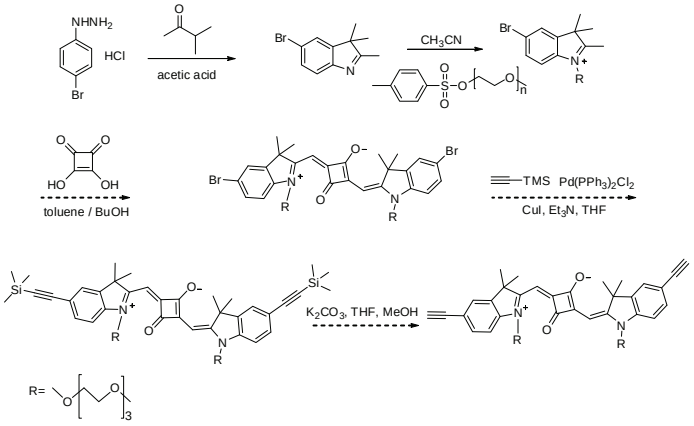

Figure 2. Synthesis of Squaraine

Experimentation

We initially approached the development of squaraine by synthesizing 5-bromo-2,3,3-trimethyl-3H-indole.

Preparation of Indoline compound

A mixture of 4-bromophenylhydrazine hydrochloride (4.27 g, 19.1 mmol) and 3-methyl-2-butanone (1.64 g, 19.1 mmol) were combined in a round bottomed flask. About 50 mL of acetic acid was added and the mixture was heated to 100 ºC overnight. The reaction mixture was extracted using dichloromethane as the solvent. Anhydrous sodium sulfate powder was added to remove any water particles. The dichloromethane solvent was then removed via rotary evaporator. The pure product was a reddish-orange liquid, 4.19 g (92 %).

^{1}H NMR (300 MHz, $CDCl_3$) δ (ppm) 7.24-7.39 (m, 3H), 2.24 (s, 3H), 1.27 (s, 6H).

The alkyl group, 1-(bromomethyl) tricosane was reacted with the indole to possibly enhance solubility of the compound.

Preparation of Mesylate

A solution of methane sulfonyl-chloride (19.1 g, 167 mmol) in dry diethyl ether (100 mL) was added drop wise to a solution of $HO(CH_2CH_2O)_2Me$ (20 g, 167 mmol) and triethylamine (16.9 g, 167 mmol) in diethyl ether (75 mL) over a 60 min period. This mixture was stirred for 30 min and then filtered. The filtrate was evaporated to dryness to yield the product, 24.14 g of a colorless liquid (73.1%).

^{1}H NMR (300 MHz, $CDCl_3$) δ (ppm) 4.38 (d, J = 13 Hz, 2H), 3.54 (m, 2H), 3.53 (m, 2H), 3.52 (m, 2H), 3.37 (s, 3H), 3.06 (s, 3H).

Preparation of 2,5,8,11,14-pentaoxahexadecan-16-ol

Triethylene glycol (3 g, 20 mmol) was added drop wise under nitrogen to a solution of sodium hydride (0.528 g, 22 mmol) in THF (30 mL) in an ice bath. The reaction was stirred for 15 min and a solution of 2-(2-methylethoxy) ethyl methane sulfonate (2.1 g, 10.6 mmol) in THF (4.3 mL) was added. The ice bath was removed and the reaction was refluxed overnight. The solid was then filtered out. The filtrate was concentrated and purified by silica gel chromatography (CH_2Cl_2: EtOAc = 3:1), and the product was isolated via evaporation of solvent using the rotary evaporator, 0.113 g (4.5%).

^{1}H NMR (300 MHz, $CDCl_3$) δ (ppm) 4.23 (s,

Preparation of Indolium compound

A mixture of 5-bromo-2,3,3-trimethyl-3H-indole (4.74 g, 19.9 mmol) and 2,5,8,11,14-pentaoxahexadecan-16-yl-4-methylbenzenesulfonate (6.30 g, 19.9 mmol) were combined in a round-bottomed flask under N_2. The mixture was heated to 100 ºC for 12 h. The mixture was diluted with 20 mL of dichloromethane and extracted with 40 mL of deionized water. The aqueous phase was washed with 30 mL of dichloromethane and the water was evaporated under reduced pressure to give the crude product which needs further purification.

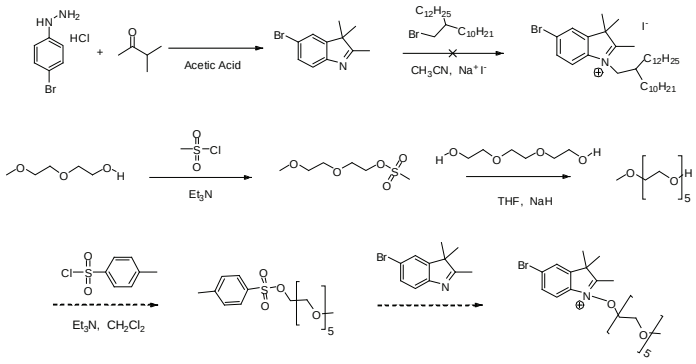

Figure 3. Synthesis

Results and Discussion

To begin synthesis of the squaraine molecule, it required the preparation of the indoline compound. During the reaction, the solution turned from clear to an orange speckled solution. The successful reaction process of this compound yielded about 92.3% of deep reddish- orange product.

During preparation of the indolium compound, an initial deep red color was observed. After one day of reflux, the solution had turned a dark brown color. Thin layer chromatography was performed on the solution in dichloromethane. There was no product spotting found. After five days of refluxing and no progression, microwave (Figure 4) was used to accelerate the reaction at 150 °C.

Figure 4. CEM Discover Microwave

However, further experimentation suggested that the compound might be too bulky to add to the indole. Thin layer chromatography was performed on a sample of the reaction to make sure it had been driven to completion. Thin layer chromatography (TLC) is a method of separation whereby a mixture is separated by a moving phase permeating a stationary phase (Figure 5). In this experiment, the reaction mixture was spotted on a glass TLC plate made of silica gel and put into dichloromethane that moved up and separated the reaction mixture via capillary action. Also, a gas chromatography-mass spectrometry (GC) machine helped determine whether the reaction was complete or not. The results of the TLC and GC mass showed the reaction was still not complete.

In order to effectively separate the low-boiling solvent from the mixtures of compounds, a rotary evaporator was used.

The machine reduced the pressure in the system, which in turn lowered the boiling point of the solvent and caused a vacuum effect to remove the solvent. The structure and purity of a compound can be determined by nuclear magnetic resonance (NMR).

NMR (Figure 6) functions by sending out electromagnetic pulses that are absorbed by the nuclei in the material being examined and as a result, the nuclei exude the energy. The energy is measured out in resonance frequency. A 300 MHz NMR spectrometer was used to test the product. NMR spectral data showed the product had not been synthesized. A longer chain, like a pentaethylene glycol group, was proposed to more readily attach to the indole.

When testing the ethylene glycol molecule reactions, the spots were not UV sensitive on TLC plates so the spotted compound had to be oxidized in an iodine chamber to stain them. The products typically had to be purified via silica gel column. The compound readily dissolved in water due to several oxygen atoms in the chain. Both

dichloromethane and ethyl acetate were used to wash the compound down the column.

The mesylate, 2-(2-methylethoxy) ethyl methane sulfonate, was made and 73.1% of pure colorless liquid was recovered. This compound was in turn used to synthesize 2,5,8,11,14-pentaoxahexadecan-16-ol. NMR spectral data showed the product was indeed formed. The compound was reacted with a tosylate group in triethylamine and dichloromethane. The tosylate group is a good leaving group for the compound. The tosylate compound finally reacted with the indoline compound to form the indolium compound.

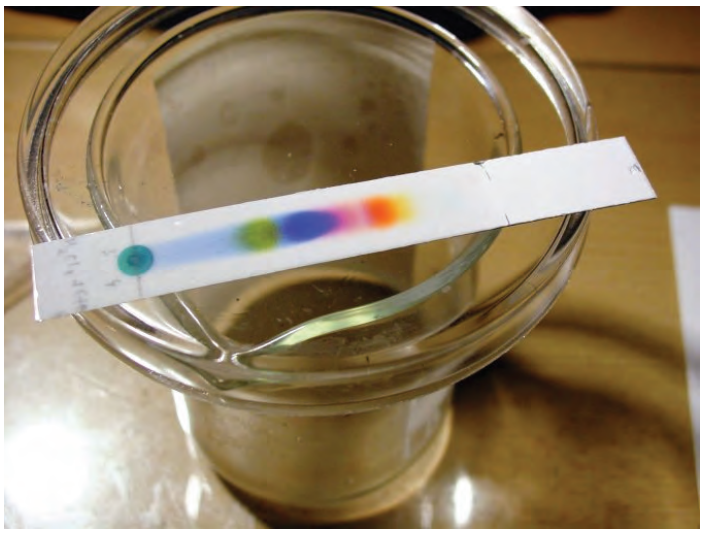

Figure 5. Thin Layer Chromatography.
<http://www.dia.unisa.it/~ads/BIOINFORMATICA/Proteomica/index.html>

Figure 6. NMR
<www.pharmacy.arizona.edu/faculty/yanglab/>

Conclusion

Although the squaraine molecule was not produced in this project, experimental data has helped us generate helpful findings. Attempts to attach the compound 11-(bromomethyl) tricosane failed possibly because of the bulky structure of the compound. Experimentation with the ethylene glycol oligomers is now underway. Ongoing work will finish development and purification of the squaraine molecule.

References

1. Beverina, L.; Salice, P. Eur. J. Org. Chem. 2010, 1207-1225.
2. Devia, D. G.; Cibina, T. R.; Ramaiahb, D.; Abraham, A. J. Photochem. Photobiol. B 2008, 92, 153-159.
3. Jisha, V.S.;Arun, K. T.;Hariharan, M.;Ramaiah, D. J. Phys. Chem. B 2010, 114, 5912-5919.
4. Sameiro, M.; Gonçalves, T. Chem. Rev. 2009, 109, 190-212.
5. Escobedo, J. O.; Rusin, O.; Lim, S.; Strongin, R. M. Curr. Opin. Chem. Biol. 2010, 14, 64-70.
6. Sreejith, S.; Divya, K. P.; Ajayaghosh, A. Agnew. Chem.. Int. Ed. 2008, 47, 7883-7887.
7. Ajayaghosh, A.; Chithra, P.; Varghese, R. Agnew. Chem. Int. Ed. 2007, 46, 230-233.

Acknowledgements

We thank the National Science Foundation No. DMR 0120967 for financing this project. I thank the Marder Group and the Georgia Institute of Technology for funding and necessary resources.

VASHTI M. CAMPBELL attends Norfolk State University where she is a chemistry major entering her junior year. Vashti plans to pursue a doctorate degree and is interested in cosmetic science.

Silicon Photonics for Biosensing Applications

ELIJAH CHRISTENSEN, University of Washington
Daniel Ratner, Michael Hochberg, University of Washington

Introduction

Background

The quantitative chemical composition of a solution is often important in providing medically relevant diagnostic information. Examples include quantifying serum biomarkers, blood typing for a successful transfusion or diagnosing an infection. Chromogenic or fluorogenic reporters in conjunction with a targeting agent, such as an antibody, are often used to quantify the concentration of specific analytes in solution. By utilizing first order enzymatic amplification of the reporter signal, the intensity can be proportional to the amount of analyte present. The enzyme linked immunosorbent assay (ELISA)[1] is an example of this and is used extensively in diagnostics and research. However, the reagents used in these assays are costly in large quantities, which can make their use prohibitive in distributed diagnostics or low resource settings. However, the development of plasmonic and photonic sensors has made it possible to measure diminutive changes in the refractive index of a solution without the need for reporter molecules. If the surface of the sensor is functionalized with a specific capture ligand, the binding of its target analyte causes a shift in the local effective refractive index that is proportional to the amount of mass captured by the ligand. Through binding kinetics the amount of mass bound to the ligand will reach equilibrium with its surroundings based on the concentration of analyte and the affinity constant of the ligand. The ability to quantify analyte in solution without the use of chemical reporters is known as label-free biosensing. The most commonly used label-free real-time biosensor is based on Surface Plasmon Resonance (SPR).[2] While this technique offers significant advantages in throughput and miniaturization, the hardware for SPR is difficult to mass produce at marginal cost and requires a carefully controlled environment (i.e. laboratory setting). A novel alternative to SPR is the use of photonics to detect changes in refractive index.

The application of photonics to biosensing coalesces many of the advantages of SPR such as high throughput and reduced reagent consumption, with the potential of scalability and portability. The silicon ring resonator is arguably one of the most promising photonic devices for biosensing due to its small size and manufacturing ease.

The Ring Resonator

The ring resonator is an annular device typically fabricated from a material such as silicon, silicon nitride or glass. Ring resonators can include microspheres,[3] microtoroids,[4] or simple ridge micro-ring resonators[5] as shown in Figure 1. A ring resonator confines light that has been coupled into it from a light source. On resonance, the optical signal experiences an integral multiple of 2π radians of phase shift for a round-trip around the ring. As a result, at a specific wavelength a noticeable decrease in the transmitted power from the light source is detected as the light is coupled into the resonator.

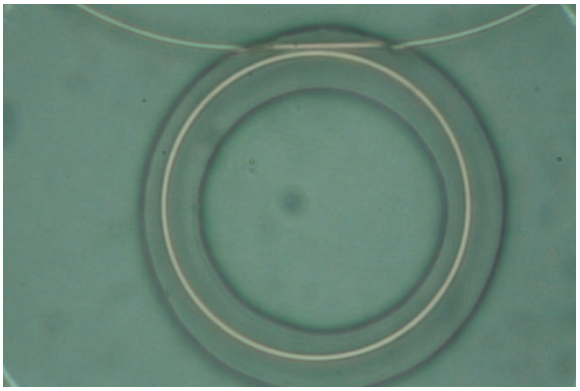

Figure 1. Brightfield image of a silicon on insulator (SOI) ring resonator lying adjacent to an incident waveguide. A fluoropolymer cladding has been lithographically eteched around the ring resonator exposing its surface.

An example transmission spectrum of a ring resonator is shown in Figure 2.

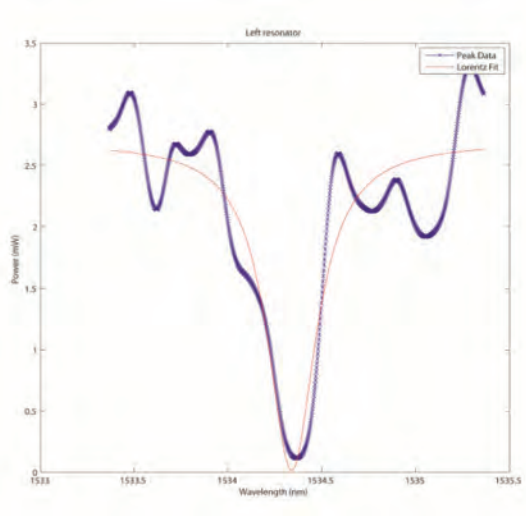

Figure 2. An example transmission spectrum from a ring resonator with a Lorentzian fit (the theoretical shape of the peak) using a multiparamter non-linear fit. As light couples into the resonator it destructively interferes with the light source causing an abrupt decrease in transmitted power.

Refractive indices in solutions are often represented as the effective refractive index, or η_{eff}. The effective refractive index is directly proportional to the concentration of the solution surrounding the resonator. Light couples into the resonator at specific wavelengths as defined by:

$$\lambda = \frac{2\pi r \eta_{eff}}{m} \quad (1)$$

Where *r* is the radius of the ring resonator and *m* is an integer. Thus, by monitoring the wavelength at which the light couples into the resonator it is possible to detect diminutive changes in the local effective refractive index. If the ring is functionalized with a unique capture ligand the change in the rings' resonant peak location upon exposure to analyte will be proportional to the mass of captured analyte on the surface of the resonator. The mass of analyte captured on the surface of the sensor will reach an equilibrium with the surroundings that is dependent on the concentration of analyte. This approach has been used to demonstrate quantized single molecule detection of molecules as small as 15 kDa using silicon microtoroids.[4] They show that molecules of this size induce a shift of 0.02 ± 0.01 pm. We can estimate the shift that would be seen in one of our ring-resonators by using equation (2).

$$\delta\lambda = 2.6 * 10^{-7} \frac{1}{nm} A\lambda \frac{L_{molecule}}{L_{resonator}} \quad (2)$$

Where *A* is the cross sectional area of the molecule, $L_{resonator}$ is the path length of the resonator, λ is the wavelength of light at resonance, and $L_{molecule}$ is the length of the molecule. If we assume a 10 x 10 x 10 nm molecule and a 15 µm radius ring resonator we would estimate a 0.004 pm shift per molecule.

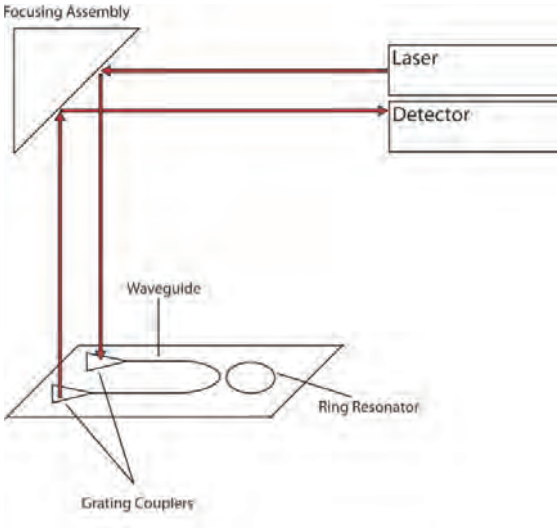

Figure 3. Diagram illustrating photonic ring resonator system. Light from a tunable laser source is directed by the focusing assembly into a silicon waveguide that guides light past a ring resonator and then returning to a detector where the transmitted power is measured.

Microring resonators can be easily fashioned on silicon wafers using electron beam lithography and traditional silicon foundry processes. Nanofabrication advances introduce the opportunity to prototype silicon devices with 10 nm tolerances.[6] Thousands of ridge micro-ring resonators can be made on a single 1 cm x 1 cm chip. With chemical functionalization, each ring can be used to detect a unique biomarker, potentially allowing multiplexed diagnostic biosensing.

The system used to execute these experiments utilizes a tunable laser source, focusing assembly, and an array of waveguides and ring resonators to measure refractive index changes. A simplistic diagram of this system is depicted in Figure 3. The focusing assembly directs the laser into the ridge waveguide, via a grating coupler, which guides the light past the resonator and back to a detector. As the laser sweeps through a set of wavelengths the detector measures the transmitted power. Analysis software is then used to identify the peak location and track its movement over time.

The photonics chip used to conduct the experiments contains an array of 32 individually addressable resonators. The surface of the chip was coated in the fluoropolymer and then lithographically removed in an annular area surrounding each resonator, exposing them to the surface environment.

η_{eff} is dependent on temperature, so fluctuations in the local thermal environment can be a significant source of noise in the system. This is known as the thermo-optic effect. Methods to control this source of noise include tightly regulating the local thermal environment or designating a resonator as a thermal control and subtracting its signal from the functional resonator.

Experimental Objectives

The objective of these experiments was to determine the noise floor of the current system and attempt to improve it. Our goal after characterizing the noise floor of the system was to reduce it by a factor of 2. To characterize the noise floor, 32 resonators were monitored continuously for 2 h without stimulus with both water and air cladding. In the water experiments the chip was allowed to equilibrate in DI water for 24 h prior to the experiment to prevent ion desorption from the surface. In an attempt to correct the noise due to thermal drift, 2 resonators were selected from the 32 to be used as a thermal references and subtracted from the other functional rings. The experiment duration of 2 h was selected as this is twice as long as a typical experiment would take. Outliers that display erratic behavior have been removed from all plots for the purpose of clarity.

Results

Air cladding, without thermal correction

An experiment was conducted under air cladding for 2 h where the data was not thermally corrected. The result of this experiment is shown in Figure 4. The root mean square (RMS) of the resonators was found to be 3.13 ± 0.85 pm.

Air cladding, with thermal correction

After the 2 h experiment was conducted under air, cladding with thermal correction was applied.

Resonators 18 and 27 were selected as thermal controls and their

mean was subtracted from the functional resonators. The noise floor on an air clad experiment after thermal referencing is shown in Figure 5.

The RMS across all functional resonators was found to be 0.86 ± 0.43 pm after thermal referencing.

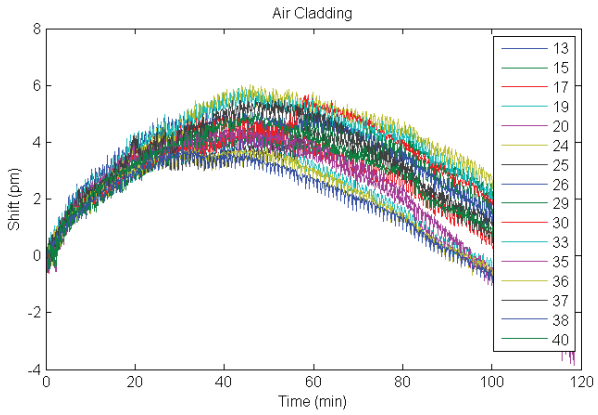

Figure 4. Plot showing the shift in the resonant peak location for a 2 h experiment without thermal correction. The ring resonator is clad in air.

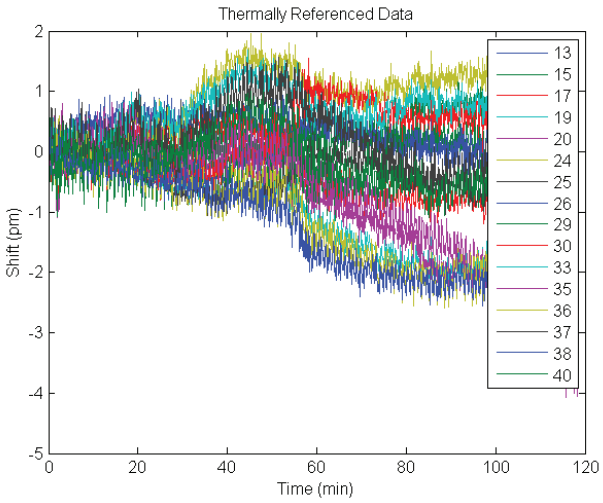

Figure 5. Plot showing the shift in the resonant peak location for a 2 h experiment where the ring resonator is clad in air and normalized to two temperature references.

Water cladding, without thermal correction

All resonators were continuously monitored under water cladding for 2 h without stimulus. The results of this experiment are displayed in Figure 6.

The RMS of each resonator was calculated for all 24 resonators and was measured to be 23.56 ± 2.47 pm. This large drift is due to cooling of the chip as it is exposed to water and exemplifies the device's high sensitivity to its thermal environment.

Water cladding, with thermal correction

A 2 h experiment was conducted under water cladding where all resonators were continuously monitored without stimulus.

As before, resonators 18 and 27 were selected and used as thermal references. The mean of these 2 resonators was calculated and then subtracted from each functional resonator to produce the thermally corrected data shown in Figure 7. The RMS of each resonator was calculated for all functional resonators and was measured to be 4.98 ± 2.32 pm.

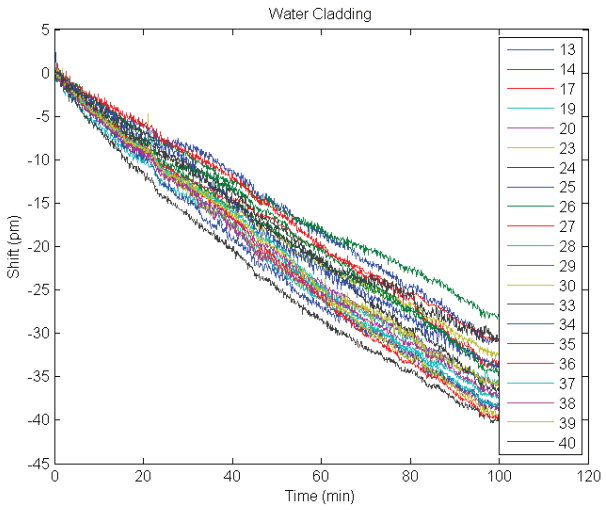

Figure 6. Plot showing the shift in the resonant peak location for a 2 h experiment where the ring resonator is clad in water. Thermal correction is not applied.

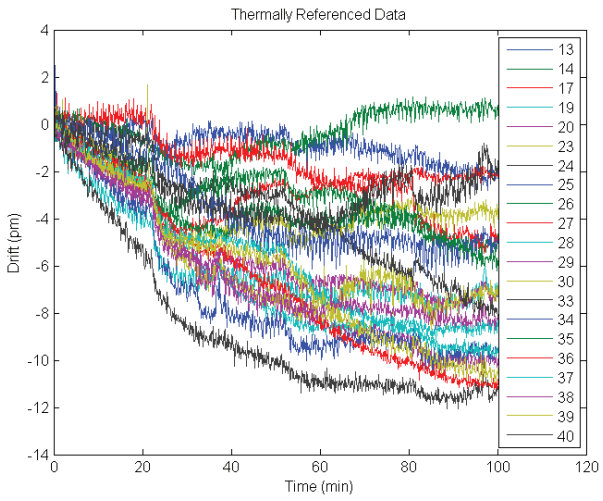

Figure 7. Plot showing the shift in the resonant peak location for a 2 h experiment where the ring resonator is clad in water and normalized to two temperature references.

	Without thermal correction	With thermal correction
Air Cladding	3.13 +/-0.85 pm (n=16)	0.86 +/-0.43 pm (n=14)
Water Cladding	23.56 +/- 2.47 pm (n=22)	4.98 +/- 2.32 pm. (n=20)

Conclusions

Non-referenced experiments show large amounts of error in the form of thermal noise which can have RMS error as high as ~23.56 pm in experiments involving fluids due to cooling of the device.

We have demonstrated that thermal correction does improve the noise floor of the system. Thermal referencing improves the noise floor by at least a factor of 3.5. This allows us to go from being able to detect single 60 MDa particles to 17 MDa particles. At this sensitivity it is theoretically possible to detect the binding of a single virus.

References

1. Engvall E., Perlmann P. Enzyme-linked immunosorbent assay, ELISA .3. quantitation of specific antibodies by enzyme-labeled anti-immunoglobin in antigen-coated tubes. Journal of Immunology 1972;109(1):129.
2. Homola J., Yee S.S., Gauglitz G. Surface plasmon resonance sensors: review. Sensors and Actuators B: Chemical 1999; 54(1-2):3-15.
3. Vollmer F., Arnold S. Whispering-gallery-mode biosensing: label-free detection down to single molecules. Nature Methods 2008;5(7):591-596.
4. Armani A., Kulkarni R., Fraser S., Flagan R., Vahala K. Label-free, single-molecule detection with optical microcavities. Science. 2007, 317(5839), 783-787.
5. De Vos K., Bartolozzi I., Schacht E., Bienstman P., Baets R. Silicon-on-Insulator microring resonator forsensitive and label-free biosensing. Opt. Express 2007, 15(12), 7610-7615.
6. Holzwarth C.W., Khilo A., Dahlem M., et al. Device architecture and precision nanofabrication of microring-resonator filter banks for integrated photonic systems. J Nanosci Nanotechnol. 2010; 10(3): 2044-2052.

Acknowledgements

Funds for this research were provided by an NSF CBET (award no. 0930411) grant, the Washington Research Foundation, the Center on Materials and Devices for Information Technology Research (CMDITR), an NSF Science and Technology Center No. DMR 0120967.

I would like to thank both the Ratner Lab and the Hochberg Nanophotonics Lab for hosting me this summer and providing the resources to conduct this research.

Special thanks to Yang Liu in the UW Nanophotonics lab for supplying the simulation data and Tom Baehr Jones and Jeff Chamberlain for editorial assistance.

ELIJAH CHRISTENSEN plans on continuing his research on silicon photonics based biosensing in the Ratner and Hochberg lab throughout the next year. He also plans on attending graduate school following graduation, pursuing work in diagnostic technologies.

Patterned Linkage of DNA to a Gold Surface to Create Large-Scale Stamping Process

ROBYN E. CROSS, Spelman College
Keith Carroll, Jennifer Curtis, Georgia Institute of Technology

Introduction

Lithography is a fabrication process that allows for spatially patterning a desired material onto a susbtrate at the micro and nano scales. Thermochemical nanolithography (TCNL) is a patterning approach that uses a heated Atomic Force Microscope (AFM) tip to thermally pattern various types of substrates.[1] This controlled patterning technique is a useful methodology for dictating the position of nano objects, such as DNA, on our substrate, a polymer surface.

The polymer used has a tetrahydropyranyl (THP) protecting group that deprotects at 180 °C exposing amine groups. A heated AFM tip can precisely deprotect the polymer substrate in a spatially controlled configuration. A post treatment process can help to covalently bind proteins and DNA onto these spatially patterned substrates. It was recently found that we are able to also use ionic binding properties to bind negatively charged DNA to positively charged deprotected amine groups.

The ideology behind TCNL can be integrated with another technique that has been found useful to our research. This method is called microcontact printing (μCP) which can pattern at the micrometer scale. It is a straightforward patterning approach that uses a master template to make a replica stamp as shown in Figure 1. Modeled after the original template, the stamp is a negative of the original template topography, and it is this stamp that is capable of being labeled with DNA to be printed on the desired substrate.[2] An inexpensive common material used to make the stamp is polydimethylsiloxane (PDMS). The PDMS is cured in the master template and then peeled away, leaving a mirror image reusable stamp capable of patterning DNA onto polymer and gold substrates.

Integrating TCNL into (μCP) (see Figure 1) will serve as an approach to patterning at the larger scale, in bulk, by way of supramolecular nanostamping (SuNS), which functions based on three pivotal steps as described by the Stellacci group[3]: hybridization on one substrate,

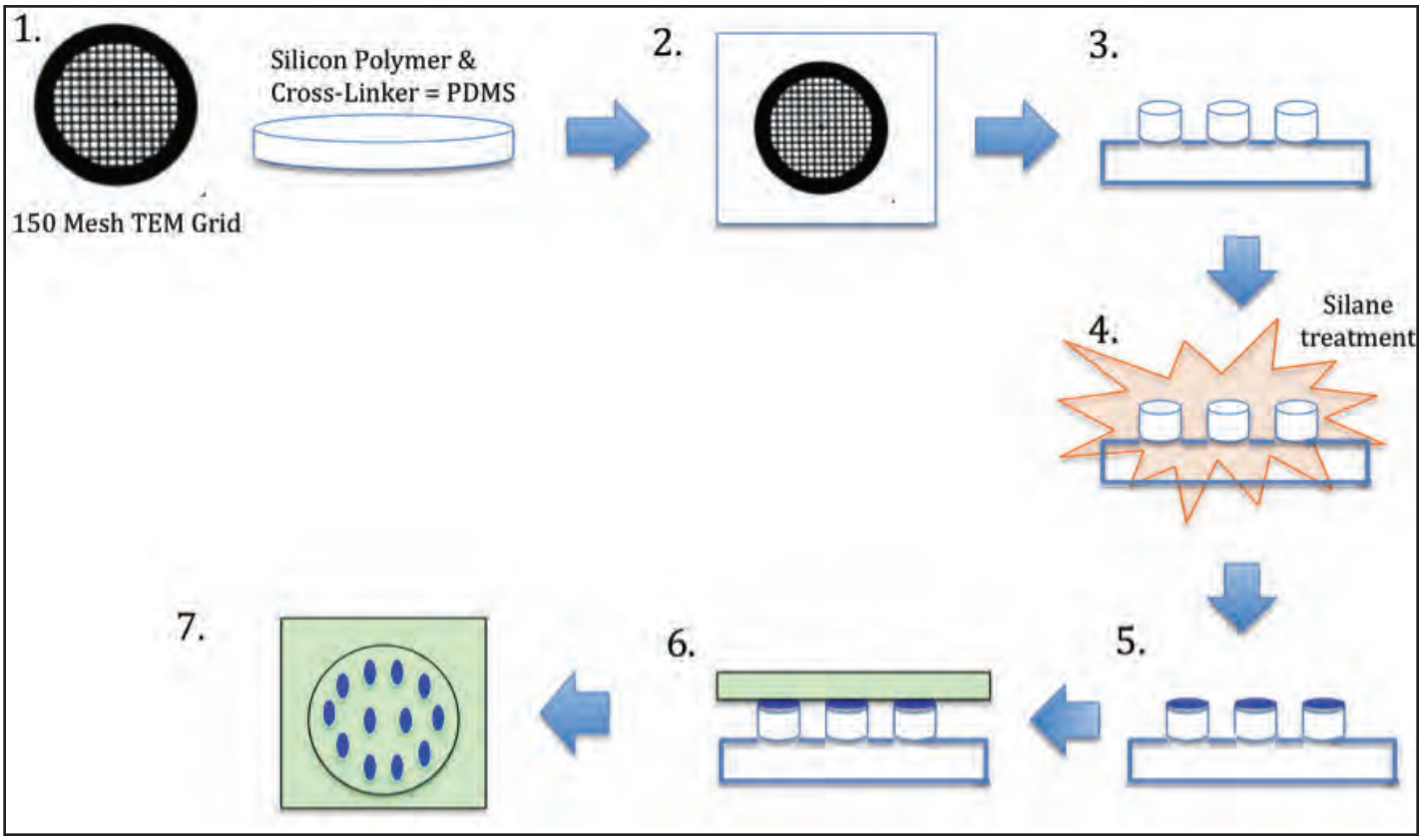

Figure 1. The step wise procedure of μCP: 1. Liquid PDMS mix made and master grid selected; 2. PDMS cures in master grid; 3. Inverse pattern of PDMS stamp revealed; 4. Stamp is silanized; 5. Stamp laced with DNA; 6. Substrate placed on top of PDMS stamp; 7. Substrate peeled away, leaving DNA "ink" pattern.

contact with a secondary substrate, and dehybridization (See Figure 2). Knowing the effectiveness of both TCNL and μCP, there is a need to develop a precise protocol for SuNS that will pattern surfaces with DNA in bulk samples, without the use of a heated AFM tip. We aim to show that using an alternative approach will be hugely cost effective and create large area patterns in a quick and reproducible manner. Additionally, our goal is to show that the proposed technique will create huge micro arrays of DNA in a fraction of time than has been required with current TCNL approaches. Ultimately, the motivation behind this project is to achieve the final goal of developing a protocol for supramolecular nanostamping (SuNS). It is through optimization of this approach that we can then create custom DNA arrays in a highly reproducible and economical process. TCNL is a functioning method, however it is time consuming for the large-scale patterning we wish to achieve. The incorporation of μCP will account for the bulk method, and serve as the platform to refining a protocol for SuNS. Developing this stamping protocol will allow DNA microarray application in advancements towards biotechnology such as genetic screening and anticancer detection treatments.

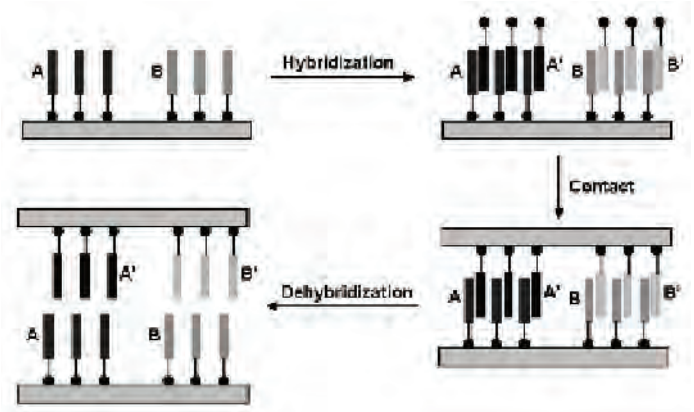

Figure 2. Originally shown in the Journal of Material Chemistry, this figure shows DNA molecules on an initial surface that are hybridized and placed in contact with a secondary surface.[3] The two surfaces separate upon dehybridization, leaving two copies of the single stranded cDNA.

Experimental

Our laboratory procedures were conducted using three different substrates: polymer, functionalized glass, and gold. Deprotection of the THP protecting group on the polymer surface is essential to expose NH_2 groups on the surface that will eventually link to DNA. In order to deprotect THP and pattern large areas, we developed two surface preparations that will ensure effective patterning.

The polymer surfaces are heated by a hot plate to at least 180 °C. Once deprotected, the polymer is cooled and ready to be patterned. An alternative method uses a glass surface functionalized with aminopropyltriethoxysilane (APTES) eliminating the heating step and use of the polymer (see Figure 3). Glass surfaces have been treated with the silane solution, leaving a new coating of exposed NH_2 groups on the surface. This type surface chemistry is proven to be just as effective and is a time-conserving substitute to prior heating polymer surface methods.

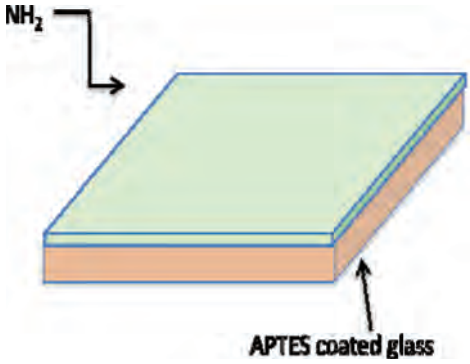

Figure 3. The polymer surface has been functionalized with APTES, leaving exposed amines on the surface.

In μCP, the creation of the PDMS stamp is a straightforward procedure. Polymer and cross-linker (10:1) are mixed thoroughly, making PDMS, which is the molding poured onto the master pattern and cured. The two types of PDMS stamps we use to pattern the polymer or gold surfaces are made from either an AFM grid or Transmission Electron Microscopy (TEM) grid master (see Figure 1).

The master is then inverted into the PDMS, sinks down into this mixture and is heated for three hours until the pattern has sufficiently hardened within the PDMS. Once cured, the master is peeled away, leaving the copied stamp within the new PDMS. Figure 2 illustrates this step-wise process. Our beginning use of the PDMS stamp shows that they have minimal ability to transfer the DNA onto the surfaces. We have found that with modification of the PDMS, the transfer is much more successful. Therefore, the PDMS stamp is silanized with a chemically balanced silane group, which is necessary to enhance DNA attraction during μCP.

To begin the procedure for μCP, the PDMS stamp is laced with primary NH_2-DNA. Meanwhile, the amine surface is treated with 50% gluteraldehyde cross-linker for 45 minutes. Gluteraldehyde is essential because it is configured with two aldehyde groups on each end that are reactive with amines, and it will theoretically link the amine surface with the 5' amine terminus DNA strand (NH_2-DNA) covalently. However, our research has shown that gluteraldehyde is not the most effective cross-linker for this experiment, because it does not block charge binding on the surface. A more appropriate treatment will be the use of Sulfo-MBS, another cross-linking reagent. Following both treatments, the amine surface is briefly placed in contact with the PDMS stamp using a 75 g mass, and then separated. Now the PDMS stamp and NH_2-DNA are patterned on the amine surface. Once initial patterning has occurred, the patterned substrate is immersed in 150 μL of complementary Cy5 fluorescently labeled DNA (DNA-Cy5) for 4 h at 4 °C. Cy5 is a fluorescent dye that is labeled with DNA for imaging and visualization purposes, an important component for recognition of DNA on the patterned surfaces. Imaging with the microscope shows successful μCP onto the amine surface.

The process for patterning onto a gold substrate is done in a similar method compared to using a regular or APTES substrate. Preparation of the gold substrate begins with Piranha solution (3:1 of H_2SO_4 & H_2O_2, respectively). Piranha is used to eliminate organic materials

from the gold surface and then soaked in H_2O for 30 min. A TEM PDMS stamp is incubated with 50 µL SH-DNA. The gold surface will then briefly adhere to the stamp in order to be imprinted with the TEM pattern. Incubation with primary NH_2-DNA at 4 ºC will complete hybridization on the gold surface, and imaging under fluorescence microscopy confirms this (see Figure 4).

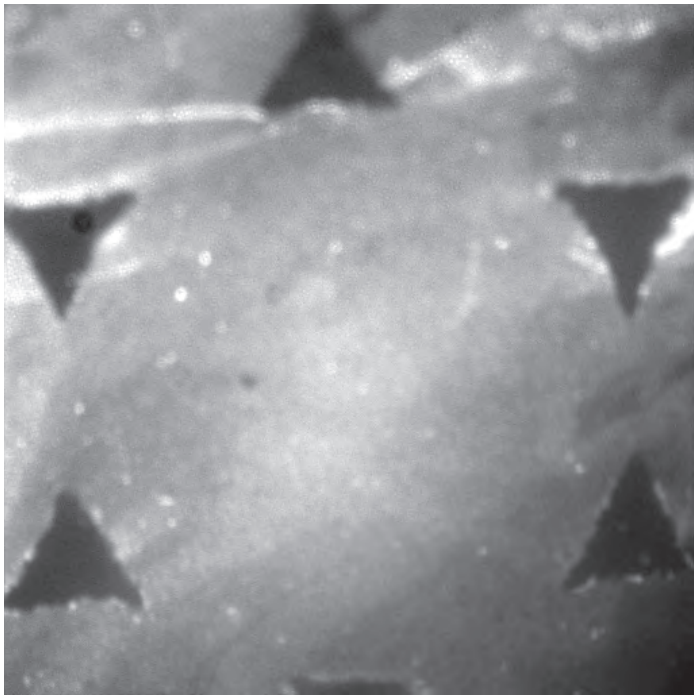

Figure 4. 50 µL reduced SH-DNA hybridized with DNA-Cy5 on Gold. (60x, 2s scan).

Keeping the ideology of a developed protocol for DNA array replication in mind (supramolecular nanostamping, SuNS), we develop our own protocol. Figure 2 demonstrates the typical SuNS protocol for stamping, involving three steps: hybridization, contact, and dehybridization.[3] We will, instead of consecutively executing SuNS, independently hybridize our amine and gold substrates through µCP first. Once the amine surface hybridizes separately, now having double stranded DNA, the gold and thiol interaction will be hybridized next by directly attaching our functional thiol-DNA to the secondary gold surface. These two components provide us with a template to resume with SuNS.

After hybridization completes, the amine surface is contacted face down on gold in a desiccation apparatus for 24 h. The thiol from the amine surface and gold will form a covalent bond, which is necessary to link the cDNA onto the gold surface. Dehybridization occurs through separation and heating of the original polymer and gold surfaces, exposing a second strand of cDNA on the gold substrate. Theoretically, this implies that the gold surface is now a functioning stamp to further replicate this patterning process on other surfaces. Through use of fluorescence microscopy to illuminate the initial pattern on the gold surface, we have successfully executed the initial stages of SuNS.

Results/Discussion

We take an approach to SuNS that uses established procedures and optimizes them for the greatest function and results. The simple method of using an inexpensive polymer and cross-linker to create a PDMS stamp for µCP is effective in generating patterns and hybridizing DNA onto our desired substrate as shown by Figure 3.

We know that SuNS involves a dehybridization step to separate the double-stranded DNA into two strands. In order to confirm the functionality and reproducibility of this step, we dehybridized the gold surface, and showed the successful separation of our double-stranded DNA. In Figure 5, we are able to rehybridize and show DNA on the patterned surface again, which is confirmation that SuNS should work.

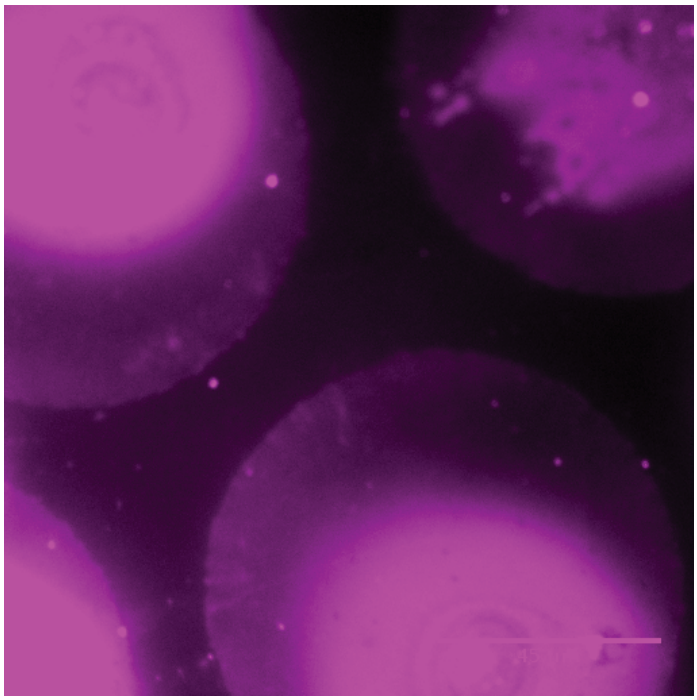

Figure 5. Dehybridization on the gold surface shows there is no patterning. However, after rehybridization this patterning appears again as shown.

Less resource consuming than TCNL, we use µCP to formulate the best SuNS protocol compatible with TCNL. We have developed protocols to bind DNA to polymer, glass and gold surfaces, and demonstrated its reversible hybridization. Bringing the polymer surface with DNA into contact with the secondary gold surface, we are now working on transfer of the secondary DNA using knowledge of dehybridization. Completion of this step will further complete the SuNS process.

Conclusions

In conclusion, we show that we have the necessary components to use TCNL and μCP to optimize a protocol for SuNS of bulk samples. We have shown that hybridization onto a microcontact printed surface is an appropriate procedure to perform SuNS. TCNL is an effective patterning method, but with integration of a model system, mCP, we will be able to execute SuNS at the large scale pattern in a manner that conserves time, energy, and resources. This research will be continued and progress towards the goal of SuNS with plans to make contact between the amine and gold surfaces.

References

1. Wang, D.; Kodali, V.; Underwood II, W.; Jarvholm, J.; Okada, T.; Jones, S.; Rumi, M.; Dai, Z.; King, W.; Marder, S.; Curtis, J.; Riedo, E. Adv. Funct. Mater. 2009, 19, 3697.

2. Mrksich, M.; Whitesides, G. M. Tibtech. 1995, 13, 228.

3. Yu, A. A.; Stellacci, F.; J. Mater. Chem., 2006, 16, 2869.

Acknowledgements

This research was made possible by the help and guidance of Keith Carroll as well as Jennifer E. Curtis, Elisa Riedo and the Curtis Research Group. Funds for this research were provided by the Center on Materials and Devices for Information Technology Research (CMDITR), an NSF Science and Technology Center Grant No. DMR 0120967. Thank you also to my summer program director, Olanda Bryant.

ROBYN E. CROSS is a senior Chemistry major who plans to pursue her interest within the field of Chemistry by working in the industry.

High Density Bio-nano Device Fabrication with Supramolecular Nanostamping

MAITRI D. DESAI, Augusta State University
ROBYN E. CROSS, Spelman College
Keith Carroll, Jennifer Curtis, Georgia Institute of Technology

Introduction

Advanced studies in medicine and in biology have invoked the need for smaller complex devices, known as microarrays, which offer increasing information densities at a low cost.[1] Microarrays have added great contributions in the biomedical field: for example, Genetic Screening, Gene Expression Profiling, etc. High information density biological materials such as DNA, RNA, and proteins, are currently being investigated for fabrication on nanopatterns. Several methods exist that allow the fabrication of biological materials. ThermoChemical NanoLithography[2] (TCNL) uses an AFM tip to thermally alter surface chemistry, providing a substrate to link biomolecules site-specifically. Micro-Contact Printing[3] (μCP) uses a polydimethylsiloxane (PDMS) stamp that is carved with micron-sized patterns. These patterns are transferred on other surfaces by means of contact. Dip-pen nanolithography[1] (DPN), photolithography,[2] and electron beam lithography[2] are other examples of approaches to assemble molecules on surfaces. All of these methods have advantages and disadvantages. For example, TCNL provides high resolution but takes more time to pattern the large areas whereas μCP provides larger and faster surface modification with lower resolution.

More recently, a technique, Supramolecular NanoStamping (SuNS),[4] has been developed to allow efficient replication of DNA microarrays. SuNS is performed in three steps: Hybridization of the DNA to the primary surface, contact of the secondary surface, and dehybridization to replicate primary surface. In this method, DNA is allowed to bind to a surface and to hybridize with a functionalized complementary strand (cDNA). The surface is then heated to dehybridize DNA and cDNA is transferred to the secondary surface providing that the cDNA's functional group can attach to secondary surface. As a result, the DNA microarray is replicated.[4] Figure 1 provides a schematic of Supramolecular Nanostamping (SuNS).

SuNS is a promising technique and is able to produce large numbers of microarrays. However, fabrication of the initial array is still an intricate task. Our group focuses on creating these initial arrays for SuNS using TCNL with potentially higher resolution (~15 nm) and density. TCNL uses a thermal AFM tip to alter local surface chemistry. With a correctly chosen surface, namely a spin-coated polymer on glass with a protected amine group, we can form a template pattern to organize high density molecules. Our goal is to combine TCNL and SuNS to fabricate DNA nanoarrays. As mentioned earlier, TCNL is very time-consuming and is difficult to master in a short period of time. In order to expedite the process, we developed a protocol to apply an alternate method on polymer used for TCNL: μCP.

μCP allowed us to successfully achieve first two steps of SuNS on TCNL polymer: Hybridization and Dehybridization of DNA which are essential to the repeatability of SuNS. We also achieved rehybridization of the DNA bound primary surface after dehybridization before transferring cDNA to the secondary surface in order to ensure dependability of the surface. Thus, we successfully developed a protocol to make large scale patterned areas and execute SuNS by showing hybridization, dehybridization and rehybridization. Once the SuNS is performed successfully and repeatedly using μCP, ultimately, we will apply this method to nano resolution TCNL patterns and consequently combine TCNL and SuNS.

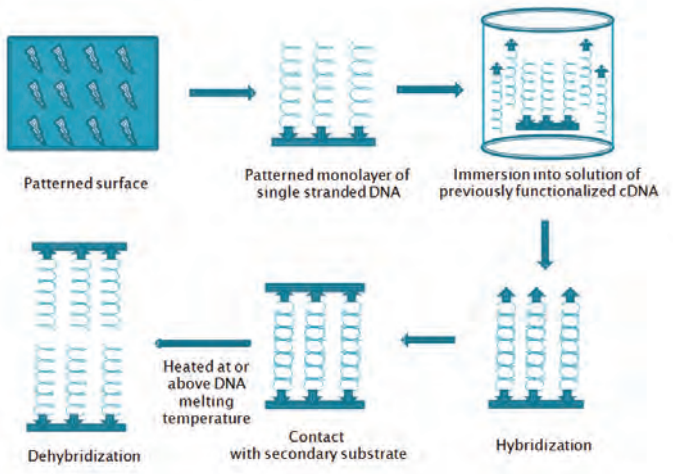

Figure 1. Overview of SuNS

Results and Discussion

We wanted to establish a consistent DNA stamping method that is also faster and cheaper than TCNL. The best way to achieve this goal was to make large scale patterns using bulk printing.

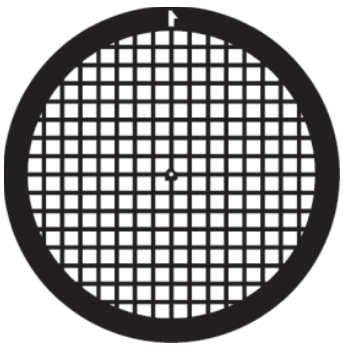

Figure 2. TEM grid*
(Dimensions: 125x125x44 μm)

We decided to utilize a potential bulk printing method: Micro-Contact Printing (μCP). This method uses the stamps prepared by pouring the PDMS into the molds followed by baking. The PDMS stamp is removed from the mold after curing. We used three different designs of molds to print surfaces: a traditional photolithographic mold, TEM (transmission electron microscopy) grids (Figure 2) and AFM (atomic force microscopy) grids (Figure 3). PDMS stamps were then silanized before use. Silanization is the process in which the surface, in this case the stamp, is coated with alkoxysilane molecules making the surface hydrophilic.

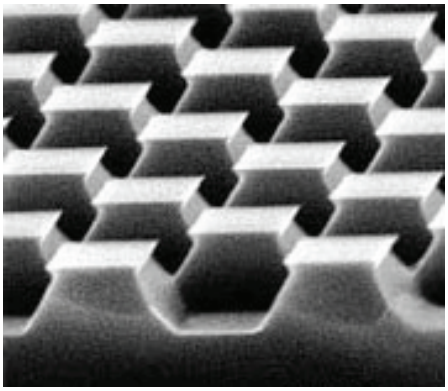

Figure 3. SEM image of AFM grid.[5]
(Dimensions: 5x5x0.6 μm)

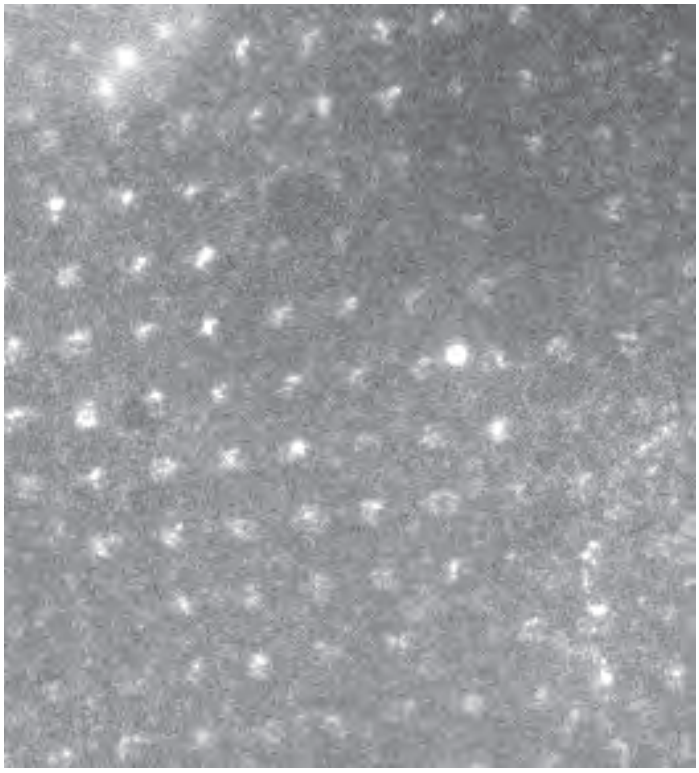

Figure 4. Microscope image of PDMS stamp.

After the stamp is ready, DNA is placed on the stamp and a surface is placed on top of this assembly. This process, stamping, allows DNA to bind to the surface and transfer from the stamp. The following Figures 4, 5 and 6 show images of the polymer when Cy5-functionalized fluorescently labeled DNA binds to the surface via μCP. Here, DNA binds to the surface non-specifically with electrostatic interactions of positive charge of amines and negative charge of DNA. However, for hybridization, the functionalized DNA has to attach to the surface in proper orientation with covalent bonds for perfect end anchoring.

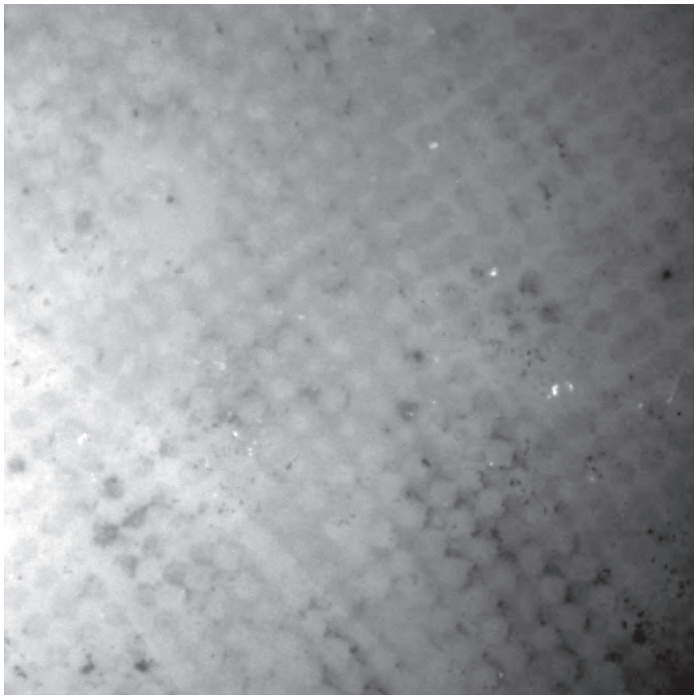

Figure 5. Microscope image of AFM stamp.

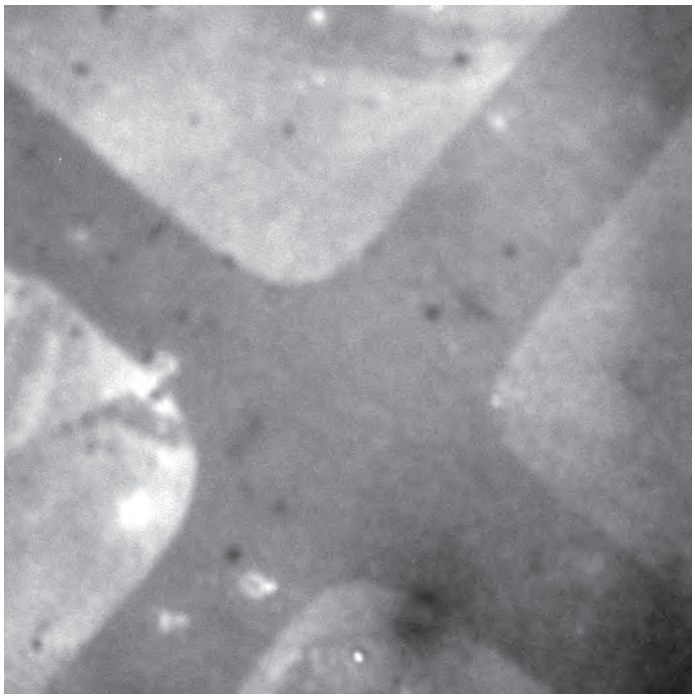

Figure 6. Microscope image of TEM stamp.

Micro-Contact Printing proved to be the successful printing method and became a protocol to print desired surfaces shown in Figure 7: polymer surface, APTES surface, and gold surface.

We used four types of 5' functionalized DNA (50 base pairs, 15 nm): amine-functionalized DNA and Cy5-functionalized cDNA, thiol-functionalized DNA and Cy5-functionalized complementary DNA. Cy5 is a fluorescence dye and thus it is visible in the fluorescence channel during its microscope analysis. Cy5 fluorescence dye was added whenever appropriate to DNA to make it visible during analysis.

The polymer surface has protected amine groups that require deprotection by heating prior to printing. The APTES surface is modified earlier by silanization using APTES (aminopropyltriethoxysilane) and has exposed amine groups.

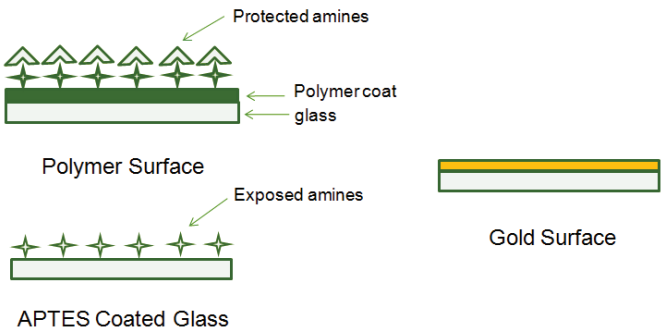

Figure 7. Overview of surfaces.

In order to bind functionalized DNA to the amine surfaces, a cross-linker is required. A cross-linker is a molecule that has two functional groups which link the surface and the DNA. We used sulfo-MBS (m-Maleimidobenzoyl-hydroxy sulfosuccinimide ester) as a cross-linker between amine surfaces and the DNA.

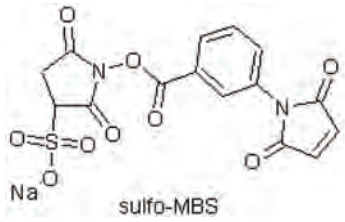

Figure 8. Structure of sulfo-MBS with functional groups NHS ester (left) and maleimide (right).

As shown in Figure 8, sulfo-MBS has two active functional groups: NHS ester and maleimide. The NHS ester is reactive towards amines and maleimide is reactive towards thiols at neutral pH.

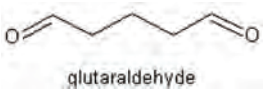

Figure 9. Cross-linker glutaraldehyde with identical functional groups at both ends.

Therefore, we may use either amine surface but must use thiol DNA in order to use sulfo-MBS. On the other hand, glutaraldehyde, shown in Figure 9, has identical aldehyde groups at both ends which are reactive towards amines. In this case, therefore, the surface and the DNA both must have active amine ends.

After printing the surface and attaching the ssDNA, the surface is incubated with fluorescently labeled cDNA at 4 °C for about four hours. We expect to hybridize ssDNA and cDNA in this process. Cy5-functionalized cDNA will assist in order to visualize hybridization successfully.

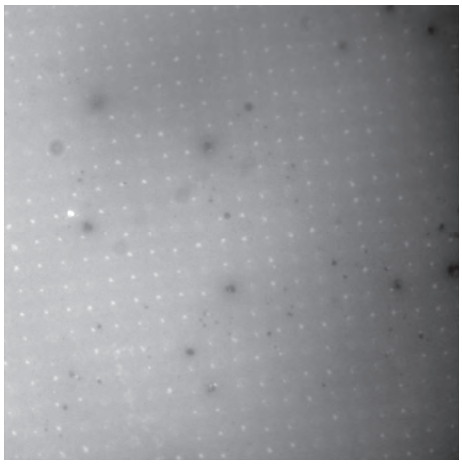

Figure 10. Hybridization of primary thiol DNA with Cy5-functionalized cDNA using cross-linker sulfo-MBS and PDMS stamp on polymer.

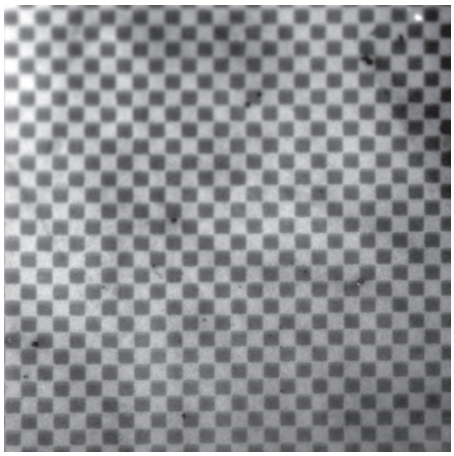

Figure 11. Hybridization of primary thiol DNA with Cy5-functionalized cDNA using sulfo-MBS and AFM stamp on polymer.

Figures 10 and 11 show hybridized patterns produced on polymer surfaces. Figure 11 shows the stamp patterns more visibly than Figure 10. Comparing these two stamps, we chose to use AFM stamp repeatedly. The clarity and efficiency of the AFM and its analogous TEM stamps are better than PDMS stamp.

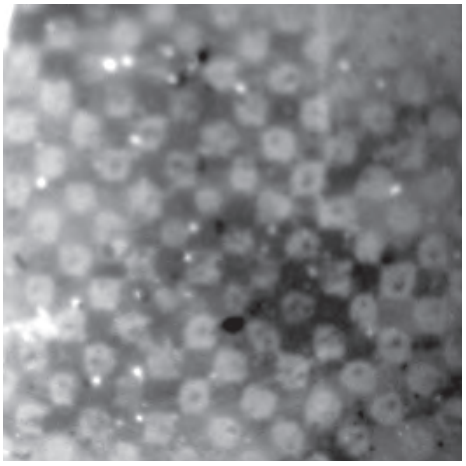

Figure 12. Hybridization of primary thiol DNA with Cy5-functionalized cDNA using sulfo-MBS and AFM grid on an APTES surface.

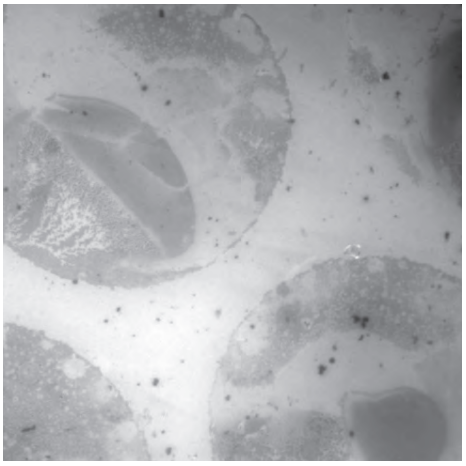

Figure 13. Hybridization of primary amine DNA with Cy5-functionalized cDNA using glutaraldehyde and TEM grid on an APTES surface.

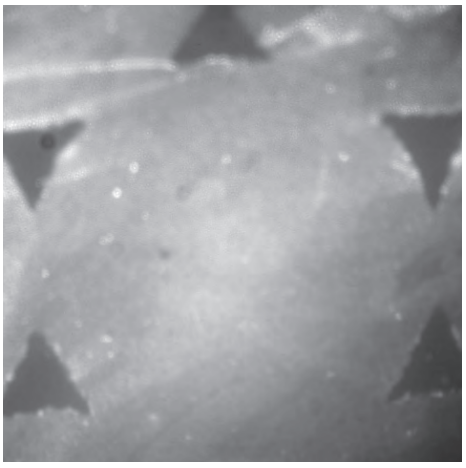

Figure 14. Hybridization of primary thiol-functionalized DNA with Cy5-functionalized cDNA using TEM stamp on a gold surface.

Figures 12 and 13 show the difference between two cross-linkers sulfo-MBS and glutaraldehyde. From the images, we can see that sulfo-MBS is a better cross-linker and blocks the Cy5 dye better on unwanted areas whereas glutaraldehyde does not do as well blocking the fluorescence. The experiment of glutaraldehyde is still under investigation.

Gold surfaces prove to be the easiest way to print thiol DNA because of Au-S (gold-thiol) interaction without performing additional chemistry. Even though no cross-linking is needed for gold surfaces, thiol DNA is required to allow printing. Figure 14 illustrates the successful hybridization achieved on a gold surface.

We confirm, proven with images, that we can hybridize on any of the three surfaces successfully and repeatedly. Since hybridization worked satisfactorily, we moved on to testing dehybridization and rehybridization of surface bound DNA.

Dehybridization and rehybridization are crucial for the repeatability of SuNS. The hybridized surface is incubated at 90 °C for half an hour. We expect to see no Cy5 fluorescence after incubation indicating successful dehybridization. Fluorescence imaging of the surfaces after this process revealed no detectable fluorescence. We were therefore, able to rehybridize the same surface after the dehybridization.

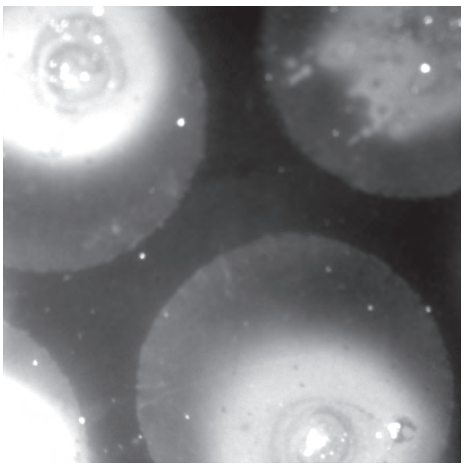

Figure 15. Rehybridization of primary thiol-functionalized DNA with Cy5-functionalized cDNA on the same gold surface.

We have demonstrated most of the independent steps of SuNS: (i) Controlled domain anchoring of functionalized DNA to gold and amine surfaces, (ii) hybridization on two different surfaces, including the polymer for TCNL, and (iii) dehybridization. The full implementation of SuNS is nearly accomplished with just one step remaining: transfer via contact.

Conclusions

We determined that Micro-Contact Printing is a successful, fast and inexpensive way of making stamps and printing a variety of surfaces. SuNS can be a feasible technique to fabricate DNA microarrays once the whole protocol of micro-contact printing works successfully. Because of the repeatability and replication capability of SuNS, microarrays can be easily transformed into DNA-RNA, RNA-protein assemblies. Making nanoarrays will be easier with TCNL and SuNS and will offer novel bio-nano devices.

References

1. Thevenet, S:, Chen, H. Lahann, J. Stellacci, F. Adv. Mater. 2007, 19, 4333-4337.

2. Wang, D. Kodali, V. Underwood, W. Jarvholm, J. Okada, T. Jones, S. Rumi, M. Dai, Z. King, W. Marder, S. Curtis, J. Riedo, E. Adv. Funct. Matter. 2009, 19, 3696-3702.

3. Mrksich, M. Dike, L. Tien, J. Ingber, D. Whitesides, G. Experimental Cell Research. 1997, 235, 305-313.

4. Yu, A; Savas, T; Cabrini, S; diFabrizio, E; Smith, H; Stellacci, S. J.Am.Chem.Soc. 2005, 127, 16774-16775.

5. http://www.tedpella.com/grids_html/Pelco-TEM-Grids.htm, July 14, 2010.

6. http://www.spmtips.com/tgx, July 14, 2010.

Acknowledgments

- Center on Materials and Devices for Information Technology Research (CMDITR), an NSF Science and Technology Center No. DMR 0120967.
- Keith M. Carroll
- Jennifer E. Curtis
- Georgia Institute of Technology

MAITRI D. DESAI's future endeavors include pursuing a PhD in the field of molecular biophysics.

Synthesis of Naphthalene Diimide Based N-type Organic Semiconductors

SARAH ESPINOZA, New Mexico Highlands University
Selvam Subramaniyan, Samson A. Jenekhe, Univeristy of Washington

Introduction

Organic semiconductors have been attracting considerable attention due to their unique advantages of having high through-put, being low in cost to produce, light in weight as well as their potential application in flexible large-area devices. P-type organic semiconductors are hole (positive charge) carriers, and, in contrast n-type are electron (negative charge) carriers. In the past decade, there has been a lot of research focused towards the development of many stable high performance p-type organic semiconductors, whereas very few air-stable, solution processable n-type organic semiconductors have been developed so far. Recently, solution-processable naphthalene diimide-based organic semiconductors have shown to exhibit high electron mobility, even at ambient conditions.[1,2] The main objective is to design and synthesize new air-stable, solution processable n-type organic semiconductors based on naphthalene diimide for high performance plastic electronics, organic thin film transistors, and solar cells.

Results and Discussion

Our strategy to synthesize the n-type organic semiconductors is outlined in Scheme 1. The key intermediate compounds, tetrabromo naphthalene diimide **8a** and **8b** were synthesized according to the available literature procedure.[2] Reaction of 2-Butyl-1-octanol with carbon tetrabromide and triphenylphosphine in dichloromethane at 0 °C for 1 h gave 1-Bromo-2-butyloctane 2 in 57% yield. The bromo compound **2** was then converted into corresponding amine **4** by hydrolysis of pthallimide derivative **3** using hydrazine hydrate. Bromination of compound **5** using dibromoisocyanuric acid as a brominating agent afforded tetrabromo compound **6**, which in turn reacts with the amine **4** or 2-ethyl-1-hexylamine gave an intermediate **7a/7b** in good yields. This crude was further cyclized using phosphorous tribromide in toluene gave corresponding tetrabromo napthalenediimide **8a/8b** in 17-29% yields. Reaction of 2-bromothiophenol with tetrabromo compound **8a/8b** in presence of potassium carbonate in dry DMF at room temperature gave **9a/9b** in good yields.

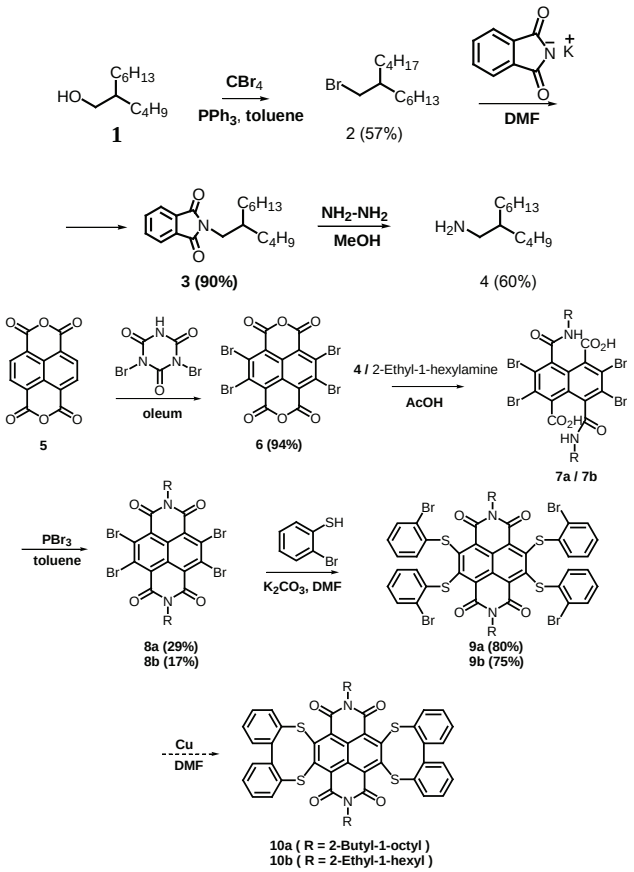

Scheme 1. Synthesis of naphthalene-diimide based organic semiconductors.

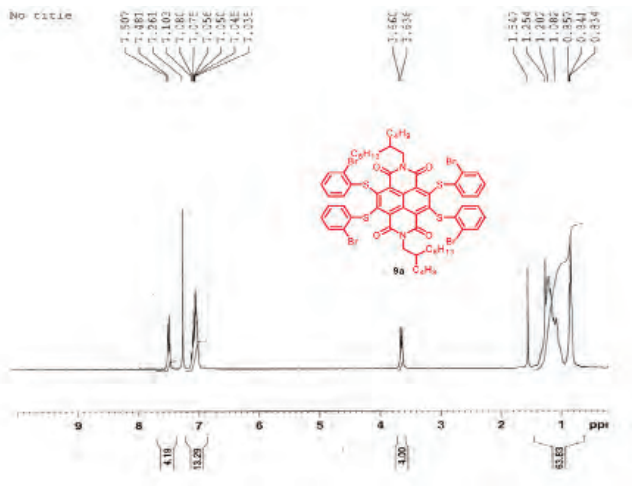

Figure 1. ^{1}H NMR spectra of compound **9a** ($CDCl_3$)

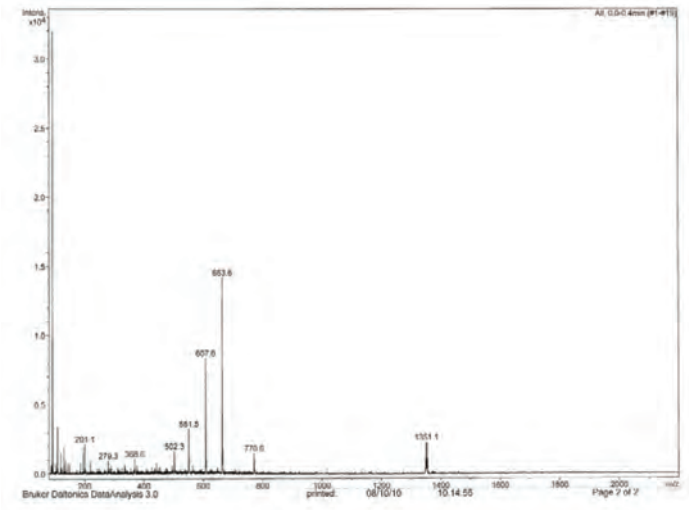

Figure 2. Mass spectra of compound **9a**.

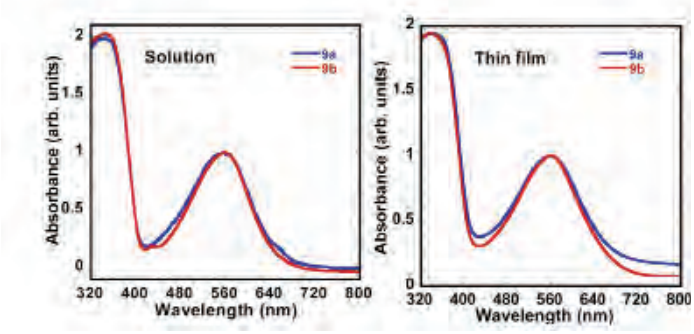

Figure 3. Absorption spectra of **9a/9b** in solution and thin film.

The compound **9a** was confirmed from NMR and Mass spectroscopic techniques (Figure 2 and 3). ^{1}H NMR spectrum of compound **9a** showed a doublet at δ 3.65 for the two N-CH_2 protons, a multiplet in the region of δ 0.83-1.25 for the remaining alkyl protons and eight protons in the aromatic region. The compound **9a** was further confirmed by a prominent peak at 1251 (Fig 2).

Both compounds **9a/9b** are soluble in common organic solvents such as chloroform, dichloromethane, THF, etc. Figure 3 shows the absorption spectra of **9a/9b** in both solutions and thin films. Absorption maxima in solutions and thin films was found to be 559-561 nm. The optical bandgap determined from the absorption edge of thin film is 1.79 eV.

Experimental Methods

1-Bromo-2-butyloctane (2)

A solution of CBr_4 (57.84 g, 0.174 mol) and 2-butyl-1-octanol (30 mL, 0.134 mol) in CH_2Cl_2 (150 mL) was added dropwise at 0 ºC to the solution of PPh_3 (49.26 g, 0.188 mol) in CH_2Cl_2 (65 mL). The mixture was stirred for 45 min, then poured into hexane/thanol (4:1 v/v, 100 mL) and the resulting precipitate (PPh_3PO) was filtered and discarded. The filtrate was passed through a plug of SiO_2 and evaporated to afford 57% of **2** and used for the next step without further purification. Colourless liquid.

^{1}H NMR($CDCl_3$, 300 MHz, ppm): 3.45 (d, 2H, J = 4.8 Hz), 1.54-1.60 (m, 1H), 1.28-1.33 (m, 16H), 0.89-0.93 (m, 6H).

2-(2-Butyl-octyl)-isoindole-1,3-dione (3)

Potassium pthalimide (19.72 g, 0.107 mol) was added to a solution of bromo compound **2** (24.68 g, .099 mol) in 45 mL dry DMF. The reaction was stirred for 14 hours at 95 ºC. After cooling to room temperature, the reaction mixture was poured into 150 mL water and extracted with dichloromethane (3 x 100mL). The combined organic layers were washed with 200 mL 0.2 M NaOH, water, saturated ammonium chloride, dried over anhydrous Na_2SO_4, and concentrated under reduced pressure. The resulting crude yellow oil was purified via column chromatography giving **3** as pale yellow oil. Yield: 90%

^{1}H NMR ($CDCl_3$, 300 MHz, ppm): 7.83-7.86 (m, 2H), 7.70-7.73 (m, 2H), 4.08 (d, 2H, J = 5.7 Hz), 1.88 (bs, 1H), 1.25-1.27 (m, 16H), 0.84-0.90 (m, 6H).

2-Butyl-1-octylamine (4)

Compound **3** (10.44 g, 0.033 mol), hydrazine monohydrate (hydrazine 65%) (5.184 g, .102 mol) and 100 mL MeOH were stirred at 95 ºC and monitored by TLC. After disappearance of the starting imide, the methanol was evaporated under reduced pressure, the residue diluted with 100 mL dichloromethane and washed with 10% NaOH (2 x 50 mL). Aqueous layers were combined and extracted with dichloromethane (3 x 40 mL). The combined organic layers were washed with brine (2 x 100 mL) and dried over Na_2SO_4. The removal of dichloromethane afforded yellow oil as product which was used in NBI synthesis without further purification. Yield: 60%

^{1}H NMR ($CDCl_3$, 300 MHz, ppm): 3.51 (d, 2H), 2.90 (s, 2H), 1.27 (bs, 17H), 0.86-0.90 (m, 6H).

2,3,6,7-Tetrabromo-1,4,5,8 naphthalenetetracarboxylic Acid Dianhydride (6)

A solution of dibromoisocyanuric acid (7.18 g, 0.025 mol) in oleum (20% SO_3, 50 mL) was poured into a solution of 1,4,5,8 naphthalenetetracarboxylic acid dianhydride **5** (2.68 g, 0.01 mol) in oleum (20% SO_3, 80 mL), and the reaction mixture was stirred vigorously for 3 h at room temperature. The resulting orange suspension was poured into ice (800 g), and water was added (1200 mL). The yellow precipitate was filtered, washed with water (100 mL), and dried over potassium hydroxide. Yield: 2.70 g (94%). ^{1}H NMR (300 MHz, DMSO-d6): No proton signal was observed.

2,3,6,7-Tetrabromo-4,8-bis-(2-butyl-octylcarbamoyl)-naphthalene-1,5-dicarboxylic acid (7a)

(4.45 g, 0.008 mol) **6** and (5.65 g, 0.031 mol) 2-Butyl-1-octylamine 4 in 70 mL acetic acid were stirred under an argon atmosphere at 125 ºC. The reaction was stopped before the color of the reaction mixture turned red (approx. 30 min). Mixture was added to ice after cooled to room temperature and filtered. The obtained solid was washed with water (200 mL) and petroleum ether (200 mL), then dried in the oven.

2,3,6,7-Tetrabromo-4,8-bis-(2-ethyl-hexylcarbamoyl)-naphthalene-1,5-dicarboxylic acid (7b)

(10 g, 0.017 mol) **6** and (11.2 mL, 0.068 mol) 2-Ethyl-1-hexylamine in 200 mL acetic acid were stirred under an argon atmosphere at 125 ºC. The reaction was stopped before the color of the reaction mixture turned red (approx. 30 min). Mixture was added to ice after cooled to room temperature and filtered. The obtained solid was washed with water (200 mL) and petroleum ether (200 mL), then dried in the oven.

4,5,9,10-Tetrabromo-2,7-bis-(2-ethyl-hexyl)-benzo[lmn][3,8]phenanthroline-1,3,6,8-tetraone (8b) or 4,5,9,10-Tetrabromo-2,7-bis-(2-butyl-octyl)-benzo[lmn][3,8]phenanthroline-1,3,6,8-tetraone (8a)

A solution of 1.2 g **7b** (or 1.1 g **7a**) with (9.64 mL, 0.1026 mol) PBr_3 (phosphorus tetrabromide) in 100 mL dry toluene was refluxed for 12 h under an argon atmosphere. The mixture was cooled to room temperature and then poured into 400 mL water. The product was extracted using toluene (200 mL x 3), and the combined organic solvent was evaporated. Yield: **8a**: 29%; **8b**: 17%

4,5,9,10-Tetrakis-(2-bromo-phenylsulfanyl)-2,7-bis-(2-butyl-octyl)-benzo[lmn][3,8]phenanthroline-1,3,6,8-tetraone (9a) or 4,5,9,10-Tetrakis-(2-bromo-phenylsulfanyl)-2,7-bis-(2-butyl-octyl)-benzo[lmn][3,8]phenanthroline-1,3,6,8-tetraone (9b)

Compound **9a/9b**: To a mixture of (61.8 mg, 0.000327 mol) 2-Bromothiophenol and (60 mg, 0.0000653 mol) tetrabromo compound **8a/8b** in dry DMF (0.04 mL) were stirred at room temperature for 2 h under Argon atmosphere. Then the reaction mixture was poured into water and extracted using dichloromethane (2 x 50 mL). The combined organic layers were washed with brine solution (2 x 50 mL) and dried over anhydrous sodium sulfate. The removal of dichloromethane afforded a violet solid **9a/9b**.

Compound **9a**: Violet solid. Yield: 80%.^{1}H NMR (300MHz, $CDCl_3$) **δ**: 7.49 (d, 4H, J = 7.8 Hz), 7.04-7.10 (m, 12H), 3.65 (d, 4H, J = 7.2 Hz), 1.25-1.08 (m, 34H), 0.86-0.83 (m, 12H). (ESI mode): Found M+1, 1251, requires 1250.1.

Compound **9b**: Violet Solid. Yield: 75%. ^{1}H NMR (300MHz, $CDCl_3$) **δ**: 7.43 (d, 4H, J = 6.6 Hz), 6.94-7.06 (m, 12H), 3.51-3.65 (m, 4H), 0.76-1.47 (m, 30H).

Conclusions

We have designed and synthesized new precursors of NDI based organic semiconductors **9a/9b** and characterized then by NMR and Mass Spectroscopic techniques. Absorption spectra of **9a/9b** showed a broad absorption band in the region visible range (550-560 nm). Optical band gap measured at the absorption edge of thin films was found to be 1.79 eV. The synthesis and characterization of highly conjugated core expanded NDI based n-type organic semiconductors **10a/10b** are under investigation.

References

1. Yan, H.; Chen, Z.; Zheng, Y.; Newman, C.; Quinn, J. R.; Dötz, F.; Kastler, M.; Facchetti, A. Nature 2009, 457, 679–686.

2. Gao, X.; Di, C.; Hu,Y.; Yang, X.; Fan, H.; Zhang, F.; Liu, Y.; Li, H.; hu, D. J. Am. Chem. Soc. 2010, 132, 3697-3699.

3. Kim, F. S.; Guo, X.; Jenekhe, S. A. Adv. Materials, 2010, 22, 478.

Acknowledgements

Research was supported by the NSF Science and Technology Center No. DMR 0120967 on Materials and Devices for Information Technology Research (CMDITR) and the NSF research experiences for undergraduates program Hooked on Photonics. Special thanks to Dr. Samson A. Jenekhe, Dr. Selvam Subramaniyan, and the Jenekhe lab group.

SARAH ESPINOZA is in her senior year at New Mexico Highlands University. After earning a Bachelor's degree in chemistry, Sarah hopes to return to the University of Washington for graduate school.

Construction and Characterization of a 1550nm Mode Locked Fiber Laser and its Applications in Optical Coherence Tomography

ANNA EVANS, Boston University
Qiang Fang, Khanh Kieu, University of Arizona

Introduction

The field of nonlinear fiber optics developed from an outgrowth of the use of silica fibers in optical communications.[1-6] The field was propelled forward by the manufacturing of fiber gain mediums by doping silica fibers with rare-earth elements.[7-9] Fiber lasers have many advantages over conventional bulk lasers due to their low costs, durability and compact format.[10] A subtype of fiber lasers is the mode locked laser, which produces an ultra-short optical pulser. Principles of mode locking, in this research passive mode locking, will be necessary to create an ultrafast laser.[11] Passive mode-locking is achieved by incorporating a saturable absorber into the laser cavity. The particular saturable absorber used was a non-linear optical component, which absorbs less light at higher optical intensities.[12] Ultrafast lasers have gained notoriety in various applications, such as non-linear imaging and sensor systems, such as Optical Coherence Tomography,[13] and in the field of metrology.[14]

This project was separated into several phases. The first phase involved building a continuous wave fiber laser. Next, an ultrafast pulse fiber laser was constructed via mode locking, and optimized for maximum bandwidth and output power. It was characterized using an optical spectrum analyzer, power meter, and a home-built interferometric autocorrelator. Lastly, an all reflective time domain OCT system was built and used with an ultra broadband fiber laser source, the basis of which was a broadband laser, much like the one constructed in this project.

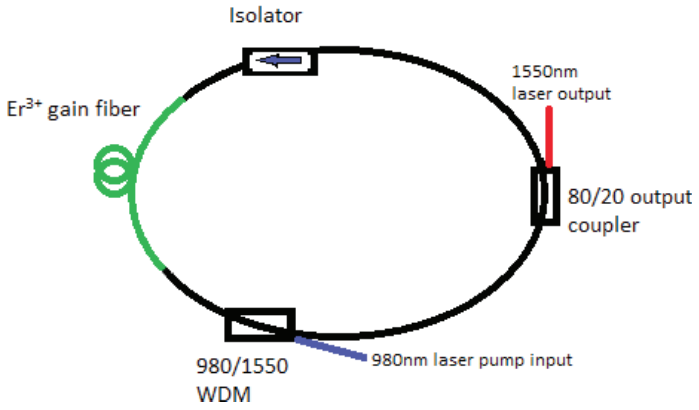

Figure 1. Schematic of continuous wave laser.

Experimental Methods

The first objective was to construct a continuous wave fiber laser. It was an all-fiber ring configuration, utilizing an Er^{3+}-doped fiber for the gain medium. A 980 nm diode laser was used as the pump to the laser resonator. The 980 nm pump laser was launched into the laser cavity through a 980/1550 nm wavelength division multiplexer (WDM) to in-core pump the Er^{3+}-doped gain fiber. An 80/20 coupler was used to obtain the 1550 nm wave at the output with the 20% port. The laser cavity, also, included an isolator, to ensure the light was unidirectional, which guaranteed stable operation of the laser. The laser was characterized by its central wavelength, bandwidth, output power and efficiency. The output power of the laser was measured as a function of the input power from the 980 nm pump. A spectrum analyzer provided a measure of the central frequency and bandwidth.

By adding a saturable absorber, the CW laser was converted to a mode locking laser. The saturable absorber was comprised of a tapered fiber encompassed in a carbon nanotube composite.[10] A 30% percent saturable absorber was initially used. The length of the cavity was modified to obtain the maximum bandwidth.

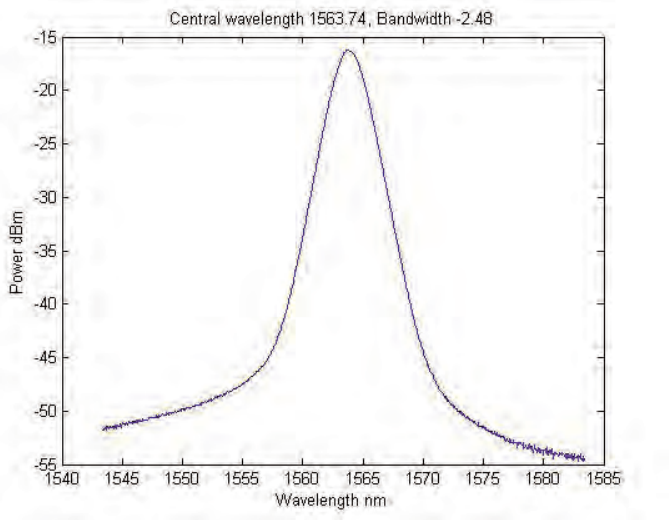

Figure 2. Maximum bandwidth obtained and central wavelength of mode locked laser with 30% saturable absorber.

To increase the bandwidth, the gain medium was changed from an Er^{+3} doped fiber to an Er doped fiber and the length of cavity was altered by adding more anomalous fiber. Upon still not obtaining a broad enough bandwidth, the 30% saturable absorber was replaced by a 70% saturable absorber.

Upon configuring the laser, an interferometric autocorrelator was set up to measure the pulse duration of the laser. A fast detector covering 1550 nm wavelength together with an oscilloscope was used to measure the pulse repetition rate. The bandwidth, central wavelength and power output were measured the same way as for the continuous wave laser.

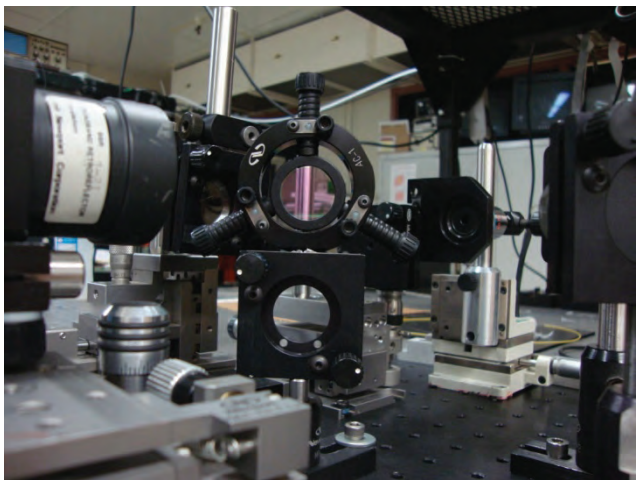

Figure 3. Photograph of the interferometric autocorrelator with 50/50 beam splitter in the middle and two photon absorption non-linear detector to the right.

Concurrently, an all reflective time domain optical coherence tomography system was constructed and optically aligned. The system was built to be wavelength independent to be best suited to incorporate an ultra broadband source without introducing extra chromatic dispersion into the system.

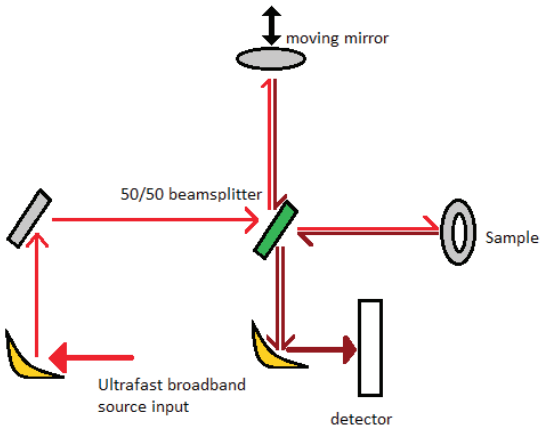

Figure 4. Schematic of optical coherence tomography system.

The system was first tested with a Super Fluorescent Diode laser source, the best commercially available source for OCT, and the point spectrum function was measured. Lastly, the Ultra Broadband Fiber laser source was used to obtain a point spread function and high resolution images.

Results and Discussion

Mode Locked Laser

The broadest bandwidth mode locked laser was obtained with the 70% saturable absorber with a bandwidth of 7.19 nm, measured at an input of 14.8 mW or 50 mA driving current from the pump source. This configuration utilized the 20% port on the coupler as the output and passed the 80% port back into the cavity. Although this produced the widest bandwidth, the laser did not produce enough output power and therefore the ports of the coupler had to be switched.

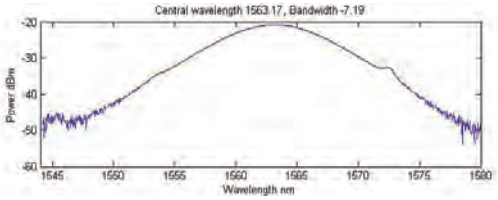

Figure 5a. Optical Spectrum of mode locked laser with a 70% saturable absorber and 20% coupler output.

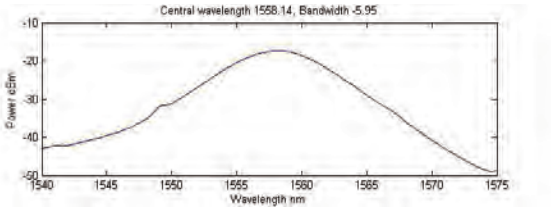

Figure 5b. Optical Spectrum of mode locked laser with an 80% coupler output.

In its final configuration, the maximum bandwidth, obtained once again at 50 mA driving current, was decreased by approximately 1 nm, corresponding to an increase in pulse duration. The output power was 1.5 mW, as measured by an optical powermeter. The central wavelength was 1558 nm, as depicted in Figure 5.

Next, the interferometric autocorrelator was used to obtain a laser pulse duration of 480 fs using the following equation:

$$t_{pulse}=2*v_{stage}*t/c \quad (1)$$

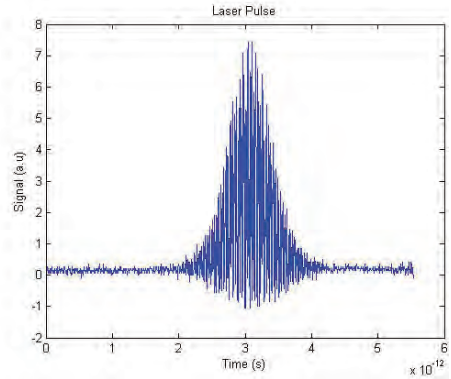

Figure 6. Interferometric autocorrelation trace.

Lastly, using a fast detector and an oscilloscope, the pulse train was obtained. The repetition rate, calculated as $1/\tau$, was 26.3 MHz.

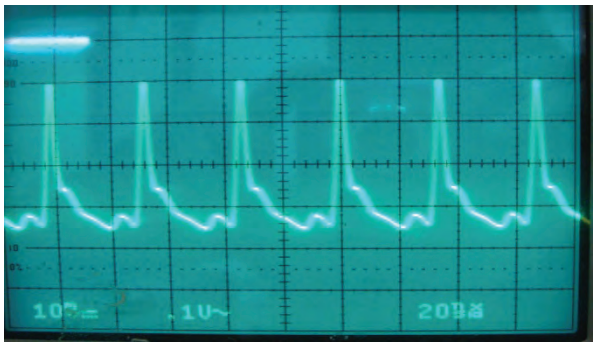

Figure 7. Laser pulse train on oscilloscope.

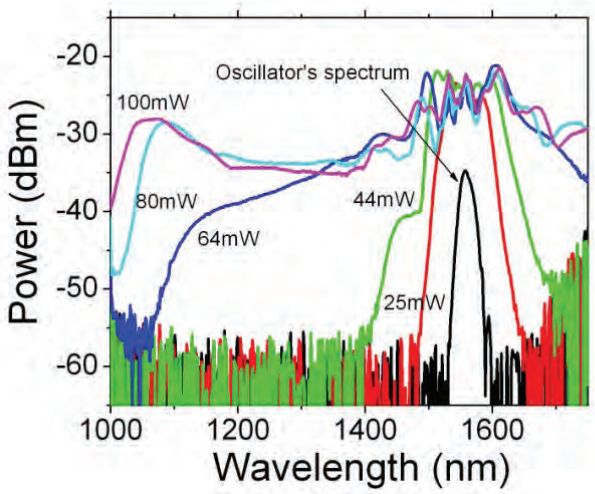

Figure 8. Optical Spectrum of Ultra Broadband Fiber Laser at different input powers, the spectrum of the mode locked laser is indicated in black.

The mode locked laser is the basis for the construction of an Ultra Broadband Fiber Laser. The mode locked laser is then amplified by being passed through anomalous fiber and highly nonlinear fiber.[15] This ultimately results in a laser system with a bandwidth of up to 500 nm. This OCT system was the first to utilize a laser of this sort.

Source	Super Fluorescence Diode Laser	Ultra Broadband Fiber Laser
Point Spread Function	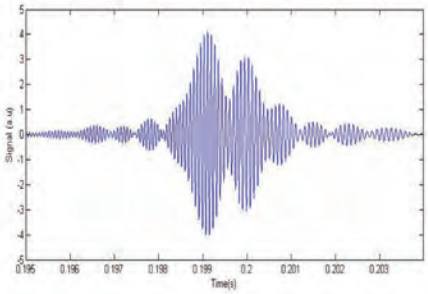	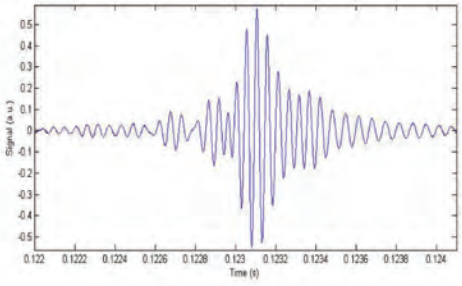
Gold Coated Mirror	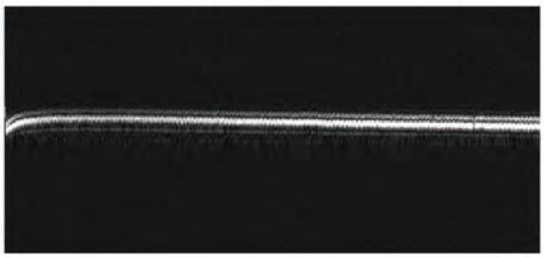	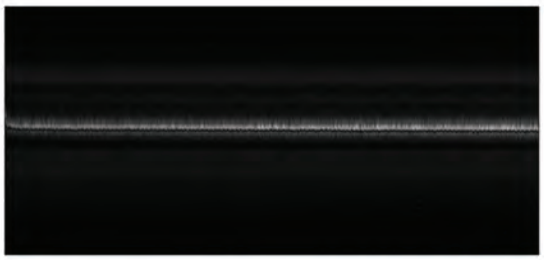
Paper sample	Tissue paper 	Regular paper 

Table 2. Comparison of OCT resolution and images obtained by standard laser source and by the broadband fiber laser.

Optical Coherence Tomography

In the OCT system, a Super Fluorescent Diode Laser, was used as a reference to compare the results from the broadband fiber laser. The theoretical axial resolutions of the Super Fluorescent Diode Laser and of the Ultra Broadband Fiber Laser were obtained as follows:

$$l_c = 2\ln(2) * (\lambda_0)^2/\pi\Delta\lambda \qquad (2)$$

The point spread function was then used to obtain the actual values of axial resolutions.

Next the two laser sources were used to obtain several images.

Source (in air)	Super Fluorescence Diode Laser	Ultra Broadband Fiber Laser
Theoretical	3.2µm	1.9 µm
Actual	4.5 µm	2.0 µm

Table 1. Axial resolution comparison between the standard laser source and by the broadband fiber laser.

Conclusions

A 1550 nm mode-locked laser was successfully built and characterized. A continuous wave laser was first built and then used as the basis for the mode-locked laser through the addition of a saturable absorber. A tapered fiber coated with a single wall carbon nanotube served as a 70% light absorbing saturable absorber. The cavity was then modified for an appropriate amount of dispersion to obtain a broadband soliton mode locked laser. The laser was then characterized for bandwidth, central wavelength and output power. An interferometric autocorrelator was used to measure the pulse duration and a fast detector was used to obtain the repetition rate.

Figure 9. Photograph of mode locked laser in its final configuration.

The new OCT system is still in its early stages of development. It, first and foremost, necessary to improve the point spread function of the Super Fluorescent Diode laser. This is obvious from the current asymmetrical point spread function obtained for the source. Next, the Ultra Broadband source needs to be tested to produce biological images. Yet, even in its early stages the new system shows potential to almost double the axial resolution of the current best available commercial system.

References

1. Agrawal, G. P. Nonlinear Fiber Optics. (San Diego: Academic, 2001).
2. Dziedzic, J. M.; Stolen, R. H. Appl. Phys. Lett. 22, 1973, 294, 1403-1406.
3. Stolen, R. H.; Bjorkholm, J. E. Appl. Phys. Lett. 24, 1974, 308, 1533-1537.
4. Hill, K. O. Johnson, D. C. J. Appl. Phys. 49, 1974, 5098.
5. Stolen, R. H. IEEE J. Quantum Electron. 11, 1975, 100.
6. Stolen, R. H. Lin, C. Phys. Rev. A. 17, 1978, 1488.
7. Koester, C. J. Snitzer, E. Appl. Opt. 1964, 3, 1182-1186.
8. Desurvire, E. Simpson, J.R.; etc. Opp. Lett. 11, 1987, 22, 888-890.
9. Desurvire, E. Bayart, D. Erbium Doped Diber Amplifiers: Device and System Development (Wiley, New York, 2002).
10. Kieu, K. Mansuripur, M. Opt. Lett. 32, 2007, 2242-2244.
11. Rüdiger, P. Encyclopedia of Laser Physics and Technology. (Wiley-VCH, Weinheim, 2008).
12. Bahaa, S. Teich, M. C. Fundamentals of Photonics. (Hoboken, N.J.: Wiley-Interscience, 2007).
13. David, H. Swanson, E. A. Science 254, 1991, 1178-1181.
14. Diels, J. C. Wolfgang, R. Ultrashort Laser Pulse Phenomena. (Elsevier, Burlington, 2006).
15. Kieu, K. Jones, J. Peyghambarian, N. in Conference on Lasers and Electro-Optics, OSA Technical Digest (CD) (Optical Society of America, 2010), paper CTuII2.

Acknowledgments

Funds for this research were provided by the Center on Materials and Devices for Information Technology Research (CMDITR), an NSF Science and Technology Center No. DMR 0120967.

Many thanks to Justin Klein from the Barton group for his OCT system expertise.

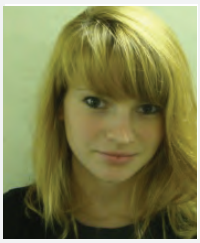

ANNA EVANS is finishing her senior year in Electrical Engineering at Boston University and is preparing to pursue a doctorate degree in Optical Engineering. She hopes to become a professor and looks forward to teaching, doing research with nonlinear optics and traveling the world.

Li^+ Cation Complexation by 15-Crown-5 Derivative: A Computational Study

ALEXANDR FONARI, New Mexico Highlands University
Jean-Luc Brédas, Georgia Institute of Technology

Introduction

Organic sensors are molecules of abiotic nature capable of interacting selectively and irreversibly with a specific substrate (ion, molecule) with corresponding changes in one or more characteristics of the system. In general a sensor molecule consists of a fluorophore connected to a receptor. Crown ethers, discovered by Pedersen,[1] occupy a special position among receptors and are widely used in the design of new sensors (chromogenic, fluorescent or photo-switchable) due to their unique ability to bind to metal cations[2] and neutral molecules, their fairly high selectivity, and their accessibility.

Recently, molecules consisting of tetra substituted quinoxalino-phenanthrophenazine (TQPP) fluorescence core derivatized with crown ether group as binding ligand, namely shown in Figure 1, was synthesized.[3]

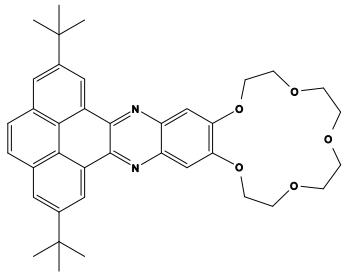

Figure 1. Scheme of 1.

The binding ability of **1** to the metals was investigated using absorption spectroscopy.[3] The addition of alkali earth metal cations: Li^+, Na^+, K^+, Ca^{2+}, Rb^+, Cs^+ and Ba^{2+} to **1** results in an appearance of a new band at 525 nm. This behavior indicates strong binding interactions between **1** and the metal ion. The greatest effect was observed for the titration with Li^+, as can be seen from Figure 2.

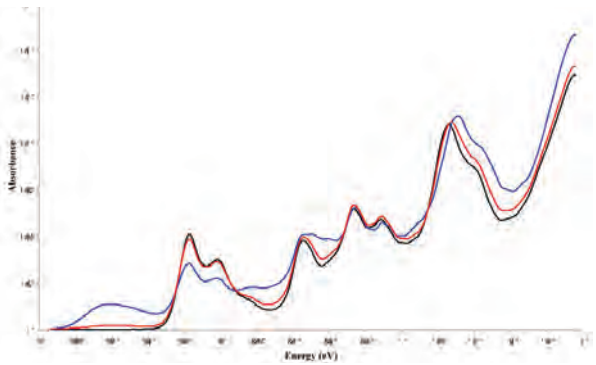

Figure 2. UV/Vis spectra of **1** upon titration with solution of lithium ions in 1:1 CH_2Cl_2/CH_3CN. 1– black; with 1.28 eq of Li^+ – red; with 10.39 eq of Li^+ – blue.[3]

In order to understand the nature of binding interactions and effectiveness of **1** as an organic sensor we investigated the electronic structure of **1** and related metal complexes. In particular we report here the ground states properties, binding energies and excited states for the compound **1** and the **1** + Li^+ complex.

Computational Approach

Molecular geometries have been optimized at the density functional theory (DFT) level using the B3LYP functional and the 6-31G** basis set.[4] The solvent effect has been taken into account by using the IEFPCM formalism[5] within the continuum polarization model (PCM). Acetonitrile was used in all solvent calculations. In the case of metal complexes, charge was set equal to *+1* and spin multiplicity to *1* (closed shell). Following geometry optimization, the frequency calculations were also performed in order to insure that the obtained geometries correspond to a stationary point. Excited states have been derived by means of time dependent (TD) DFT calculations at B3LYP/6-31+G** level of theory. The binding energy (ΔE^C) of the reaction (1)

$$Me^+ + 1 \rightarrow 1Me^+ , \quad (1)$$

in gas phase has been calculated using Eq. 2:

$$\Delta E^C = (E^{1Me+} + ZPE^{1Me+}) - (E^1 + ZPE^1) - E^{Me+} + E^C \quad (2)$$

Here E^{1Me+} and ZPE^{1Me+} represent the total energy of the complex and its zero point energy correction, respectively; E^1 and ZPE^1 are the corresponding energies of isolated molecules; E^{Me+} is the energy of metal ion, and E^C is the basis set superposition error (BSSE) energy which was calculated using counterpoise method[6]. Using B3LYP/6-31G** optimized geometries, ΔE^C were computed with two, B3LYP and ωB97X[7] functionals and with several basis sets, 6-31G**, 6-31+G** and 6-311++G**. Additional calculations were performed taking into account the solvent effect. In this case the solvent, BSSE values were taken at the same level of calculations as in the gas phase. All DFT calculations have been carried out using the Gaussian 09 package.[8]

Results and Discussion

Electronic structure of 1.

It is well known that the crown ether in solution can posses a big number of low energy lying conformations.[9] Therefore in absence of experimentally determined molecular structure it is crucial to find all configurations of the lowest energies. Therefore the geometry optimizations were performed with different starting geometries. The

three isomers obtained with the lowest energies, referred to as **1a**, **1b** and **1c**, are shown in Figure 3. The normal mode calculations reveal that all these structures represent a true minimum on the potential energy surface.

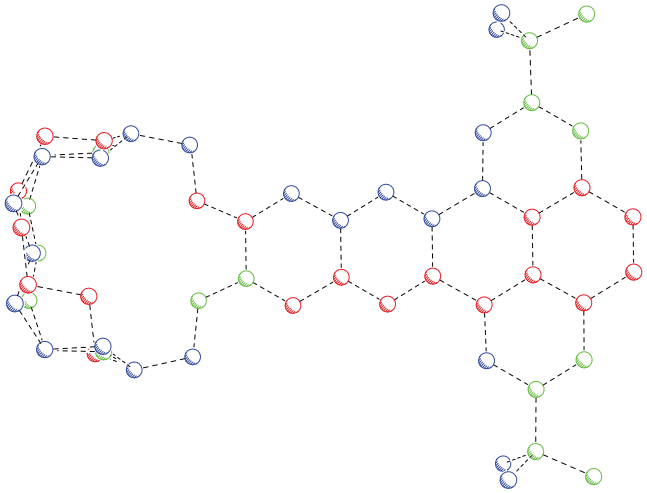

Figure 3. Fitted isomers of **1**. **1a** – blue, **1b** – red and **1c** – green.

The relative isomers energies are given in Table 1 for both gas phase and solvent case. As can be seen from Table 1 energies differ only slightly indicating that a mixture of these conformers should be present in solution. As expected, the energies in the solvent are to some extent lower than in the gas phase.

Isomer	GP	PCM
1a	0.00	-13.26
1b	1.15	-10.00
1c	1.62	-12.56

Table 1. Relative energies (corrected for ZPE) of isomers of **1** in gas phase and solvent in kcal/mol.

In general, the orbitals describing the lowest excited states of **1** are mainly localized in the TQPP core and first two oxygen atoms of the macrocyclic part. The highest occupied molecular orbital (HOMO) and lowest unoccupied molecular orbital (LUMO) of **1a** and **1b** derived for gas phase case are shown in Figure 4. As seen from Figure 3, different isomers of **1** have almost identical frontier molecular orbitals. The LUMO is mostly localized on the middle part of the molecule while HOMO is delocalized on entire molecule, excluding the macrocyclic part. A HOMO to LUMO transition will result thus in a minor charge redistribution.

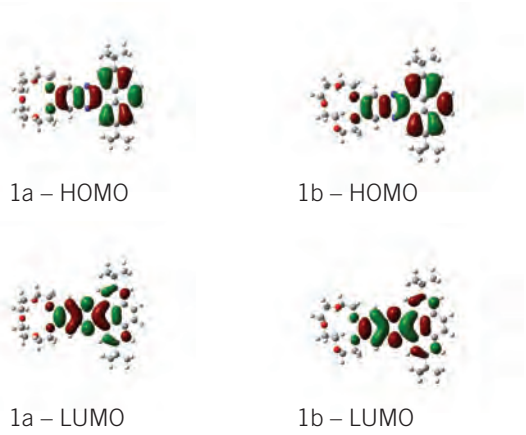

Figure 4. HOMO-LUMO orbitals of **1a** and **1b** in gas phase.

Selected molecular orbital energies are listed in Table 2. From Table 2 it can be seen that there are only minor differences between energy levels of these isomers.

Orbital	**1a**, eV	**1b**, eV	**1c**, eV
HOMO-2	-5.99	-6.08	-5.96
HOMO-1	-5.60	-5.66	-5.56
HOMO	-5.16	-5.22	-5.13
LUMO	-1.71	-1.82	-1.71
LUMO+1	-1.20	-1.27	-1.19
LUMO+2	-0.34	-0.42	-0.34
L - H	-3.45	-3.40	-3.42

Table 2. Selected orbital energies for **1** isomers in gas phase.

The results of geometry optimization show that the molecule-solvent interaction does not lead to any significant changes in geometries. The orbital energies derived from the calculations in solvent, as expected, are lower than those derived from the gas phase calculations, see Table 3.

Orbital	**1a**, eV	**1b**, eV	**1c**, eV
HOMO-2	-6.27	-6.28	-6.27
HOMO-1	-5.89	-5.89	-5.88
HOMO	-5.46	-5.46	-5.45
LUMO	-2.08	-2.09	-2.07
LUMO+1	-1.52	-1.53	-1.52
LUMO+2	-0.67	-0.67	-0.67
L - H	-3.38	-3.37	-3.38

Table 3. Selected orbital energies for **1** isomers in solvent.

The shapes of the frontier orbitals obtained from calculations in solvent are shown in Figure 5. As seen from Figures 4 and 5 HOMO and LUMO in gas phase and solvent are nearly identical. We conclude here that the differences in the conformations of the macrocyclic part do not affect qualitatively the ground state properties of **1** in both gas phase and solvent case.

1Li⁺ Complex. The geometries of **1Li⁺** obtained from calculations in the gas phase and in the acetonitrile are shown in Figure 6.

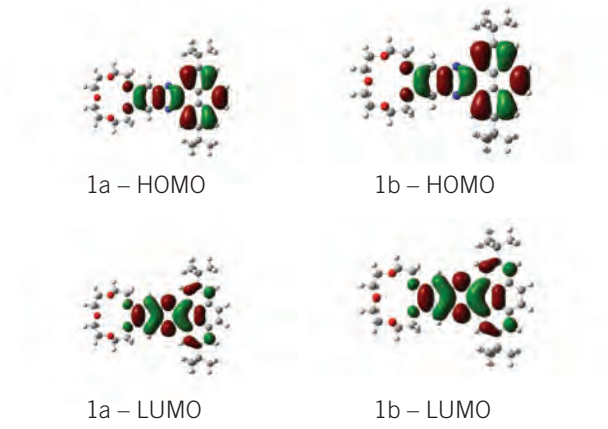

Figure 5. The lack of effect of solvent on HOMO and LUMO orbitals.

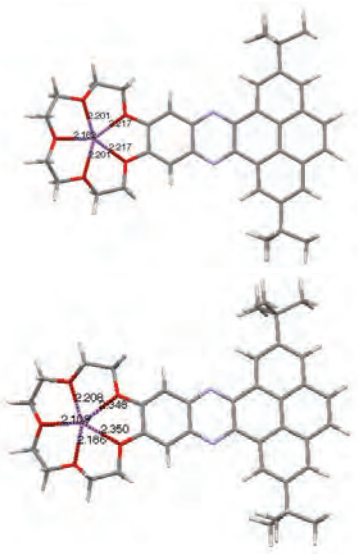

Figure 6. Molecular geometry of **1Li**+ in gas phase (left) and PCM (right). Distances are shown in angstroms. Lithium - purple; Oxygen - red; Nitrogen - blue; Carbon - grey; Hydrogen - white.

The Li-O bond lengths derived from calculations both in gas phase and solvent are listed in Table 4. These are in good agreement with Li+-O distances obtained for 15-crown-5 Li+ complex optimized at MP2/6-31+G* level in gas phase (**15CLi+**) by Hill and Feller.[9]

1Li+, GP	1Li+, PCM	15CLi+, GP
2.201	2.208	2.130
2.182	2.109	2.263
2.201	2.186	2.133
2.217	2.350	2.162
2.217	2.348	2.167

Table 4. Li+-O distances of 1Li+ in gas phase and solvent. All distances are in Å.

Binding energies. Binding energies derived from the calculations both in gas phase and solvent with different functionals and basis sets are given in Table 5. Comparing the performance of two different functionals in gas phase, it is observed that ωB97X gives lower binding energies for all tested basis sets. For B3LYP ΔE^c lies between –102.7 and –97.5 kcal/mol, for ωB97X between –100.4 and –95.9 kcal/mol while increasing basis set. With introduction of diffuse functions BSSE was lowered by approximately 4.6 kcal/mol for both gas phase and solvent, further increase of basis set does not bring significant effect.

When solvent is taken into account, the binding energy drops by approximately 80 kcal/mol mainly because of the stabilization effect of the lithium ion. The energies obtained in gas phase are in good agreement with the value of 98.2 kcal/mol obtained by Hill and Feller[9] for **15CLi**+.

Excited states. The excited states of **1** were computed for all three isomers in both gas phase and solvent. As expected, all three isomers exhibit similar excited states. The computed (gas phase and solvent) energies, oscillator strengths and the description of the lowest excited states of **1a** are given in Table 6; for the sake of comparison the experimental energies are also given.

	Method	ΔE^C, kcal/mol	BSSE, kcal/mol
GP	B3LYP/6-31G**	-102.74	6.86
GP	B3LYP/6-31+G**	-97.72	2.09
GP	B3LYP/6-311++G**	-97.57	2.33
GP	ωB97X/6-31G**	-100.35	6.30
GP	ωB97X/6-31++G**	-95.83	1.82
GP	ωB97X/6-311++G**	-95.86	1.99
PCM	B3LYP/6-31G**	-17.04	6.86
PCM	B3LYP/6-31+G**	-11.13	2.09
PCM	B3LYP/6-311++G**	-10.91	2.33

Table 5. **1Li**+ binding energies at 298 K with BSSE and ZPE corrections.

E^1 (eV)	ε^1	E^2 (eV)	f^2	E^3 (eV)	f^3	transitions
2.83	0.20	2.95	0.2959	2.89	0.3359	H → L (95)[4](98)[5]
3.45	0.19	3.68	0.1904	3.66	0.2643	H → L+1 (71)(52) H-3 → L (17)(40)
3.72	0.26	3.77	0.3423	3.73	0.3160	H-2 → L (60)(0) H-1 → L (15)(70)
4.25	0.44	4.22	0.5412	4.19	0.6145	H → L+2 (39)(42) H-3 → L+1 (30)(32)

[1] experimental obtained values; [2, 3] values calculated for 1 in gas and PCM, respectively; [4, 5] percentage of expansion coefficient in gas and PCM, respectively.

Table 6. Observed and calculated (states of interest) UV/Vis data.

DFT calculations reveal that the lowest experimental band at 2.82 eV corespond to the first excited state (that can be described as a HOMO to LUMO transition) with an energy of about 3.89 eV in PCM and 3.95 eV in gas phase.

Finally, the excited states of **1Li**+ were computed for the gas phase case. The results of **1** and **1Li**+ along with experimental spectra are shown in Figure 7. The first band observed for **1Li**+ is also attributed the first excited state (HOMO → LUMO transition). The TDDFT results suggest a red shift of about 0.43 eV for the first optical band when going from **1** to **1Li**+; the computed energy shift agrees very well with the related experimental value of 0.47 eV.

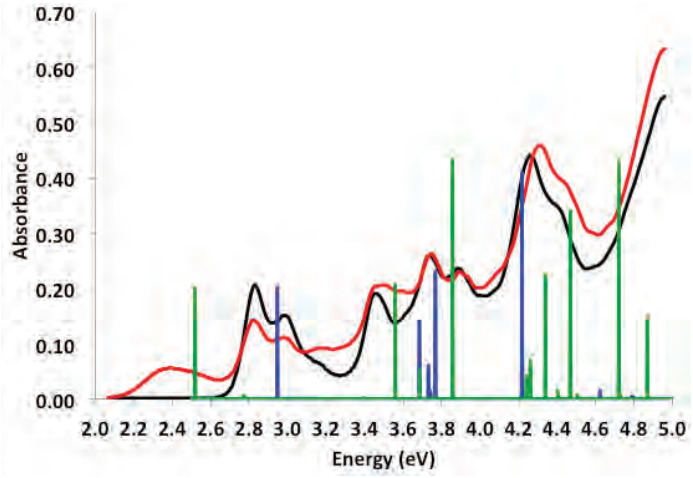

Figure 7. Experimental **1** – black, **1Li**$^+$ (10.28 eq) – red and calculated excited states for **1** in GP – blue, **1Li**$^+$ in GP – green.

Conclusions

In conclusion we note: (1) different conformations of the crown part of the molecule introduce only minor changes into ground state properties; (2) binding energies of the **1Li**$^+$ complex are much smaller in solvent then in gas phase; and (3) the excited states for both **1** and **1Li**$^+$ are well reproduced by DFT calculations. Our future work will include evaluation of the binding energies and excited states of **1** with other alkali metal cations Na^+, K^+, Ca^{2+}, Rb^+, Cs^+ and Ba^{2+}.

References

1. Pedersen, C. J. J. Am. Chem. Soc. 1967, 89, 2495.
2. Jradi, F. M.; Al-Sayah, M. H.; Kaafarani, B. R. Tetrahedron Lett. 2008, 49, 238.
3. Kaafarani, B. R. et al. Manuscript in Preparation.
4. Becke A. D. J. Chem. Phys. 1993, 98, 5648.
5. Miertus S.; Scrocco, E.; Tomasi, J. Chem. Phys., 1981, 55, 117.
6. Boys, S. F.; Bernardi F. Mol. Phys., 1970, 19, 553.
7. Gaussian 09, Revision A.2, Frisch, M. J. et al. Gaussian, Inc., Wallingford CT, 2009.
8. Chai, J; Head-Gordon M. J. Chem. Phys., 2008, 128, 084106.
9. Hill S. E.; Feller D. Int. J. Mass. Spec., 2000, 210, 41.

Acknowledgements

This work has been supported by NSF under the PREM program (Awards, DMR 0934212, CHE 0832622 and DMR 0120967).

ALEXANDR FONARI is pursuing a masters degree in Chemistry at New Mexico Highlands University. His graduate research is focused on data collection, analysis and structure refinement from single crystal X-ray diffraction. He would like to continue his research with the emphasis on quantum chemical calculations, and expects to graduate in May 2011.

Fabrication of Single Layer Phosphorescent Organic Light-Emitting Diode (OLED)

JASMINE FREEMAN, Fort Valley State University
Cai Dengke, Canek Fuentes-Hernandez, Benard Kippelen, Georgia Institute of Technology

Introduction

Organic Light-Emitting Diodes (OLEDs) are a light-weight ultra-thin light emitting technology composed of a thin, multi-layered organic film placed between a transparent anode, and a metal cathode.

OLEDs are considered the future of display as well as lighting technologies. They offer many benefits over current information display technologies like Liquid Crystal Displays (LCDs).[1] It was reported that "The highly efficient organic LEDs that can now be produced are becoming an attractive alternative to those based on conventional inorganic luminescent materials." For example, since OLEDs do not require a backlight like their LCD counter parts, they can emit much brighter light and require less energy to operate. In addition, OLEDs will be cheaper than current display technologies and also have the potential to revolutionize the lighting business with thin, flexible, mass-producible lighting fixtures. "Wallpaper lighting" and electronic paper are two future applications.[1] The improvements being made to OLEDs will cause their use in various technologies to dramatically increase within the next few years, creating a very large and prominent industry.

The structure of an OLED device is just like a sandwich. Each layer is stacked on top of another. A clear substrate acts as a foundation and is made of glass or polymer. The next layer is the anode made of indium tin oxide otherwise known as ITO. The organic materials compose a multi-layered thin film, which typically includes a hole transporting layer (HTL), emission layer (EML) and the electron transporting layer (ETL). By applying the appropriate electric voltage, holes and electrons are injected into the EML from the anode and the cathode, respectively. The holes and electrons combine inside the EML to form excitons, after which electroluminescence occurs. The hole and electron transport material, emission layer material and choice of electrodes are the key factors that determine the quality of the OLED. A metal cathode covers over the top. Calcium is the metal of choice for the cathode as it has a relatively low work function to facilitate the electron injection. However, calcium is very reactive in air. To protect it from reacting with its surroundings, it is usually covered with a more inert metal like silver.

The purpose of my research was to replace the multilayered organic structure which is typically composed of the HTL,EMLand ETL, by a single layer which combines these functionalities. This layer will be composed of one oxadiazole-carbazole-based polymer layer with hole and electron transport properties. OEP1 polymer will then be combined with $Ir(ppy)_3$, as light emissive moiety. My main goal was to demonstrate OLED behavior when the $Ir(ppy)_3$ was added to the polymer layer.

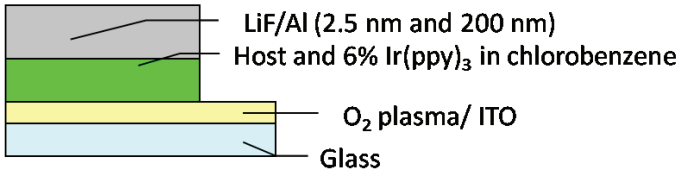

Figure 1. OLED structure.

Experimental (Research Methods):

Glass cutting

Pure Indium Tin Oxide (ITO) glass was cut using a Steel Wheel Unit into a size of 1 in x 1 in. The cut pieces of ITO/glass was placed in a glass holding rack.

Cleaning substrate

There are four main steps to cleaning a substrate. Step one: Glass pieces were cleaned and placed into the bowl. Bowl was filled with soap and distilled water and placed in an ultrasonic cleaner for twenty minutes. Step two: Once twenty minutes are up, soap and water was poured out, and glass was then filled with distilled water. Glass was then placed in the ultrasonic cleaner for twenty minutes. Step three: Once twenty minutes were up distilled water was poured off, and then glass again was filled with isopropanol. Glass was then placed in the ultrasonic cleaner for twenty minutes. Step four: Once twenty minutes were up isopropanol, was poured off and then glass was filled with acetone. Glass was then placed in the ultrasonic cleaner for twenty minutes

Preparing organic material

Approximately 0.0295 g of oxadiazole-carbazol was weighed out. Approximately 0.0019 g of $Ir(ppy)_3$ was also weighed out and placed into a glass vial. This corresponds to a weight percent of $Ir(ppy)_3$ of 6 wt. %, and 94 wt.% of the host material. Three milliliters of toluene were placed in the glass vial along with a magnetic stirring rod. Glass vials with solvent were then placed on a stirring plate for twenty four hours.

ITO coated glass substrates (20 Ω/□ Colorado Concept Coatings, L.L.C.) were first cleaned in an ultrasonic bath using a dilute solution of Triton-X (Aldrich) in deionized (DI) water (20 min) followed by a final ultrasonication for 20 min in DI water. Further organic cleaning was done in the ultrasonic bath using acetone and ethanol for 20 min each. Cleaned ITO substrates were then dried in a vacuum oven at 70 °C under a pressure of 1×10^{-2} Torr for 1 hour.

The surface modification was performed in a glove box filled with N_2 having O_2 and H_2O levels of <20 ppm and <1 ppm, respectively, by dipping the cleaned ITO substrates in a solution of the phosphonic acid (1 mM in $CHCl_3$:C_2H_5OH:2:1) for 30 min, followed by annealing at 120 °C for 1 hour.

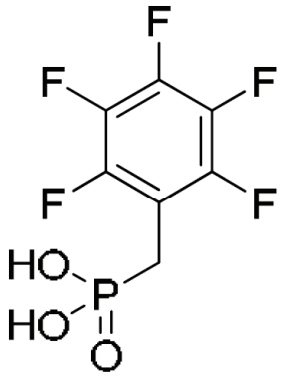

Figure 2. Chemical structure of F5BPA.

O_2 plasma

The surface of the subrate was treated in O_2 plasma for 3 mintues.

Spin coating

Spin coating is a procedure used to apply uniform thin films to flat substrates. In short, an excess amount of a solution which was mixed is placed on the substrate, and then the substrate was rotated at high speed in order to spread the fluid by centrifugal force. A machine used for spin coating is called a spin coater, or simply spinner. There are two distinct stages to the spin coating process. Step one: A coating of solution was placed onto a substrate. This was done by using a syringe and pouring the coating solution onto the center surface of the substrate. A substantial excess of coating solution is usually applied compared to the amount that is required. Step two: The substrate was spun at its final, desired, and rotational speed for sixty seconds.

Measuring thickness of thin film deposited on substrate

The Dektak 6M takes measurements electromechanically by moving the sample beneath a diamond- tipped stylus. The high- precision stage moves a sample beneath the stylus according to a user-programmed scan length (600 mu), speed (6500 nm), and stylus force (3 mg). The stylus is mechanically coupled to the core of a Linear Variable Differential Transformer (LVDT).

As the stage moves, the stage moves the sample, and the stylus rides over the sample surface. Surface variations cause the stylus to be translated vertically. Electrical signals corresponding to stylus movement are produced as the sore position of the LVDT changes. The LVDT scales an AC reference signal produced to the position changes, which in turn is conditioned and converted to a digital format through a high precision, integrating, analog-to-digital converter.

The digitized signals from performing a single scan are stored in computer memory for display, manipulation, measurements, and printing. The Dektak 6M stores programs that can easily be changed to suit both production and laboratory use.

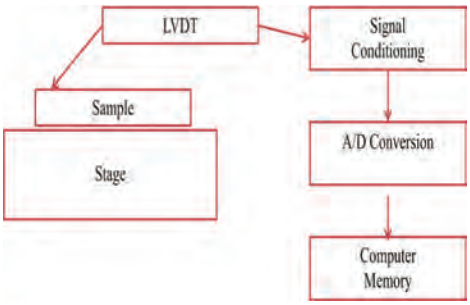

Figure 3. Block Diagram of Dektak 6M Architecture.

Results and Discussion

Figures 4 and 5 show the performances of three OLEDs having different organic layer thicknesses: 40, 55, and 68 nm. The luminance and efficiency of the OLED with the 40 nm organic layer which is indicated on Figures 5 and 6 was 0.1 % EQE at 100 cd/m^2. The luminance and efficiency of the 55 nm single layer which is indicated on the graph was 0.3 % EQE at 100 cd/m^2. The luminance and efficiency of the 68 nm single layer which is indicated on the graph was 0.4 % EQE at 100 cd/m^2. This showed us that the thicker the organic layer was, the better OLED performance was obtained.

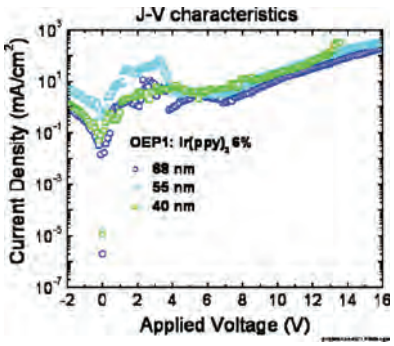

Figure 4. J-V Characteristics.

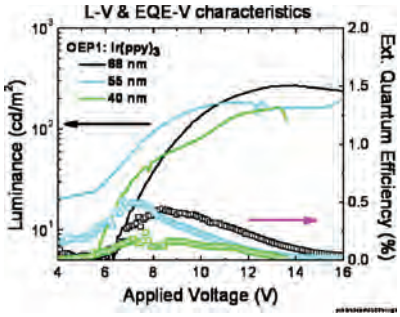

Figure 5. L-V & EQE-V Characteristics.

Figures 6 and 7 show the influence from surface treatments on the device performance between O_2 and F5BPA. The OLED with an O_2 plasma treated ITO had a 0.14% EQE at 100 cd/m^2 and the OLED with the F5BPA-treated ITO had a 0.04% EQE at 100 cd/m^2.

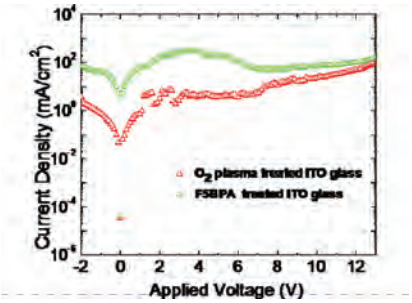

Figure 6. Current Density vs. Voltage.

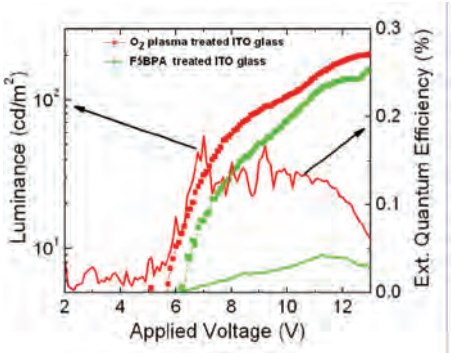

Figure 7. L-V & EQE-V Characteristics.

Figures 8 and 9 show the influence from annealing vs. no annealing on device performances. We annealed the device at 80°C/h and found the luminance and efficiency to be 0.14% EQE at 100 cd/m^2. The device with no annealing had an luminance and efficiency of 0.07% EQE at 100 cd/m^2.

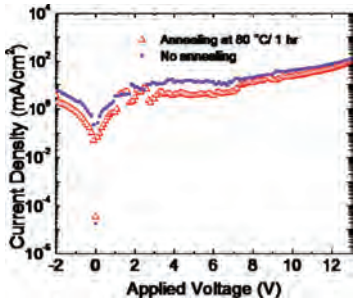

Figure 8. Current Density vs. Voltage.

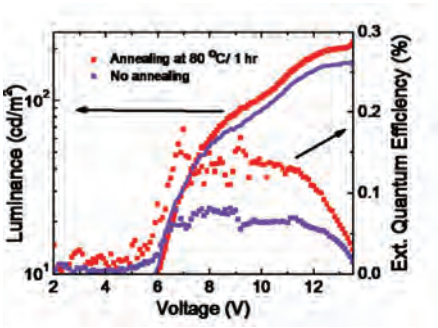

Figure 9. L-V & EQE-V Characteristics.

Conclusion

In summary, we have successfully demonstrated single layer phosphorescent OLEDs and verified the thickness of layer. We found that the thicker the emissive layer, the better the performance the device will have. To improve the efficiency of OLEDs with a single organic layer, we investigated the influences from substrate surface treatments and annealing on OLED device performance. It is identified that O_2 plasma surface treatment is better than F5BPA on improving single layer luminance and efficiency. We also found that devices that undergo annealing are better than those without annealing.

References

1. A. Köhler, J. Wilson and R. Friend. 2002. Fluorescence and phosphorescence in organic materials. Advanced Materials. 10:701-707.
2. H. N. Raval, S. P. Tiwari, Ramesh R. N., V. Ramgopal Rao, IEEE Electron Device Letters, Vol. 30, Issue 5, 484-486, 2009.
3. S. P. Tiwari, X.-H. Zhang, W. J. Potscavage, and B. Kippelen, Applied Physics Letters, Vol. 95, 223303, 2009.
4. S. P. Tiwari, W. J. Potscavage, T. Sajoto, S. Barlow, S. R. Marder and B. Kippelen, Organic Electronics, Vol. 11, 860-863, 2010.
5. S. P. Tiwari, E. B. Namdas, V. Ramgopal Rao, D. Fichou, S. G. Mhaisalkar, IEEE Electron Device Letters, Vol. 28, Issue 10, 880-883, 2007.

Acknowledgments

Funds for this research were provided by the Center on Materials and Devices for Information Technology Research (CMDITR) and the NSF Science and Technology Center No. DMR 0120967.

JASMINE FREEMAN's goal is to pursue a career where her educational background and training in chemistry can be utilized.

Conversion of Waste Thermal Energy into Electrical Energy Using Ionic Liquid Thermogalvanic Cells

BRANTLY FULTON, Morehouse College
Theo Hicks, Virendra Singh, Pablo Salazar, and Baratunde A. Cola, Georgia Institute of Technology,
Renchong Hu, Ray H. Baughman, University of Texas

Energy conversion with current thermogalvanic cells is limited by the use of aqueous electrolytes because many attractive applications require an electrolyte that is stable at temperatures higher than 100 °C, and because the efficiency of thermogalvanic energy conversion is known to increase with temperature. Here the use of ionic liquids (ILs) as solvents for thermocell electrolytes will be explored. ILs allow higher ion and thermal conductivity than water, are stable in air and high temperatures, and designable because they are constructed solely of ions. 1-ethyl-1-methylimadazolium (EMISCN) is one particular IL studied due to its relative low viscosity and cost effectiveness. Cyclic voltammetry (CV) was used to measure the redox behavior of I^-/I_3^- in EMISCN at platinum and carbon nanotube (CNT) electrodes. CV scans were also used to characterize platinum and CNT electrodes in organic electrolytes for comparison with ILs. The maximum peak current produce by these tests was 55 µAmps. This low current is believed to be the result of the low solubility of I^-/I_3^- in EMISCN. The results suggest that ILs can be used for thermogalvanic energy but more work is required to identify combinations of ILs and redox couples that produce large currents.

Introduction

Thermo-electrochemical cells have been studied for many years to understand their functions and how they have an impact in both the scientific and industrial realm. The basic understanding of this system consists of two electrodes submerged in an electrolyte solution with a redox couple which is affected by a temperature gradient which generates an electrical current.[1] The reason for this is known as the Seebeck Effect which is of prime importance in the topic of this research and will be discussed in greater detail later. A pair of thermal couples was used for this particular cell as the load which displays a voltage.

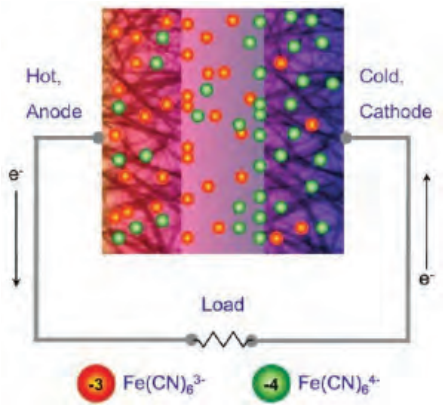

Figure 1. Schematic of thermocell showing redox pair concentration gradient.[2]

Reasons for Using Carbon-Nanotubes

Most electrochemical cells have been tested using Platinum foil (Pt) electrodes which is inefficient in terms of current output. Alternatively, multiwalled carbon nanotube (MWNT) buckypaper[2] provides large surface area for fast redox reaction. Due in part to the high cost of Pt these technologies have been limited. Carbon nanotube (CNT) based electrodes have shown better thermogalvonic performance along with a cost reduction, which opens new windows of opportunity for renewable energy sources. The CNT's dimensions used for the thermocell experiment were 2.5 cm x 0.8 cm which is a small surface area in which the current can be affected by the dimensions. A larger surface area will produce a higher current. The identical CNTs were each attached to copper wire (Cu) and copper tape to hold the electrode in place. Nail polish was used to coat the copper wire which is a contraceptive measure to decrease the onset of corrosion. Corrosion in these cells is usually caused by the oxidation of copper at the hot temperature electrode because the high temperature causes condensation in the cell if not kept under a stabilizing gas.

Aqueous vs. Non-Aqueous Solvents

Though water is the universal solvent and can take higher concentrations of the redox system of Potassium Ferricyanide ($K_3[Fe(CN)_6]$) and Potassium Ferrocynaide ($K_4[Fe(CN)_6]$) which are used in this system; the cell operating temperature range is limited to the boiling temperature of water (100 °C). Non-Aqueous solvents such as Ionic Liquids (ILs) can offer a higher temperature range due to their high thermal conductivity and stability. These liquids mostly contain ions, thus have the ability to carry greater charge throughout the system. Their organic structure also allows them to be designable which means that catalyst or more complex ionic liquids can be formed which can become even more ion conducive for this system. With negligible vapor pressure ILs are safe to use at higher temperature. Tests were performed with DMSO and Propylene Carbonate (PC) but each solvent showed an inability to concentrate all of the redox solution. PC proved to be the more stable of the two liquids but still does not work well under ambient temperatures the way that ILs are able to do. The principal solvent used for experimentation was 1-ethyl-1-methylimadazolium (EMISCN); a low viscous IL that works well under ambient temperatures due to its low freezing point and high boiling point. Its low viscosity is key because it allows for faster transfer of electrons which is equally as important as the Seebeck effect.

Purpose of the Redox Couple

The redox couple of $K_3[Fe(CN)_6]$/ $K_4[Fe(CN)_6]$ is used to create an

oxidation and reduction reaction in the electrolyte solution to create an electrical potential. This process is created when the temperature gradient forces an electron to transfer. This process is continuous as this single electrode bounces back and forth from the hot to the cold electrode. As the electron moves, a charge is generated creating a voltage gradient within the system. This concept is suggested through the Seebeck Effect which states that a temperature gradient creates a concentration gradient which in turn creates a voltage gradient ($\Delta T=\Delta C=\Delta V$). Though the redox pair of $K_3[Fe(CN)_6]$/ $K_4[Fe(CN)_6]$ was used primarily as the supporting electrolyte for aqueous and organic liquids it would not be suitable for ionic liquids.

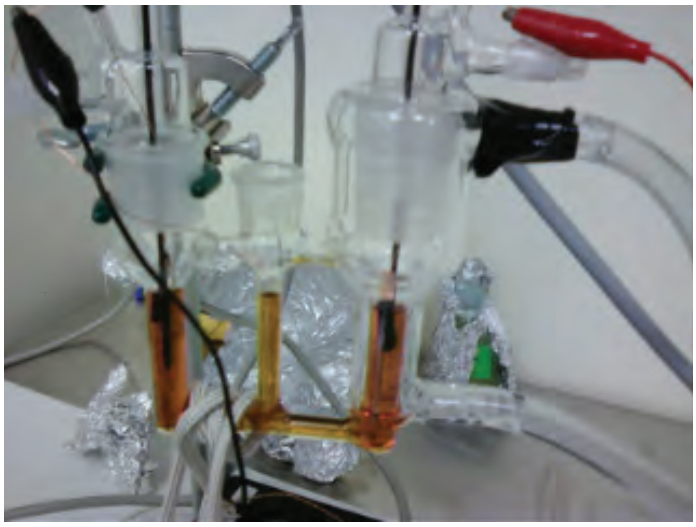

Figure 2. Shows the galvanic thermocell set-up.

The redox pair of I^-/I_3^- is formed by using an Iodide ion from the ionic liquid 3-propyl-1-methylimadoleum (PMII) and Iodine (I_2). The reaction happens in two different sequences where the first is the formation of Triiodide (I_3^-) from Iodide ions (I^-). Triioide then forms Iodine (I_2). The first reaction is more favorable. The favorability of these reactions can be determined through their oxidation numbers. The redox reaction is detailed below to show how it may affect cyclic voltammetry:

$$3I^- \rightarrow I_3^- + 2e^- \qquad [1]$$

$$2I_3^- \rightarrow 3I_2 + 2e^- \qquad [2]$$

The Role of Cyclic Voltammetry

Cyclic Voltammetry is a graphical method used to show the oxidation/ reduction reaction peaks for the redox couple. This graph is plot of potential vs. current. The reversibility of the reaction can be observed by the potential difference of the redox peak.

The current is directly affected by the concentration of the redox couple in the solvent. Theoretically when concentration is near its threshold then the current output should be near its peak. For this research reversibility is very important because the system needs to be capable of self regeneration.

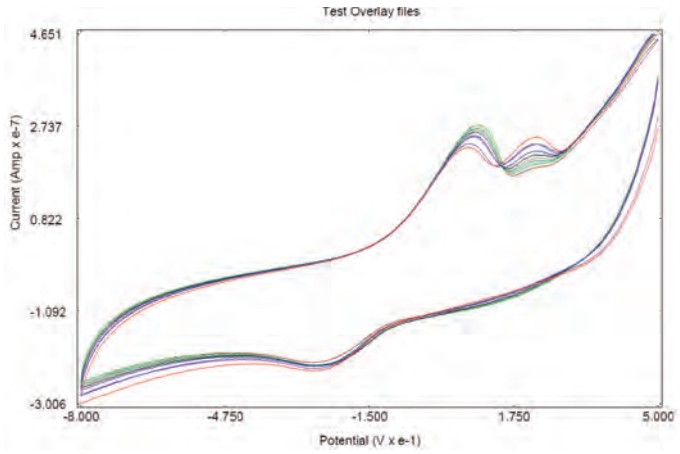

Figure 3. Cyclic voltammogram of redox pair in propylene carbonate.

The cyclic voltammetry scan Figure 3 shows the scan of PC and the I^-/I_3^- redox pair. From the graph both redox peaks are visible which proves that this particular reaction happens in two sequences. The above data also shows this reaction happening at multiple scan rates. The highest current from the above reaction was detected at 100 mV/s. The second highest current for the above reaction was detected at 75 mV/s. The third highest current for the above scan is 50 mV/s. The smallest scan rate was 25 mV/s. This graph shows us that as the scan rate decreases the detectable redox reaction current peaks also decrease. This is an indicator of how fast this reaction takes place which is a critical step for understanding the mechanisms of how efficient a thermogalvanic cell can become. The scans give an indication of the current that the redox pair is able to produce. An increase in concentration is the primary tool used to generate a higher current. A problem when using ionic liquids is the solubility for different redox couples have not been widely tested therefore calculations are frequently based on estimates or trial and error.

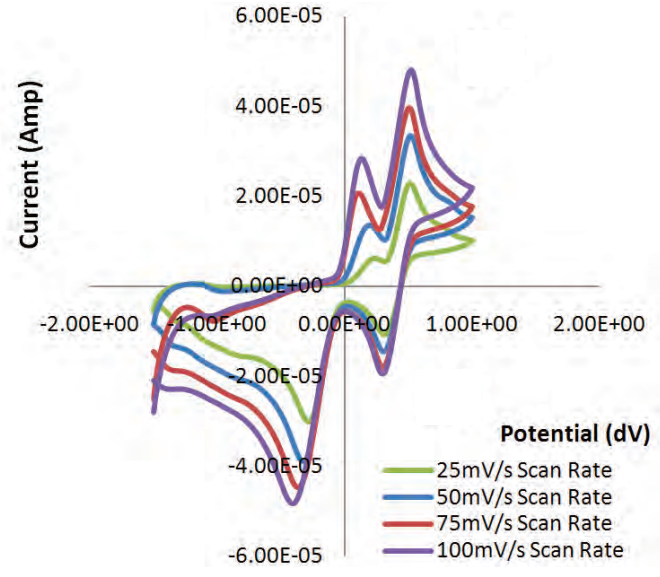

Figure 4. Cyclic voltammetry scan shows the scan of PC and the I^-/I_3^- redox pair.

Time (Hrs)	ΔT (°C)	ΔVoc (mV)	Se (mV/°C)
	0	-355	0
	0	843	0
0	6.4	*-18	-2.81
1.15	6.9	*-22	-3.38
14.15	6.0	*9	1.49
16	5.7	-11	-1.94
17	5.5	16	2.87
19	20.9	*1	.006
24	80.0	112	1.40

Table 1. Shows a stability test taken using EMISCN and CNT electrodes. The concentration of the 20 mL electrolyte solution was 0.009 M PMII, .003 M I_2.

Table 1 shows that a Seebeck coefficient greater than 1.4 mV/s (which is known as an average coefficient) can be obtained by using ILs. The table also shows that ILs have the ability to cause both a positive and negative Seebeck effect which suggests that at different temperatures one electrode side is favored over the other.

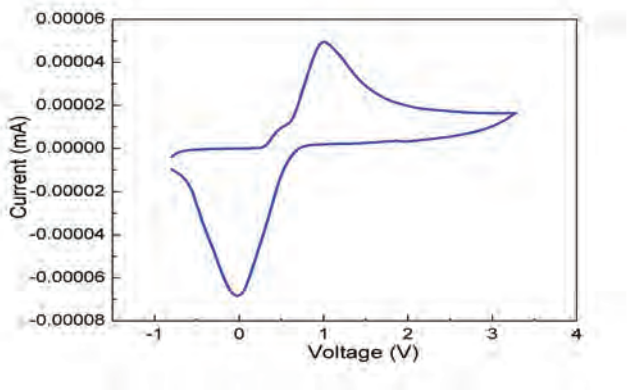

Figure 5. Shows a CV scan with EMISCN using Pt electrodes. The current is 55 µAmps.

Figure 5 shows that the redox pair is able to produce similar oxidation and reduction peaks. These peaks produce a low current of around 55 µAmps which is believed to be induced by the low concentration of the redox couple. If concentration in the redox pair is increased, current is suggested to improve. The electrochemical potential for this scan is also very large equaling 1 V between peaks which shows that this is a slow reaction. The slow reaction may be caused by the low concentration of the redox pair or it could be due to the viscosity of the electrolyte causing slower ion diffusion.

References

1. T. I. Quickenden and Y. Mua, Electrochem. Soc., Vol. 1, 1995.
2. R. Hu, B. A. Cola, N. Haram, J. N. Barisci, S. Lee, T. Stoughton, G. Wallace, C. Too, M.Thomas, A. Gestos, M. E. dela Cruz, J. P. Ferraris, A. A. Zakhidov and R. H. Baughman; Nano Lett., 2010, 10 (3), 838–846.
3. M. Zistler et. al. Electrochemica Acta 52, 2006, 161-169.
4. K. J. Hanson et. al. J. Electrochem. Soc. (134) 9, 1987.

Acknowledgements

I would like to thank the Center on Materials and Devices for Information Technology Research (CMDITR), NSF Science and Technology Center No. DMR 0120967, The NEST Lab and collaborators, Georgia Tech, and Morehouse College. I also would like to give a special thanks to Theo Hicks, Kyarra Thompson, and Sameer Rao.

BRANTLY FULTON is a Sophomore Chemistry major at Morehouse College from Pontiac, Michigan. He has enjoyed his research so far while working on thermogalvanic cells and is eager to continue as new technological breakthroughs are on the horizon.

Investigation of Charge Transfer Characteristics of Distyryl Substituted Poly (Phenylene Ethynylens)

ASHLEY GANS, Dominican University
Ariel Marshall, Joseph Perry, Georgia Institute of Technology

Introduction

Multi-photon absorption processes are currently of considerable interest for applications such as optical limiting. Previous studies have shown that molecules with centrosymmetric donor-acceptor (D-A) configurations show very large two-photon absorption cross sections (δ) due to intramolecular charge transfer upon excitation.[1] Studies have also shown that increased δ values can be obtained by extending the π conjugation of the D-A structure, Therefore, much research effort has been devoted to the development of these materials. Currently small molecules such as fullerenes and metalloporphyrins are used for optical limiting but they are often difficult to process and can have problems with aggregation during fabrication. Conjugated polymers offer a more easily processed and tunable alternative for optical limiting.

Poly(*p*-phenyleneethylene)s, PPEs, are conjugated polymers which have received much attention because of their interesting non-linear optical properties. These materials possess properties such as two-photon absorption (TPA), reverse saturable absorption (RSA), and excited state absorption (ESA) which can be applied towards the application of optical limiting (OL).[2] Through OL processes, these polymers may provide a means to create safety products for operators and sensors to be used in circumstances where intense light radiation is being utilized.

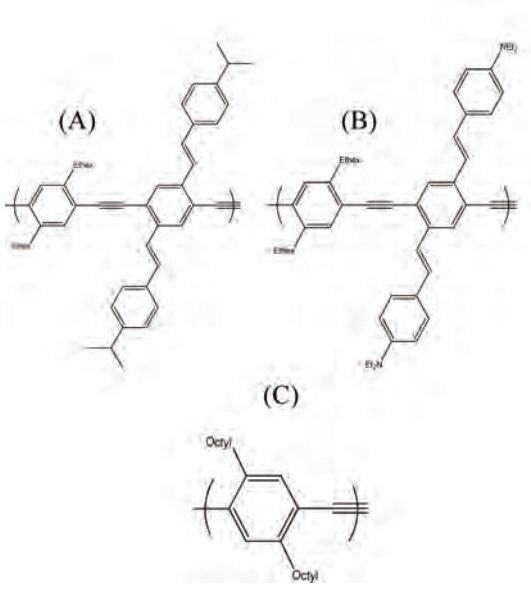

Figure 1. Molecular structures of distyryl substituted PPE polymers used in this study: isopropyl distyryl substituted PPE (A- ISP PPE), diethylaminostyryl substituted PPE (B-DEA PPE), and dioctyl substituted PPE (C-Octyl PPE).

Distyryl substituted PPE polymers have been synthesized (see Figure 1). Initial spectroscopic investigation of these PPE polymers have revealed interesting optical properties including (1) uncharacteristic PPE absorption and emission profiles, (2) significantly increased triplet yields, (3) increased fluorescence lifetimes, and (4) relatively large δ values. All of these properties suggest intramolecular charge transfer character. The objective of this project is to understand the excited state dynamics and degree of charge transfer (CT) character in these substituted PPE polymers.

Results from this study may lead to advancements in the molecular design of materials used in optical limiting.

Experimental

The following materials were obtained from the Uwe Bunz research group of Chemistry and Biochemistry at Georgia Institute of Technology and were used as received.

Octyl PPE: poly(2,5-dioctylphenyleneethynylene)

ISP PPE: 2,5-bis(isopropylstyryl)-1,4-phenylene-b-alkyne-b-1,4-bis(2-ethylhexyl)benzene terpolymer

DEA PPE: 2,5-bis(diethylaminostyryl)-1,4-phenylene-b-alkyne-b-1,4-bis(2-ethylhexyl)benzene terpolymer

All spectroscopic measurements were performed using spectroscopic solvents received from Aldrich.

UV-Vis absorption spectra were obtained using Shimadzu UV-Vis NIR scanning spectrometer (UV-310PC).

Emissions spectra were obtained using a Spex Fluorolog-2 spectrofluorimeter. To obtain fluorescence spectra, all polymers were excited at their maximum absorption value, λ_{max}Abs (see Table 1). All spectra have been corrected by subtraction of the spectrum of a solvent blank spectrum and the instrument correction factor. Low concentration polymer solutions (10^{-6} M) were used during all steady-state fluorescence measurements to minimize inner filter effects.

Charge transfer characteristics of the PPE polymers were studied via solvatochromic effects on absorbance and emission profiles. The following solvents were used: toluene, chloroform, chlorobenzene, tetrahydrofurane (THF), and dichloromethane (DCM). The solvents ranged in dielectric coefficients from 2.4 to 9.1.[4] Solution concentrations were determined per repeating unit.

Polymer	Solvent	Dielectric Constant[5]	λ_{Max} Abs (nm)	λ_{Max} Em (nm)	Stokes Shift (10^3 cm^{-1})	(ε-1)/ (2ε+1)	Δμ (D)
Octyl PPE	Toluene	2.4	391	423	1.84	2.41E-01	1.12
	Chloroform	4.8	393	425	1.92	4.22E-01	
	Chlorobenzene	5.6	393	422	2.20	4.06E-01	
	THF	7.5	397	426	1.68	3.58E-01	
	DCM	9.1	391	426	2.17	3.77E-01	
ISP PPE	Toluene	2.4	361	443	5.13	2.41E-01	1.21
	Chloroform	4.8	360	444	5.26	3.58E-01	
	Chlorobenzene	5.6	363	445	5.08	3.77E-01	
	THF	7.5	360	443	5.28	4.06E-01	
	DCM	9.1	359	444	5.33	4.22E-01	
DEA PPE	Toluene	2.4	398	532	6.33	2.41E-01	2.88
	Chloroform	4.8	397	548	7.06	4.22E-01	
	Chlorobenzene	5.6	401	544	6.69	4.06E-01	
	THF	7.5	398	566	7.46	3.58E-01	
	DCM	9.1	399	566	7.39	3.77E-01	

Table 1. Maximum absorption and emission wavelengths and solvent parameter values.

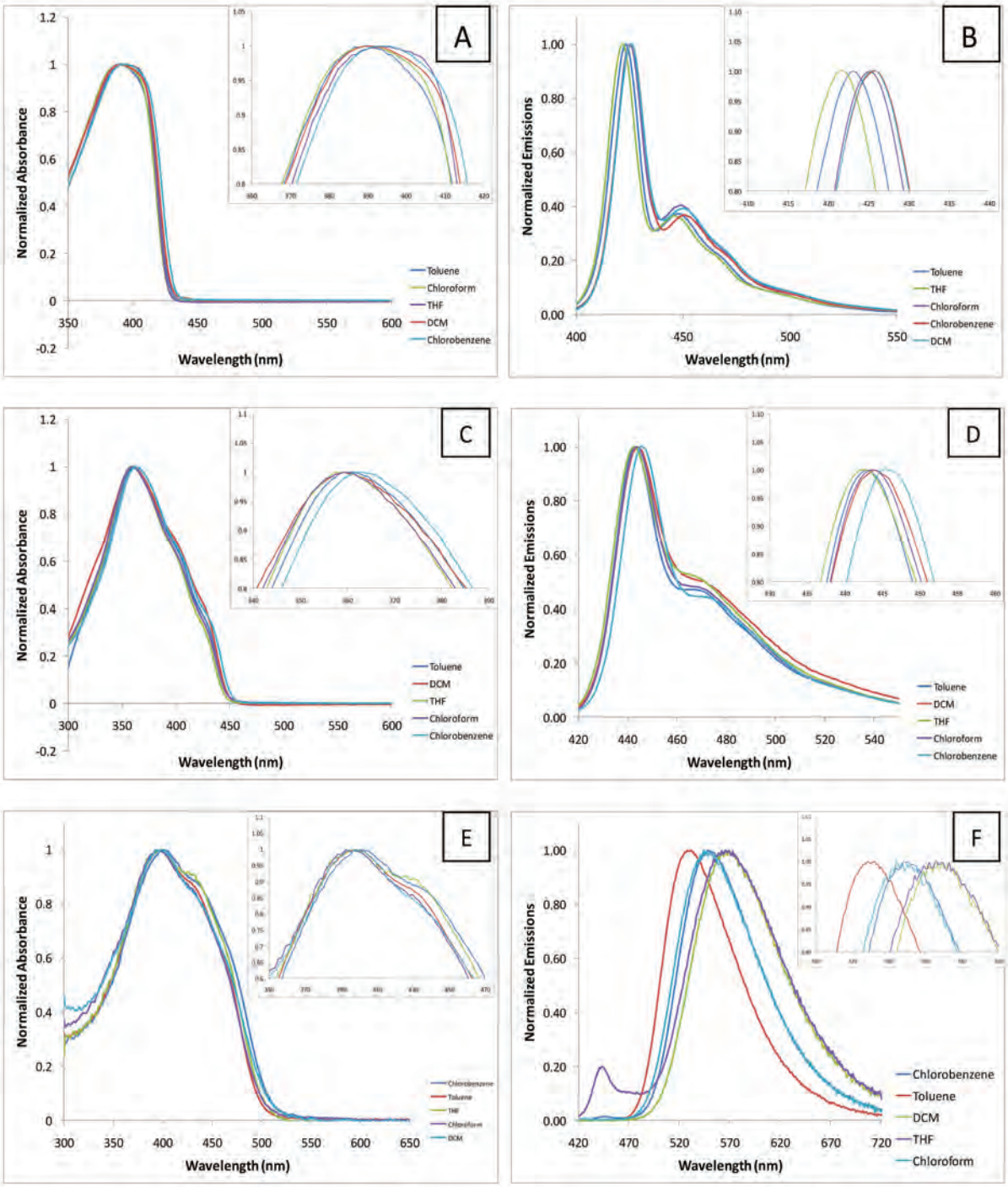

Figure 2. Normalized steady-state absorbance and emission of octyl PPE (A and B), ISP PPE (C and D), and DEA PPE (E and F), respectively.

Results and Discussion

3a. The steady-state spectra of each polymer solution can be seen in Figure 2. Octyl PPE shows characteristic PPE spectra with broad absorption and narrow emission profiles and a very small Stokes shift. The addition of the distyryl arm results in a drastic change in steady-state spectra. While both ISP and DEA PPE show broad absorbance bands, their emission profiles are very different. However slightly red shifted, the emission spectrum of ISP PPE shows characteristic PPE photoluminescence with a large, prominent electronic transition followed by a small shoulder. The emission spectra of DEA PPE is very broad and absent of vibronic structure, deviating from the sharp electronic transitions expected from PPE polymers. DEA PPE also shows an increased Stokes shift compared to Octyl PPE, along with a shift of maximum fluorescence wavelength to longer wavelengths, all of which suggest intramolecular charge transfer character within the polymer. As seen in Figure 2, there is very little solvatochromic shift observed in the absorbance spectra. As solvent polarity is increased, the absorbance maxima were slightly red-shifted ~3 nm for all three polymers. Slight obscurities can be seen in THF which showed a slight hypsochromatic shift with respect to toluene. Because toluene is slightly polarizable, the spectra seen are not only a result of solvent-solute interactions, but also solvent interaction with the incident field.

A bathochromic shift is more observable in the emissions spectra of the polymers, indicating the excited state is more polarizable than the ground state of the polymer, with DEA PPE showing the largest amount of solvatochromic shift (~30 nm).

Despite bathochromic shifts seen in emission spectra, both absorbance and emission spectra of Octyl PPE and ISP PPE indicate that solvent environment has little effect on the both substituted and unsubstituted PPE polymers. Large spectral shifts (~20 nm) indicate strong charge transfer character due to stabilization of ground or excited state potentials due to solvent effects.[4] The small shift observed from ISP PPE (~3 nm) does not suggest strong charge transfer character within the polymer. In contrast, DEA PPE showed a much larger bathochromic shift (~30 nm) attributed to intramolecular charge transfer of electron density from the distyryl amine group to the PPE polymer chain.

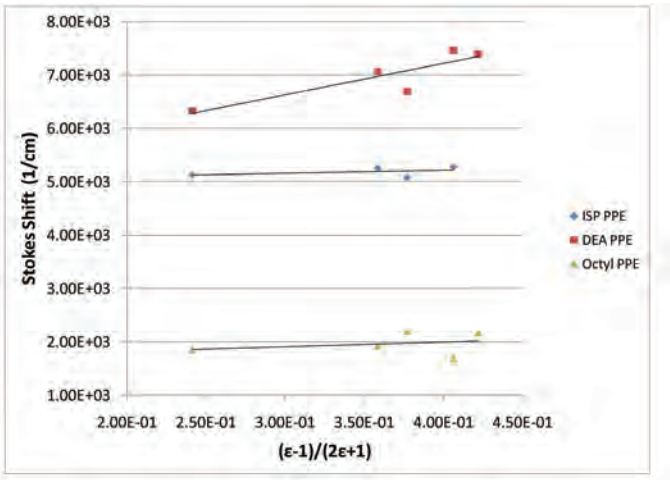

Figure 3. Graph of the linear relationship between change in dipole moment and the dielectric constant of Octyl PPE, ISP PPE and DEA PPE based on the Lippert-Magata equation.

3b. To get insight into the solvatochromic behaviors of distyryl substituted PPEs, the spectral dependency of the polymers on solvent polarity was studied using the Lippert-Magata equation.[4]

$$\bar{V}_a - \bar{V}_f = \frac{2(\Delta\mu)^2}{cha^3} F$$

where V_a -V_f is the Stokes shift in of the molecule in the solvent, c is the speed of light, h is Planck's constant, α radius of the cavity where the fluorophore resides, and $\Delta\mu$ is the change in dipole moment.

F is an equivalent constant which expresses the effect of dielectric and refractive index of the solvent expressed by:

$$F = \frac{\varepsilon - 1}{2\varepsilon + 1} - \frac{n^2 - 1}{2n^2 + 1}$$

where ε is the dielectric constant and n is the refractive index of the solvent. Tabular data of calculated values can be found in Table 1.

The relationship between Stokes shift and the portion of F that represents the effect of dielectric constant on the potential field of the solvent were graphed and found to have a linear relationship (see Figure 3). The portion of F containing the refractive index was removed in order to remove the effect of solvent polarization on the system. The change in dipole ($\Delta\mu$) was calculated from the slope of the linear regression. The polymer was assumed to be spherical, and a was the overall bond length of the repeating PPE units. Larger $\Delta\mu$ values obtained for DEA PPE indicate significant dipole changes due to the solvent environment. This indicates a potentially useful excited state activity within the distyryl substituted polymer, justifying further research which may lead to advancement in optical limiting technology.

Conclusion

Knowledge of intramolecular charge transfer characteristics of these PPE polymers is important to the understanding of their potential use as optical limiters. Solvent polarity showed very little effect on Octyl PPE, ISP PPE, Octyl PPE absorbance spectra; however, all PPE polymers studied showed fluorescence solvatochromic shift due to solvent environment, with DEA PPE showing the largest shift of ~30 nm. The large bathochromic shift seen in DEA PPE emission indicates moderate charge transfer character within the polymer, likely due to charge transfer from the amine group of the substituent. Values of $\Delta\mu$ agree with spectroscopic data by ranging from a small $\Delta\mu$ of 1.12 D for Octyl PPE to a larger $\Delta\mu$ of 2.88 D for DEA PPE. Further investigation of the charge transfer character of the PPE polymers include investigation of solvatochromic effect along a broader range of solvent dielectric polarities. Ultrafast spectroscopic techniques can also be used to observe solvatochromic effects on the more polarizable excited states of the polymers.

References

1. Albota, M.; Beljonne, D.; Brédas, J.-L.; Ehrlich, J. E.; Fu, J.-Y.; Jeikal, A. A.; Hess, S. E.; Kogejj, T.; Levin, M. D.; Marder, S. R.; McCord-Maughon, D.; Perry, J. W.; Röckel, J.; Rumi, M.; Subramaniam, G.; Webb, W. W.; Wu, X.-L.; Xu, C., Design of Organic Molecules with Large Two-Photon Absorption Cross Sections. Science 1998, 281, 1653-1656.
2. R. Giesa. Synthesis and Properties of Conjugated Poly(Aryleneethynylene)s Polymer Reviews, 36(4), 1996, 631-670.
3. Levitus, M.; Schmieder, K.; Ricks, H.; Shimizu, K. D.; Bunz, U. H. F.; Garcia-Garibay, M. A., Steps To Demarcate the Effects of Chromophore Aggregation and Planarization in Poly(phenyleneethynylene)s. 1. Rotationally Interrupted Conjugation in the Excited States of 1,4-Bis(phenylethynyl) benzene. Journal of the American Chemical Society 2001, 123. (18), 4259-4265.
4. J. R. Lakowicz, Principles of Fluorescence Spectroscopy, Plenum, New York, 1983, 205-215.

Acknowledgements

Acknowledgements should be made to the Center on Materials and Devices for Information Technology Research (CMDITR), NSF Science and Technology Center No. DMR 0120967 for making this research possible, as well as the Georgia Institute of Technology. A special thanks to Dr. Joseph Perry, Ariel Marshall, Hyeongeu Kim, and Dr. Wojciech Haske of the Georgia Institute of Technology, also Dominican University and Dr. Robert Faltynek, Dominican University for his support and mentorship.

ASHLEY GANS majors in chemistry at a small private school west of downtown Chicago called Dominican University. The opportunity to work and learn at a research university such as Georgia Tech opened her eyes to the possible education and career options there. She is enthusiastic to continue her education and career, with hopes of obtaining a PhD and working in government or education. The experience she gained at GT with the Perry Group really helped cement her plans for the future.

Enhancement of Plasmon Resonance in Silver Nanostructures Deposited with MEH-PPV Thin Films

KEEGAN M. HANKS, University of Texas at San Antonio
Binh Duong, Jayan Thomas, University of Arizona

Introduction

We report the enhancement of plasmon resonance in a nanostructured silver plasmonic device, coated with a conducting polymer. We have focused on the absorption spectra of the spin coated polymer thin film in this study. Previous studies have shown that film thickness must play a considerable role in the morphology and electro-optic properties of conjugated polymers and polymer based devices.[1] Controlling the film thickness may become a very important aspect in organic polymer based device manufacture and design.

Conjugated polymers such as poly[2-methoxy, 5-(2'-ethylhexyloxy)-1,4-phenylene-vinylene] or MEH-PPV, have attracted a vast interest for their applications in electro-optic materials application and design, including thin film transistors, polymer light emitting diodes, photovoltaic cells and electrochromic devices.[1] Generally, these polymers are spun on in sub micrometer thicknesses for their use in electronics and opto-electronic devices. For applications in light emitting devices and photovoltaic materials, films are usually within the range of 50 to 200nm.[1]

Experimental Methods

Initially, a 0.226 wt% solution of MEH-PPV was prepared by dissolving 0.06 g of MEH-PPV (Sigma Aldrich) in 20 mL of dichloromethane (Sigma Aldrich) using a probe sonicator. Glass substrates were cleaved and cleaned in ethanol and acetone, followed by application of 9 drops of polymer solution from a glass syringe through a 2.2 µm filter to prepare for spin coating. Slides were spun at various rates and UV-Vis absorbance spectra were taken afterwards.

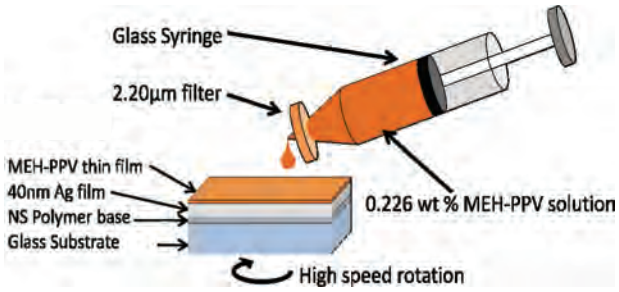

Figure 1. Diagram of experimental procedure showing the use of a glass syringe and 2.2 µm filter. Glass syringe was used to avoid impurities from partially dissolved plastic syringes, and the filter was used to reduce the presence of large chunks of undissolved MEH-PPV.

Soft nanoimprint lithography was performed on a glass substrate coated with a thin polymer film to produce a uniform array of nano-pillars with precise optical properties. This nanoarray was then deposited with a 40 nm thin film of silver. This silver coated nanostructure was then coated with a thin film of MEH-PPV using the technique described in Figure 1. UV-Vis absorbance spectra were taken both before and after the application of MEH-PPV to the silver coated nanopillar array, shown in Figure 2.

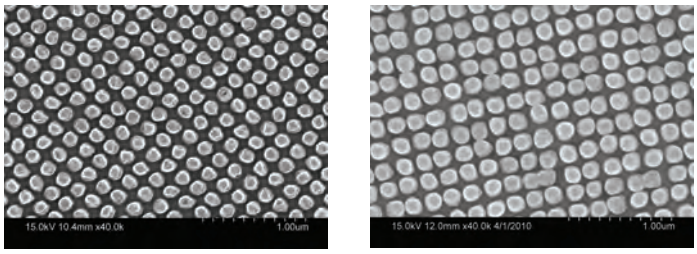

Figure 2a. Scanning electron microscopy images taken of the nanopillar arrays before (left) and after (right) the 40 nm silver film was deposited.

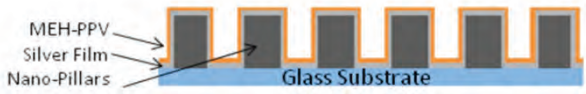

Figure 2b. Diagram of the finished nanostructure/Ag/MEH-PPV device.

Results and Discussion

MEH-PPV is an organic semiconducting electroluminescent polymer with large pendant groups and a highest occupied molecular orbital to lowest unoccupied molecular orbital (HOMO-LUMO) band gap of around 2.5 eV. When combined with a metallic interface, this develops into an intriguing characteristic due to the applicability of this band gap energy in photon harvesting and light emitting devices.

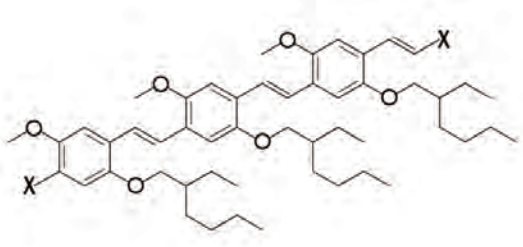

Figure 3. Molecular structure of the conjugated polymer MEH-PPV, showing placement of large pendant groups, double bonds, and oxygen molecules.

The band gap energy is roughly on the order of 500 nm wavelength of light, which is where we expect to see a maximum in the UV-Vis absorption spectrum. Placement of the large pendant groups, double bonds, and oxygen atoms in the polymer matrix give rise to interesting opto-electronic properties, increasing with molecular uniformity and stacking order.

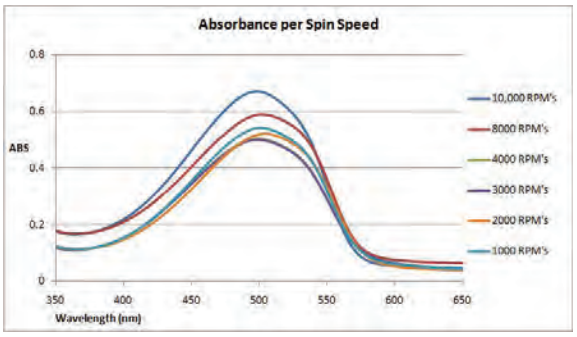

Figure 4. UV-Vis absorption spectra of MEH-PPV films deposited on glass slides at different speeds. This data displays the peaks in the range of expected absorbance maximum for the HOMO-LUMO gap of 2.5 eV.

These results show that the light absorbing character of MEH-PPV is independent of film thickness and spin speed. This suggests that the morphology of the spun on conjugated polymer will remain constant at spin speeds greater than 1000 RPMs. This would lead one to expect a similar absorbance peak when the polymer is spun on to a nanostructured material.

The measured absorbance curves for all three of the nanostructured slides reveals a unique difference in the observed curves, shown in Figure 5. Apparently the early nanostructures were a bit different from the latest structures and this led to the difference in absorption peaks from sample 1 to sample 3. Using sample 2 as our control, we realize that spinning with solvent by itself has no effect on the absorption properties of the silver nanostructures.

Figure 5a represents the early nanostructure design and the absorbance peaks related to the surface characteristics of the nanostructure with and without MEH-PPV. This graph indeed shows an absorbance peak around 500 nm as expected for MEH-PPV. Figure 5b depicts the absorbance of the silver coated nanostructure with and without spinning with dichloromethane (DCM) on the nanostructure. Figure 5c shows the latest nanostructured imprint before and after MEH-PPV spin coating. Both absorbance peaks have been shifted to longer wavelengths suggesting the successful enhancement of surface plasmon polaritons along the interface between the silver film and the MEH-PPV spin coating.

Looking at the peak shifts in the spectrographs, we can see that the evanescent electric field at the interface of the silver film and MEH-PPV film has indeed been enhanced. This enhancement may have increased the sensitivity of the device, possibly even the fluorescence.

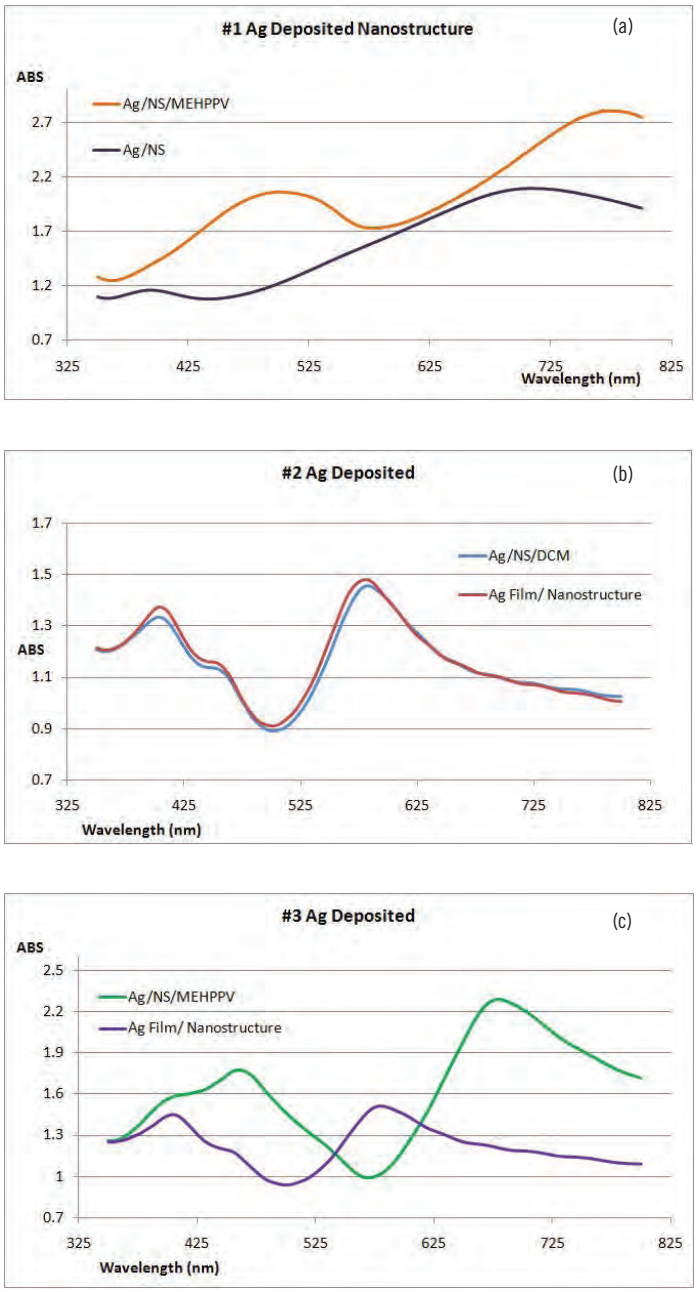

Figure 5. (a), (b), and (c) are absorption spectra of the silver coated nanostructure polymer film on glass before and after spin coating MEH-PPV and DCM.

Conclusions

Spin coating of the conjugated polymer MEH-PPV has been done on a nanoimprinted polymer bed of nanopillars and the enhancement of absorbance peaks were observed. The spun on film thickness appeared to have no effect on the absorbance of the organic polymer film, which stayed close to 500 nm throughout all spin speeds.

Future work with this project may involve investigation of the fluorescence enhancement due to the presence of a thin film of conjugated polymer, MEH-PPV. We could involve a change in the concentration of MEH-PPV spin on solution and consider using other organic conducting polymers.

References

1. C. C. Chang, C. L. Pai, W. C. Chen, S. A. Jenekhe: Thin Solid Films 479 (2005) 254.
2. Schasfoort, R. B. M., Tudos, A. Handbook of Surface Plasmon Resonance. Cambridge: RSC, 2008.
3. D. K. Chambers, S. Karanamy, D. Qi, S. Selmic,Y. B. Losovyj, L. G. Rosa, P. A. Dowben: Appl. Phys. A 80, 483, (2005).
4. V. Kažukauskas: Semicond. Sci. Technol. 19 (2004) 1373.
5. J. Yao, A. P. Le, S. K. Gray, J. S. Moore, J. A. Rogers, R. G. Nuzzo: Adv. Mater. 22 (2010) 1102.

Acknowledgments

Funds for this research were provided by the Center on Materials and Devices for Information Technology Research (CMDITR), an NSF Science and Technology Center No. DMR 0120967.

KEEGAN M. HANKS will graduate from UTSA in spring of 2011 with a bachelor in physics. He will be moving on to graduate school to pursue a PhD specializing in advanced nanomaterials for applications in energy harvesting and storage.

Wetting Properties and Surface Energy

ALEX HARTSELL, Georgia Institute of Technology
Deborah Ortiz, Douglas Chui, Eliza Riedo, Georgia Institute of Technology

Introduction

The phenomenon of wetting is important in a variety of fields due to the wide range of processes it controls, e.g. printing, adhesion, cleaning, and lubrication.[1] The processes governing wetting are not completely understood; however, models for small drops exist which can characterize the wetting properties of a material.

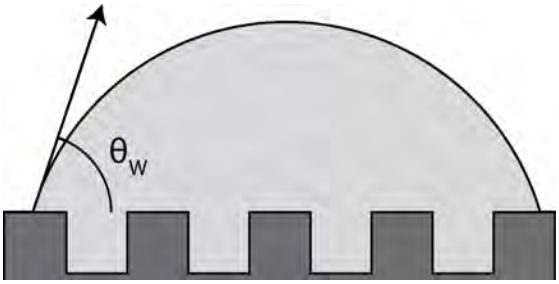

Figure 1. Young's Model.

$$\gamma_{LV}\cos(\theta_E) = \gamma_{SV} - \gamma_{SL}$$

In 1805, Thomas Young derived a formula[2] relating interfacial energies (γ) of the solid, liquid, and vapor phases in equilibrium to the contact angle between the drop and surface (see Figure 1). The interfacial energy measures all interactions between two phases, be they Van Der Waals or capillary adhesion forces, letting the macroscopic contact angle measurement describe interactions between the liquid and solid molecules. The model also allows the comparison of contact angles for two different surfaces with the same γ_{SV} using the modified form: $\gamma_{LV}\Delta\cos(\theta) - \Delta\gamma_{SL}$. Despite its power, the model provides no means to control the contact angle outside of modifying the surface chemistry.

To fill this gap, Wenzel and Cassie extended Young's relation to accommodate patterned surfaces. Wenzel modeled a drop on a rough surface which fills the gaps between the patterns[2] and finds a new contact angle dependent on the "Wenzel roughness factor," a ratio of real surface area to apparent surface area ($r_w = A_{Actual}/A_{Apparent}$, see Figure 2). The Wenzel wetting mode is known as a "sticky" wetting mode,[3] due to it adhering to the substrate better than its counterpart, the Cassie wetting mode. In the Wenzel state, drops use both capillary action in the pattern's grooves and the fact that there are no nucleation sites for dewetting in the pattern to adhere to the surface, often even when inverted.

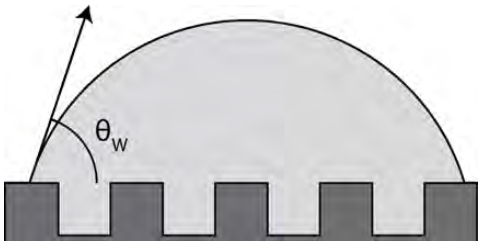

Figure 2. Wenzel's Model.

$$\cos(\theta_W) = r_w\cos(\theta_E)$$

Cassie, on the other hand, developed a relation for when the drop traps vapor in the pattern and rests on a heterogeneous surface of vapor and solid.[2] This model depends solely on the surface area fraction, a ratio of the solid base area to total base ($\theta = A_{Solid} / A_{Total}$, see Figure 3). Because the dewetting process only needs to take place on the surface peaks and vapor is already beneath the drop, drops in the Cassie state roll more freely than Wenzel drops.

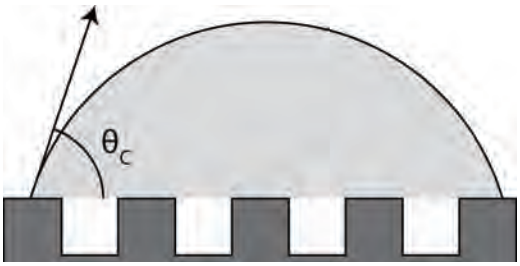

Figure 3. Cassie's Model.

$$\cos(\theta_W) = \theta\,[\cos(\theta_E) + 1] - 1$$

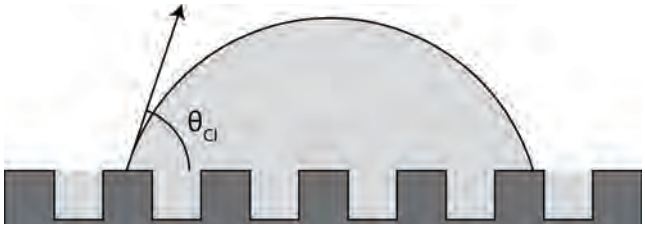

Figure 4. Cassie-Impregnation Model.

$$\cos(\theta_W) = \theta\,[\cos(\theta_E) - 1] + 1$$

For hydrophilic surfaces, there is another model known as the Cassie-Impregnation model. This applies when capillary action draws the liquid through the grooves in the surface (a process known as hemiwicking) and depends on the same θ as the Cassie model. The conditions for this state are strict, with the most lax being $\theta_E < 90^o$ and the most strict being $\cos(\theta_E) > 1 - \theta/rw - \theta$.

Figure 5. Hysteresis measurement.

$$H = \theta_A - \theta_R$$

Even with these models, it is not possible to characterize drop motion on the surface. While the Wenzel model is "sticky" and the Cassie model shows "roll-off" drop behavior, another measurement is needed to quantify these terms. When a surface is tilted, a drop must accumulate energy to overcome a barrier to motion before it can roll freely. The energy accumulated is stored in the drop's shape and characterized by it's deformation. To measure the deformation, and thus the motion barrier, the advancing contact angle (where wetting events occur) and receding contact angle (where dewetting events occur) are recorded. The difference between the two angles, called hysteresis (see Figure 5) completes the models to provide a comprehensive toolset to analyze surface wetting without understanding the complex wetting and dewetting mechanisms. However, the models have been questioned numerous times because of their simplicity and inability to explain certain situations.[4, 5] This research aims to test the validity of the modified Young's relation on patterned surfaces.

$$\text{Wenzel: } \Delta\gamma_{SL} = (r_w - 1)(\gamma_{SL} - \gamma_{SV})$$

$$\text{Cassie: } \Delta\gamma_{SL} = (1 - \emptyset)(\gamma_{SV} - \gamma_{SL} + \gamma_{LV})$$

If a patterned surface is viewed as a smooth surface with a different solid-liquid interfacial energy, then the Wenzel and Cassie models can be rewritten in terms of the change in solid-liquid interfacial energy. Both models show that the change in interfacial energy with respect to the pattern parameter is linear (Note $\Delta_{SL} = \gamma^*_{SL} - \gamma_{SL}$). Therefore, the modified Young's relation should hold for patterned surfaces even though it is derived for smooth surfaces.

Experimental

To analyze advancing and receding contact angles, a stage capable of tilting a sample was assembled for the SEO Phoenix 150 Contact Angle analyzer (see Figure 6) The stage was built using a Hitec servo and Lynxmotion pan-tilt assembly. To control the tilt stage, a Pololu usb servo controller was used. In measuring the advancing and receding contact angles, the patterned area of the samples was not large enough to support hysteresis measurements.

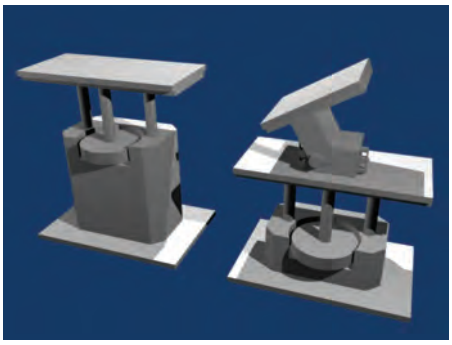

Figure 6. A render of the stage before (left) and after (right) the modifications.

The samples were prepared using Sylgard-184 Polydimethylsiloxane (PDMS), the base was mixed with the crosslinker in a 3:1 ratio and patterned by placing either a Pelco GC150 TEM Grid or 5 µm checker patterned AFM calibration grid in the unset PDMS. After the samples were thermally cured, contact angle measurements (static, advancing, and receding angles) were taken using the previously mentioned contact angle analyzer. The PDMS samples were then silanized using either 3-aminopropyltriethoxysilane aminopropyltriethoxysilane (APTES) or 3-(Trimethoxysilyl) propylmethacrylate (TMSPM). Contact angles were remeasured immediately after silanization. APTES treatment is expected to lower the surface-liquid interfacial energy due to the dipole on the amine group, converesly the TMSPM is expect to raise the interfacial energy to make the surface more hydrophobic.

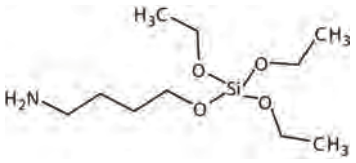

Figure 7. 3-aminopropyltriethoxysilane aminopropyltriethoxysilane (APTES).

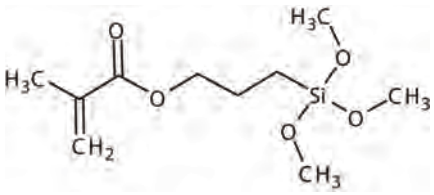

Figure 8. 3-(Trimethoxysilyl)propylmethacrylate (TMSPM).

The silanizations took place in ethanol, which swells PDMS. To ensure the pattern was not damaged after the surface modification, images of the sample were taken to verify the pattern dimensions and geometery. The sample stamped with an AFM calibration grid was imaged with an AFM and the TEM grid stamped sample was imaged with an SEM. The pattern parameters, r_w and θ, were calculated from these images, and were found to agree with the master's specifications.

During the experiment, it was noted that samples made from the TEM Grid would often exhibit unusually low contact angles, sometimes as low as 70°. Further investigation showed that all drops could enter this state through slight perturbation, such as rocking the stage, (amplitude 2°-5°, frequency 2-5 Hz). The drops achieved a stable minimum contact angle. This was then tested on the AFM grid

patterned samples, which also reached a minimum contact angle after slightly more vigorous light rocking.

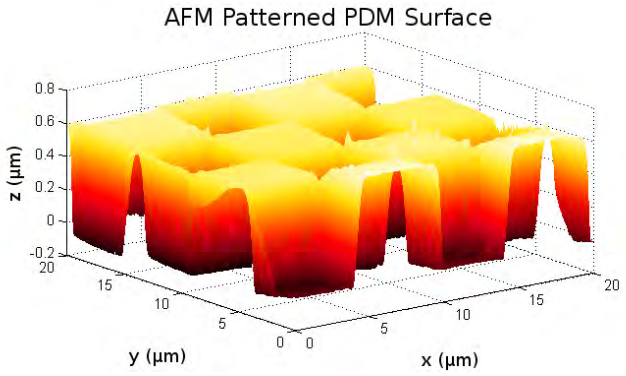

Figure 9. AFM Image of PDMS sample patterned with an AFM Grid.

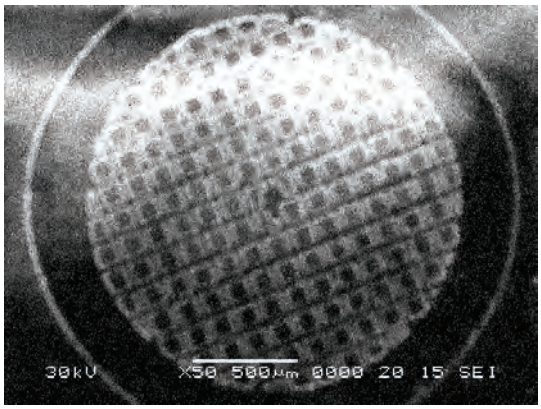

Figure 10. SEM Image of PDMS sample patterned with a TEM Grid.

Pattern	Feature Size	r_W	ϕ
AFM Grid	$\sim 5\mu m$	1.26	0.50
TEM Grid	$\sim 100\mu m$	1.77	0.55

Table 1. Comparison of pattern features.

Results and Discussion

A summary of the contact angles measured are presented in Figure 11 and Table 2. The hysteresis data has been omitted due to the experimental problems encountered. The large difference between the AFM and TEM patterned contact angles points to the Wenzel wetting mode for all samples (the wenzel roughness values are very dissimilar; however, the surface fractions are not). This is supported by the Wenzel model's predicted contact angles, plotted alongside the contact angles.

Using Young's relation ($-\gamma_{LV}\Delta\cos(\theta) = \Delta\gamma_{SL}$), the change in solid-liquid interfacial energy caused by the surfactant was determined. Only the smooth contact angles are used to calculate this value, as Young's relation is only accepted for smooth surfaces. Note that this relation does not depend on SV under the assumption that silanizing and patterning affect only γ_{SL}.

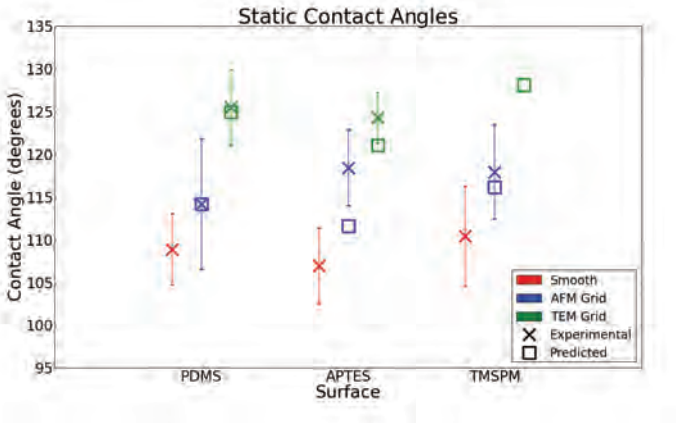

Figure 11. Graph of Static Contact Angles and Wenzel Predictions.

Sample	Smooth	AFM Grid	TEM Grid
PDMS	108.9	114.2	125.5
Predicted		114.2	125.0
APTES	106.9	118.5	124.3
Predicted		111.6	121.0
TMSPM	110.4	117.9	N/A
Predicted		116.2	128.2

Table 2. Sample Contact angles and Wenzel mode Predictions for each pattern.

Surface A	Surface B	$\gamma_{SL,B} - \gamma_{SL,A}\ (N/m)$
PDMS	APTES	-2.3×10^{-3}
PDMS	TMSPM	1.8×10^{-3}
APTES	TMSPM	4.1×10^{-3}

Table 3. Calculated change in surface energy with respect to surface treatment.

It was found it that APTES has a lower surface energy than PDMS, and TMSPM higher than PDMS, as expected. Using these values and the same equation for each sample, the patterned and smooth contact angles for TMSPM or APTES can be found from the corrosponding PDMS values. A plot of these values compared to the prediction given by Young's Relation is given Figure 12.

The graphs show that Young's relation holds, as all the relation is within the standard deviation of all points. However, the TMSPM seems shifted from the prediction. The TMSPM samples had the fewest data points and largest standard deviation in contact angles (due to having less TMSPM samples), possibly leading to error in the interfacial energy calculation and the shift in the graph.

It was mentioned in the experimental section that unusually low contact angles could be found for all rough surfaces. The contact

angles could be modeled by a less common model -the Cassie-Impregnation model[6]: $\cos(\theta_{CI}) = \emptyset[\cos(\theta_E) - 1] + 1$. The strict conditions for this state were not met; however, the surfaces still appear to exhibit this wetting mode (albeit not spontaneously).

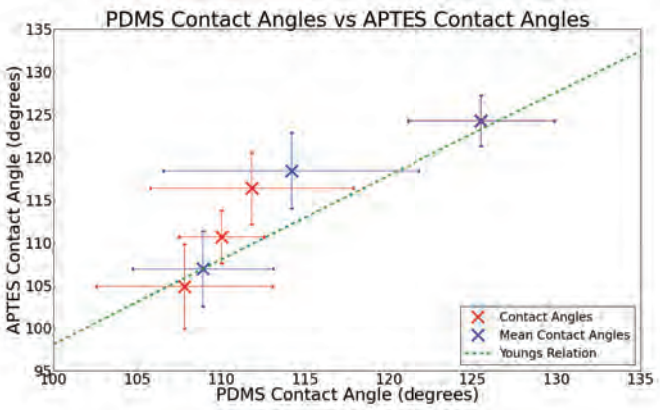

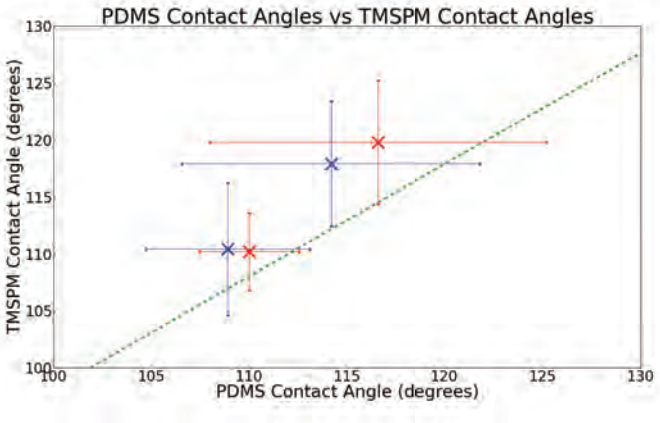

Figure 12. Comparison of contact angles before and after silanization.

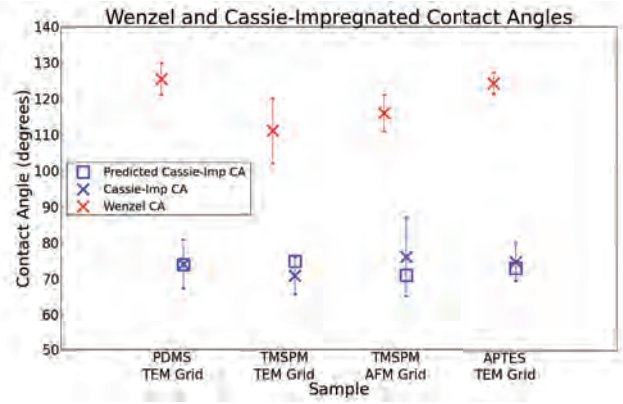

Figure 13. Predicted and measured Cassie-Impregnated contact angles.

Conclusions

The contact angles measured reasonably matched the Wenzel predictions, indicating a Wenzel wetting state. An uneven or incomplete silanization treatment may be the cause of larger deviations in the silanized samples. Young's Relation accurately predicted contact angles for rough silanized surfaces from a rough unsilanized surface, indicating that patterning can be viewed as raising the solid-liquid interfacial energy. Initial experiments show that the Cassie-Impregnation wettingmode was achieved on hydrophobic surfaces despite the hydrophilic restriction.

Future work includes acquiring larger patterns to measure the hysteresis and creating patterns with roughness parameters besides those presented. If the hysteresis changes with surface treatment, then Fermidge's equation states that γ_{SV} also changes,[3] invalidating an assumption made by the modified Young's relation. Fine control over roughness parameters would allow for this experiment to be repeated with drops in the Cassie state as well as the Wenzel state.

References

1. Marmur, A. Annual Review of Materials Science 2009, 39, 473–489.
2. de Gennes, P.-G.; Brochard-Wyart, F.; Quere, D. Capillarity and Wetting Phenomena: Drops, Bubbles, Pearls, Waves; Springer, 2003.
3. Balu, B.; Breedveld, V.; Hess, D. W. Langmuir 2008, 24, 4785–4790.
4. McHale, G. Langmuir 2007, 23, 8200–8205.
5. Gao, L.; McCarthy, T. J. Langmuir 2007, 23, 3762–3765.
6. Bormashenko, E.; Pogreb, R.; Stein, T.; Whyman, G.; Erlich, M.; Musin, A.; Machavariani, V.; Aurbach, D. Physical Chemistry Chemical Physics (Incorporating Faraday Transactions) 2008, 10, 4056.

Acknowledgments

I would like to thank Deborah Ortiz, Douglas Chiu, Debin Wang, and Elisa Riedo of the Riedo Lab for their guidance and support. I would also like to thank Keith Carroll and the Curtis Lab for supplying the materials to make the patterned samples. I would finally like to acknowledge the Center on Materials and Devices for Information Technology Research (CMDITR), the NSF Science and Technology Center No. DMR 0120967.

ALEX HARTSELL is a Materials Science and Engineering major at Georgia Institute of Technology. As a rising sophomore, he is expected to graduate in 2013.

Synthesis and Characterization of Anisotropic Silver Nanostructures

BRANDON LEE HENRY, South Seattle Community College
Nathan B. Sylvain, Larry R. Dalton, University of Washington

Introduction

Metallic nanoparticles (MNP) have many interesting properties that are of interest to a variety of fields such as glass, chemical sensing/detectors, catalysis and the bio industry.[1, 2, 3, 4, 5, 6] While research on much of the physics behind the properties making MNP such a desirable and able platform for this myriad of industries is still ongoing, the photophysics behind the bright coloration often observed with noble metal nanoparticle colloidal solutions can be understand using the Drude model for free electrons.[5, 6]

Using the Drude model, we can view the conduction electrons as a gas of electrons whose density is given as

$$n= (\mathbf{N_A}\, Z_c\, \rho_m)/A \quad (1)$$

where N_A is Avogadro's number, Z_c is the number of conduction (valence) electron, ρ_m is the density of the metal and A is the atomic number. Using Ohm's Law

$$\mathbf{j}=\sigma\mathbf{E} \quad (2)$$

with $\mathbf{j}$ being the current density and σ the conductivity of the metal, we can derive the dispersion relationship, or the frequency-dependent response, of the free electron gas. Applying Maxwell's equations and frequency dependent form of eq. 2, we find the following dispersion relationship

$$k^2c^2=(\omega^2-\omega_p^2) \quad (3)$$

and the plasma frequency is given as

$$\omega_p=(ne^2)/(m\epsilon_0)$$

For any frequency of light above this, the material becomes transparent – k is real corresponding to a travelling wave – and the material reflects frequencies that are less than the plasma frequency.

In the presence of an electromagnetic field (such as light), the surface conduction electrons can be excited and we refer to these coherent oscillations as surface plasmon resonance (SPR) for a planar surface and localized surface plasmon resonance (LSPR) for nanoscale objects.[6] The difference between the two is illustrated schematically in Figure 1.

For spherical and eliptical MNPs, Mie's solutions to the Maxwell-Garnett equations and Gan's extensions work well for predicting their optical properties.[2, 5] These particles, however, are of less interest in that they show limited tunabilty of their surface plasmon response in the visible region of the EM spectrum.[3, 5] Anisotropic

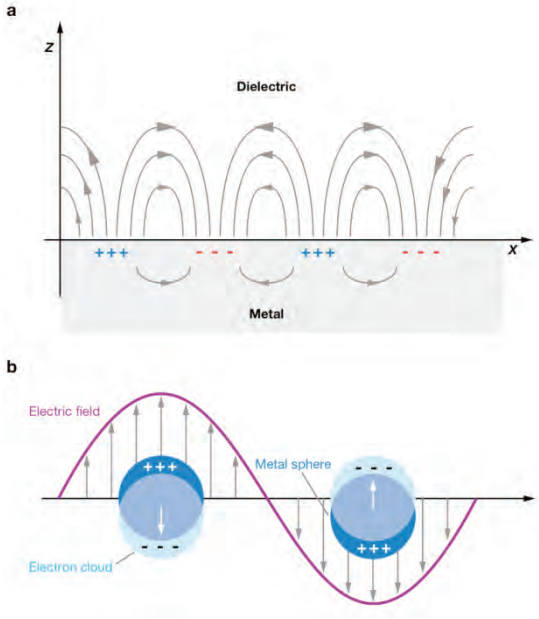

Figure 1. Schematic diagram illustrating (a) a surface plasmon polariton (or propagating plasmon) and (b) a localized surface plasmon.[6]

MNPs, however, have been shown to be highly tunable with silver MNPs showing exceptional tunability from about 400nm to the near IR.[1, 3, 4, 5] This has largely been attributed to their size, shape or local environment.[1, 3, 4]

The ability to tune the resonance of these particles is of great interest in the optical field because of the way these particles concentrate light around them. The sensitivity of the LSPR to changes on the MNP surface is already being exploited in sensing where is it known to enhance the linear response of molecules near the MNP.[2, 3, 5, 6, 7] Devices, such as the one shown in Figure 2, are showing promise in enhancing the optical sensing capability of optical fibers but these devices still rely on spherical particles and linear enhancement.[7] Given the wealth of research performed on the linear enhancement offered by these systems, few have explored the non-linear enhancement of molecules in close proximity to MNPs.

We propose to aid in filling in this gap by studying several rapid thermal synthesis methods for forming anisotropic nanoparticles. A successful method must be i) repeatable, ii) predictable, iii) provide a monodisperse distribution of particles that have roughly the same size, shape and thickness and iv) be easily tunable throughout the 500 nm to 900 nm range. Ideally, the solutions will remain stable in solution, given reasonable storage concerns. Optical properties will be characterized primarily through the use of UV-Vis spectroscopy.

To ensure that the particles exhibit the desired triangular prismatic shape, they will be imaged through scanning electron microscopy (SEM).

It is known that these particles are susceptible to etching, or the truncation of the apexes leading to hexagonal prisms. Several capping ligands, washing procedures and storage solutions will also be investigated to examine their effects on stabilizing the AgNPrs in the desired configuration. Finally, routes for forming self-assembled films will be examined and the optical properties of the films compared to the original solutions.

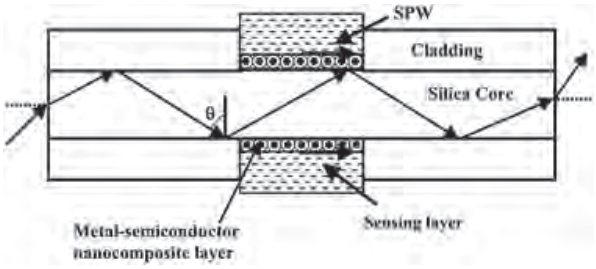

Figure 2. A fibre-optic sensor with core-shell metal-semiconductor nanocomposite layer; a surface plasmon wave (SPW) exists at the interface of the metal-semiconductor nanocomposite layer and the adjacent sensing layer. [7]

Results and Discussion

Anisotropic nanostructures (NPrs) were synthesized using a seed mediated growth procedure[4] and a single pot rapid reduction procedure[7] with either poly(4-vinylpyrrolidone) (PVP) or sodium polystyrene sulfonate (PSS) as growth directing agents.

A photostability test was performed using NPrs made with PVP and with PSS. PVP produced unpredictable colors, but appeared to hold up better than PSS when left out in ambient lighting conditions. The PSS produced more reproducible results and when stored out of ambient light conditions maintained their color. Utilizing PSS was found to be a method that met with requirements i and ii as listed above.

It was observed using the PSS method that as the concentration of seed particles is reduced, the in-plane surface plasmon resonance response is red-shifted as the resulting anisotropic structures become larger. This is observed visibly by a shift from the pale yellow of the isotropic seed solution to a pale blue as shown in Figure 3.

As the particle size increases, the in-plane dipole SPR is shifted across the visible spectrum from ~400 nm – for the seed particles – to longer wavelengths with the largest particles showing a shoulder near ~465 nm which is believed to be caused by the in-plane quadrapole resonance (see Figure 3).[7]

The films were created using self-assembly or drop-casting on ITO slides covered by a layer of 5% w/w poly(4-vinylpyridine)(P4VP). The in-plane dipole SPR peak was near ~586 nm. In the solid state, the SPR response shifted for both the drop-cast and self-assembled films.

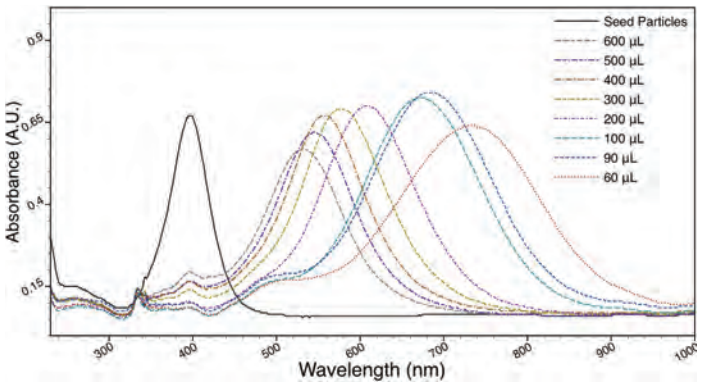

Figure 3. Absorption spectra of colloidal anisotropic silver nanoparticles synthesized using a seed mediated, rapid thermal synthesis carried out at room temperatures. The inset shows the color range as the particles become increasing larger in size.

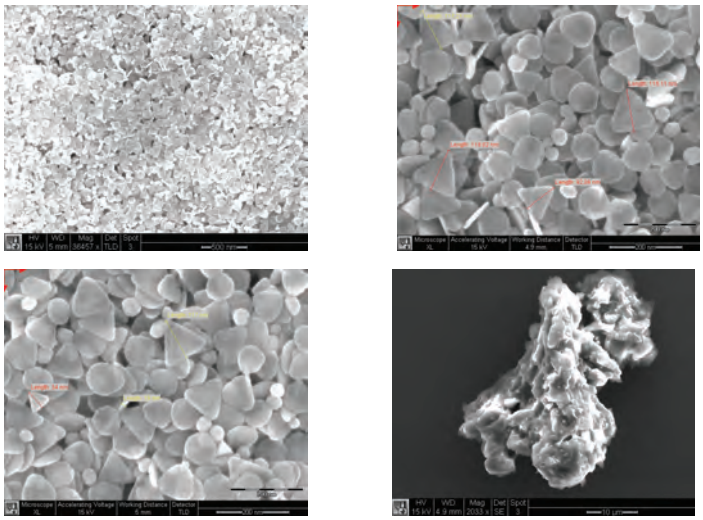

Figure 4. Typical SEM images of silver nanoprisms from a dropcast film.

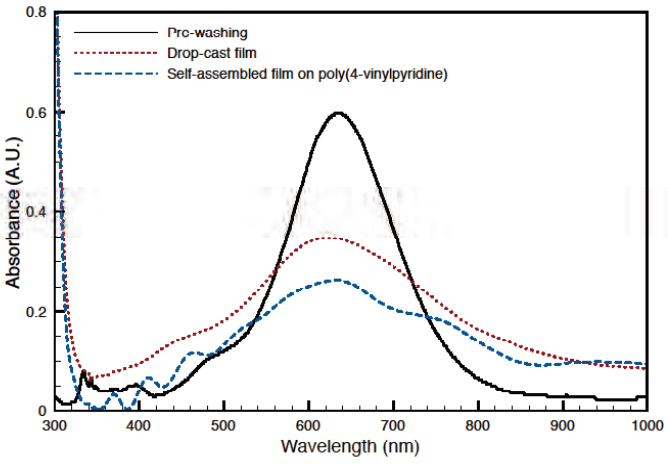

Figure 5. Absorbance spectra of silver MNPs in solution (black), a drop-cast film (red) and a self-assembled film on poly(4-vinylprytidine).

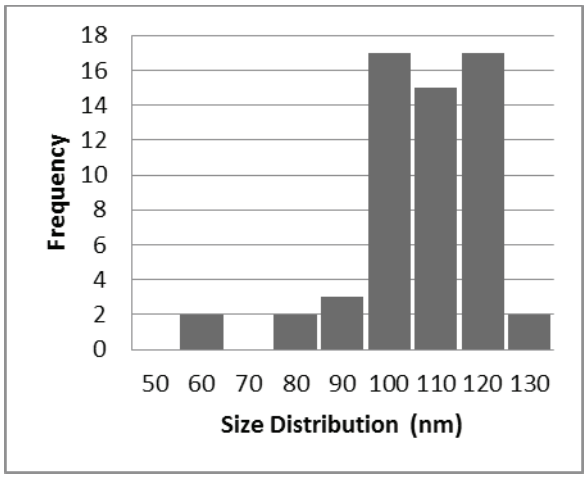

Table 1. Size distribution of MNPS from a drop cast film.

Conclusions

The PSS method provided more reproducible and stable results for particles stored in the dark. The PVP method provided better photostability, but showed greater etching of particles left in solution. The silver nanoparticles were shown to self-assemble into a film on a substrate coated with P4VP in a manner that is visually distinctive from those formed from drop casting or spin casting.

Future work will include testing the ability of modified chromophores to self-assemble on the surface of immobilized silver nanostructures. Also, testing the bare silver nanostructures for second harmonic generation to obtain a baseline for future measurements is something that can be explored.

References

1. Metal-semiconductor Nanocomposite Layer Based Optical Fibre Surface Plasmon Resonance Sensor. Sharma, A. K. and Gupta, B. D. 2, 2007, Journal of Optics A: Pure and Applied Optics, 9, 180-185.

2. Localized Surface Plasmon Spectroscopy and Sensing. Willets, Katherine A. and Van Duyne, Richard P. 1, 2006, Annual Review of Physical Chemistry, 58, 267-297.

3. The Incorporation of Noble Metal Nanoparticles into Host Matrix Thin-films: Synthesis, Characterisation and Applications. Walters, Gillian and Parkin, Ivan P. 5, 2009, Journal of Materials Chemistry, 19, 574-590.

4. Optical Properties and Growth Aspects of Silver Nanoprisms Produced by a Highly Reproducible and Rapid Synthesis at Room Temperatures. Aherne, Damian, et al. 14, 2008, Advanced Functional Materials, 18, 2005-2016.

5. On the Linear Response and Scattering of an Interacting Molecule-Metal System. Masiello, David J. and Schatz, George C. 6, 2010, The Journal of Chemical Physics, 132, 064102.

6. Rapid Thermal Synthesis of Silver Nanoprisms with Chemically Tailorable Thickness. Mirkin, Chad A. and Mètraux, Gabriella S. 4, Advanced Materials, Vol. 17, pp. 412-415.

7. Colloidal Gold and Silver Triangular Nanoprisms. Millstone, Jill E., et al. 6, 2009, Vol. 5, pp. 646-664.

Acknowledgments

The Center for Materials and Devices for Information Technology Research, National Science Foundation (DMR 0120967) and the Air Force Office of Scientific Research (FA9550-09-1-0589 MOD) is gratefully acknowledged for funding.

BRANDON LEE HENRY is currently pursuing his BS in Chemistry. He plans on obtaining his Ph.D. and working in the field of Nanotechnology.

Effect of the Molecular Weight and Tacticity of Polymer Matrix on Soluble Acene-Polymer Blend Organic Field Effect Transistors

KATHERINE HENRY, North Carolina State University
Do Kyung Hwang, Jungbae Kim, Bernard Kippelen, Georgia Institute of Technology

Introduction

The ultimate goal of organic field effect transistors (OFETs) is to replace hydrogenated amorphous Si (a-Si:H) based FETs. Vacuum-sublimed as well as solution-processed organic semiconductors show comparable hole and electron field-effect mobility values to inorganic devices. Solution-processed materials are particularly attractive for the realization of large area and low-cost electronics. TIPS-Pentacene (see Figure 1), a small molecule soluble acene is a promising candidate, which has been observed to have a comparable hole mobility of 1 cm^2/Vs.[1] However, the drawback of using pure TIPS-Pentacene is its non-uniformity,[2] which can lead to problems for large area device applications by printing or solution processing methods. Polymers offer enhanced uniformity across a substrate, and therefore are advantageous in semiconductor blends. The blends of TIPS-Pentacene and polymer matrix such as polystyrene (see Figure 2) offer high electrical mobility as well as enhanced film uniformity.

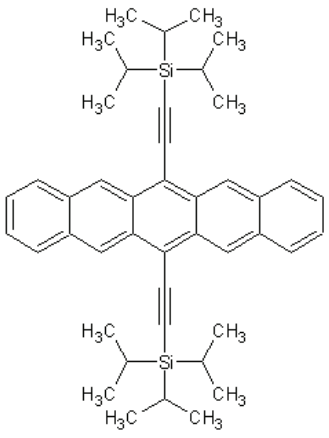

Figure 1. TIPS-Pentacene small molecule.

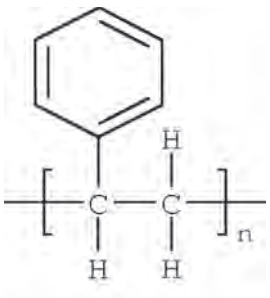

Figure 2. Polystyrene monomer.

Tacticity and molecular weight affect the characteristics of polymers. Tacticity is the orientation of side groups on the hydrocarbon backbone, as shown in Figure 3. Atactic polymers, molecules with random variation of side groups, are typically amorphous. Isotactic polymers have all side groups along one axis and are semi-crystalline. Syndiotactic is crystalline with a regular orientation. Crystallinity and molecular weight (MW) of polymer matrix directly affect the phase separation and morphology of TIPS-pentacene and polymer blend films, which result in differences in device performance.[3-5]

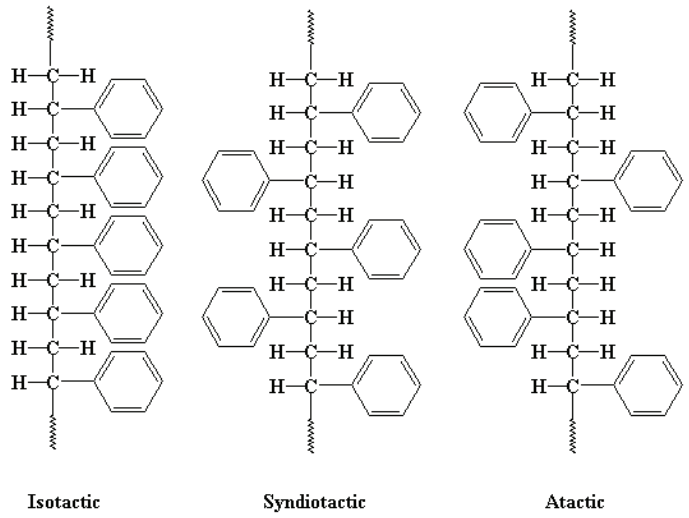

Figure 3. Polystyrene tacticity.

In this work, we investigate the effects of both 400,000 MW atactic polystyrene and 2,500 MW atactic polystyrene. The effects of crystallinity are also examined by comparing 400,000 MW atactic polystyrene with 400,000 MW isotactic polystyrene.

Research Methods

OFETs were fabricated on heavily n-doped silicon substrates (n^+-Si, as the gate electrode) with 200 nm-thick thermally grown SiO_2 as the gate dielectric. Ti/Au (10 nm/100 nm) was deposited by electron beam (e-beam) evaporation to enhance the gate electrical contact on the backside of the substrate. The n-doped silicon substrates were cleaned with acetone, isopropyl alcohol, and de-ionized water. A top contact geometry (BG-TC) and a bottom contact geometry (BG-BC) were used for the fabrication of OFETs. Three solutions were spin-coated onto both top and bottom contact devices. Sample

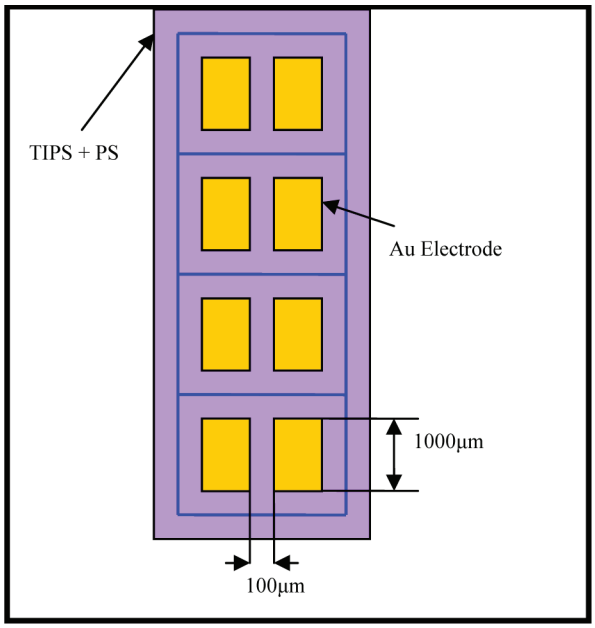

Figure 4. Patterning design and details.

PS1 was 15 mg atactic polystyrene with a molecular weight (MW) of 400,000. Sample PS2 was 15 mg atactic polystyrene with a MW of 2,500. Sample PS3 was 15 mg isotactic polystyrene with an MW of 400,000. Each sample was dissolved in 0.5 mL of tetralin (tetrahydronapthalene) solvent. Finally, 60 mg of TIPS-Pentacene was dissolved separately into 2 mL of tetralin. The individual PS and TIPS-pentacene solutions were mixed to yield a weight ratio of 1:1.

For the top contact geometry, TIPS-pentacene and PS blend films were spin-coated at 500 rpm for 10 s and 2000 rpm for 20 s. The films were dried at room temperature for about 5 min and annealed at 100 °C for 15 min. Gold (Au) was then deposited by thermal evaporation through a shadow mask.

For the bottom contact geometry, after Au deposition, to improve contact at the metal and organic semiconductor interface, a self-assembled monolayer of pentafluorobenzenethiol (PFBT) was formed on the Au electrodes by immersion in a 10 mM PFBT solution in ethanol for 15 min in an N_2-filled dry box, rinsing with pure ethanol, and drying. TIPS-pentacene and PS blend films were then spin-

Geometry	Polymer	*W/L*	μ (cm^2/Vs)	V_{Th} (V)	I_{on}/I_{off}	*SS* (V/decade)
BG-TC	PS1	1000 µm/100 µm (best dev.)	.201	-6.54	10^4	0.71
		1000 µm/100 µm (average 4 devices)	.188 ±.009	-5.76 ±0.75	8×10^3	0.77 ±0.48
BG-TC	PS2	1000 µm/100 µm (best dev.)	.077	-1.27	10^4	0.55
		1000 µm/100 µm (ave. 4 dev.)	.049 ±.019	1.09 ±1.68	8×10^3	0.66 ±0.25
BG-TC	PS3	1000 µm/100 µm (best dev.)	.320	-6.91	10^4	0.40
		1000 µm/100 µm (ave. 4 dev.)	.199 ±.091	-5.16 ±1.70	10^4	0.39 ±0.15
BG-BC	PS1	1000 µm/100 µm (best dev.)	.007	3.72	10^3	0.88
		1000 µm/100 µm (ave. 4 dev.)	.004 ±.0003	3.97 ±2.45	5×10^3	0.60 ±0.22
BG-BC	PS2	1000 µm/100 µm (best dev.)	.001	9.98	10^4	0.45
		1000 µm/100 µm (ave. 4 dev.)	.001 ±.0002	9.66 ±3.29	5×10^3	0.68 ±0.50
BG-BC	PS3	1000 µm/100 µm (best dev.)	.233	1.96	10^5	0.36
		1000 µm/100 µm (ave. 4 dev.)	.129 ±.072	2.51 ± 0.38	10^5	0.59 ±0.16

Table 1. Summary of electrical parameters for TIPS-Pentacene and PS blend OFETs.

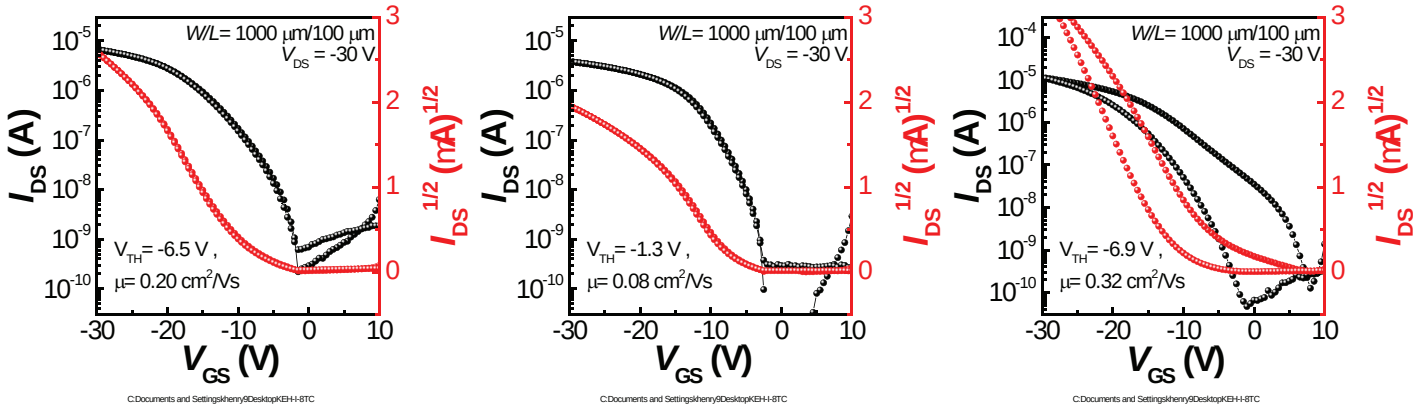

Figure 5. Transfer characteristics of OFETs with BG-TC. From left to right: PS1, PS2, PS3.

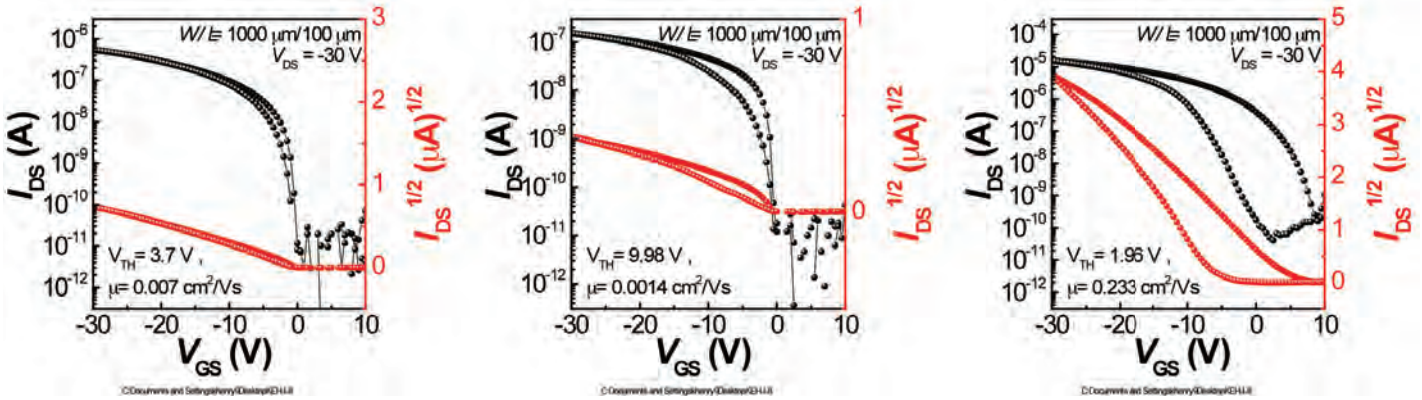

Figure 6. Transfer characteristics of OFETs with BG-BC. From left to right: PS1, PS2, PS3.

coated using the same condition for the top contact geometry. All spin coating and annealing processes were carried out in an N_2-filled dry box.

All current-voltage (I–V) characteristics were measured in an N_2-filled glove box (O_2, H_2O < 0.1 ppm) with an Agilent E5272A source/monitor unit. Before measurement, the sample was patterned to reduce leakage current. A probe needle was used to pattern the active area of transistors (see Figure 4). After the devices were patterned, they were then used to measure transfer and output characteristics.

The following settings were used for Transfer Hysteresis measurement:

V_{ds} = -30 V
$V_{gate,start}$ = 10 V
$V_{gate,end}$ = -30 V
$V_{gate,step}$ = 0.5
Dwell Time = 50 ms

The following settings were used for Output Characteristics measurement:

$V_{gate'start}$ = 0 V
$V_{gate'end}$ = -30 V
$V_{gate'step}$ = 5 V
$V_{ds'i}$ = 0 V
$V_{ds'f}$ = -30 V
$V_{ds'step}$ = 0.5
Dwell Time = 20 m

Results and Data

PS1: Atactic polystyrene with MW of 400,000

PS2: Atactic polystyrene with MW of 2,500

PS3: Isotactic polystyrene with MW of 400,000

BG-TC: Bottom Gate – Top Contact

BG-BC: Bottom Gate – Bottom Contact

Discussion

Figures 5 and 6 show transfer characteristics of TIPS-pentacene and PS blend OFETs with BG-TC and BG-BC (best devices). The trend in mobility indicates that high MW samples (PS1 and PS3) offer better charge carrier mobility. This is true in both top and bottom contact devices, as in shown Table 1, and is most likely due to the difference in phase separation. Phase separation occurs within polymer-polymer blends and is driven by mixing entropy as well as interactions between polymer chains.[2] A higher concentration of TIPS-pentacene film at the conducting interface allows for increased charge transfer. Based on the previous report, low molecular weight polymers are more difficult to separate the phase, and therefore tend to offer lower mobility.[4,5] Hence, the mobility values from OFETs with PS1 and PS3 matrix had significantly higher mobilities (>0.2 cm^2/Vs) than those from OFETs with PS2. Besides Mw, Tacticity also influences the mobility. OFETs with PS3 matrix show higher mobility values than those with PS1 matrix. This is because semi-crystalline polymers, such as isotactic polystyrene, used in conjunction with a variant of TIPS-pentacene concentrations yielded the necessary phase separation.[2]

OFETs with PS1 matrix and PS2 matrix showed significantly lower mobility by a factor of 100 and 10, respectively, than OFETs with PS3 matrix in the bottom contact geometry. Furthermore, OFETs with PS3 matrix in the bottom contact geometry maintained mobility comparable to the top contact geometry, which suggests that the mobility of OFETs with PS3 matrix is fairly independent of the geometry of OFETs. Although not significant, OFETs with PS3 matrix also showed lower mobility in the bottom contact geometry. This indicates that the charge carrier mobility in the bottom contact geometry is, in general, lower than that in the top contact geometry.

Tacticity effect is more significant for the bottom contact devices. Comparing the same molecular weight, the mobility of PS1 matrix was a factor of 100 lower than that of PS3 matrix. However, with the same geometry, samples from PS1 and PS2 achieved comparable mobility values. This indicates that tacticity has a greater effect on mobility than molecular weight in bottom gate – bottom contact devices.

In Figure 5 and Figure 6, we observed hysteresis behavior from OFETs with PS3 matrix. This is partly due to the concentration of TIPS-pentacene to polystyrene. As the weight fraction of TIPS-pentacene decreases, hysteresis decreases.[3]

Conclusion

Tacticity, molecular weight and device geometry were all examined as variables affecting mobility and device performance. Mobility was found to be higher in isotactic and high molecular weight structures. This is largely due to the phase separation necessary for superior charge mobility. Tacticity seemed to have a greater effect to the mobility than molecular weight, as shown in isotactic polystyrene OFETs with both bottom and top contact geometries.

Works Referenced

1. Park, S. K.; Jackson, T. N.; Anthony, J. E.; Mourey, D. A. Applied Physics Letters, 2007, 91, 063514.

2. Hamilton, Richard; Smith, Jeremy; Ogier, Simon; Heeney, Martin; Anthony, John E. Advanced Materials, 2009, 29, 1166-1171.

3. Madec, M.-B.; Crouch, D.; Llorente, Gonzalo R.; Whittle, T. J.; Geoghegan, M.; Yeates, S. G. Journal of Materials Chemistry 2008, 18, 3230-3236.

4. Kang, J.; Shin, N.; Jang, D. Y.; Prabhu, V. M.; Yoon, D. Y. Journal of the American Chemical Society 2008, 130, 12273-12275 .

5. Ohe, T.; Kuribayashi, M.; Tsuboi, A.; Satori, K.; Itabashi, M.; Nomoto, K. Applied Physics Express, 2009, 2, 121502.

Acknowledgements

Thanks to Do Kyung Hwang for mentoring me throughout this project. This research was made possible by the help and guidance of William Potscavage as well as Bernard Kippelen and the Kippelen Research Group. Funds for this research were provided by the Center on Materials and Devices for Information Technology Research (CMDITR), the NSF Science and Technology Center No. DMR 0120967.

KATHERINE HENRY

Non-aqueous Thermogalvanic Cells using Lithium Intercalated Nanostructure Electrodes

THEO HICKS, Morehouse College
Virendra Singh, Sameer Rao, Baratunde Cola, Georgia Institute of Technology

Background

Thermogalvanic cells consist of two similar electrodes at different temperatures, placed in a common solution to generate electricity. Solutions are aqueous or non-aqueous solvents with the redox pair $[Fe(CN)_6]^{3-/4-}$ as the solute. The temperature gradient of the system leads to a concentration gradient, which accelerates the redox reaction known as the Seebeck effect. The constant electron exchange between the redox pair and electrode is exploited to create electrical energy.

Studies on thermogalvanic cells in the past have used platinum electrodes[1]. Platinum is not a practical electrode material for use on a large scale due to its low abundance and high cost. Carbon nanotubes (CNTs) have been of considerable interest for electrochemical applications, due to their exceptional electronic, mechanical, and electrochemical properties. Recently, Multi-Walled CNT-based thermocells were reported with scalable performance.[2] The structure of carbon nanotubes provides a large surface area for the redox reaction. Concurrently, CNTs allow for lithium intercalation, providing a possibly higher voltage in the system.

$$S = \frac{\partial V}{\partial T} = \frac{\Delta S_{B,A}}{nF}$$

Eq. 1. Seebeck coefficient.

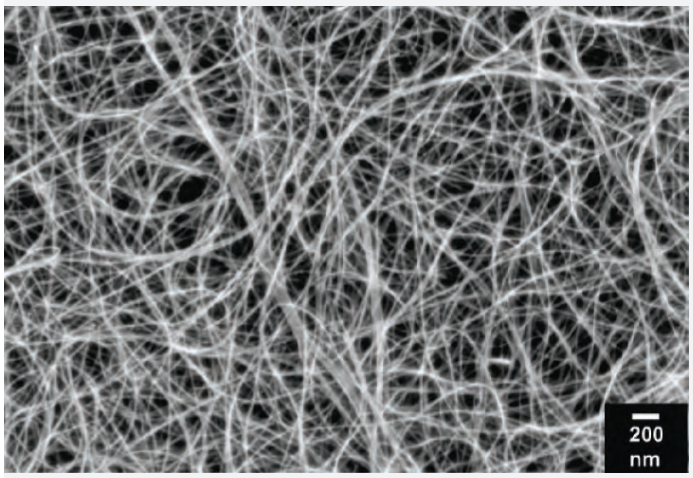

Figure 1. Multi Wall Carbon Nanotube under electron microscope.[2]

Silicon nanowire structures deposited on a metallic substrate have demonstrated lithium intercalation ability. Graphite sheets also have a nanostructure that promotes lithium intercalation and surface area for redox reaction.

Non-aqueous solvents allow for a larger operating temperature range than aqueous solutions and higher possibility for lithium intercalation. Higher operating temperatures allow for thermocell use in more waste heat situations.

Objective/Hypothesis

The purpose of this research is to find a combination of non-aqueous solvent and electrode that provides the highest voltage and current at a higher temperature range than aqueous solutions (above 100 °C). Lithium intercalation of nanostructure electrodes will allow the thermogalvanic cell to operate at a higher starting voltage and demonstrate a capacitive effect.

Research Methods

Lithium Perchlorate and the Potassium Ferrocyanide redox couple were dissolved in non-aqueous solvents like Propylene Carbonate (PC) or Dimethyl Sulfoxide (DMSO). The redox behavior of the various solutions is tested at different electrodes with Cyclic Voltammetry (CV) using a Basi Epsilon Potentiostat. The Potentiostat is also used to intercalate the electrodes in the thermocell described in Figure 1. Intercalation is performed using Chronopotentiometry at 20 mA for different time intervals. The voltage of the cell is measured throughout this procedure. The electrodes are left in the solution after intercalation and before the thermocell test.

The thermocell test reveals the effect of temperature on voltage throughout the system (Seebeck effect). A chiller is used to maintain a constant cold temperature and a rope heater is used for the hot side. An additional electrode is placed in the middle as a reference. The reference is used to find the voltage of hot and cold electrodes at different temperatures. The hot side of the thermocell is set to a higher temperature than the cold water jacket. The thermocell is run below the boiling point of the solvent. Open circuit voltage (V_{oc}), current (I_{sc}) and electrode voltage data is recorded at various temperature differences (ΔT). The data collected from the thermocell test is compared to a similar setup using conventional electrode materials and/or aqueous solution.

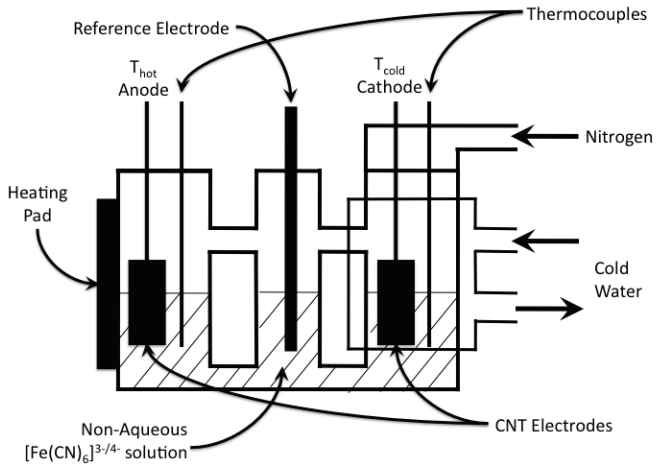

Figure 2. Glass U-Cell used in intercalation and thermocell experiments.

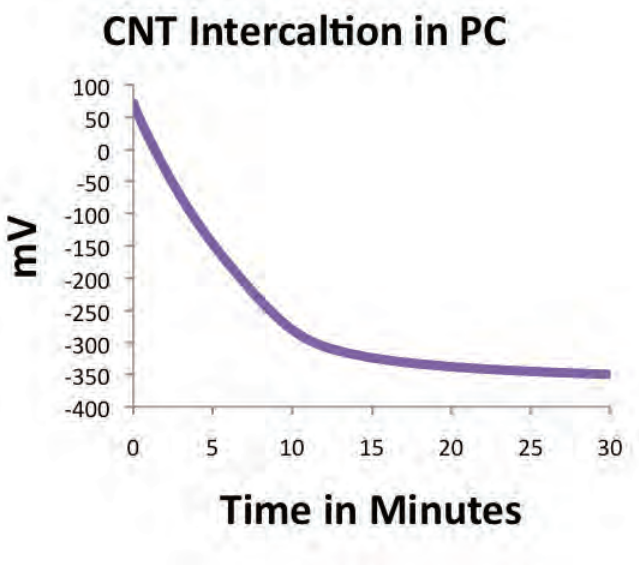

Figure 3. 30 Minute Lithium Intercalation of CNT Electrode in PC.

Results

CNT electrodes were intercalated to maximum capacity of lithium within 30 minutes in PC. The open circuit voltage before intercalation was 120 mV. The open circuit voltage after intercalation was -250 mV. When left in solution, the voltage of the cell moved back into the positive range.

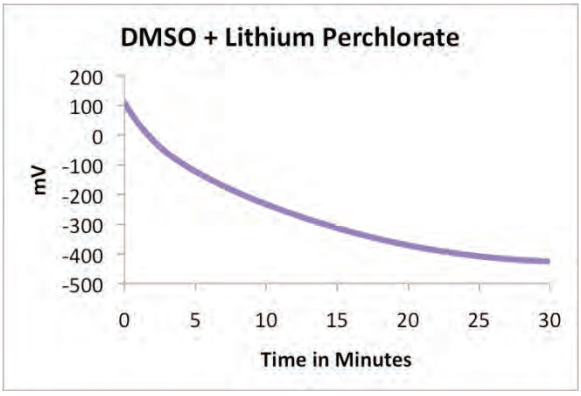

Figure 4. Lithium Intercalation of CNT Electrode in PC.

The open circuit voltage of the system was 145 mV before intercalation and -58 mV after. This voltage deteriorated over time.

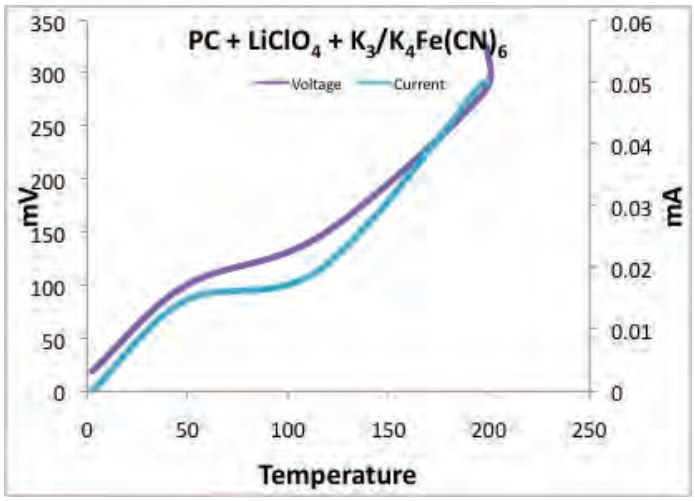

Figure 5. Thermocell test. Li intercalated CNT electrodes in PC.

Open circuit potential for the cell is described in Figure 5: 130 mV at start, -120 mV after intercalation. The voltage was 90 mV after 24 h. The voltage stopped at -250 when reintercalated for 20 min.

Maximum intercalation occurred in a shorter time in PC solutions. Intercalating electrodes with a solution sans redox couples also resulted in higher stored lithium content. Imposing defects in the CNT sheets using ozone may provide even higher intercalation values. Re-intercalation resulted in higher voltages.

Conclusions

Intercalation of carbon nanotubes is possible but is not sustainable. Lithium ions are deposited on the surface of the CNTs. Surface intercalation is easily reversible. Other nanomaterials such as silicon nanowire and graphite may allow below surface intercalation and long term sustainability.

Non-aqueous solutions were successful in operating thermogalvanic cells at higher thermal ranges than water based systems. Long term stability of non-aqueous systems will be tested for practical use. DMSO may have unpredictable results over long time periods.

References

1. T. Quickenden and C. F. Vernon. Thermogalvanic Conversion of Heat to Electricity. Solar Energy 36 (1986), 31 (1), 63.

2. R. Hu, B. A. Cola, N. Haram, J. N. Barisci, S. Lee, S. Stoughton, G. Wallace, C. Too, M. Thomas, A. Gestos, M. E. dela Cruz, J. P. Ferraris, A. A. Zakhidov, and R. H. Baughman. Harvesting Waste Thermal Energy Using a Carbon-Nanotube-Based Thermo-Electrochemical Cell. Nano Lett 2010, 10 (3), .838.

Acknowledgements

Funds for this research were provided by the Center on Materials and Devices for Information Technology Research (CMDITR), the NSF Science and Technology Center No. DMR 0120967. Experimental assistance from the thermocell group in the NEST Lab is appreciated: Brantly Fulton, Kyarra Thompson, Sameer Rao.

THEO HICKS is currently in pursuit of a Chemistry/Chemical Engineering dual-degree from Morehouse College and the Georgia Institute of Technology. Theo plans to pursue a Doctorate of Philosophy in Chemical Engineering.

Increasing the Electro-Active Area on a Partially Blocked Electrode in an Organic Solar Cell

JEROME R. LAREZ, Cochise Community College
Brian Zacher, Neal R. Armstrong, University of Arizona

Introduction

One of the problems responsible for the current inefficiency of organic solar cells is the presence of a partially blocked electrode which facilitates recombination of holes and electrons within the device. The research objective was to increase the electro-active area of the partially blocked electrode through the use of a conductive polymer in order to maximize the extraction of carriers in an organic solar cell, therefore making the organic solar cell more efficient.

The partially blocked electrode, Indium Tin Oxide (ITO), is a thin layer (approximately 200 nm) metal oxide that is deposited onto a glass substrate. ITO is widely used for two fundamental reasons: it is conductive and transparent.

The ITO deposit on glass contains areas that are not electrically conductive due to its heterogeneity.

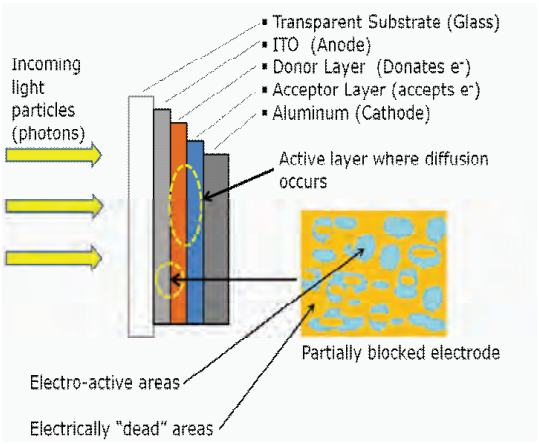

Figure 1. Model of organic solar cell and partially blocked electrode.

Experimental Methods

The research primarily consisted of electrode modification via electrochemical polymerization of 3-Hexylthiophene (E-P3HT) to various thicknesses on top of a "seed layer", over the ITO. The first step needed to polymerize 3HT was to add this "seed layer" of 3-Thiophene Acetic Acid (3-TAA) onto the ITO. The 3-TAA molecules are chemisorbed onto the substrate.

Once the 3-TAA is chemisorbed onto the ITO substrate, the ITO is then placed in an electrochemical cell (ECC) with 3HT solution. Current is then applied to the ECC at predetermined levels that dictate the different thicknesses of E-P3HT to be electro-chemically grown. The thiophene rings on the 3HT molecules bond to the thiophene rings on the 3-TAA molecules in order to polymerize 3HT.

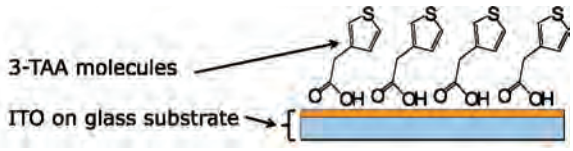

Figure 2. 3-TAA molecules chemisorbed onto ITO substrate.

After the E-P3HT is grown to each determined thickness, the 3HT solution is drained from the ECC and an electrolyte solution is added. This serves as the doping agent which oxidizes the polymer to make it more conductive.

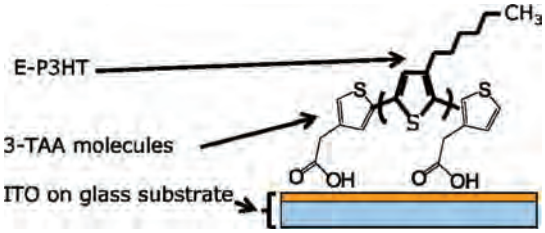

Figure 3. Polymerization of E-P3HT with 3-TAA on top of ITO.

Regioregular P3HT (RR-P3HT) is then spin coated onto the E-P3HT to act as the donor layer during testing. The regioregular structure affects the charge carrier mobility during testing.

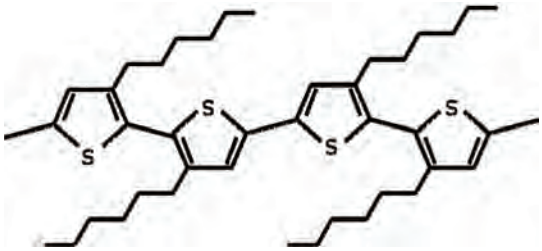

Figure 4. Showing regioregular structure of RR-P3HT.

The substrate containing ITO, E-P3HT, and RR-P3HT is then assembled into a Hole Only Device (HOD) where voltage is applied to the device to test for current.

E-P3HT was grown ranging in thicknesses from 20 nm to 100 nm.

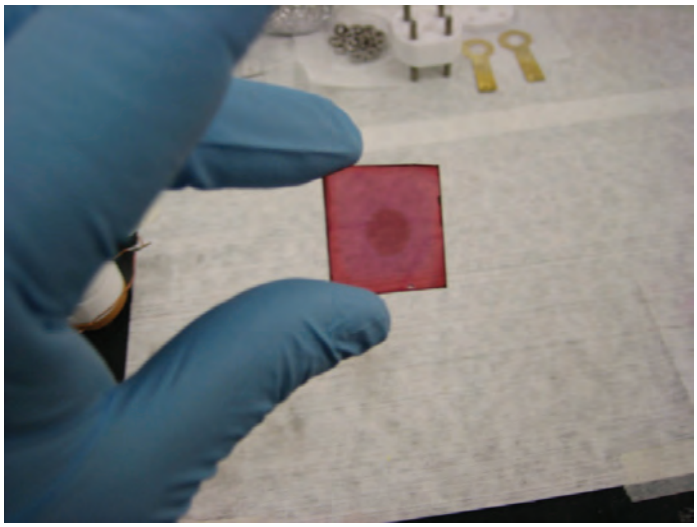

Figure 5. RR-P3HT over E-P3HT on ITO.

A mercury drop is added to the top of the polymers inside the HOD to act as the cathode during testing. Mercury is used because of its conductivity and physical characteristics where it covers the entire surface to be tested.

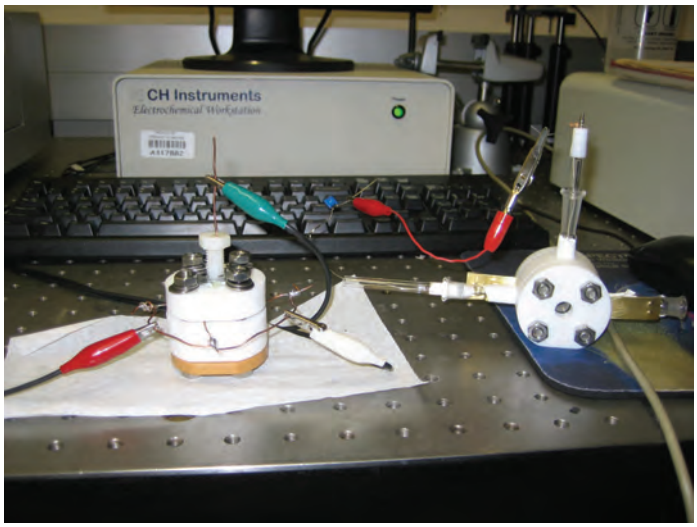

Figure 6. Hole Only Device (HOD).

Results and Discussion

The performance of the different thicknesses were tested and then compared to the performance of PEDOT:PSS {poly(3,4 ethylenedioxythiophene) poly(styrenesulfonate)}, which is currently used as an industry standard for comparability. 60nm – 80nm thicknesses of E-P3HT were found to be most conductive, or least resistant, at lower potentials (voltages).

As Figure 7 indicates, 60 nm – 80 nm thicknesses of E-P3HT outperformed thicknesses of 20 nm – 40 nm, and 100 nm at the desired lower potentials.

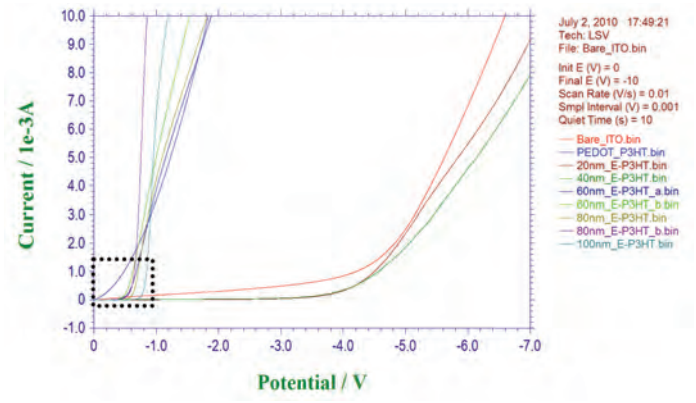

Figure 7. Current/Potential(Voltage) graph displaying performances of bare ITO, PEDOT:PSS, and varied thicknesses of E-P3HT.

A surprising result occurred at the more extreme lower potentials of all E-P3HT thicknesses. Fiure 8 shows that PEDOT:PSS is more conductive at potentials < 1.0 V. The E-P3HT didn't "turn on" at these lower potentials. The highlighted area in Figure 7 is examined more closely in Figure 8.

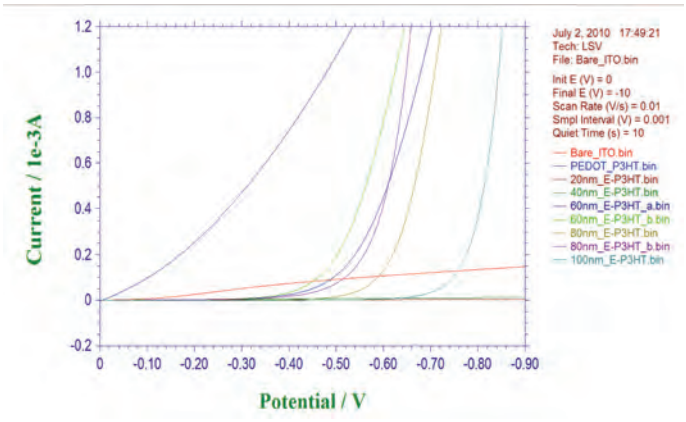

Figure 8. Graph displaying lower potentials and performances of bare ITO, PEDOT:PSS, and varied thicknesses of E-P3HT.

Conclusions

The research goal was to increase the electro-active area on a partially blocked electrode in an organic solar cell. By electro-chemically growing and polymerizing 3-Hexylthiophene (E-P3HT) we successfully increased the electro-conductivity of the electrode (ITO). At higher potentials (1.0 V - 1.8 V) the substrates with the E-P3HT, at thicknesses ranging from 60 nm to 80 nm, outperformed PEDOT:PSS.

However, at slightly lower potentials (< 1.0 V), the E-P3HT exhibited a "dormant" phase where the substrates with this electrochemically grown polymer didn't perform as well as the substrate with PEDOT:PSS.

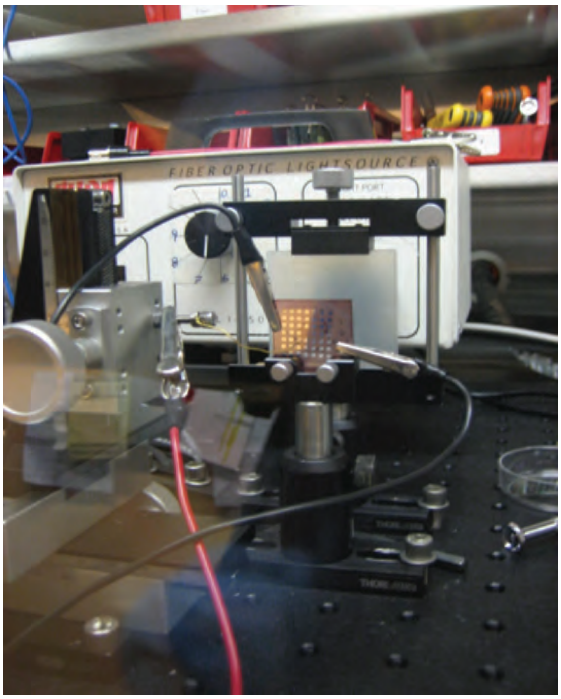

Figure 9. A completed organic solar cell. Aluminum (cathode) deposited on top of a substrate with E-P3HT.

An organic solar cell was constructed by depositing aluminum, as the cathode, on top of the substrate with E-P3HT in order to confirm the performance. Organic solar cells operate at lower potentials (< 1.0 V).

	Solar Cell		
Parameter	Bare ITO	PEDOT: PSS	E-P3HT
Open-Circuit Voltage (V)	0.431	0.424	0.476
Short_Circuit Current Density (mA/cm^2)	8.129	8.915	0.261
Fill Factor (%)	50.1	47.8	33.1
Power Conversion Efficiency (%)	1.76	1.81	0.04

Table 1. Data chart comprised of test results from organic solar cell constructed with E-P3HT.

A data chart from an organic solar cell constructed with bare ITO, PEDOT:PSS, and E-P3HT confirms the performance of the electrochemically grown polymer (E-P3HT) at lower potentials. The power conversion efficiency of the cell assembled with E-P3HT shows a 0.04% power conversion efficiency.

Future Work

The data indicates that research regarding E-P3HT's performance at lower potentials needs to be conducted in order to better evaluate the polymer's ability as an interface for electro-conductivity. The future research will need to explain why the "dormant" phase occurs at the lower potentials.

Organic solar cells, or organic photovoltaic cells (OPV) and organic light emitting diodes (OLEDs) operate under similar principles but in a reverse course from one another. OPVs use light to generate current whereas OLEDs use current to generate light. The E-P3HT's performance at higher potentials may be beneficial to the overall performance of OLEDs, as they operate at higher potentials.

Acknowledgment

Special thanks to the National Science Foundation (NSF) and the Center on Materials and Devices for Information Technology Research No. DMR 0120967. I would also like to thank Dr. Neal Armstrong and the entire Armstrong group for all the guidance and support they showed me during my research at the University of Arizona (go CATS!). Thank you to my mentor Brian Zacher who was a more than perfect mentor. Thank you to Kimberly Sierra-Cajas who always directed me to the right course of actions throughout the entire program. I would also like to thank Janeen Crockett whose hairs stood up on the back of her neck as she instructed students in chemistry.

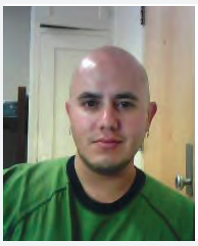

JEROME R. LAREZ is a student at Cochise College and is majoring in electrical engineering. He plans on attending the University of Arizona in the fall of 2011 to continue his research in organic solar cells.

Intercalation of Organic Nonlinear Optical Chromophores into DNA to Improve Acentric Ordering

LUKE N. LATIMER, Pacific Lutheran University
Lewis E. Johnson, Bruce H. Robinson, University of Washington

Introduction

As predicted by Moore's law, the development of electronics has been proceeding at an astonishing rate during the last 50 years.[1] In order to match these advancements, the electro-optical (EO) field has increased focus on developing organic non-linear optical (NLO) devices as a means of improving device performance. These organic NLO devices have the potential to replace inorganic EO modulators, and replace electronic, chip-scale communications with optical interconnections. Such technologies could have ramifications of increased internet bandwidth by 100 fold as well as better thermal management and reduced electrical crosstalk.[2]

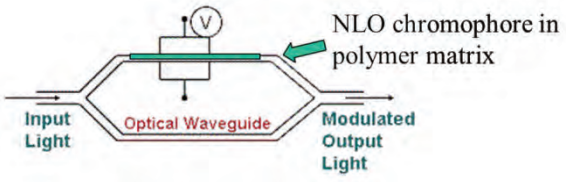

Figure 1. Diagram of a Mach-Zehnder EO Modulator used in telecommunications.

Organic EO devices function by having a polymer matrix infused with NLO chromophores. In addition to material characteristics such as thermal stability and optical transmittance, the NLO activity of a material is often measured by its electro-optical coefficient, r_{33}, which is proportional to the number density of the chromophore within the host polymer, the hyperpolarizability of the chromophore, and the acentric ordering of the chromophores within the matrix as shown in Equation 1.[2]

$$r_{33} \propto \rho_N \beta \left\langle \cos^3 \theta \right\rangle$$

Number density; hyperpolarizability; Acentric ordering

Equation 1. Electro-optical coefficient proportionality.

The acentric ordering parameter, $\langle \cos^3\theta \rangle$, or alignment of the chromophores within the bulk material is typically induced by electric-field assisted poling; a strong electric field is applied to the material while the chromophores have mobility within the host (e.g. near the glass transition temperature of the material) followed by conformational restriction while the electric field is still in effect.[4] To date, low $\langle \cos^3\theta \rangle$ has been achieved for high-β chromophores, which has spurred research into improving acentric ordering by restricting available chromophore conformational states during poling using techniques such as attachment of liquid crystal moieties to chromophores.[5]

In this project, deoxyribonucleic acid (DNA) is investigated as a potential host polymer that can reduce chromophore dimensionality. Because of its highly ordered, double-helix structure, certain molecules tend to intercalate in between DNA base pairs.[6] If a chromophore intercalates into DNA, it should achieve significantly higher levels of acentric ordering when poled due to the rotational restrictions induced by the DNA base pairs. The likelihood of chromophore intercalation into DNA seems promising because most NLO chromophores have a long conjugated system of double bonds and aromatic rings and tend to be planar, which are key characteristics of many DNA intercalators.[7] Research focused on observing DNA intercalation by UV-Vis spectroscopy, screening an assortment of NLO chromophores for intercalation and development of DNA thin films for later poling and r_{33} measurements is presented below.

Experimental

CTAB-DNA

Random-sequences of salmon sperm Na-DNA (50-100 kDa) were used as purchased from Sigma Aldrich. Formation of hexadecyltrimethylammonium-DNA complexes (Figure 2) was conducted as described by Heckman et al.[8] Excess water was removed by freeze-drying in a lyophilizer overnight to yield CTAB-DNA (est. MW = 90-180 kDa based on 1CTAB:1DNA base).

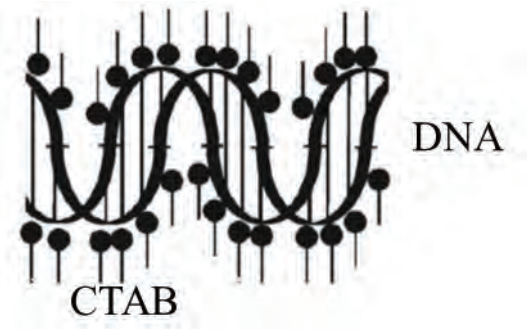

Figure 2. Diagram of CTAB-DNA complex.[9] The ammonium ion in CTAB replaces Na^+.

UV-Visible (UV-Vis) Spectroscopy

Previous research in our lab by Frei et al. established the UV-Vis protocol used.[10] Equilibration times were reduced by shaking samples between DNA additions. UV-Vis absorption data were collected with an Ocean Optics diode array spectrophotometer temperature controlled at 25 °C with a thermal plate. All aqueous titrations were conducted in TE buffer (10 mM Tris-HCl, 10 mM KCl, 1 mM EDTA, pH 7.2). Aqueous titrations of ethidium bromide (EtBr), crystal violet (CV), and 4(4-dimethylamino styryl)-1-methylpyridinium tosylate (DAST) with Na-DNA (50-100 kDa, 1 mg/mL) were conducted and analyzed with MATLAB using a monte carlo fitting program (MCfit) written by L. E. Johnson and N. W. Bigelow to determine the binding constant and mode of binding for each dye. Further titrations of TV-1-107,[10] Disperse Red 1 (DR1), and a hexanol-modified DR1 with CTAB-DNA (90-180 kDa, 2 mg/mL) in methanol were similarly analyzed.

Thin Films

Glass substrates were cleaned with soap then sonicated in acetone and isopropanol. Before spin-coating, slides were rinsed with acetone, methanol & isopropanol. CTAB-DNA was dissolved in butanol (6-15% wt/wt) at 80 °C, filtered in a 0.45 µm filter and allowed to settle overnight. Films were cast from 275 µL of butanol solution and then stored at 80 °C for one hour to produce clean, even films. Films developed from CTAB in butanol using the same protocol were opaque and highly uneven, which led to the complexing of CTAB and polystyrene sulfonate (PSS; 30 kDa). CTAB-PSS was formed and spin-coated using the same procedure as CTAB-DNA except purification and isolation of CTAB-PSS suspensions required centrifugation for 5 minutes followed by evaporation of excess water in a 75 °C water bath prior to freeze-drying.

Results

Titration of ethidium bromide (EtBr) with Na-DNA as described above yielded Figure 3. A shift of 30 nm was observed in λ_{max}. Fitting of the spectra to MCfit showed that EtBr best fits an n = 2 binding curve, where n is the occupation number, or ratio of base pairs to dye (ligand) molecules. The occupation number indicates the mode of DNA binding. Typically n = 0.5 or 1 represents independent binding, while n = 2 represents nearest-neighbor exclusion, where ligand binding at one site blocks the two adjacent binding sites, which is characteristic of intercalation. A summary of tested chromophores that bound to DNA is displayed in Table 1.

Identical conditions were used in titrating DAST with Na-DNA, and the resulting UV-Vis spectra are shown in Figure 4. The observed shift in λ_{max} for DAST was 10 nm.

When CTAB-DNA was used for titrations, no DNA binding was observed for any molecules. As a representative example, the UV-Vis spectra for the titration of EtBr with CTAB-DNA in methanol is shown in Figure 5.

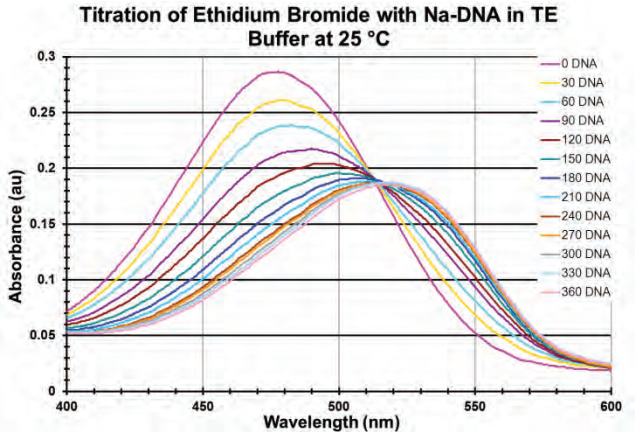

Figure 3. UV-Vis spectra of the titration of EtBr with Na-DNA in TE buffer at 25 °C. DNA values are in µL.

Dye	Fitting, n	Binding Constant (K)
EtBr	2	24000 ± 3000
CV	1	380000 ± 50000
DAST	2	5600 ± 400

Table 1. Fitting data produced by MCfit3 for all dyes that showed Na-DNA binding upon titration of the dye with Na-DNA. Fitting model refers to the ratio of DNA base-pairs to dye molecules. The sum of squares is an error analysis of the fit compared to the data.

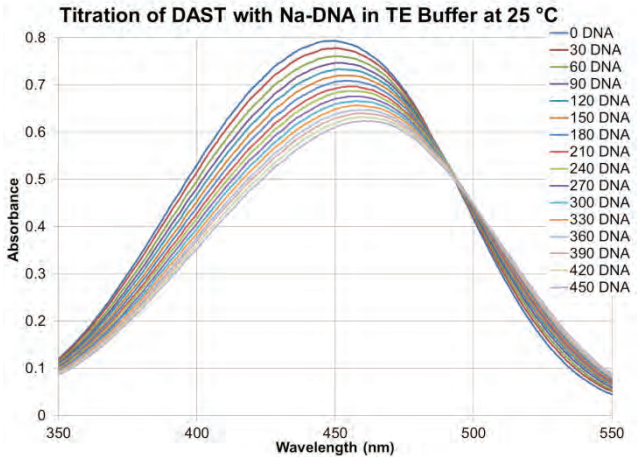

Figure 4. UV-Visible spectra of the titration of DAST with Na-DNA in TE buffer at 25 °C. DNA values are in µL.

Thin films of CTAB-DNA and CTAB-PSS were spin-coated in order to investigate the possibility of using CTAB-PSS as a control film for comparison with CTAB-DNA films. Both film types show transmittances >90% between λ = 300-1100 nm. Additionally, CTAB-DNA films containing EtBr, DR1, and CV were cast (15% wt/wt dye/CTAB-DNA) as shown in Figure 6. The resulting films were smooth and uniform.

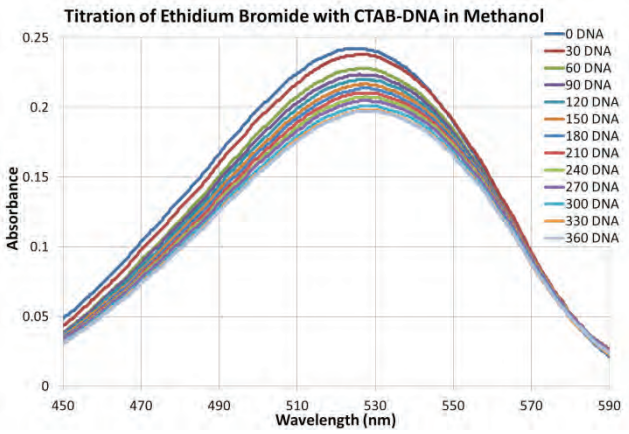

Figure 5. UV-Vis spectra of the titration of EtBr with CTAB-DNA in methanol at 25 °C. DNA values are in µL.

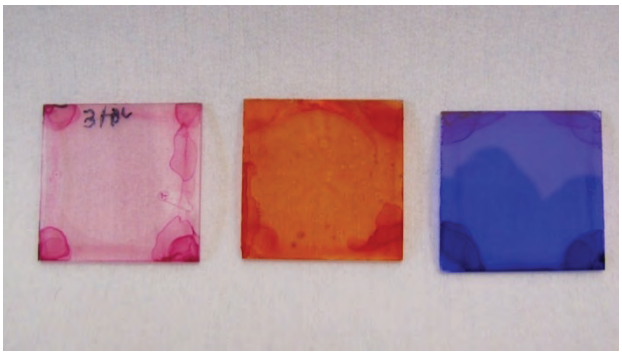

Figure 6. Photo of CTAB-DNA (7.5% wt in butanol) thin films spin-coated on glass with 15% solid wt EtBr, DR1, and CV (from left to right).

Discussion

The titration of ethidium bromide with DNA functions as a control for later titration of chromophores, as the binding data confirms that EtBr binds to DNA in an exclusion method (at alternating base pairs), which is consistent with literature.[7,11] Additionally, crystal violet's independent binding matches literature.[7] Interestingly, DAST showed weak binding to DNA which is promising for further testing in developing NLO chromophore intercalated DNA thin films using DAST. The weak exclusion binding of DAST is expected because it has greater conformational freedom then most intercalators with two rotating bonds within the core structure; however it still is planar, conjugated, and cationic, which are key characteristics observed in the majority of DNA intercalators.[7]

When titrating dyes with CTAB-DNA in methanol, no DNA binding was observed, even with ethidium bromide. Research conducted by Steckl and co-workers has shown that some DNA intercalators will preferentially associate with the CTAB surfactant layer in CTAB-DNA solutions,[12] which is likely why no CTAB-DNA binding is observed with EtBr. This lack of interaction presents an interesting challenge for testing the affects of DNA intercalation on acentric ordering during electric-field assisted poling.

It is possible that as a film is dried, dyes will intercalate into DNA. This possibility of solid-phase intercalation led to developing CTAB-DNA thin films and control films of CTAB-PSS. Previous work has shown that CTAB-DNA makes films with good optical characteristics, such as thermal stability, resistance to most organic solvents, high transmittance, and a good index of refraction.[13] Using a published procedure, CTAB-DNA was prepared and the spin-coating process was optimized. These techniques were applied to Polystyrene-sulfonate (PSS) to develop comparable films, which can hopefully be used as a control to observe chromophore interaction in DNA, as intercalation is not possible in CTAB-PSS films.

Conclusions

UV-Visible spectroscopy was used to observe DNA-chromophore interaction. An assortment of NLO chromophores were screened, and DAST was the only chromophore to show DNA binding to Na-DNA, though not to CTAB-DNA. Future work will involve dye intercalation into CTAB-DNA, which may be possible either by removing solvent while forming a thin film or by intercalating dye into the Na-DNA prior to attachment of the CTAB surfactant. Additionally, a different surfactant with a weaker DNA binding constant or a different surfactant:DNA ratio may allow for DNA intercalation. Initial work was conducted on testing for CTAB-DNA intercalation in thin films by developing CTAB-DNA and CTAB-PSS spin-coating procedures. These films can be used to test EtBr and DAST intercalation with the ultimate goal of intercalating DAST into CTAB-DNA such that the hypothesis of improved r_{33} for intercalated chromophores can be tested.

References

1. Intel main page. http://www.intel.com/technology/mooreslaw/ (accessed July, 3 2010).
2. Sullivan, P. A.; Dalton L. R. Theory-inspired development of organic electro-optic materials. Accounts of Chemical Research 2010, 43, 10-18.
3. Lui, Ansheng"Announcing the world's first 40G silicon laser modulator!" http://blogs.intel.com/research/2007/07/40g_modulator.php (accessed 26 August 2010).
4. Inaba, R.; et al. In situ observation of the orientational motion of chromophores during corona poling of electro-optic polyimides. Macromolecules, 1996, 29, 2954-2959.
5. Benight, S. et al. Reduced Dimensionality in Organic Electro-Optic Materials: Theory and Defined Order. J. Phys. Chem. B., 2010, ASAP article.
6. Neto, B. A. D.; Lapis, A. A. M. Recent Developments in the Chemistry of Deoxyribonucleic Acid (DNA) Intercalators: Principles, Design, Synthesis, Applications and Trends. Molecules, 2009, 14, 1725-1746.
7. Del Castillo, P.; Horobin R. W.; Blazquez-Casto, A.; Stockert, J. C. Binding of cationic dyes to DNA: distinguishing intercalation and groove binding mechanisms using simple experimental and numerical methods Biotech. & Histochem. 2010, Early Online, 1-10.
8. Heckman, E. M.; et al. Processing techniques for deoxyribonucleic acid: Biopolymer for photonics applications. Appl. Phys. Lett., 2005, 87, 211115.
9. Kawabe Y.; et al. Amplified Spontaneous Emission from Fluorescent-Dye-Doped DNA-Surfactant Complex Films. Adv. Mater., 2000, 12, 1281-1283.
10. Frei, D. J.; Johnson L. E.; Robinson B. H. Use of Ion-Exchange Functionalized DNA as a Host Material for Enhanced Poling Induced Order and Molecular Hyperpolarizability. Photonics CMDITR Rev. of Undergrad. Research, 2009, 6, 42-45.
11. Yuzaki, K.; Hamaguchi, H. Intercalation-induced structural changes of DNA as studied by 1064 nm near-infrared multichannel Raman spectroscopy. J. Raman Spectrosc., 2004, 35, 1013-1015.
12. You H.; et al. Role of Surfactants in the Intercalation of Dye Molecules in Natural DNA polymers. Langmuir, 2009, 25, 11698.
13. Grote J. G.; et al. DNA Photonics [Deoxyribonucleic acid]. Mol. Cryst. Liq. Cryst., 2005, 426, 3-17.

Acknowledgments

Many thanks are due to our collaborators and fellow researchers: Delwin Elder & Forrest Michael for help with synthesis procedural development, Bill Cusworth for UV-Vis spectrophotomer use, Stephanie Benight for thin film 'device' fabrication, Ben Olbricht and Jeff Hurst for ATR measurements and film preparation, Emily Heckmen for discussions on CTAB-DNA films, Nicholas Bigelow for equipment, Bruce Eichinger and Rainbow Photonics for supplying DAST, and Meghana Rawal, Chris Palmer, Terry Villarreal for synthesis consultation and providing TV-1-107 & DR1 derivatives. The authors would like to extend special thanks to Zach Watanabe for assistance in UV-Vis titrations and analysis as well as synthesis development.

Funding was provided by NSF Science and Technology Center on Materials and Devices for Information Technology Research No. DMR 0120967, NSF Research Experiences for Undergraduates Program Hooked on Photonics No. CHE 0851730, and UTC Air Force Grant FA8650-06-D-5401/0005, Task Order 0014.

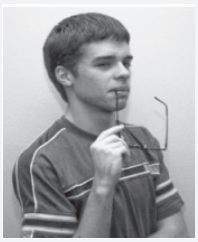

LUKE LATIMER is a senior biochemistry major at Pacific Lutheran University intending to pursue a Ph. D. in biochemistry.

The Development of Bimodal Dielectric Materials for use in Capacitors

COURTNEY D. LEMON, Georgia Perimeter College
O'Neil Smith, John Tillotson, Joseph W. Perry, Georgia Institute of Technology

Introduction

Materials with high dielectric permittivity are desirable for use in making simple capacitors. Capacitors in their simplest form are comprised of a dielectric material placed between two charged plates. These devices are a core part of many electronic components. Therefore, they are of importance to the industry.

As the size of devices continues to shrink, new materials are needed that will perform better than existing materials on the small scale. Many studies on ceramics and polymers have been conducted for their use as dielectric materials. Polymers have been shown to give high dielectric strength, low cost, and low processing temperatures. Ceramics, on the other hand, have a high dielectric constant value, high processing temperatures and high costs.

It is expected that the combination of both polymer and ceramics could yield favorable dielectric properties. This approach was taken in this study. The polymer used was Poly(vinylidene fluoride-co-hexafluoro propylene), commercially recognized as Viton (see Figure 1).

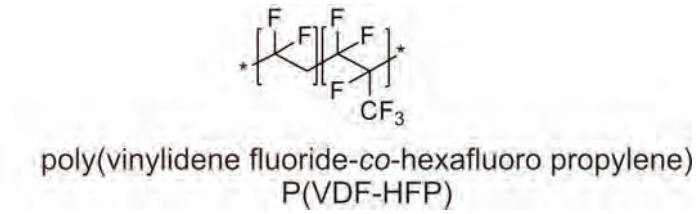

Figure 1. Viton polymer.

The ceramic nanoparticles of choice were barium titanate (BT) owing to their relatively large permittivity.

It is important to have a homogenous dispersion of particles in the polymer matrix to ensure high performance, however BT tends to agglomerate in organic matrices. In order to minimize aggregation, the surfaces of the BT nanoparticles were modified by attaching pentaflurobenzylphosphonic acid (PFBPA). This allowed for a homogenous dispersion of BT in Viton. Another issue that arose is the creation of porous domains that are generally formed within organic-inorganic matrices. In order to minimize the void fraction, a bimodal particle packing approach was employed. By using a bimodal packing approach, the smaller particles will fill the space between the larger particles and the polymer.

Experimental

Synthesis of PFBPA

Several steps were done in order to conduct this research. Figure 2 shows the synthetic scheme of PFBPA that was used in this study.

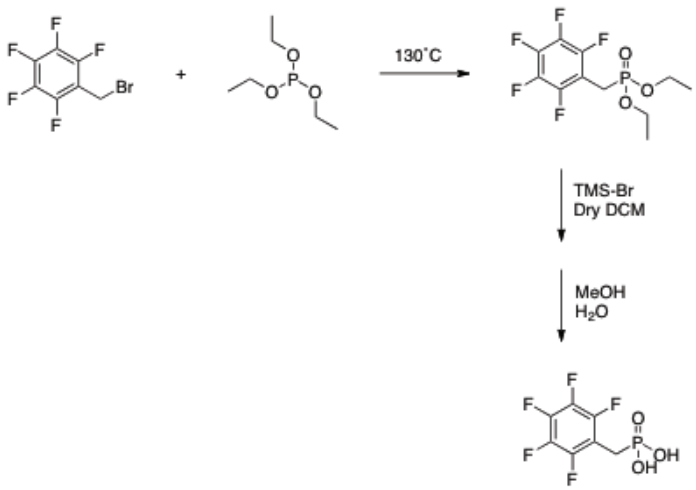

Figure 2. Synthetic scheme of PFBPA.

Step 1 of the two step synthesis process consisted of refluxing Pentaflourobenzyl bromide (12 mL) and triethylphosphite (40 mL) overnight at 130 °C to yield phosphonate (83%). The phosphanate was placed on a pump overnight to rid the reaction of volatile Bromide. To ensure the reaction was pure, gas chromatography-mass spectrometry (GC-MS), ^{1}H, ^{19}F, and ^{31}P nuclear magnetic resonance (NMR) spectroscopy characterizations were done. After allowing dichloromethane (DCM) to stir on a hotplate for 5 min, it was combined with tetramethylsilane (TMS) bromide (23 mL) and added to the phosphante to stir overnight. A 10:1 methanol water ratio was added and left to stir overnight. The next day the reaction was set on the rotavapor (waterbath temperature was set to 40 °C, pressure (p) was set between 150-175 torr, and change in pressure (Δp) was set between 15-20 torr) for approximately 20 min to crystallize and rid the DCM solvent. As a continuation, Acetonitrile (ACN) was used to recrystallize the reaction and obtain PFBPA crystals. These crystals served as the modifying organic ligand for the ceramic BT nanoparticles.

Surface Modification of BT Nanoparticles

Surface modification of the BT particles with PFBPA was the next step of this research. It is critical to the experiment to obtain compatibility and a homogenous dispersion of the particles within the matrix. As Figure 3 illustrates, BT was reacted with PFBPA in ethanol at 70 °C. Seven washes consisting of the addition of ethanol and centrifugation to the modified particles removed any excess, unbounded PFBPA.

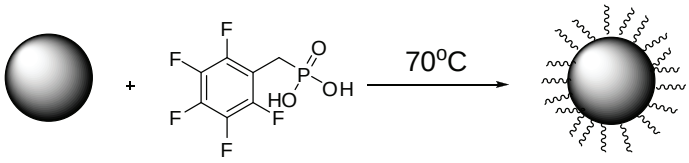

Figure 3. Reaction of BT an dethanol (spheres).

Characterization of Modified BT Nanoparticles

Upon surface modification, the particles were characterized by FT-IR and XPS. The results of these tests were necessary to be certain the particles were fully covered. XPS is a technique used to determine what is on the surface of a sample (see Graph 1). It was used to measure the elemental composition of the surface of the modified BT particles.

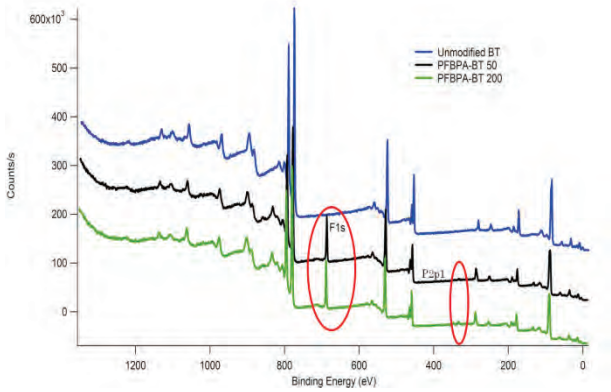

Graph 1. XPS data.

The unmodified BT lacks two peaks that are displayed on the modified particles. The peaks indicate the presence of Phosphorous and Fluorine. The Phosphorous peaks are both displayed at the same binding energy, 689.09 eV. Likewise the Phosphorous peaks are located at the same locations on the x axis as well (334.49 eV).

Preparation of Nanocomposite

Nanocomposite preparation was the next step of the research (Figure 4). The 50 nm and 200 nm modified particles, Viton, dimethylformamide (DMF), and three different sizes of grinding media (15.02-15.72 grams of the small, 58.10-58.57 grams of the medium, and 11.60-11.80 grams of the large) were combined in plastic vials based on a volume fraction loading scale (Table 1.1). The samples were measured on an analytical scale, massed and recorded in the lab notebook. Table displays the masses of the ceramic particles and polymer used in each sample. Once appropriately combined, each bottle was parafilmed and placed on the ball mill to mix for approximately two weeks.

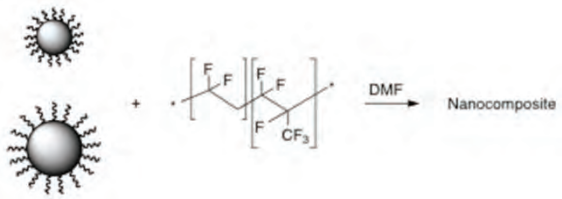

Figure 4. Preparation of nancomposites.

BT (%)	Viton (%)
10 (sample A)	90
20 (sample B)	80
30 (sample C)	70
40 (sample D)	60
50 (sample E)	50

Table 1.

Sample	BT 50nm	BT 200nm	Viton
A	.0157g	.9855g	2.6615g
B	.0284g	1.8366g	2.1999g
C	.0447g	2.9560g	2.0658g
D	.0565g	3.7542g	1.6737g
E	.0814g	5.3751g	1.6091g

Table 2.

Bimodal Particle Packing

A face center cubic (FCC) model, shown in Figure 5, was used to ensure maximum density of the BT particles within the matrix. Based on the FCC model, two possible sites are able to be occupied by the ceramic, tetrahedral and octahedral. Equations 1 and 2 below represent the maximum size radius (r) of the small BT particles permitted in the sites based on the radius (R) of the large particles. The particles of BT that were used in this research had measurements of r=25 and R=100. In theory, this automatically eliminates the usage of the tetrahedral site as an option for nanoparticle alignment within the FCC model. Overall, the 50 nm BT particles accounted for 1.5% of the entire model.

Equation 1: Octrahedral Site
r= 0.414R = 0.414(100) = 41.4

Equation 2: Tetrahedral Site
r = 0.225R = 0.225(100) = 22.5

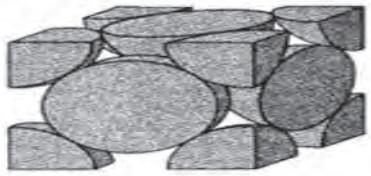

Figure 5. FCC model.[2]

Film and Device Fabrication

Aluminum (Al) coated glass substrates (Newport Thin Film Lab) were plasma cleaned with O_2 and N_2 plasma. The purpose of this was to increase the hydrophilicity of the substrate to reduce beading of the samples on the Al. Nanocomposite films were produced by spin casting and were dried on a hot plate at 70°C for 10 minutes. Dried films were annealed in a vacuum oven overnight at 70°C. Al top electrodes were deposited on the films with the use of a shadow mask in a Filament evaporator (Kurt J. Lesker PVD 75). Samples were affixed flush to the mask by Kapton tape. It is important that the masks are flush against the films to ensure complete deposition of Al electrodes. Figure 6 displays two photos of a spin-coated film and a finished device after electrodes were deposited in the clean room.

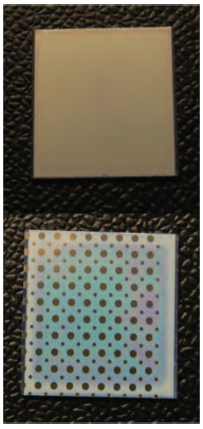

Figure 6. Pre- and post-device fabrication.

Future work involves testing the finished devices. This would involve their placement into a glove box designed to characterize the devices. Also the compilation of data from XPS and thermogravimetric analysis (TGA) will allow for proper analyzation to determine if the desired results were achieved by the completed capacitors.

Conclusion

The overall summer research consisted of effective synthesis of PFBPA, BT nanoparticle surface modification, development of bimodally loaded nanocomposites, and the construction of capacitors.

References

1. Kim, Philseok, Natalie Doss, John Tillotson, Peter Hotchkiss, Ming-Jen Pan, Seth Marde, Jiangyu Li, Jeffery Calame, and Joseph Perry. "High Energy Density Nanocomposites Based on Surface-Modified $BaTiO_3$ and a Ferroelectric Polymer."ASC NANO 3.9 (2009): 2581-2592.

2. http://info.lu.farmingdale.edu/depts/met/met205/fcc-jpg.JPG

Acknowledgements

I would like to thank the National Science Foundation (NSF) for funding as well as the Center on Materials and Devices for Information Technology Research Hooked on Photonics (CMDITR-HoP) Program and the Georgia Institute of Technology for allowing me the opportunity to participate in undergraduate summer research. I would like to give a special thanks to Dr. Joseph W. Perry, O'Neil Smith, and John Tillotson as well as the entire Perry Lab for providing me with the guidance to learn and acquire new skills that helped me throughout my research during the summer.

COURTNEY DE'VON LEMON is currently a sophomore at Georgia Perimeter College majoring in mathematics. She will be attending Georgia Institute of Technology to major in biochemistry in Spring 2011. Her future goals include attending graduate school to earn a Ph. D. and pursue a career in biochemical research. She enjoys laughing and spending time with family and friends.

Spin Coating Process Development and Spin Curve Analysis of PMMA Resist

ISAAC LOPEZ, Arizona State University
Oscar D. Herrera, Robert A. Norwood, University of Arizona

Introduction

Spin coating is widely used to coat substrates with photoresist.[1] We use this technique to form PMMA films on silicon substrates at different speeds and concentrations (PMMA in anisole). We compared commercially available PMMA solutions of known concentrations to self-prepared PMMA solutions. We verified that the self-prepared PMMA solutions were of equal quality, with reproducible results. Further analysis of low concentrations of PMMA for sub-100 nm thick films were made. Poly(methyl methacrylate) (PMMA) is the most commonly used high resolution resist for electron beam lithography. It is a positive resist in which the portion of the photo resist that is exposed results in chain scission. The resulting lower-molecular-weight polymer dissolves in the developer leaving the unexposed region intact.[2] Our motivation for this research was to optimize the PMMA spin coating process for electron beam lithography. The thickness of PMMA is related to the resolution and structure definition of the exposure. Films that are both thin and planarized are essential for well defined high resolution structures. Furthermore, these spin coating techniques can be applied to other polymers such as electro-optic polymers.

Experimental Methods

Our spin coating procedures were standardized in order to eliminate any uncontrollable variables or errors that may arise when the procedures change during any part of the experiment. The measurements that we made were primarily the spin speed versus the thickness of the PMMA. Other measurements that were of interest were the roughness and waviness of the surface of the PMMA. Roughness, which is a high frequency oscillation along the surface, was measured along a surface length of 30 µm. Waviness, which is a low frequency oscillation of the surface, was measured along a length of 5 mm. The process of spin coating involves five standard steps: (1) silicon wafer cleaning; (2) static dispense PMMA onto a sample wafer; (3) spin wafer at a low speed spin for a short period; (4) spin wafer at a final desired speed spin for a long period; (5) perform softbake of wafer to allow solvent to evaporate. The first step of the spin coating process is to make sure that that silicon wafer substrate is clean. This cleansing process includes bathing the wafers first in acetone and then secondly in isopropanol. We had previously used methyl alcohol as an intermediary cleaning solvent between the acetone cleanse and isopropanol, however the wafers ended up being cleaner with just the acetone and isopropanol rinse, which also reduced time spent cleaning the wafers. After the chemical cleaning, we dried off the samples with clean nitrogen gas. The wafers were then placed inside a plasma etcher for 5 minutes in order to remove any organic material left after the chemical rinse. After cleaning, the wafer was placed in the spinner. We would then statically dispense the PMMA onto the sample and spin the sample. The sample would spin for five seconds at 500 rpm to spread the PMMA and then ramp up to the desired test spin speed and spin for 45 s.

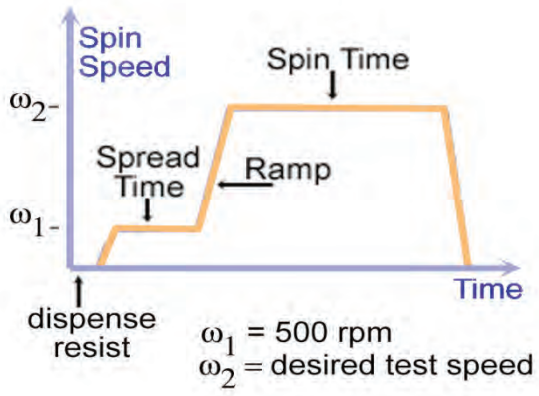

Figure 1. Spin Coat Graph: Time vs. Spin Speed.

Once the PMMA was spun on the wafer, we would perform a pre-bake or softbake of the sample at 180 °C for two minutes. This softbake would evaporate the anisole solvent, reduce the film thickness, improve film adhesion and leave the film less tacky and less prone to particulate contamination.[3] After the softbake, we would measure the thickness of the film using a Veeco Profilometer.

Measurements

The surface profiler gives measurements of scan length and PMMA thickness in nanometers. We also noted waviness and roughness to quantify planarization in the film. Waviness is the measurement of low frequency oscillations in the top coating of the PMMA layer. We measured waviness along a length of 5 mm. Roughness is the measurement of high frequency oscillations on the surface of the film. We measured roughness along a length of 30 µm.

We observed waviness and roughness in order to assess the degree of PMMA surface planarization. Planarization is the reduction of waviness. The purpose of planarization is to get the surface as flat as possible for further processing. The fluctuation limit of waviness we wanted to achieve was less than 10 nm. The planarization of the surface enables a high and predictable resolution when exposure with e-beam is performed. If the waviness is greater than the desired

10 nm, the e-beam will expose the resist inaccurately and result in a thicker or thinner width of exposure along the resist.

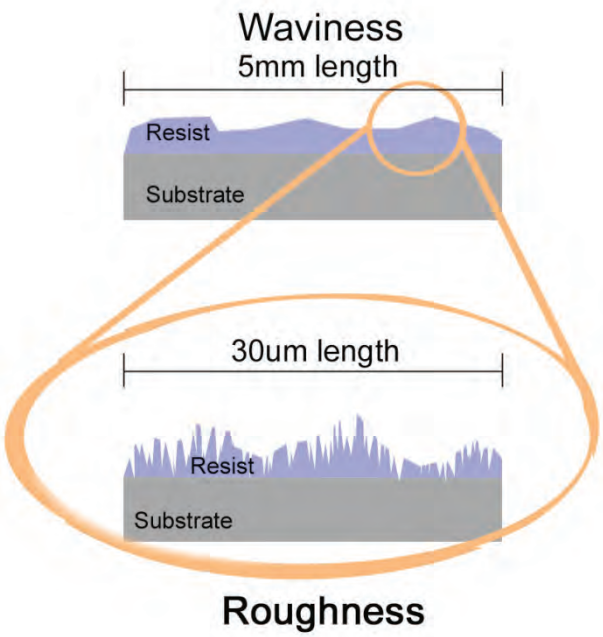

Figure 2. Waviness and roughness measurements.

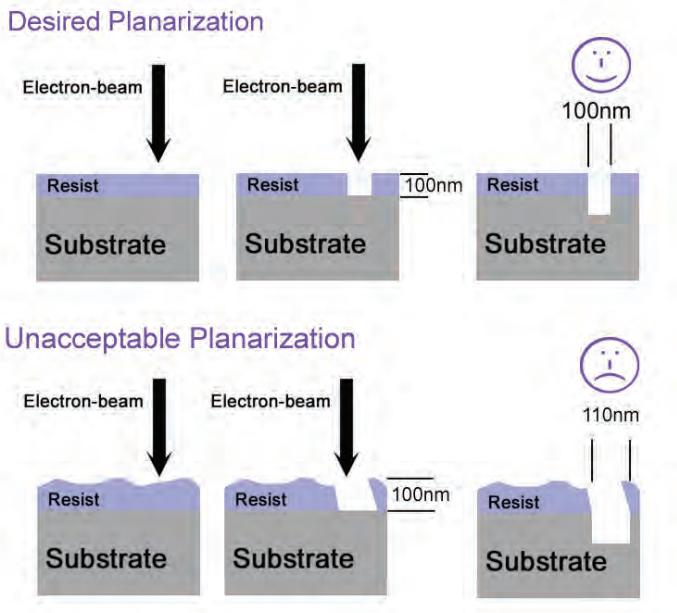

Figure 3. Desired and undesired planarization of resist.

Results and Discussion

The first goal was to determine spin curve values for Michrochem 950k PMMA A7 and A4 by performing polymer resist spin coating on silicon wafers. Using the profilometer and measuring the thickness of the polymer, the data populated the spin curve tables. Data from these experiments were then compared to spin curves of Michrochem data sheets. The characterization of the PMMA in our cleanroom lab was essential to find out what variables besides spin speed determine film thickness. We can see the spin curves of PMMA A7 in Figure 4. Comparing our spin curve with Michrochem's spin curve of PMMA A7 allowed us to control certain procedures and variables within the spin coating process. We found that the spin curve generated by Michrochem was not matching up with the spin curve performed in our lab. We learned that there were several factors that we could control to get more precise data from our spin curves. One factor was the way that the PMMA was dispensed onto the wafer. Michrochem uses a spray coat method which enables more uniform PMMA dispense. Our method of dispensing the PMMA with a filtered syringe could introduce more contaminants into the sample and also produce an uneven distribution of PMMA along the substrate. We also became aware of the spinners used in the processes; Michrochem uses a different spinner and with performance that differs from that of our system.[2]

The environment that we perform our research is also quite different from the environment at Michrochem's lab. They have a higher level of control and cleanliness by automating all of their spin coating processes. Our process has to be done by hand and will introduce a less controlled, less clean environment during the spin coating process. Another reason for the difference in results was the experience of our researchers. This was a new process performed for the very first time, so we learned the process through practice. This would prove to help our results in the second spin curve of PMMA A4. We controlled and eliminated any procedure that would introduce contaminants within the cleaning process of the silicon wafers and during the spin coat process while dispensing the PMMA onto the wafer. While we learned to control the cleaning process and make the spin coating process more efficient we were able to achieve better results for the spin curves of PMMA A4. Figure 5 shows how the spin curves from Michrochem and our experiment follow each other quite closely.

The average roughness data for our experimental PMMA A4 spin curve was 0.32 nm. This gave us the suggestion that with less roughness, waviness is also reduced. The average waviness for the PMMA A4 spin curve was 7.86 nm, which was well within the 10 nm deviation that we desired.

PMMA Dilutions

After determining the PMMA A7 and A4 spin curves in the lab, we were able to improve the spin coating process and get better comparable results with known spin curves that Michrochem performed in their lab. Another component of the spin curve analysis was to dilute Michrochem 950k PMMA A11, which is an 11% PMMA concentration in an anisole solvent. We diluted all three 4% sample dilution sets within a 0.01% error between our calculated and experimental values. We wanted to make three different dilution sets in order to compare dilution processes within those three sets. From our first dilution set we mixed the solution for one hour after dilution. This did not render good PMMA and anisole mixture solutions because the PMMA and anisole solvent that we added began separating. So the first spin speed data was not accurate. For the second dilution set, we mixed the solution for one hour and then right before the spin coat process. This rendered better data

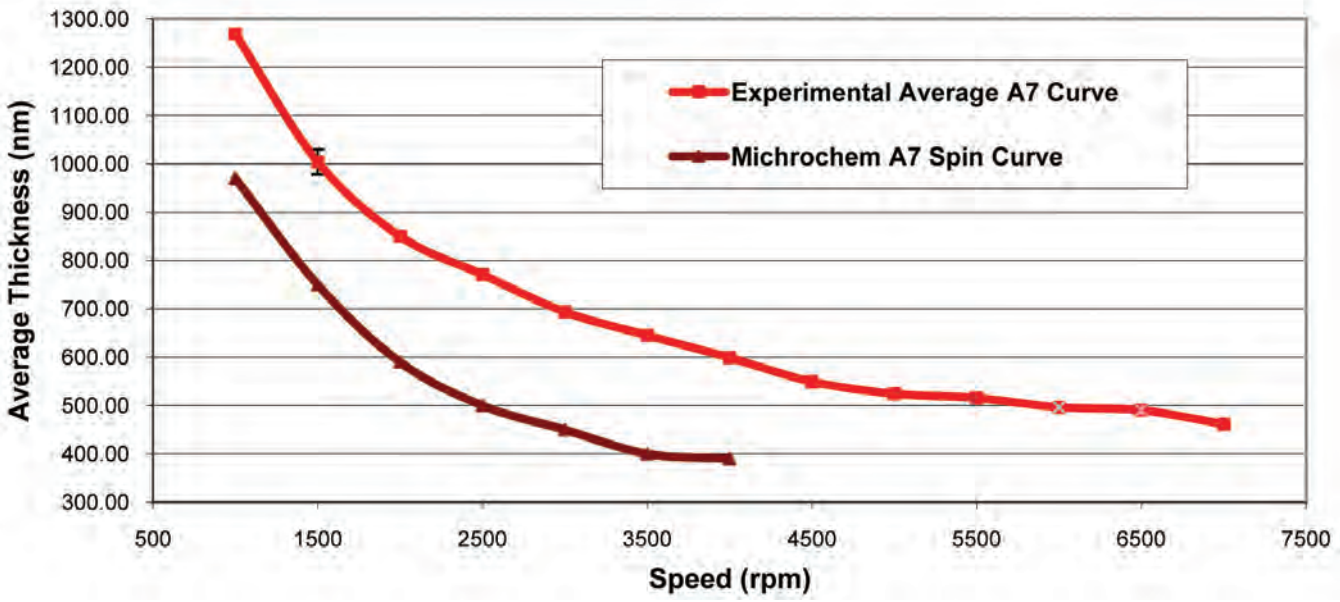

Figure 4. Michrochem 950k PMMA A7 spin curve data vs. experimental data.

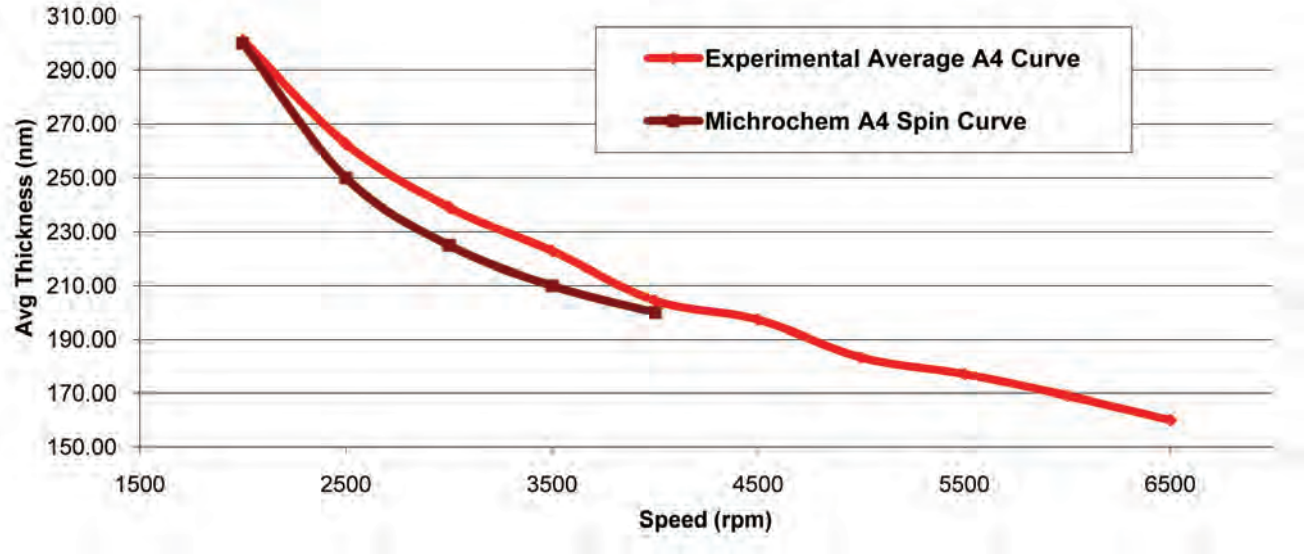

Figure 5. Michrochem 950k PMMA A4 spin curve data vs. experimental data.

for the first test spin speeds but the solution was still separating and the error was still apparent in the comparison with our experimental value for the PMMA A4 spin curve. The third dilution set rendered the best results because the solution was kept continuously stirred immediately after dilution up to the spin coating of the wafer. The spin curves from all three sample sets of 4% dilution showed continuous improvement with each subsequent sample. The first dilution sample had the worst data and the last and third dilution sample gave more accurate results. Figure 6 shows the comparison of spin curves for all three 4% dilution sample sets and the experimental A4 spin curve performed in our lab. The average roughness data for all three 4% dilution spin curves was 0.31 nm. This is almost the same roughness for our experimental A4 spin curve. The average waviness for all three 4% dilution spin curves was 6.12 nm, which was well within the desired 10 nm deviation. After learning that the dilution needed to be stirred continuously, we used this dilution process for the dilution of Michrochem 950k PMMA A11 to 2% PMMA solution. We made two separate dilution sample sets of 2% PMMA. With an improved dilution process we were able to produce good data for both sample set spin curves. The average roughness data for both 2% dilution spin curves was 0.23 nm. The average waviness for both 2% dilution spin curves was 4.75 nm, which was well within the desired 10 nm deviation. Figure 7 shows the spin curves for the 2% dilutions.

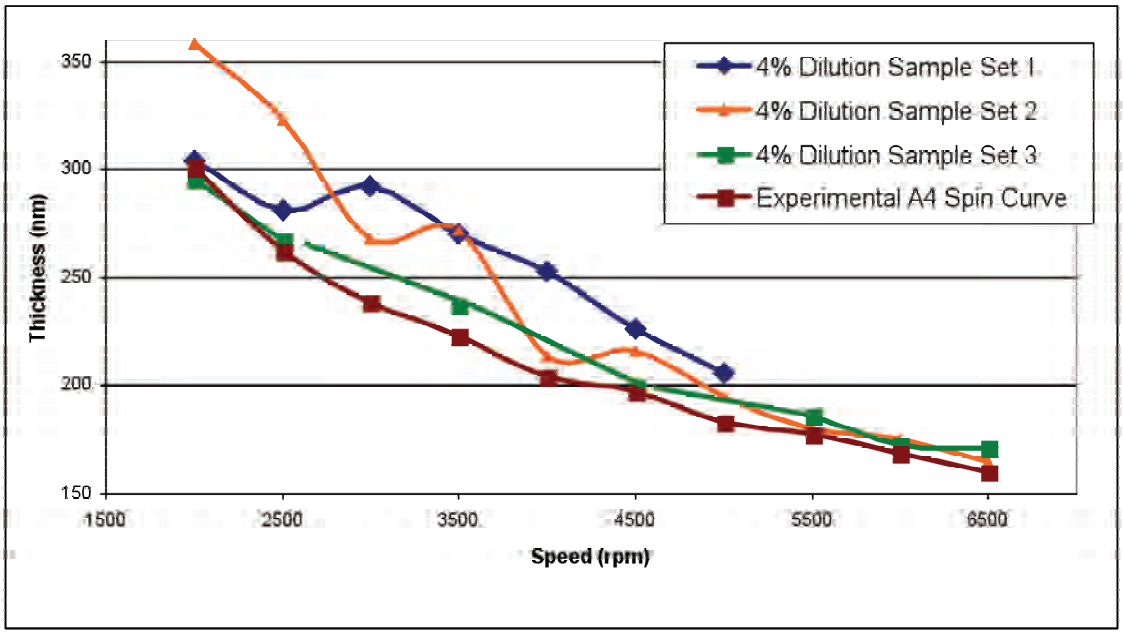

Figure 6. Spin Curves for three sample dilutions for 4% PMMA and experimental A4 spin curve.

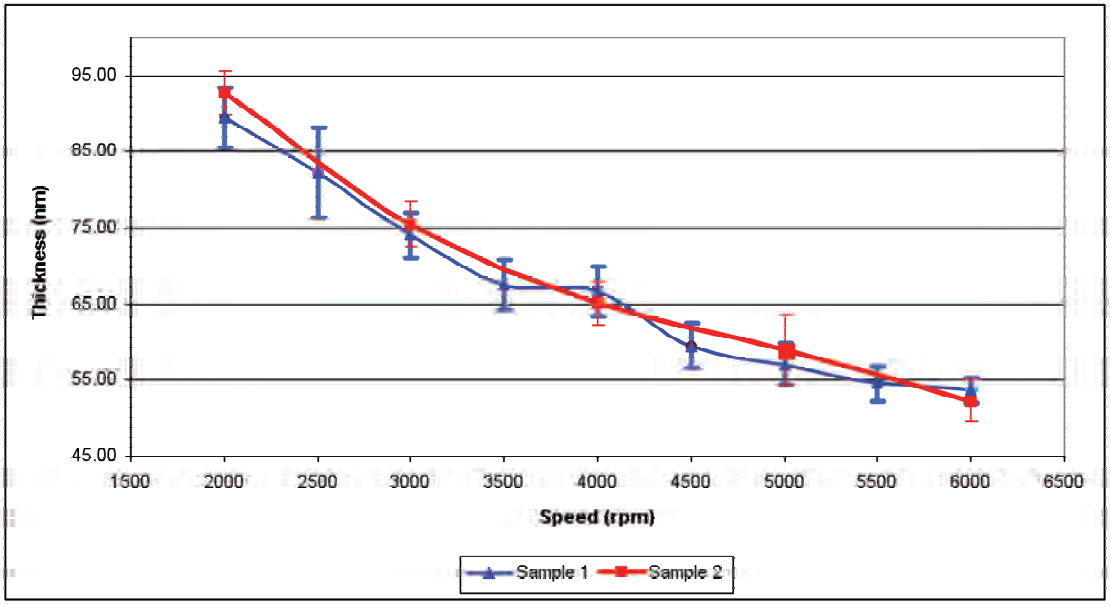

Figure 7. Spin Curves for two separate sample sets for 2% dilution.

Conclusions

From the first comparisons of the PMMA A7 and A4 spin curves we concluded that we can reproduce spin curves with accuracy and minimal errors. The improvements in controlling the environmental variables and cleaning processes in the spin coat procedures proved to be very detrimental to the rendering of reproducible processes. Throughout the entire experiment, the spin coating process was improved and made more efficient throughout all experiments. This improvement of the spin coating processes allowed for further analysis of dilutions of PMMA. The dilution process was optimized to yield better spin curves with each subsequent sample of the 4% dilution set. The use of the best dilution process in the 4% dilution test also confirmed that the 2% dilution rendered accurate data. The roughness of the polymer was consistent and minimal throughout all sample sets and thus provided minimal waviness. Waviness with all samples was within acceptable limits of deviations. Planarization was improved due to minimization of waviness factors within the spin coat process and the optimization of the dilution process. We verified that the self-prepared PMMA solutions were of high quality with reproducible results.

References

1. Sheats, James R., and Bruce W. Smith. "Resist Processing." Microlithography: Science and Technology. New York: Marcel Dekker, 1998.

2. Suzuki, Kazuaki, and Bruce W. Smith."Electron Beam Lithography." Microlithography: Science and Technology. Boca Raton: CRC, 2007.

3. Mack, Chris A., “Field Guide to Optical Lithography”, SPIE (2006); 4-5.

Acknowledgments

Funds were provided by the Center on Materials and Devices for Information Technology Research (CMDITR), an NSF Science and Technology Center No. DMR 0120967. I wish to acknowledge the NSF, STC MDITR for providing funds and the opportunity for this research. I would like to thank Dr. Robert Norwood and Oscar D. Herrera for their assistance and constant guidance throughout my research experience.

ISAAC LOPEZ is currently attending Arizona State University and hopes to graduate in May 2011 and go on to obtain a Masters and PhD in Electrical Engineering.

The Synthesis of Diamine Containing Compounds for use in OPVS

RACHAEL LUCERO, New Mexico Highlands University
Joshua Davies, Alex Jen, University of Washington

Introduction

Since the mid 1950's crystalline silicon had been used to convert solar light into useable electrical energy.[1] These solar cells are highly efficient, however they are expensive to manufacture and they cannot be mass-produced. An alternative to these cells is the organic solar cells. These cells are not as efficient as the traditional silicon cell. Currently research is being conducted on organic materials for thin layer photovoltaic cells that are completely polymer based. These cells can be mass-produced by solution processing, making it possible to use roll-to-roll technology to manufacture them. However, the organic photovoltaic cells, (OPVs), are not yet efficient enough to compete with the crystalline solar cells that currently lead the market. Organic photovoltaic cells contain both positive and negative channels. To date, positive channels have been reasonably well studied and are, according to Wei et al., highly developed.[2] For this reason this research is focused on the negative type channels. 4(1,3-dihydro-2,3-dihydro-1H-benzoimidazol-2-yl)phenyl)dimethylaine (N-DMBI) is currently being used in the research because it has been found to be more effective in conducting charge than zinc oxide, which is currently used in OPV cells to compete with crystalline silicon.

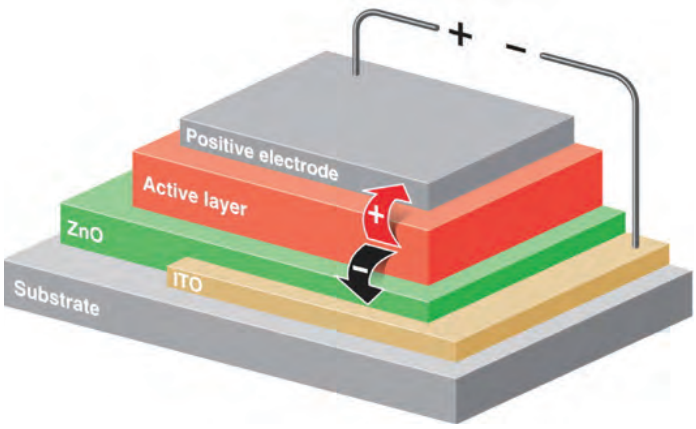

Figure 1. This is a representation of an inverted OPV cell. This research was focused on finding a replacement for the zinc oxide layer that has a better conductivity.[3]

Experimental

N, N'-di (p-toluenesulufonyl)-o-phenylenediamine (1)

In a 200 mL round bottom flask equipped with a stir bar we dissolved TsCl (19.51 g 0.1023 mol) in pyridine (50 mL). After the TsCl was completely dissolved, 1,2-phenylenediamine (diamine, 5.4 g 0.0499 mol) was added to the solution. The reaction was then refluxed with a water-cooled condenser and stirred for about 18 h with an oil bath temperature of 100 ºC. An orange solid precipitated out. The solids then re-crystallized from ethanol. The white solids that had precipitated out of the solution were washed with ethanol and placed in the freezer.

N,N'-dimethyl-N,N'-di(p-toluenesulufonyl)-o-phenylenediamine (2)

In a 200 mL three necked round bottom flask equipped with a stir bar the diamine (7.15 g, 0.0171 mol) was stirred with acetonitrile (100 mL) for about 5 min. Then dry potassium carbonate (9.4 g 0.0686 mol) was added and this was allowed to stir for about an hour at room temperature. Next, MeI (3.21 mL, 0.0515 mol) was added drop wise while the reaction was stirring in an ice water bath. The reaction was allowed to stir for five minutes in the ice bath. Then it was allowed to come to room temperature while stirring for an hour. The reaction was then heated to reflux with a water-cooled condenser and was stirred for 16 h. The reaction was then taken off the heat and allowed to cool to room temperature. It was then transferred into a single neck round bottom flask and the acetonitrile was rotovaped off. The solids that were left behind were washed with distilled water (150 mL). The water was then washed with DCM (4x100). The DCM was then dried over Na_2SO_4. The DCM was then rotovaped off. The remaining solids were then recrystallized in 200 proof EtOH (50 mL) and ethyl acetate (20 mL).

N,N'-dimethyl-o-phenylenediamine

In a 200 mL three neck round bottom flask equipped with a stir bar diamine (7 g) was stirred in H_2SO_4 (10 mL) and H_2O (1 mL). This reaction was stirred for three hours with an oil bath of 85 ºC. After three hours a TLC was done to check the progress of the reaction. This showed that it was done. The reaction was then worked up. The reaction was allowed to stir at room temperature for an hour. Then the reaction was poured into ice (75 mL) and NaOH until the reaction was neutral. This was then washed with diethyl ether and the wash was then dried over Na_2SO_4 and was then rotovaped down and placed on the high vacuum for an hour and then it was placed under nitrogen.

(4(1,3-dimethyl-2,3-dihydro-1H-benzoimidazol-2-yl)phenyl)dimethylaine

In a 50 mL three neck round bottom flask equipped with a stir bar and a dean-stark trap with a water-cooled condenser, diamine (0.200 g, 0.00465 mol) was stirred in benzene with camphorsulfonic acid (0.0171 g) and aldehyde (0.219 g, 0.0466 mol). The reaction was heated at reflux for 24 h. The reaction was allowed to come to room temperature, then washed with 5% NaOH. It was then rotovaped down. The solids were re-crystallized in 200 proof EtOH. They were washed with ice-cold methanol.

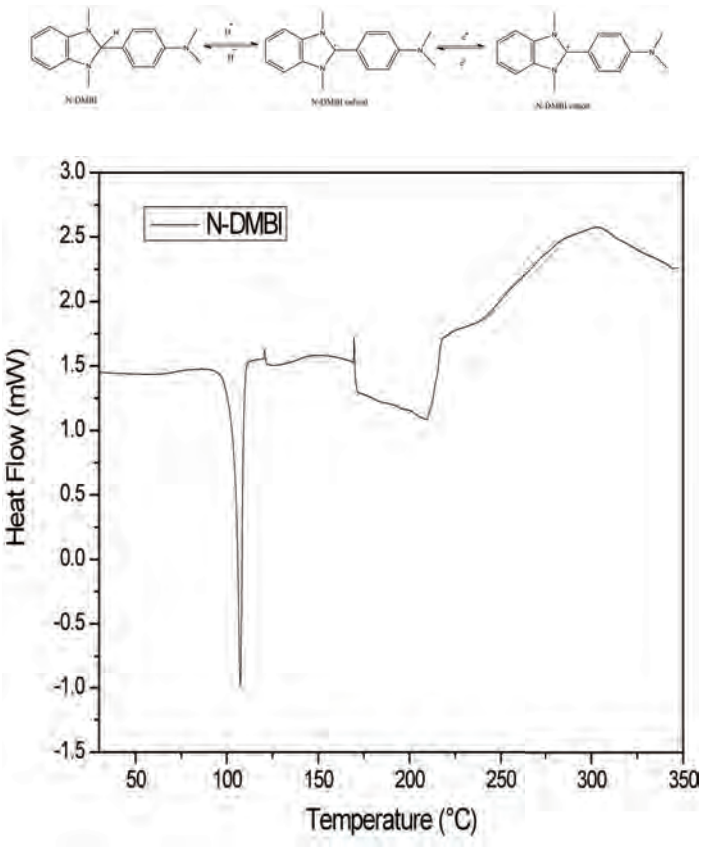

Figure 2. DSC spectra of N-DMBI.

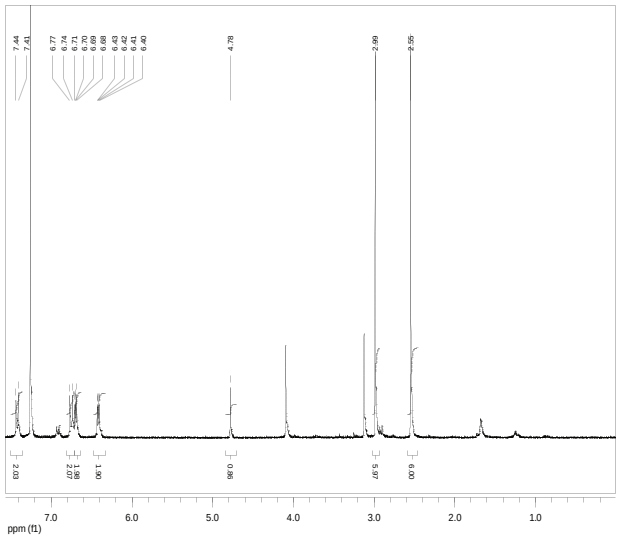

Figure 3. NMR of N-DMBI.

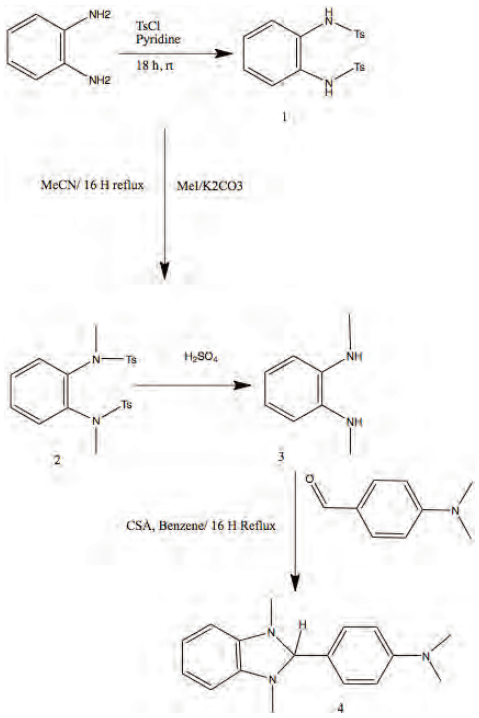

Figure 4. Reaction scheme of N-DMBI.

Results and Discussion

Product 1 two different types of product were obtained in high yields. Product 2 was in crystal form and again was pure product as shown by TLC and NMR. TLC was also used to follow this reaction and NMR was used to verify that the product was the product that was wanted. The yields again were high. Product 3 was produced as a crude product without purification. Neither NMR nor Mass Spectroscopy was used because it was found that this product degrades rapidly in air and light. Product 4 was more difficult than expected. This product seemed also to be air, light and heat sensitive. The only means of pushing it forward was the use of a Lewis acid catalyst. Literature had reported the use of acetic acid, however it was found that this did not work very well. We made product but it would degrade before the reaction was complete. A different catalyst was used along with a dean-stark trap. This seemed to prevent the product from degrading when more products were being made. By TLC the reaction had still not reached completion but it was worked for fear that the product would began degrading. An NMR was taken to confirm the crystals were the product that was wanted, after which DSC testing was done on the crystals. This testing showed that N-DMBI did in fact dope PCBM.

Conclusions

The OPV cell is preferred to traditional cells because it can be mass-produced and solution processed, meaning that they can be fabricated using roll-to-roll technologies. The synthesis of NDMBI is don't in four steps in which all have been synthesized with overall good yields. N-DMBI is currently being tested as an n-dopant for PCBM. Organic field transistor electron mobility and OPV device testing are currently underway in order to access its's ability to be a highly efficient electron transport layer.

Future work

Currently there is still work that needs to be done on N-DMBI. This includes testing its n-doping abilities on PCBM in photovoltaic cells as a replacement for zinc oxide. Depending on these results, another derivative may be needed for OPVs, possible one with higher enthalpy.

References

1. Wikipedia. Solar cell. http://enwikipedia.org/wiki/solar_cell. 2010.

2. Wei, P.; Oh, J. H.; Dong, G; Boa, Z. J. Am. Chem. Soc. 2010, 132, 8852.

3. Shaheen, S. E.; Kopidakis, N; Ginley, D.S; White,M.S and Olson, D. C. SPIE, 2007http://spie.org/x14269.xmlarticleID=x14269.

Other references

1. Brunet, P.; Wuest, J. D.; Can. J., Chem. 1996, 74, 689.

2. Hasegawa, E; Seida, T.; Chiba, N.; Takahashi, T.; and Ikeda, H., J. Org. Chem. 2005, 70, 9632.

3. Zhu, X; Zhang, M; Yu, A.; Wang, C.; and Chen, J., J. Am. Chem. Soc. 2008, 130, 2501.

RACHAEL LUCERO is a junior at New Mexico Highlands University, where she is researching therapeutic applications of light-sensitive materials. She plans to attend medical school after completing her undergraduate degrees in chemistry and biology.

Give Me an "e⁻!": Creating Ambipolar Donor-Acceptor Oligomers

KENNETH LYONS, JR., Morehouse College
Lauren Hayden, Seth Marder, Georgia Institute of Technology

Introduction

Today electronics are both prolific and important. One encounters electronic devices in every facet of daily life. While most gadgets are useful in their current incarnation, there is a desire to expand their area of application. Within many electronic components is the inorganic semiconductor, silicon. Though this semiconductor has performed well up to this point, it has limitations.[1] Thus it may prove valuable to evaluate the potential of organic semiconductors within electronic devices.

Some potential advantages of using organic semiconductors are a lowered cost due to simpler fabrication techniques and the compatibility with multiple modes of processing.[2] These materials may also be useful for projects that take up a large (physical) area or those applications requiring flexible electronics.[1] To make these dreams of organic electronics possible, one viable starting point would be the transistor, a key component in many electronics. Transistors are devices that amplify current and can be used as a switch.[3] Currently much work is being done to create an organic analog of a silicon-based field-effect transistor. Since transistors are so abundant in electronics, organic field-effect transistors (OFETs) have the potential to become a primary component in flexible, inexpensive electronics.[4]

The heart of OFET research lies in producing efficient organic semiconductors. The majority of attempts to make organic semiconductors have resulted in materials that are hole transporting and work to make p-type OFETs.[4] P-type materials move holes (the absence of electrons) from the electrode into the highest occupied molecular orbital (HOMO) of the material.[1] N-type materials accept electrons from the electrode into the lowest unoccupied molecular orbital (LUMO) of the material; this type of material is difficult to design due to a few major problems. The metals that would work well as the electrodes of n-type transistors (i.e. calcium or lithium) and also the charge carriers themselves readily oxidize when exposed to water or oxygen.[1]

A third type of material is the ambipolar material. An ambipolar material is able to function in both a p-type and n-type device. One proposed solution is to decrease the band gap to allow for injection of both charges from the electrodes into either the HOMO or LUMO. One method to achieve a low band gap is to create an oligomer that has a repeating series of electron- donating and electron-accepting units as shown in Figure 1.[5] Previously dithieno[3,2-b:2',3'-d]pyrrole (DTP), a strong electron donor, and benzo[c][2,1,3] thiadiazole (BTD), an electron acceptor, were used. After studying this class of materials, only hole (p-type) mobility was observed (see Figure 2).[6]

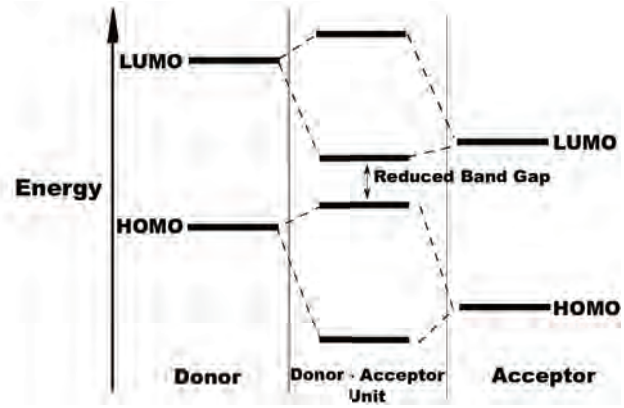

Figure 1. A relatively low band gap may be achieved by forming an oligomers using a donor and an acceptor groups.[5]

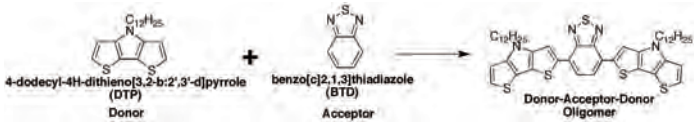

Figure 2. Previously a donor acceptor oligomer was created. It was not ambipolar, but rather only p-type.[6]

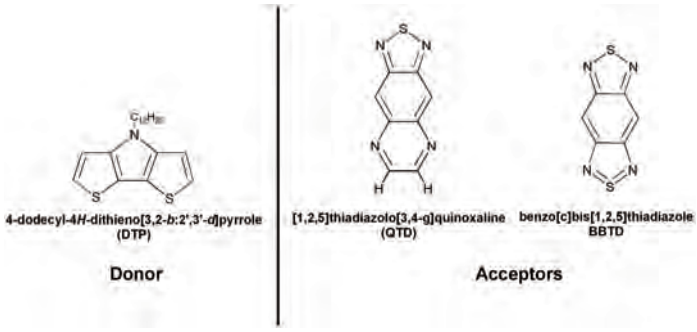

Figure 3. Two new donor-acceptor oligomers will be synthesized using two new acceptors, QTD and BBTD.

The next stage of the research looks to make oligomers using stronger acceptors, [1,2,5]thiadiazolo[3,4-g]quinoxaline (QTD) and benzo[c] bis[1,2,5]thiadiazole (BBTD), with donor DTP to produce a material that has a low enough band gap to allow for ambipolar charge injection. The BBTD showing in Figure 3 is a stronger acceptor than QTD, similarly QTD is stronger than BTD. Making oligomers involving these acceptors of various strengths may allow a trend to be established.

The focus of this research is to produce the two donor-acceptor oligomers, benzo[c]bis[1,2,5]thiadiazole - dithieno[3,2-b:2',3'-d] pyrrole (BBTD-DTP) and [1,2,5]thiadiazolo[3,4-g]quinoxaline - dithieno[3,2-b:2',3'-d]pyrrole (QTD-DTP). Upon synthesizing these compounds, they will be thoroughly characterized in order to fully understand what was created. The compounds' semiconducting properties will then be analyzed.

Experimental

To create the two target molecules, a series of reactions were carried out (see Figure 4). The initial goal was to create a stock of starting material from which the target molecules could be synthesized. Through previously done work by Kristen Brown, a stock of 4,7-dibromobenzo[c][1,2,5]thiadiazole has been prepared. Hence work was done to nitrate the compound and proceed through the rest of the reaction scheme. The compounds from each reaction were purified through column chromatography and recrystallization methods. To insure that the desired material was created, all new products were subjected to full synthetic characterization including: ^{1}H NMR, ^{13}C NMR, high-resolution mass spectrometry (HRMS), and elemental analysis (EA). Additional experiments will be performed to study the optical, electrochemical, and thermal properties. Ultimately, the new oligomers will be sent to the Kippelen Group for device measurements.

Results

A large amount of brominated-BTD (**1**) was recrystallized from previously made material (59% recovered). Using a protocol based on the work of Uno, et. al., the brominated benzothiadiazole (BTD) is believed to have been nitrated (**2**).[7] A glittery pale yellow powder in a 10% yield was obtained. The addition of the dithienopyrrole (DTP) groups involved two immediate sequential steps (**3**).[8] A deep blue, inky solid was obtained with a 38% yield. ^{1}HNMR, ^{13}CNMR, HRMS and EA were taken to analyze the blue product. It was observed that compound **3** was pure by ^{1}HNMR (Figure 5), ^{13}CNMR, and HRMS spectra that were reasonable clean and a mass spectrum that was also clean. Compound **3** nearly passed elemental analysis. The difference between the calculated and found amounts of each element was 0.44 when the goal was a difference of 0.40.

The reduction of compound **3** gave (65% yield) a reddish brown solid that was initially characterized by ^{1}HNMR (see Figure 6), ^{13}CNMR, HRMS and EA (**4**). Similar to compound **3**, clean NMR and mass spectra resulted. This compound did not pass elemental analysis having a difference of 0.46. Synthesis of compound **5b** was begun. A greenish-black oil resulted from the reaction. Attempts were made to purify this compound though column chromatography.

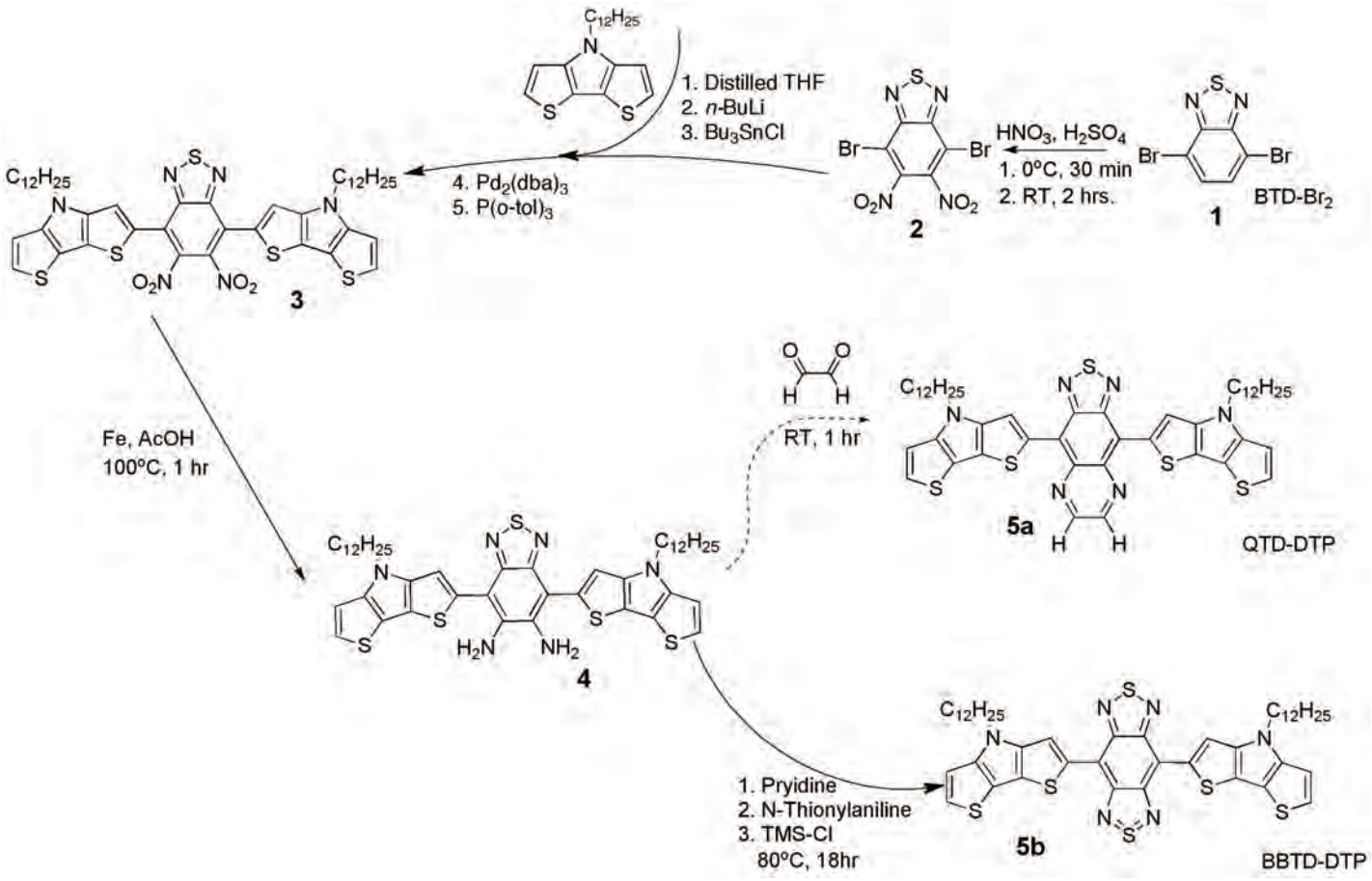

Figure 4. Overall reaction scheme to synthesize donor-acceptor oligmers, BBTD-DTP and QTD-DTP.

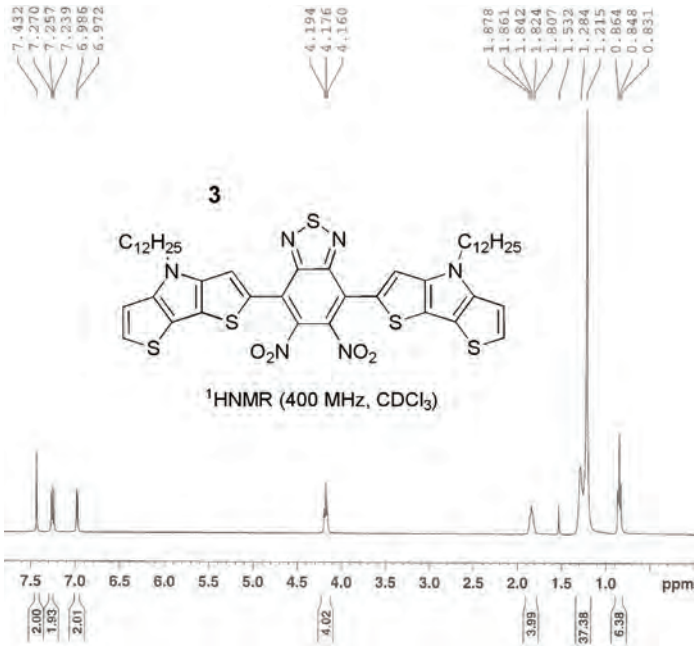

Figure 5. ^{1}HNMR of compound **3**. Though fairly pure, there are small peaks suggesting impurity.

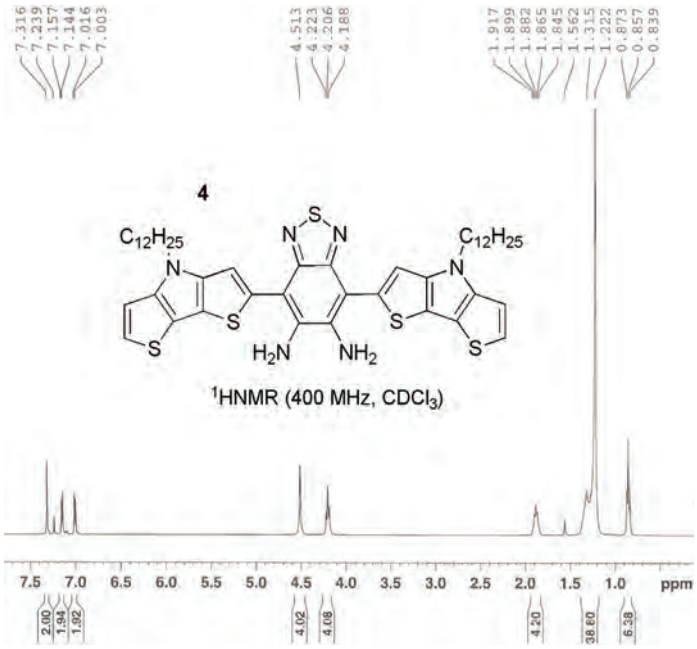

Figure 6. ^{1}HNMR of compound **4**. Though fairly pure, there are small peaks suggesting impurity.

Discussion

The nitration of the brominated BTD had a low percent yield, however this was also seen in the literature. Using a similar method, a yield of 20% was observed.[7]

It was observed that compounds **3** and **4** dissolve readily in dichloromethane and also chloroform. Due to the presence of the amine groups, it was thought that compound **4** might be susceptible to oxidation in the presence of both heat and light. Therefore, compound **4** was given very minimal exposure to both light and heat where possible.

Conclusion

Two compounds (**3** and **4**) are key to the formation of the target molecules (**5a** and **5b**), which were successfully synthesized and characterized. This helped to establish a pathway for generating the target compounds.

References

1. Mas-Torrent, M.; et. al. Chem. Soc. Rev., 2008, 37, 613-872.
2. Murphy, A.; et. al. Chem. Rev., 2007, 107, 1066-1096.
3. http://www.kpsec.freeuk.com/components/tran.htm
4. Zaumseil, J.; et. al. Chem. Rev., 2007, 107, 1296-1323.
5. van Mullekom, H.; et. al. Mat. Sci. and Eng., 2001, 32, 1-40.
6. Lauren Hayden's Semiannual Report, 9/6/09.
7. Uno, T.; et. al. Chem. Pharm. Bull., 1980, 28, 1909-1912.
8. Lauren Hayden's Notebook II-108-109.

Acknowledgements

Funding for this research were provided by the Center on Materials and Devices for Information Technology Research (CMDITR), an NSF Science and Technology Center No. DMR 0120967. The author would also like to thank: Lauren Hayden for her seemingly infinite patience, Dr. Seth Marder and the Marder group at large for their assistance, and Dr. Brian Lawrence for helping to open the door to this opportunity.

KENNETH LYONS, JR. is a senior Chemistry major at Morehouse College in Atlanta, GA. Though interested in science, he is unsure in what direction he will proceed post-commencement.

Single-Molecule Fluorescence Spectroscopy of Colloidal Manganese Doped ZnSe/ZnS Quantum Dots

AN T. M. NGUYEN, Highline Community College
Eric D. Bott, Philip J. Reid, University of Washington

Introduction

Since its initial development, the incorporation of transition metal ions into cationic sites (doping) of semiconductor nanocrystals, also termed quantum dots (QDs), has unearthed a host of fascinating photophysical phenomena. Doped QDs have been proposed for use in solar cells, optical sensors, light-emitting diodes (LEDs), lasers, bioimaging, and in these and more, areas that wish to exploit or control their photoluminescent properties. It is therefore becoming increasingly important to study the critical role of doping in the luminescence of doped QDs.

At the same time, luminescence intermittency, also known as blinking and an intrinsic characteristic of QD luminescence, threatens to compromise their usefulness as single photon sources. Blinking is characterized by the observation that under continuous photoexcitation (e.g. by a laser), a single QD will fluctuate between light-emitting "on" periods and dark, non-emissive "off" periods.[1,2] A better understanding of the mechanism behind QD blinking is highly valued in progress towards greater control over QD luminescence and perhaps even towards non-blinking QDs.

Single-molecule microscopy and spectroscopy (SMS) now makes it possible for scientists to probe the behavior of individual QDs. By avoiding the effects of ensemble averaging, SMS studies increasingly guarantee the direct observation of properties of single QDs and have great potential to uncover information that is typically lost on the ensemble level.

In this study, we use SMS to investigate the photoluminescence (PL) decay kinetics of manganese doped ZnSe/ZnS core/shell QDs (Mn^{2+}:ZnSe/ZnS). In these doped QDs, exitonic luminescence is quenched via efficient energy transfer to manganese-related excited states that reside within the bandgap of the host QD, (see Figure 1).[3]

The high PL quantum yield of this transition has attracted considerable attention to Mn^{2+} as a dopant. Additionally, ZnSe QDs have shown potential to replace commonplace cadmium selenide QDs as a low-toxic alternative in biological applications.[4] Core/shell QDs like ZnSe/ZnS in which the bandgap of the shell material is larger than that of the core have also been shown to exhibit enhanced resistance to photobleaching and improved PL quantum yield.[5] This has been largely attributed to the passivation of surface trap states and the spatial confinement of excitons to the core region upon the addition of an inorganic shell layer.[6] High quantum yields and high photostability make Mn^{2+}:ZnSe/ZnS QDs attractive not only for SMS but also for application in new systems and devices.

In this study, we demonstrate the use of SMS to observe PL intensity fluctuations indicative of blinking in single Mn^{2+}:ZnSe/ZnS QDs and present time-correlated single-photon counting (TCSPC) fluorescence lifetime decay data for individual QDs. We propose that the observed variation in PL intensity with time, evidence for spectral diffusion, relatively short fluorescence lifetimes, and non-single exponential PL decay all point towards interesting time-dependent decay kinetics for these QDs.

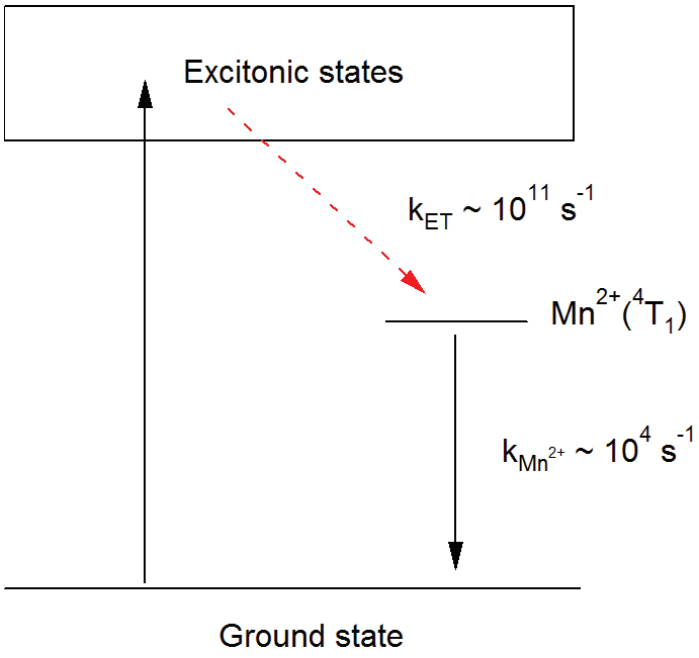

Figure 1. Three-level energy diagram illustrating manganese related decay kinetics in Mn^{2+}:ZnSe/ZnS QDs. k_{ET} describes the rate constant for the nonradiative energy transfer from the host QD to Mn^{2+}.

Methods

Mn^{2+}:ZnSe/ZnS QDs surface-capped with trioctylphosphine (TOP) and oleylamine were synthesized by the Gamelin research group at the University of Washington using previously established methods.

Samples were prepared for detection at the single-molecule level by drop casting a solution of QDs in toluene (99.8%, Fischer) onto glass coverslips.

A home-built diffraction limited confocal scanning microscope was used to constructQD fluorescence images. Figure 2 illustrates the

confocal microscope setup.

Laser excitation was provided by a 470 nm pulsed laser diode pumped at 40 MHz and powered at 6.00 mW (PDL 800-B, Picoquant). The excitation wavelength was attenuated by a filter and half-wave plate and subsequently coupled into the optical path by a dichroic mirror. An inverted 100x oil-immersion objective (1.40 NA, Nikon) was used to both focus the laser light into a diffraction limited spot at the focal plane in the sample and collect QD emission. A 420 nm long-pass (LP) filter was employed to filter out laser light from the back-collected emission, which was then separated at 600 nm between two avalanche photodiode detectors (APDs) by a 600 nm LP dichroic mirror.

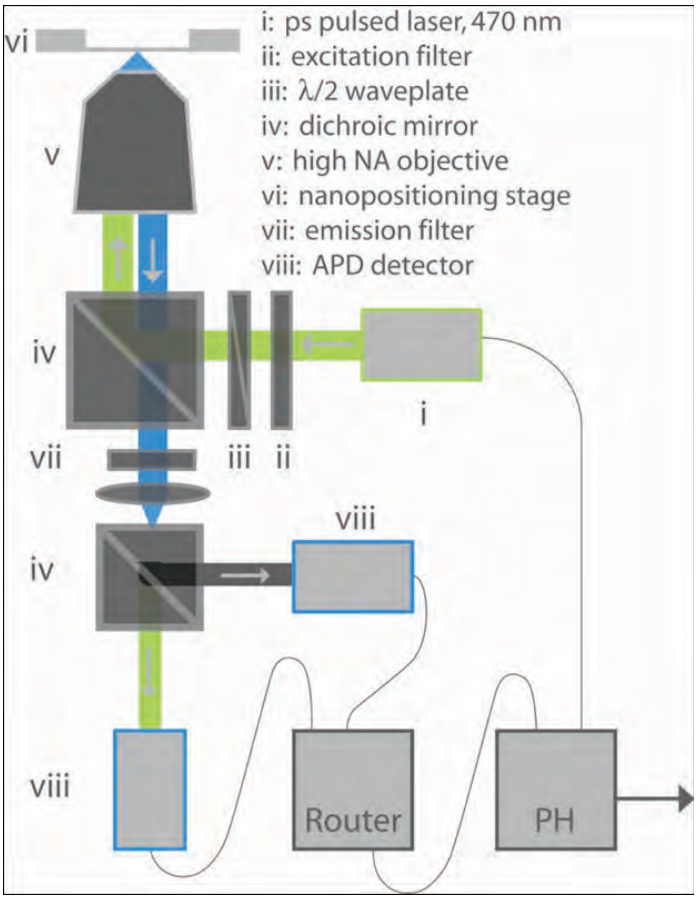

Figure 2. Schematic of the confocal microscope used to obtain QD fluorescence images.[7]

QD fluorescence images were monitored and displayed in a LabVIEW-based software suite previously developed by the Reid group. Scans were constructed in pairs (one per APD detector) on a point by point basis by raster scanning the excitation area and integrating at 100 ms time bins. QD emission is split at 600 nm between the two resulting images so that one image displays PL <600 nm while the other displays PL >600 nm. The QDs themselves are noticeable as bright features by the magnitude of their emission, as shown in Figure 3.

Once fluorescence images were obtained, single QDs could be isolated. Emission intensity time traces and fluorescence lifetime measurements for single QDs were subsequently carried out using

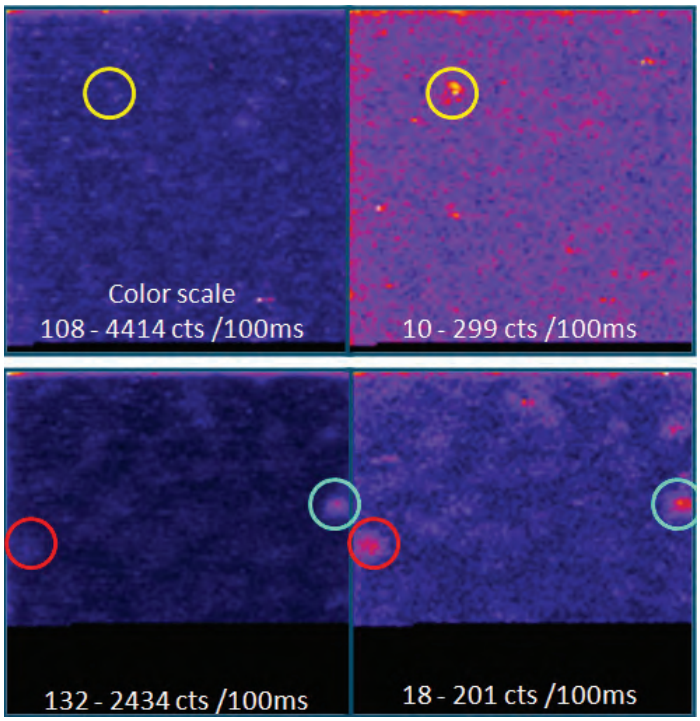

a time-tagged time-resolved (TTTR) time-correlated single-photon counting instrument (PicoHarp 300, Picoquant).

Figure 3. Pairs of 10x10 µm scans integrated at 100 ms time bins are shown in false-color. Paired images represent the same excitation area with the left scan displaying <600 nm PL and the right scan displaying >600 nm PL. A single QD's location is highlighted twice as denoted by color.

Results and Discussion

Evidence for Spectral Diffusion

The bulk emission and absorption profile for Mn^{2+}:ZnSe/ZnS QDs, shown in Figure 4, suggests a fairly even distribution of luminescence intensity above and below 600 nm. In contrast, by strategically separating QD emission at 600 nm on the single-molecule level, significant discrepancy between paired QD fluorescence images is observed. All three QDs shown in Figure 3 exemplify this and exhibit uneven distribution of emission intensity above and below 600 nm. This is qualitatively observed as the unequal brightness of the QD between the pair images it was found on. This deviation from bulk observations suggests evidence for spectral diffusion.

PL Intensity Fluctuations

Emission intensity time traces were collected for single Mn^{2+}:ZnSe/ZnS QDs and graphed on semi-log plots of PL intensity in counts per 100 ms time bins as a function of time in seconds, as shown in Figure 5.

Fluorescence intensity time traces exhibit distinct variation in emission intensity with time indicative of blinking in single Mn^{2+}:ZnSe/ZnS QDs. Compared with earlier observations of blinking in undoped QDs,[8] the process of doping with Mn^{2+} induces much more dynamic blinking behavior characterized by the presence of many intermediate intensity states. Further research is needed to continue to explore the root cause of these intermediate intensity states, which may be

related to the internal relaxation pathways introduced upon doping (Figure 1).

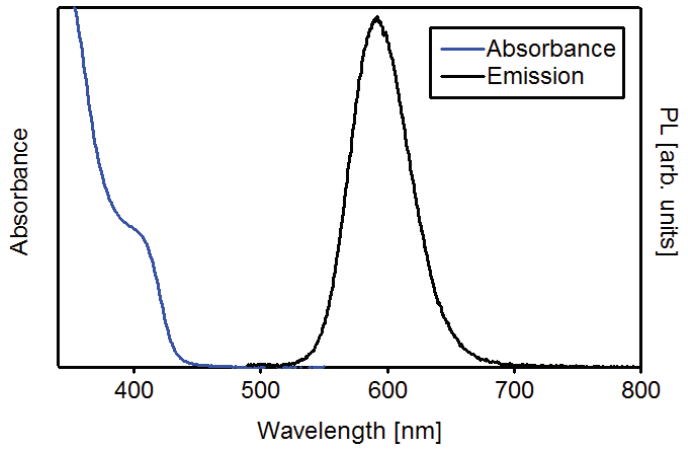

Figure 4. Bulk Mn^{2+}:ZnSe/ZnS absorption/emission spectra. Emission band centered at ~600 nm is attributed to the Mn^{2+} dopant luminescence portrayed in Figure 1.

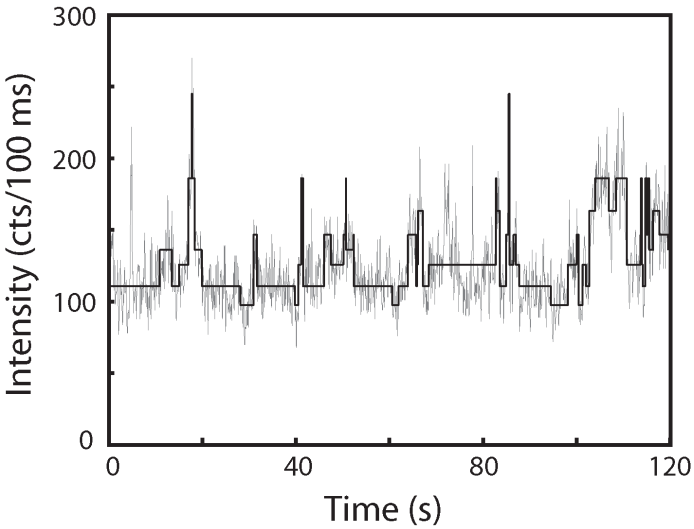

Figure 5. Fluorescence intensity time trace taken from a single Mn^{2+}:ZnSe/ZnS QD shows variation in emission intensity.

TCSPC Fluorescence Lifetime Decay

Fluorescence lifetime decay curves were constructed for single Mn^{2+}:ZnSe/ZnS QDs isolated from confocal microscopy and graphed on semi-log plots of intensity as a function of time in nanoseconds, as shown in Figure 6.

The instrumental response function (IRF) is graphed in red. The decay histogram itself (gray) is fitted to a stretched exponential function (black) of the form:

$$f \propto e^{(-t/\tau_{KWW})^{\beta}} \qquad (1)$$

τ_{KWW} represents the Kohlrausch, Williams, and Watts characteristic relaxation time,[8] while the β parameter quantifies the exponential character of the PL decay. β takes on values between 0 and 1 with $\beta = 1$ representing pure single exponential decay.[9] τ_C denotes the characteristic excited state lifetime and is a convolution of τ_{KWW} and β by the following equation:

$$\tau_c = \frac{\tau_{KWW}}{\beta}\Gamma\left(\frac{1}{\beta}\right) \qquad (2)$$

where $\Gamma(x)$ denotes the gamma function.

PL decay curves show stretched, non-single exponential PL decay in Mn^{2+}:ZnSe/ZnS QDs. The characteristic excited state lifetime for manganese luminescence (Figure 1) was measured to be ~1 ns. This is noticeably fast PL decay relative to undoped quantum dots where bandgap emission typically spans ~10-100 ns. In comparison, manganese doped QD PL has been measured to be almost two orders of magnitude faster.

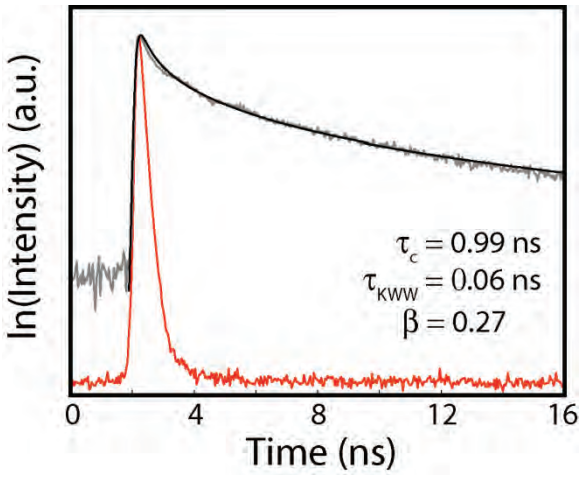

Figure 6. TCSPC fluorescence lifetime decay histogram for a Mn^{2+}:ZnSe/ZnS is fitted to Equation 1 and exhibits stretched exponential decay. a.u. = arbitrary units.

Conclusions

Initial evidence for spectral diffusion, dopant-influenced blinking behavior, non-single exponential PL, and markedly short fluorescence lifetimes relative to undoped QDs all point towards interesting time-dependent PL decay kinetics in Mn^{2+}:ZnSe/ZnS QDs.

Further research is needed to continue to explore the photophysics specific to these QDs and is attractive for their use in future applications, especially those that wish to exploit or control their luminescent properties.

With the ability to probe the behavior of individual nanoparticles, single-molecule spectroscopy will undoubtedly continue to be an important tool in the effort to shed light on the decay kinetics of Mn^{2+}:ZnSe/ZnS QD photoluminescence.

References

1. Cichos, F.; von Borczyskowski, C.; Orrit, M., Curr. Opin. Coll. Inter. Sci. 2007, 12, 272–284.

2. Frantsuzov, P.; Kuno, M.; Janko, B.; Marcus, R. A., Nat. Phys. 2008, 4, 519-522.

3. Beaulac, R.; Archer, P. I.; Gamelin, D. R., J. Solid State Chem. 2008, 181, 1582-1589.

4. Pradhan N.; Goorskey, D.; Thessing, J.; Peng, X., J. Am. Chem. Soc. 2005, 127, 17586-17587.

5. Nikesh, V. V.; Mahamuni, S.; Semicond. Sci. Technol. 2001, 16, 687-690.

6. Reiss, P.; Protiere M.; Li, L.; Small, J., 2009, 2, 154-168.

7. Figure provided by Eric D. Bott of the Reid Group.

8. Berberan-Santos, M. N.; Bodunov, E. N.; Valeur, B., Chem. Phys. 2005, 315, 171-182.

9. Fischer, B. R.; Eisler, H. J.; Stott, N.E.; Bawendi, M. G., J. Phys. Chem. B. 2004, 108, 143-148.

Acknowledgements

Financial support for this research was provided by the Center on Materials and Devices for Information Technology Research (CMDITR), an NSF Science and Technology Center, No. DMR 0120967. We graciously thank Prof. Daniel R. Gamelin and the Gamelin group at the University of Washington for providing the quantum dots used in this study and for many valuable discussions. An would also like to thank the Hooked on Photonics REU Program staff, Prof. Philip J. Reid, Eric D. Bott, and the Reid group for their continual guidance and support throughout this project.

AN T.M. NGUYEN is currently a Bioengineering major at the University of Washington. She thanks the Hooked on Photonics REU Program for providing her a first-hand glimpse at the world of scientific research, which has inspired her to continue her venture into undergraduate research and pursue graduate studies in Bioengineering after the completion of her undergraduate degree. She aspires to one day become a research scientist in the field of biotechnology.

The Effect of Atom Size on Electronic Properties of Organic Semiconductors for N-Channel Field Effect Transistors

THOMAS PURCELL, New York University
Yulia Getmanenko, Seth R. Marder, Georgia Institute of Technology

Introduction

Organic semiconductor materials are being explored to replace their inorganic counterparts in certain areas. Due to organic semiconductor's potential to be deposited on plastics at low temperature through solution-based printing, devices can be less costly to produce than those from inorganic materials. The cost effectiveness, the flexibility, and the large coverage area are benefits involved in using organic semiconductors, but they will not replace silicon where high speeds and density are needed.[1]

The development of electron transporting semiconductors is currently lagging behind that of hole transporting materials. The further development of electron transporting materials is necessary because in order to have an efficient circuit both p-channel and n-channel organic field effect transistors (OFETs) need to be used.[2] An OFET is comprised of a source and drain contact, a gate, a dielectric and a semiconductor material. When a large enough voltage is applied to the gate it produces an electric field which changes the electronic characteristics of the semiconductor allowing for more current to pass through it from the source contact to the drain contact.[2] A main problem that needs to be solved for the effective use of n-channel OFETs is air stability. Many n-type materials can be oxidized by oxygen or water under OFET operation, making devices unstable in ambient conditions. It has been shown that a semiconductor with the first half-wave reduction potential more positive than -0.40 V vs. SCE might produce a device that shows little degradation under ambient conditions.[3] The focus of the research is to see the effect of substitution of S with Se on the electronic properties of the electron transporting material. One way to test the impact of the atomic radius is to create the same thiophene and selenophene derivatives and test their electronic properties. Since there have not been reports on the effectiveness of dithieno[3,2-b:2',3'-d]pyrroles and diselenopheno[3,2-b:2',3'-d]pyrroles for electron-transporting materials, part of the research will be done to test the viability of these cores for n-channel OFET.

Experimental

Rasmussen et al. work[4] on dithieno[3,2-b:2',3'-d]pyrroles (DTP) showed a surprising result when DTP was reacted with tetracyanoethene (TCNE).[3] The first two species were mono-tricyanovinyl-DTP and bis-tricyanovvinyl-DTP, which were expected. The surprising one was a dicyano-methylene-capped quinodial species of DTP. This was unprecedented for direct TCNE addition to unsubstituted oligomers. The addition of the tricyanovvinyl group(s) gives them interesting electronic properties as the band gaps for all three of them are less when compared to DTP by itself and LUMO's were much more stable. The data presented on redox and solid state properties also suggest that these molecules will be good candidates for examination in n-channel OFETs.[4]

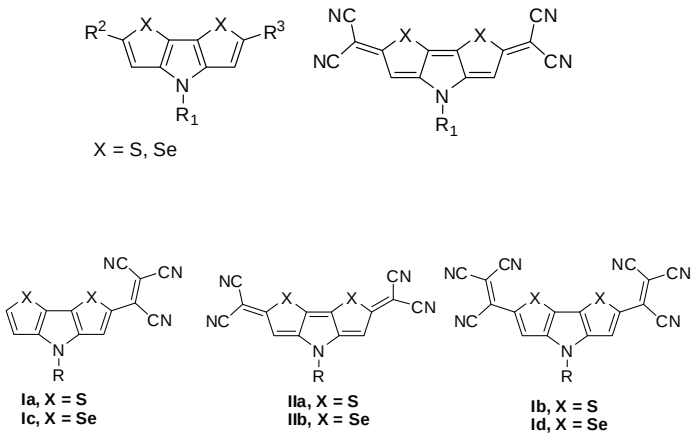

Figure 1. Target molecules.

The key intermediates for the preparation of dithiopheno(diseleno) pyrroles, 3,3'-dibromo-5,5'-bis-trimethylsilyl-2,2'-bithiophene and 3,3'-dibromo-5,5'-bis-trimethylsilyl-2,2'-biselenophene are prepared from 2-bromo-5-trimethylsilyl-thiophene or 2-bromo-5-trimethylsilyl-selenophene respectively by a sequence of the base-catalyzed halogen dance reaction and $CuCl_2$-promoted oxidative coupling.[5] A pyrrole ring is then formed by Pd-catalyzed reaction of the corresponding dibromides with an amine. Finally the TMS groups are removed from the molecule and dithieno- and diselenopheno-pyrroles are reacted with excess of tetracyanoethene (TCNE).

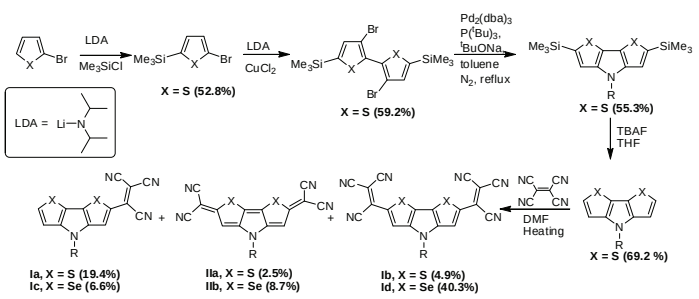

Scheme 1. Preparation of Dithieno[3,2-b:2',3'-d]pyrrole and diselenopheno[3,2-b:2',3'-d] pyrrole and their reactions with Tetracyanoethene.

Once the final products are synthesized, ^{1}H NMR, ^{13}C NMR, high resolution mass spectroscopy (HRMS) and elemental analysis will be performed to determine the structure and purity of the products. After that cyclic voltammetry (CV) and UV-vis absorption spectroscopy will be performed to determine the electronic properties of the materials. Once these properties are determined then the materials should be transferred to the Kippelen group at the Georgia Institute of Technology to fabricate OFET devices.

Experimental

2-Bromo-5-trimethylsilyl-thiophene (1)

2-Bromothiophene (375.1 mmol, 61.159 g,) was dissolved in THF (375 mL) and lithium diisoproplyamide (LDA) (1.4 M in hexanes-THF, 335 mmol, 239.3 mL) was added dropwise at -78 °C. After stirring the reaction for 55 minutes, trimethylsilyl chloride (358 mmol, 38.85 g) was added dropwise. The mixture was stirred overnight, treated with water (100 mL) and the organic layer was separated. The aqueous phase was extracted with hexanes (25 mL, then 15 mL and 15 mL), and combined organic phases were dried over $MgSO_4$. The drying agent was removed by filtration and the filtrate was evaporated on a rotary evaporator. The final product 2-bromo-5-trimethylsilyl-thiophene was separated from the byproducts by the vacuum distillation at 40 °C and 1.2 mm Hg. The product was obtained as yellow oil (44.75 g). GC/MS indicated that the product was 92.91% pure with the expected molecular ion of 236 g/mol. Given the 92.91% purity the percent yield was 52.76%.

3,3'-Dibromo-5,5'-bis-trimethylsilyl-2,2'-bithiophene (2)

2-Bromo-5-trimethylsilylthiophene (**1**) (22.526 g, 95.757 mmol) was dissolved in anhydrous THF (200 mL) under nitrogen atmosphere and cooled in an acetone and CO_2 bath. LDA (1.08 M in hexanes-THF, 115 mmol, 106 mL) was added dropwise to the solution. The reaction was monitored for completion by GC/MS analysis. The reaction was deemed complete at 40 min by GC/MS (the retention time of the starting material is 8.28 min; retention time of the rearranged species is 8.54 min). Anhydrous $CuCl_2$ (16.2 g, 141 mmol) was added and the solution was stirred overnight (the reaction was monitored by GC/MS). An additional amount of $CuCl_2$ (2.8 g) was added and the mixture was allowed to warm to room temperature and then was diluted with approximately 200 to 300 mL of hexanes, filtered through silica gel plug using hexanes as eluant. Solvents were removed by rotary evaporation to give crude product as brown oil. The material was then taken through another silica plug filtration, and the solvents were removed by rotary evaporation. The residue was then purified by Kugelrohr distillation at a pressure of 2 mm Hg and a temperature of 175 °C. The product was obtained as white crystals with some yellow oil, which solidified on standing. The total product mass was 13.27 g (59.15% yield).

2,6-Bis-trimethylsilyl-4-(3,4,5-tris-dodecyloxy-phenyl)-4H-dithieno[3,2-b;2',3'-d]pyrrole (3)

The (3,3'-dibromo-2,2'-bithiophene-5,5'-diyl)bis(trimethylsilane) (9.995 mmol, 4.682 g) (**2**) was mixed with 3,4,5-tris(dodecyloxy) aniline (10.53 mmol, 6.803 g), $Pd_2(dba)_3$ (0.497 mmol, 0.4550 g), $P(^tBu)_3$ (10 wt% in hexanes, 2.52 mmol, 5.10 mL), 126 mL of anhydrous toluene was added, and ^{t}BuONa (4.6 equiv, 41.07 mmol, 3.904 g) were added under nitrogen atmosphere. The reaction was then stirred for 30 min. and heated to reflux. The reaction progress was monitored by thin layer chromatography (TLC) in hexanes (to confirm consumption of the starting dibromide) and hexanes : dichlromethane (1:1) (to confirm formation of the product). Water (50 mL) was added to the solution, the organic layer was separated and the aqueous layer was extracted with 50 mL of hexanes twice. The organic layers were combined and dried over $MgSO_4$. The solution was then filtered and the solvents were removed by rotary evaporation. The 2,6-bis(trimethylsilyl)-4-(3,4,5-tris(dodecyloxy) phenyl)-4H-dithieno[3,2-b:2',3'-d]pyrrole (**3**) was then separated from the byproducts by column chromatography on silica gel (200 mL) using a hexanes : dichloromethane (2:1) as eluant. All solvents were removed by rotary evaporation and the product was obtained as yellow brown oil with mass of 5.27 g (55.30% yield).

4-(3,4,5-Tris(dodecyloxy)phenyl)-4H-dithieno[3,2-b:2',3'-d]pyrrole (4)

2,6-Bis(trimethylsilyl)-4-(3,4,5-tris(dodecyloxy)phenyl)-4H-dithieno[3,2-b:2',3'-d]pyrrole (**3**) (2.995 mmol, 2.853 g) in THF (40 mL) and tetrabutylammonium fluoride (TBAF) (1.0 M in THF, 6 mmol, 6 mL) was added dropwise at room temperature under nitrogen atmosphere. The reaction mixture was stirred for 23 min and the reaction progress was monitored by TLC (hexanes:dichloromethane (1:1)). 50 mL of water was added, the organic phase was separated and the aqueous phase was extracted with hexanes (50 mL, then 10 mL). The combined organic phases were dried over $MgSO_4$. The organic solvents were then evaporated off by rotary evaporation and the crude product was purified by column chromatography (silica gel (75 mL), dichloromethane : hexanes (2:1) and (dichloromethane : ethyl acetate (10:1) as eluants). The organic solvents were removed by rotary evaporation and the product was dried under vacuum. 4-(3,4,5-Tris(dodecyloxy)phenyl)-4H-dithieno[3,2-b:2',3'-d]pyrrole (**4**) was obtained as a yellow solid. The total mass of the product was 1.675 g (69.2% yield).

2-(4-(3,4,5-Tris(dodecyloxy)phenyl)-4H-dithieno[3,2-b:2',3'-d]pyrrol-2-yl) ethene-1,1,2-tricarbonitrile

4-(3,4,5-Tris(dodecyloxy)phenyl)-4H-dithieno[3,2-b:2',3'-d]pyrrole (**4**) (1.594 g, 1.972 mmol) was added to dimethylformamide (DMF) (25 mL) and TCNE (1.0362 g, 8.09 mmol). After the TCNE was added the solution went from colorless to red-purple color. The solution was stirred and heated overnight at a temperature of 80 °C (after initial temperature of 110 °C). The solution became a purple color after it was left overnight, and was monitored by TLC. Starting material was still present the next day and an additional amount of TCNE (1.028 g, 8.026 mmol) was added. The solution was stirred at 110 °C overnight until the starting material was all consumed (the reaction progress was monitored by TLC, hexanes:dichloromethane (1:1) as eluant). The solution was allowed to cool and became a brown sludge. The sludge was vacuum filtered and washed with water. The dark residue was dissolved in dichloromethane and combined with the filtrated. The organic phase was removed and the aqueous phase was extracted with dichloromethane (20 mL of CH_2Cl_2, 30 mL of CH_2Cl_2, and 50 mL of CH_2Cl_2). The organic phases were combined, dried over $MgSO_4$, and the drying agent was filtered off. The purple solution was subjected to rotary evaporation and the crude product was purified by column chromatography on silica gel (hexanes:dichloromethane (1:1)). The initial pure fractions (compound **Ia**) were combined to

form a red solution and dried to form a film that was green on the inside of the flask and red-purple on the outside (0.515 g, 28.3% yield). MS (MALDI) calculated for $C_{55}H_{80}N_4O_3S_2$ 908.5672; found 908.5626. ^{1}H NMR (400 MHz, $CDCl_3$): δ 8.04 (s, 1H), 7.66 (d, J = 4.95 Hz, 1H), 7.14 (d, J = 4.78 Hz, 1H), 6.67 (s, 2H), 4.04 (t, J = 6.42 Hz, 2H), 4.00 (t, J = 5.87 Hz, 4H), 1.85 (m, 6H), 1.50 (m, 6H), 1.27 (m , 48H), 0.89 (appears as poorly resolved t, 9H). ^{13}C NMR (400 MHz, $CDCl_3$): δ 154.26, 152.59, 145.47, 137.98, 134.54, 132.66, 131.94, 121.76, 116.76, 113.33, 112.92, 112.38, 102.21, 73.77, 63.53, 31.93, 30.39, 29.79, 29.72, 29.67, 29.64, 29.41, 29.38, 29.31, 26.14, 26.08, 22.70, 14.13. Some of the ^{13}C NMR peaks are missing because of low concentration. Elemental analysis calculated for $C_{55}H_{80}N_4O_3S_2$: C, 72.64; H, 8.87, N, 6.16. Found: C, 72.89; H, 8.71; N, 6.13.

2,2'-(4-(3,4,5-Tris(dodecyloxy)phenyl)-4H-dithieno[3,2-b:2',3'-d]pyrrole-2,6-diyl)bis(ethene-1,1,2-tricarbonitrile) (Ib)

The next pure fractions with compound **Ib** came out with an eluant of hexanes:dichloromethane (1:3). The pure fractions were combined in a dark purple solution and the solvent was removed by rotary evaporation forming a film that was green on the inside and purple on the outside. Further purification was done using pre-packed Biotage columns ($CHCl_3$ as eluant) (0.0673 g, 3.3% yield). MS (MALDI) calculated for $C_{60}H_{79}N_7O_3S_2$ 1009.5686; found 1009.5707. ^{1}H NMR (400 MHz, $CDCl_3$): δ 8.09 (s, 2H), 6.43 (s, 2H), 4.08 (t, J = 6.56 Hz, 2H), 4.01 (t, J = 6.38 Hz, 4H), 1.87 (m, 6H), 1.53(m, 6H), 1.27 (s, 54H), 0.902 (t, J = 6.65 Hz, 9H). ^{13}C NMR (400 MHz, $CDCl_3$): δ to be recorded. After repurification ^{1}H NMR (400 MHz, $CDCl_3$): δ 8.09 (s, 2H), 6.643 (s, 2H), 4.079 (t, J = 6.53 Hz, 2 H), 3.99 (t, J = 6.40 Hz, 4H) 1.87 (m, 7H), 1.53 (m, 9H), 1.40-1.20 (s, 54H), 0.928 (m, 11H). Elemental analysis calculated for $C_{60}H_{79}N_7O_3S_2$ C, 71.32; H, 7.88; N, 9.70. Found: C, 70.85; H, 7.78; N, 9.05.

2,2'-(4-(3,4,5-Tris(dodecyloxy)phenyl)-2H-dithieno[3,2-b:2',3'-d]pyrrole-2,6(4H)-diylidene)dimalononitrile (IIb)

The next pure fraction with slightly contaminated IIb was eluted with a hexanes:dichloromethane (1:3) and the fractions were combined in a red solution and dried by rotary evaporation to form a film that was green on the inside and red on the outside. Further purification was done using prepacked Biotage columns ($CHCl_3$ as eluant) (0.0634 g, 3.39% yield). MS (MALDI) calculated for $C_{56}H_{79}N_5O_3S_2$ 933.5624; found 934.6 (M+1) ^{1}H NMR(400 MHz, $CDCl_3$): δ 6.52 (s, 2H), 6.50 (s, 2H), 4.03 (t, J = 6.55 Hz, 3H), 3.97 (t, J = 6.43 Hz, 4H), 1.85 (m, 6H), 1.50 (m, 6H), 1.36 (m, 48H), 0.90 (t, J = 6.63 Hz, 9H) (this material contained about 20% of **Ib** after the first purification by column chromatography). ^{1}H NMR(400 MHz, $CDCl_3$): δ 6.52 (s, 2H), 6.50 (s, 2H), 4.03 (t, J = 6.6 Hz, 4H), 3.98 (t, J = 6.4 Hz, 4H), 1.86 (m, 7H), 1.49 (m, 7H), 1.27 (s, 56H), 0.90 (t, J = 6.5 Hz, 9H). ^{13}C NMR (400 MHz, $CDCl_3$): δ 174.20, 163.78, 154.50, 149.28, 139.41, 137.24, 132.93, 129.60, 129.22, 121.16, 112.67, 112.45, 104.42, 102.83, 102.19, 84.90, 77.36, 11.04, 16.73, 73.86,73.32, 69.68, 31.95, 31.93, 30.35, 29.78, 29.71, 29.67, 29.63, 29.60, 29.41, 29.68, 29.26, 26.06, 22.70, 14.13. Elemental analysis calculated for $C_{56}H_{79}N_5O_3S_2$: C, 71.98; H, 8.52; N, 7.50. Found: C, 72.00; H, 8.56; N, 7.39.

2-(4-(3,4,5-Tris(dodecyloxy)phenyl)-4H-diselenopheno[3,2-b:2',3'-d]pyrrol-2-yl)ethene-1,1,2-tricarbonitrile

4-(3,4,5-Tris(dodecyloxy)phenyl)-4H-diselenopheno[3,2-b:2',3'-d] pyrrole (1.80 g, 2.00 mmol) and TCNE (1.028, 4.00 mmol) were added to a flask under nitrogen atmosphere. Anhydrous DMF (25 mL was added to the flask and solution became purple within a minute. The reaction mixture was initially heated to 117 °C, and then stirred at 102 °C overnight. The reaction was monitored by TLC in hexanes:dichloromethane (1:1) and after consumption of the starting material the dark blue mixture was cooled to room temperature and treated with water (50 mL). The organic matter was extracted five times (150 mL CH_2Cl_2, 100 mL CH_2Cl_2 and 50 mL $CHCl_3$, and 100 mL CH_2Cl_2 and 50 mL $CHCl_3$). The combined organic phases were dried over $MgSO_4$ and the drying agent was filtered off. The solvents were removed by rotary evaporation. The compounds were separated by column chromatography with a hexanes:dichloromethane (2:1). The red-purple initial fractions containing mono-substituted product **Ic** were combined, the solvents were removed by rotary evaporation forming a film with green inside and red outside. Further purification was done using pre-packed Biotage columns ($CHCl_3$ as eluant) (0.2933 g, 14.6% yield). MS (MALDI) calculated for $C_{55}H_{80}N_4O_3Se_2$ 1004.4561; found 1005.4592 (M+1). ^{1}H NMR (400 MHz, $CDCl_3$): δ 8.23 (m, 2H), 7.35 (d, J = 5.94 Hz, 1H), 6.64 (s, 2H), 4.06 (t, J = 6.53 Hz, 2H), 3.98 (t, J = 6.37 Hz, 4H), 1.84 (m, 6H), 1.49 (m, 6H), 1.26 (m, 48H), 0.90(m, 9H). ^{13}C NMR (400 MHz, $CDCl_3$): δ 154.17, 153.82, 138.30, 134.07, 133.54, 132.69, 126.42, 118.70, 115.49, 113.99, 113.44, 103.13, 77.34, 77.02, 76.70, 76.15, 73.76, 69.51, 31.96, 31.93, 30.4029.77, 29.71, 29.67, 29.64, 29.40, 29.38, 29.29, 26.13, 26.07, 22.70, 14.13. Elemental analysis calculated for $C_{55}H_{80}N_4O_3Se_2$: C, 65.85; H, 8.04; N, 5.58. Found: C, 66.57; H, 8.14; N, 5.19.

2,2'-(4-(3,4,5-Tris(dodecyloxy)phenyl)-4H-diselenopheno[3,2-b:2',3'-d]pyrrole-2,6-diyl)bis(ethene-1,1,2-tricarbonitrile) (Id)

The next pure fraction containing di-substituted product **Id** came out with dichloromethane as eluant. The dark blue pure fractions were combined and the solvent was removed by rotary evaporation forming a film that was dark blue. Further purification was done using pre-packed Biotage columns ($CHCl_3$ as eluant). The amount produced (0.9856 g, 44%). MS (MALDI) calculated for $C_{60}H_{79}N_7O_3Se_2$ 1105.4575; found 1106.4667 (M+1). ^{1}H NMR (400 MHz, $CDCl_3$): δ 8.28 (s, 2H), 6.63 (s, 2H), 4.08 (t, J = 6.56 Hz, 2H), 3.98 (t, J = 6.42 Hz, 4H), 1.82 (m, 6H), 1.50 (m, 6H), 1.27 (48H), 0.90 (m, 9H). ^{13}C NMR (400 MHz, $CDCl_3$): δ 154.63, 149.77, 139.47, 139.14, 135.13, 131.33, 128.90, 125.81, 112.66, 112.50, 111.76, 103.12, 83.91, 77.36, 77.04, 76.72, 73.86, 69.65, 31.96, 31.93, 30.43, 29.77, 29.72, 29.68, 29.65, 29.41, 29.39, 29.27, 26.12, 26.06, 22.70, 14.13. Elemental analysis calculated for $C_{60}H_{79}N_7O_3Se_2$: C, 65.26; H, 7.21; N, 8.88. Found: C, 65.34; H, 7.20; N, 8.82. Material purified by Biotage column was submitted for elemental analysis. Found: C, 65.20; H, 7.12; N, 8.72.

2,2'-(4-(3,4,5-Tris(dodecyloxy)phenyl)-2H- diselenopheno[3,2-b:2',3'-d]pyrrole-2,6(4H)-diylidene)dimalononitrile (IIb)

The next fractions with contaminated **IIb** (dichloromethane as eluant) were combined and the solvent was removed by rotary evaporation to form a film that was green on the inside and red on the outside. MS

(MALDI) calculated for $C_{56}H_{79}N_5O_3Se_2$ 1029.4513; found 1030.4478 (M+1). ^{1}H NMR (400 MHz, $CDCl_3$: δ 6.52 (s, 2H), 6.50 (s, 2H), 4.23 (t, J = 5.89 Hz, 2H), 3.97(t, J= 6.4 Hz, 4H), 1.86 (m, 6H) 1.43 (m, 12H), 1.27 (m, 48H), 1.18 (s, 20H), 1.16(s, 20H), .96(m, 19H) (this material contained about 40% of **Id** after the first purification by column chromatography. This material was further purified by column chromatography using pre-packed Biotage columns ($CHCl_3$ as eluant) (.1417 g, 6.9% yield). Elemental analysis calculated for $C_{56}H_{79}N_5O_3Se_2$: C, 65.42; H, 7.74; N, 6.81. Found: C, 52.95; H, 9.00; N, 4.20. ^{1}H NMR (400 MHz, $CDCl_3$: δ 6.52 (s, 2H), 6.48 (s, 2H), 4.06 (t, J =6.5 Hz, 5.89 Hz, 2H), 3.97(t, J= 6.4 Hz, 4H), 1.86 (m, 7H) 1.43 (m, 8H), 1.26 (m, 55H), 0.96(m, 12H)

Results

Six new materials were prepared, purified by column chromatography and analyzed by ^{1}H NMR, mass spectrometry, UV-vis and cyclic voltammetry (CV). ^{13}C NMR and elemental analyses are in progress and compounds will be sent to the Kippelen group at the Georgia Institute of Technology for OFET fabrication and characterization.

Entry	λ_{max}, nm (CH_2Cl_2)	Solvent for CV	$E_{1/2}^{0/+1}$, V[1]	$E_{1/2}^{0/-1}$, V[1]	$E_{1/2}^{-1/-2}$, V[1]	$E_{1/2}^{0/-1}$, V[1] (vs SCE)[2]
Ia	286, 535	CH_2Cl_2	+0.90	-0.96	-1.63	-0.50
		THF	-	-0.96	-1.73	-0.40
Ic	239, 363, 549	CH_2Cl_2	+0.92	-0.97	-1.62	-0.51
		THF	-	-1.00	-1.8	-0.44
Ib	267, 359, 575	CH_2Cl_2	-	-0.51	-0.81	-0.05
		THF	-	-0.54	-0.85	+0.02
Id	384, 469, 597	CH_2Cl_2	+1.02*	-0.49	-0.78	-0.03
		THF	-	-0.54	-0.89	+0.02
IIa	261, 375, 509, 546	CH_2Cl_2	+1.06	-0.66	-0.96	-0.20
		THF	-	-0.62	-1.02	-0.06
IIb	433, 511, 548	CH_2Cl_2	+1.06	-0.61	-0.96	-0.13
		THF	-	-0.69	-1.10	-0.09

* Not reversible (large error) 1 0.1 M nBu4NPF6, in specified solvent, Cp2Fe internal standard at 0 V, 50 mV•s-1 rate 2 E1/20/-1(vs SCE) = E1/20/-1(vs Cp2Fe) + 0.56 (V) (for THF); E1/20/-1(vs SCE) = E1/20/-1(vs Cp2Fe) + 0.46 (V) (for CH2Cl2) 6

Table 1. Summary of UV-vis absorption spectroscopy data and CV analyses for all new compounds.

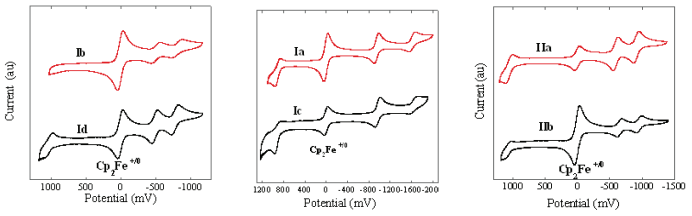

Figure 2. Cyclic voltammetry analysis (0.1 M of ^{n}BuPF$_6$ in CH_2Cl_2, $Cp_2Fe^{0/+1}$ as Internal Reference at 0 V and 50 mV/s Rate).

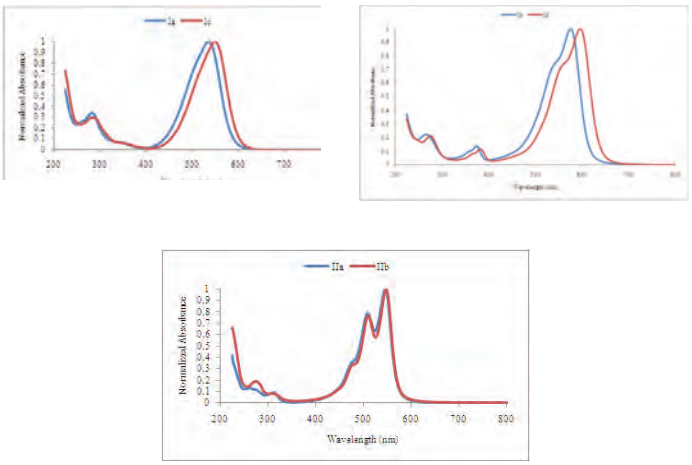

Figure 3. UV-Vis absorption spectra in dichloromethane.

Discussion

Diselenophenopyrrole was much more reactive than the dithienopyrrole as the reaction starts at room temperature while heat was required to do the same in the dithienopyrrole core. The major product for diselenophenopyrrole was the disubstituted product, while mono substituted product was a major one for DTP derivative despite having twice the equivalence of TCNE and more time to react. UV-vis data suggests that the substitution of sulfur for selenium lowers the HOMO-LUMO band gap as there is a slight red shift observed for mono- and di-substituted derivatives. First half-wave reduction potentials for di-substituted products **Ib** (X = S) and **Id** (X = Se) in 0.1 M of ^{n}BuPF$_6$ in THF are identical (-0.54 V vs Cp_2Fe, +0.02 V vs SCE), which suggests that substitution of sulfur with selenium doesn't affect the LUMO energy level. In 0.1 M of ^{n}BuPF$_6$ in CH_2Cl_2 **Ib** and **Id** are similar but **Ib** is slightly more difficult to reduce than **Id**. Mono-substituted products **Ia** (X = S) and **Id** (X = Se) have similar first half-wave reduction potential in 0.1 M of ^{n}BuPF$_6$ in THF and in 0.1 M of ^{n}BuPF$_6$ in CH_2Cl_2, but **Ia** is slightly easier to reduce. Quinoidal compounds **IIa** (X = S) and **IIb** (X = Se) have similar first half-wave reduction potentials in 0.1 M of ^{n}BuPF$_6$ in THF and in 0.1 M of ^{n}BuPF$_6$ in CH_2Cl_2, but **IIa** is slightly more difficult to reduce (see Table 1). All materials form films during removal of the solvent.

Conclusions

The cyclic voltammetry and UV-Vis data suggests that the compounds have similar electronic properties. The ease in which the compounds formed films when the solvent was removed suggests that some may have good film forming properties. Since all the compounds formed have a first half-wave reduction potential around -0.40 V vs. SCE (**Ia** and **Ic**) or more positive than -0.40 V vs. SCE (**Ib, Id, IIa** and **IIb**), they are promising candidates for n-type OFETs.

References

1. Mas-Torrent, M. et al., Chem. Soc. Rev. 2008, 37 (4), 827-838.
2. Zaumseil, J., et al., Chem. Rev. 2007, 107, 1296-1323.
3. Usta, H. et al., J. Am. Chem. Soc., 2009, 131 (15), 5586.
4. Pappenfus, T. M., et al., Org. Lett. 2008, 10 (8), 1553-1556.
5. Getmanenko, Y. A, et al., Org. Lett. 2010, 12(9), 2136-2139.
6. Connley, N. G., Geiger W. E., Chem. Rev., 1996, 96 (2), 877-910.

Acknowledgements

I would like to acknowledge the Center on Materials and Devices for Information Technology Research (CMDITR), an NSF Science and Technology Center (grant No. DMR 0120967), Dr. Yulia Getmanenko, Dr. Seth Marder, and the Marder Group.

THOMAS PURCELL is currently a rising sophomore at NYU pursuing a major in chemistry and minors in mathematics and physics. He plans to pursue a doctorate degree when he finishes his undergraduate studies.

The Synthesis of a Diphenyldithiophene Derivative Semi-Conductor for Photovoltaic Applications

LUIS E. REYES, Rowan University
Zhaokang Hu, Elsa Reichmanis, Georgia Institute of Technology

Introduction

In the search for renewable energy photovoltaic (PV) cells have been the topic of much interest due to their ability to obtain energy without the production of harmful greenhouse gasses, such as CO_2, that have a negative impact on our environment.[1] To date the majority of PV cells are fabricated using an inorganic material, silicon. This is in great part because of experience in its fabrication and availability from the semi-conductor industry.[2] These are solid-state junction devices employing silicon to absorb and transfer the energy obtained from light to electricity.[2] Silicon technology is hampered by its relatively high material requirements, which accounts for a substantial percentage of the overall cost.[3] The complexity of the design and fabrication process is another factor leading to its high cost. New breakthroughs in PV cell design are dependent on the development of new materials with the ability to replace silicon.

Organic materials have been shown to be attractive candidates for both passive and active roles in electronic devices because of their compatibility with high through-put, low cost processing techniques; and their ability to be functionalized through organic synthesis techniques to obtain specific performance attributes.[4-6] Changes in the chemical structure of these organic materials can affect solubility, chemical and environmental stability, and electrical properties such as mobility, conductivity, I_{on}/I_{off} ratio, and threshold voltage. For example, previous work with field-effect transistors (FETs) identified that the incorporation of phenylene units into a thiophene segment resulted in a small lowering of the HOMO energy level, and it has been shown that this lowering is accompanied by a reduction in the off current, increasing the devices on/off ratio and air stability.[7]

The incorporation of conjugated semiconducting polymers into PV cells has been shown to be a novel attempt to revolutionize PV technology, with the most significant impact being lower manufacturing cost. These polymer-based PV cell designs incorporate linear conjugated polymer semiconductors such as poly(3-hexylthiophene) (P3HT) and poly[2-menthoxy-5-(2'-ethylhexoxy)-1,4-phenylenevinylene] (MEH-PPV),[8] but the use of an organic semiconductor grafted onto a flexible polymer backbone has structure-property relationships that are still unknown.

The purpose of my research is to synthesize 4-(5'-(4-hexylphenyl)-[2,2'-bithiophen]-5-yl)phenethyl methacrylate (HPTTPEM) depicted in Figure 1. The diphenyldithiophene (PTTP) and its derivates are well-studied organic semiconducting materials with comparable charge carrier mobilities. As previously reported,[9] PTTP and its derivatives afford good mobility and I_{on}/I_{off} ratio. In this study, a PTTP segment was successfully incorporated into a methacrylate monomer to yield HPTTPEM by reacting bromo-modified PTTP species with stannylized methacrylate monomer in a Stille coupling reaction as outlined in Scheme 1. A hexyl terminal group is attached to the PTTP core in order to increase the solubility of the resulting compound for fabrication purpose. The HPTTPEM monomer will be eventually free radically polymerized to yield a PTTP semiconducting core grafted polymethacrylate. The electronic properties of the resulting polymer will be characterized as FETs.

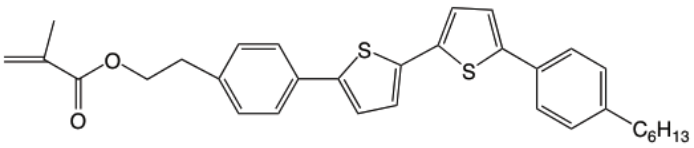

Figure 1. 4-(5'-(4-hexylphenyl)-[2,2'-bithiophen]-5-yl)phenethyl methacrylate (HPTTPEM).

Experimental

Material and General Methods

Chemicals were purchased from Aldrich and used as received. All synthetic reactions were conducted under an argon atmosphere and employed anhydrous solvents.

Preparation of Tributyl(4-hexylphenyl)stannane (1)

Tributyl(4-hexylphenyl)stannane was synthesized according to the existing procedure.[7] 1-bromo-4-hexylbenzene (1.52 g, 6.303 mmol) was sealed in a flask with a stirring bar. The system was degassed for 5 min then THF (30 mL) was added to system while stirring and cooled to -78 °C in acetone-dry ice bath. BuLi (3.93 mL, 1.6 M in hexane) was added dropwise and left stirring 70 min at this temperature. The clear light yellow solution turned to a darker yellow solution after the addition of BuLi. Tri-n-butyltin chloride (2.05 g, 6.300 mmol) was then added dropwise changing the solution's color back to a clear pale yellow. The system was then warmed to room temperature and kept stirring over night. Next, the reaction was quenched with 50 mL of hexane and washed with 50 mL of 10% aqueous $NaHCO_3$ solution. Aqueous phase was washed with 50 mL of hexane. Organic phases were combined, then sequentially washed with distilled water (3 x 30 mL) and 10% aqueous NaCl (2 x 50 mL). The organic phase was dried with $MgSO_4$, and filtered. The solvent was then removed from filtrate under reduced pressure giving a bright yellow powder. ^{1}H NMR (400 MHz, $CDCl_3$) δ 7.37 (d, 2H), 7.15 (d, 2H), 2.57 (t, 2H), 1.63 – 1.30 (m, 20H), 1.05 – 1.01 (m, 6H), 0.94 – 0.87 (m, 12H).

Preparation of 5-(4-hexylphenyl)-2,2'-bithiophene (2)

A mixture of tributyl(4-hexylphenyl)stannane (**1**, 2.0 g, 4.431 mmol), 5-bromo-2-2'-bithiophene (1.09 g, 4.446 mmol), and

tetrakis(triphenylphosphine)-palladium (0.305 g, 0.264 mmol) catalysis were sealed in a flask with a stirring bar. The system was degassed for 10 min before DMF (50 mL) was added. Next, the system was degassed for another 20 min and left heating and stirring at 85 °C for 48 h. The solution was dark in color after the reaction. A clear brown solution was obtained after filtering the dark reaction solution through a Celit system. Wet yellow product was obtained after removing DMF at reduced pressure. Thoroughly washing this crude product with cold methanol yields a gray-green colored solid, which was further purified by chromatographic column on silica gel using 1:1 dichloromethane/hexane eluent. ^{1}H NMR (400 MHz, $CDCl_3$) δ 7.51 (d, 2H), 7.22 – 7.18 (m, 5H), 7.14 (d, 1H), 7.03 (dd, 1H), 2.61 (t, 2H), 1.62 (m, 2H), 1.38 – 1.27 (quintet, 6H), 0.89 (t, 3H).

Preparation of 5-bromo-5'-(4-hexylphenyl)-2,2'-bithiophene (3)

N-bromosuccinimide (NBS) (0.317 g, 1.78 mmol) and 5-(4-hexylphenyl)-2,2'-bithiophene (**2**, 0.530 g, 1.62 mmol) were sealed in flask with stirring bar. The system was degassed 5 min before dry DMF (35 mL) was added. The system was stirred at 40 °C overnight in the absence of light. Afterwards, the system was filtered through using vacuum filtration. DMF was then removed under reduced pressure and the solution chilled in dry-ice. Yellow-tan solid product precipitate was removed through filtration. ^{1}H NMR (400 MHz, $CDCl_3$) δ 7.50 (d, 2H), 7.19 (d, 2H), 7.17 (d, 1H), 7.07 (d, 1H), 6.98 (d, 1H), 6.93 (d, 1H), 2.23 (t, 2H), 1.62 (quintet, 2H), 1.37 – 1.28 (m, 6H), 0.89 (t, 3H).

Preparation of 4-bromophenethyl methacrylate (4)

Bromo-phenethyl alcohol (10 g, 49.74 mmol) was dissolved in NEt_3 (20 mL) and pyridine (40 mL) in a degassed flask. Methacryloyl chloride (6.75 g, 64.57 mmol) was added dropwise to the stirring solution and left stirring for 48 h. Reacting solution was poured into 150 mL of chloride acid/ice mixture (75 mL HCl), stirring and partitioned between hexane/10% $NaHCO_3$ solvent. Purification was conducted through column chromatography using 1:1 DCM/hexane as an eluent. ^{1}H NMR (400 MHz, $CDCl_3$) δ 7.42 (d, 2H), 7.11 (d, 2H), 6.06 (s, 1H), 5.54 (s, 1H), 4.32 (t, 2H), 2.93 (m, 2H), 1.91 (s, 3H).

Preparation of 4-(tributylstannyl)phenethyl methacrylate (5)

This material was synthesized according to the existing procedure.[10] A mixture of 4-bromophenethyl methacrylate (2.00 g, 7.431 mmol), bis(tributyltin) (4.33 g, 7.464 mmol), and tetrakis(triphenylphospine) (0.520 g, 0.450 mmol) was sealed in a flask with stirring bar and degassed for 10 min. Toluene (75 mL) was added to the reacting system and refluxed while stirring for 4 h at 120 °C. The system was left to cool and toluene removed under reduced pressure. Hexane was added the system cooled on dry-ice and filtered to collect a tan precipitate product. The crude product was further purified by chromatographic silica gel column with 1:1 dichloromethane/hexane to give a yellow powder product. ^{1}H NMR (400 MHz, $CDCl_3$) δ 7.40 (d, 2H), 7.20 (d, 2H), 6.09 (s, 1H), 5.54 (s, 1H), 4.35 (t, 2H), 2.96 (m, 2H), 1.93 (s, 3H), 1.37 – 1.28 (m, 18H), 1.04 – 0.88 (m, 9H).

Preparation of 4-(5'-(4-hexylphenyl)-[2,2'-bithiophen]-5-yl)phenethyl methacrylate (HPTTPEM)

A mixture of 5-bromo-5'-(4-hexylphenyl)-2,2'-bithiophene (0.400 g, 0.987 mmol), 4-(tributylstannyl)phenethyl methacrylate (0.474 g, 0.987 mmol), and tetrakis(triphenylphosphine)-palladium (0.091 g, 0.039 mmol) catalysis was sealed in a flask and degassed. DMF (70 mL) was added to stirring mixture and refluxed for 3 days at 85 °C. After removing DMF under reduced pressure, the resulting crude solid product was thoroughly washed with cold methanol. A yellow product was further purified by a chromatographic column on silica gel with 1:1 DCM/hexane. ^{1}H NMR (400 MHz, $CDCl_3$) δ 7.55 (d, 2H), 7.52 (d, 2H), 7. 26 (m, 2H), 7.21 (d, 1H), 7.19 (d, 2H), 7.18 (d, 1H), 7.15 (d, 2H), 6.09 (s, 1H), 5.55 (s, 1H), 4.37 (t, 2H), 3.00 (t, 2H), 2.62 (t, 2H), 1.94 (s, 3H), 1.63 (quintet, 2H), 1.35 (m, 6H), 0.89 (t, 3H).

Characterization

^{1}H NMR (400 MHz) spectra were measured with a Varian Mercury 400 at room temperature. The thermal stability was investigated with a Perkin-Elmer Pyris 1 thermogravimetric analyzer (TGA). Differential scanning calorimetric (DSC) measurements were conducted using a Perkin-Elmer Diamond DSC. UV-Vis absorption spectra were obtained using an Agilent 8453 UV-Visible Spectrophotometer.

Transistor Fabrication

Silicon wafers were used to construct a bottom contact thin film transistor. The wafer was spin-coated with HPTTPEM solution in chloroform at 1500 rpm for 30 s. The electronic properties were characterized using an Agilent 4155C Semiconductor Parameter Analyzer in air.

Results and Discussion

It was necessary for the synthesis to be conducted in three phases, the first two beginning at opposite ends of the monomer. The first phase began at the terminal phenyl group. The structure was functionalized by tributyltin to prepare the structure for the Stille coupling reaction conducted in the next step to obtain 5-(4-hexylphenyl)-2,2'-bithiophene (**2**). After the Stille coupling reaction the completion of the first phase occurs by brominating **2** to yield 5-bromo-5'-(4-hexylphenyl)-2,2'-bithiophene (**3**). The second phase began with methacrylate, which will be the site of polymerization. Methacryloyl chloride was reacted with bromophenyl ethanol to obtain 4-bromo phenethyl methacrylate (**4**), which was functionalized with tributyltin to yield 4-(tributylstannyl)phenethyl methacrylate (**5**). Lastly, the monomer's synthesis was completed via Stille coupling reaction between **3** and **5**.

Thermal analysis was conducted by first employing thermogravimetric analysis (TGA) to obtain the decomposition temperature of HPTTPEM. The decomposition temperature is defined as the temperature at which 5% of your original sample weight has been lost. The decomposition temperature was 337 °C for HPTTPEM as shown in Figure 2. The glass transition temperature of HPTTPEM was then studied by differential scanning calorimetry (DSC). As indicated in Figure 3, there is no normal glass transition temperature for the monomer as expected, however, a reversible endothermic transition

was observed at approximately 220 °C, which was thought to be caused by the melting of the HPTTPEM monomer.

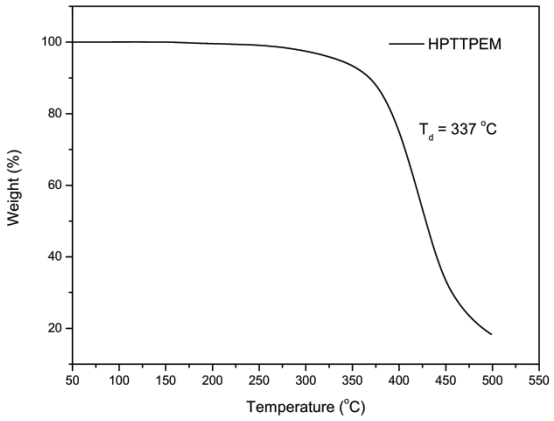

Figure 2. Thermogravimetric analysis data for HPTTPEM (heating rate, 5 °C/min).

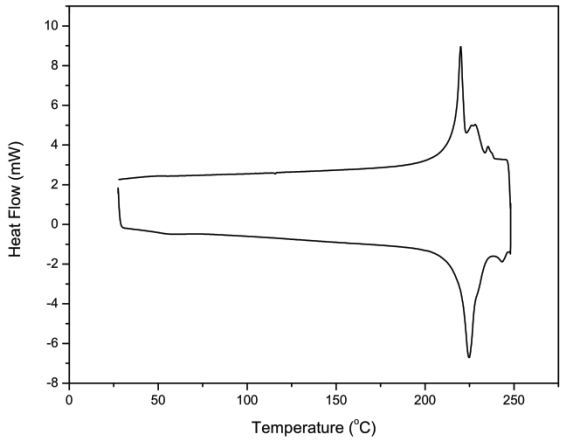

Figure 3. Differential scanning calorimetry trace (second cycle) for HPTTPEM at a scanning rate of 10 °C/min.

UV-vis absorption of HPTTPEM in chloroform is reported with an absorption maximum at 375 nm as seen in Figure 4, consistent with a previous report[7] as characteristic of π-π* transitions of PTTP.

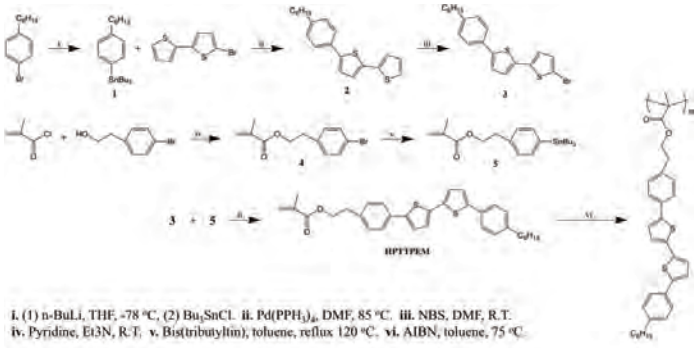

Scheme 1. Synthetic route of HPTTPEM polymer.

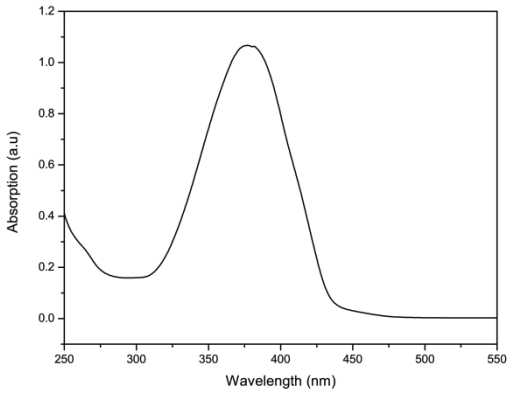

Figure 4: UV- Vis absorption spectrum of HPTTPEM in $CHCl_3$ (~0.1 mg/mL).

A FET was made of HPTTPEM as shown in Figure 5. Output characteristics in Figure 6 were conducted by keeping the gate voltage constant and sweeping the drain voltage from -60 to 0 V. Gate voltages from 0 to 50 V were used increasing in 10 V increments. The shape of each curve was indicative of a transistor, with a linear portion between -10 to 0 V drain voltage, and a saturated portion between -60 to -30 V drain voltage. Transport characteristics shown in Figure 7 were used to obtain the mobility of HPTTPEM, which is a quantification of the average velocity of charge carried across HPTTPEM in the presence of an electric field. The characterization was conducted at a constant drain voltage of -3 V that lies in the linear portion of HPTTPEM output characteristics allowing the use of the equation

$$I_d = \frac{Z}{L}\mu C_i \left(V_g - V_t\right) V_d$$

to obtain the mobility. Where I_d is drain current, Z is channel width, L is channel length, μ is mobility, C_i is capacitance of gate dielectric per unit area, V_g is gate voltage, V_t is threshold voltage, and V_d is drain voltage. The gate voltage was swept from -50 V to 30 V and a mobility of 1.83 x 10^{-6} $cm^2/V*s$ was obtained.

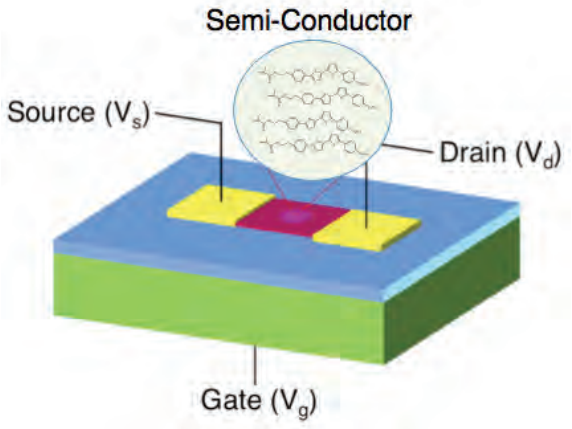

Figure 5. Field effect transistor (FET).

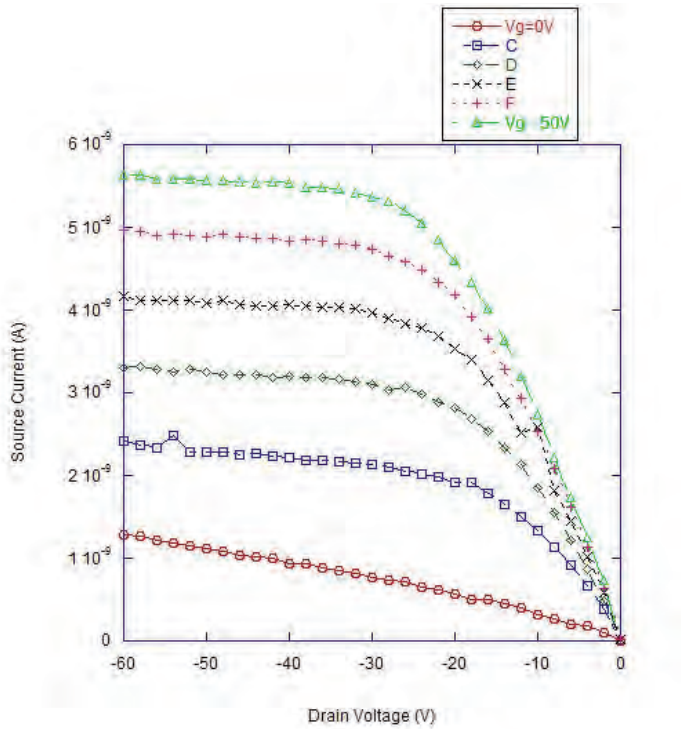

Figure 6. Output characteristics of HPTTPEM.

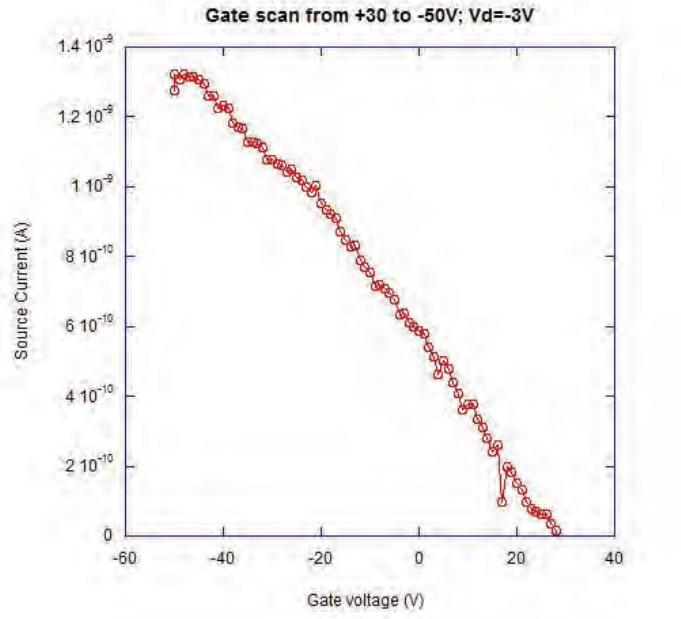

Figure 7. Transport characteristics of HPTTPEM.

Conclusions

In this work, a PTTP modified methacrylate monomer has been successfully synthesized and confirmed by multiple characterization techniques. The synthesis was straightforward and highly pure product was obrained via the column chromatography technique. TGA measurements demonstrated the materials good thermal stability. No crystalline was found during DSC scan. An endothermic peak at 220 °C indicates the melting process of the monomer. HPTTPEM shows strong π-π^* transitions with an absorption maximum at 375 nm. Electronic properties verified HPTTPEM's ability to function in a FET and mobility figures obtained confirm the use of the FETs as a good way in which to quantify HPTTPEM's electrical properties in future experiments.

In the future the HPTTPEM monomer will be polymerized via free radical polymerization. The control of the alky group positioning on the outer most phenyl ring opens the door to further solubility experimentation using larger alky chains and chains with different configurations such as tert-butyl to increase solubility leading to better processability.

New polymer backbones will be attempted in the future to help understand the structure-property relationship of non-conjugated polymers with semi-conducted unites grafted onto them. Lastly, the structure-property relationship and better solubility will be incorporated in attempts to optimize this material for photovoltaic cell and transistor applications.

References

1. Turner, J. A. Science. 1999, 285, 687-689.
2. Grätzel, M. J. Photo. Chem. Rev. 2003, 4, 145–153.
3. Johansson, T. B. (ed.); Kelly, H. (ed.); Reddy, A. K. N. (ed.); Williams, R. H. (ed.); Burnham, L (ed.) 1993, Renewable Energy Sources for Fuels and Electricity, Island Press, 337-338.
4. Katz, H. E. Chem. Mater. 2004, 16, 4748-4756.
5. Reichmanis, E.; Katz, H.; Kloc C.; Maliakal, A. Bell Labs Technical Journal 2005, 10(3), 87-105.
6. Kelly, T. W.; Baude, P. F.; Gerlach, C.; Ender, D. E.; Muyres, D.; Hasse, M. A.; Vogel, D. E.; Theiss, S. D. Chem. Mater. 2004, 16, 4413-4422.
7. Mushrush, M.; Facchetti, A.; Lefenfeld, M.; Katz, H. E.; Marks, T. J. J. Am. Chem. Soc. 2003, 125, 9414-9423.
8. Coakley, K. M.; McGehee, M. D. Chem. Mater. 2004, 16, 4533-4542
9. Vaidyanathan, S.; Dötz, F.; Katz, H. E.; Lawrentz, U.; Granstrom, J.; Reichmanis, E. Chem. Mater. 2007, 19, 4676-4681
10. Cornejo, A.; Fraile, J. M.; Garcia, J. I.; Gil, M. J.; Luis, S. V.; Martinez-Merino, V.; Mayoral, J.A. J., Org. Chem. 2005, 70, 5536-5544.

Acknowledgments

Funds for this research were provided by the Center on Materials and Devices for Information Technology Research (CMDITR), an NSF Science and Technology Center No. DMR 0120967. The author would like to thank Dr. Elsa Reichmanis, Dr. Zhaokang Hu, Avishek Aiyar, Olanda Bryant, and my fellow CMDITR participants.

LUIS E. REYES is currently a rising senior pursuing a B.S. in Chemistry at Rowan University in Glassboro, NJ. He plans to pursue a PhD in Chemistry or Material Science. After graduation his career goal is to conduct research on novel materials with electrochemical and electronic applications.

Software Implementation for Direct Laser Write (DLW) Fabrication of Optical Waveguides

VICTOR ROBLES, Arizona State University
Ram Voorakaranam, Robert A. Norwood, University of Arizona

Abstract

Optical waveguides are fabricated by a Direct Laser Writing (DLW) system by writing on top of a substrate coated with a layer of SU-8 photoresist. A LabVIEW software application was employed to control the DLW system for fabricating the optical waveguides. The LabVIEW software interface controls a UV laser, motion controller, and X-Y axis translation stages. A LabVIEW software module for fabrication of linear waveguides and optical couplers was developed allowing the user to design and fabricate these structures on the fly. User parameters provided on the front panel will allow the realization of user-designed optical devices. Preliminary fabrication results demonstrated waveguides with good optical quality.

Introduction

Direct laser writing is used to create intricate patterns in photosensitive material. Unlike traditional masked lithography, DLW avoids complex optical systems and masks that have lengthy design and fabrication cycles and are difficult to manage once implemented (Figure 1).

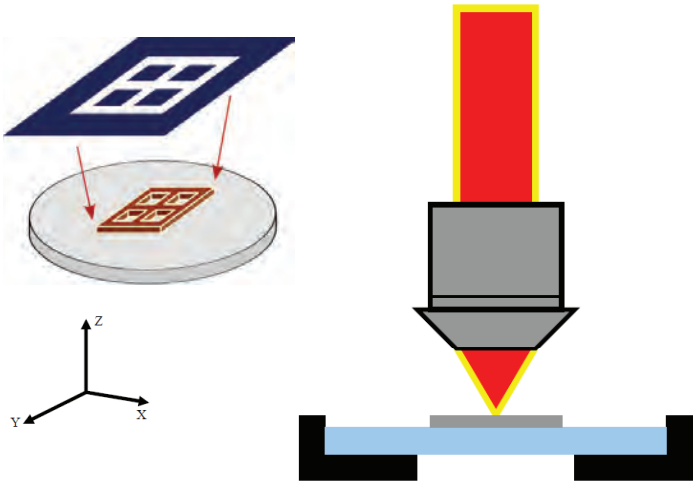

Figure 1. Masked lithography and DLW.

Why Direct Laser Writing?

- Maskless
- Rapid prototyping
- High flexibility and control
- Avoid external manufacturing

The process relies on single-photon exposure at UV wavelengths where SU-8, the photoresist, will crosslink and polymerize. With the correct amount of laser exposure the user can induce polymerization at the focal point of the laser to create patterns that are controlled by translation stages moving in a plane.

Experimental Methods

A LabVIEW software interface was developed to control the DLW system which included a UV laser, a laser shutter, a motion controller and X-Y translation stages. The stages allow for minute, precise movements that follow a highly accurate path based on the user inputs. Optical waveguides are fabricated by writing on top of a substrate coated with SU-8, a negative photoresist, using the DLW system. DLW system parameters such as speed and power of the laser are also controlled by the user. A LabVIEW module was developed to fabricate multiple linear waveguides as defined by the user. A second LabVIEW module was developed to create an optical coupler structure (Figure 4) with user-specified parameters. The user is allowed to change parameters on the front panel of each module based on the required geometrical properties for each waveguide.

The DLW system is comprised of the following equipment:

- UV laser
- Sample holder
- 2 translation stages
- ESP 301 motion controller
- NI Labview 2009

The setup used has a UV laser passing through an optical system that shapes and focuses the laser onto the plane of the sample. The sample is held in place on the translation stages whose movement is controlled by the ESP 301 Motion Controller. The motion controller communicates with the LabVIEW software via commands consisting first of a single digit to define the axis number to be modified, a two-letter code to define the action to be done, and numerical parameters related to an individual command. Samples for code are displayed in Table 1.

The implemented software interfaces with the translation stage and laser to write the user-defined shape onto the substrate. The sample is a glass substrate that is first prepared by spin coating or dipping the glass into a solution of SU-8. The sample is then placed on the DLW system to record the pattern traced by the translation stages. A schematic for the system is shown in the Figure 2.

Code	Description
1OR1	Move Axis 1 to position 0 on axis
1HC5,5,360°	Move group 1 along a circle with center at 5,5
1HL5,5	Move group 1 linearly to position X,Y = 5,5 from previous position
1VA20	Set velocity of Axis #1 to 20mm/s
1AC100	Set acceleration of Axis #2 to 100mm/s^2

Table 1. Sample Code for Controller.

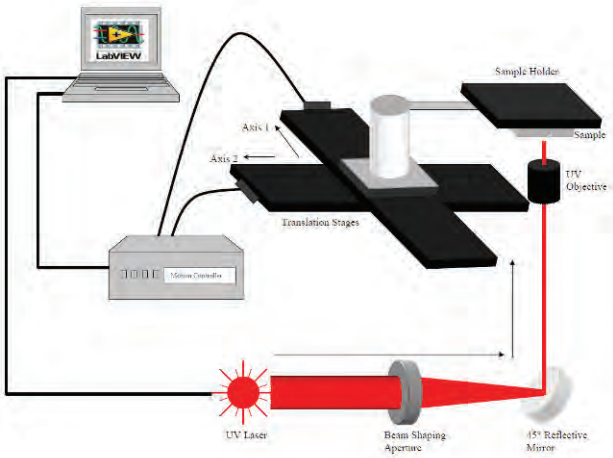

Figure 2. Schematic of the DLW setup.

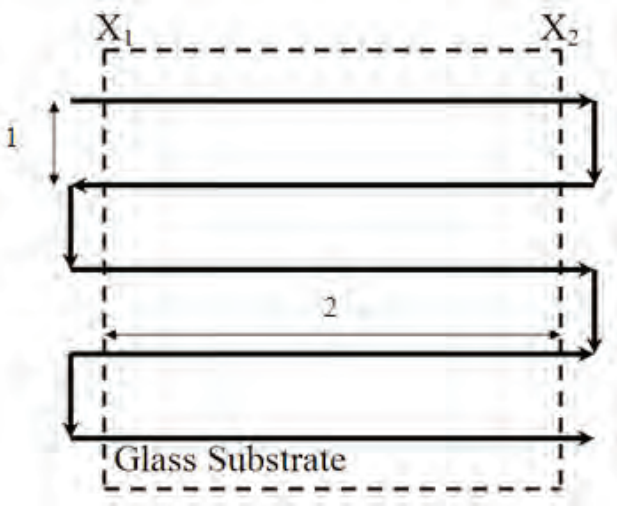

Figure 3. Linear waveguide parameterization. 1) space between waveguides 2) length of waveguide.

To create a LabVIEW module for the linear waveguide, geometric parameterization was introduced. The parameters to be defined by the user and implemented by the software are 1) the length of the linear wave guides, 2) the distance between the waveguides and 3) the number of waveguides to be traced. The movement pattern for creating multiple linear waveguides is shown in the Figure 3.

Parameters were similarly introduced for an optical coupler. Since the optical coupler has curved sections, commands for arc motions were included in the algorithm. The parameters for these designs are 1) the length of the input and output sections, 2) the height of the coupler, and 3) the length of the coupler as demonstrated in Figure 4.

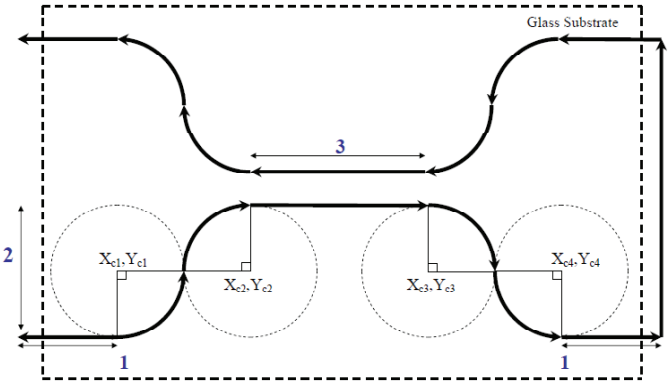

Figure 4. Optical coupler parameterization. 1) Start/end sections 2) Coupler height 3) Length of the coupling section.

Results and Discussion

Preliminary results show that the DLW system compares well with typical lithography methods.

Figures 5-7 compare the physical structures and transmitted beam profiles of the SU-8 waveguide fabricated by DLW with waveguides fabricated using traditional masked lithography. The first is a SolGel core, the second is a Dow Corning (DC) core, and third is the SU-8 patterned by the DLW system with the left side of the figure being the physical cross section and the right being the transmitted beam profile.

Preliminary results for optical loss vs. the length of the waveguide have been measured in the lab and shown below (Figure 9).

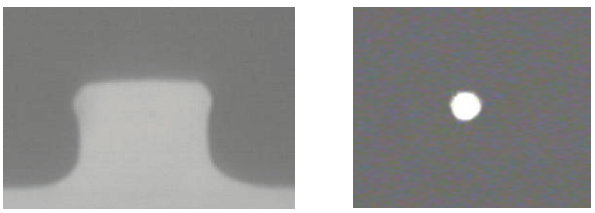

Figure 5. SolGel structure 5.5 µm x 6.8 µm.

Figure 6. DC 6 µm x 6.1 µm.

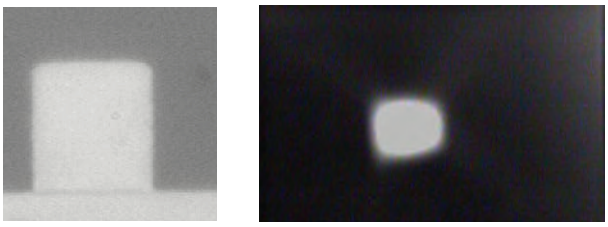

Figure 7. SU-8 6.7 µm x 7.8 µm.

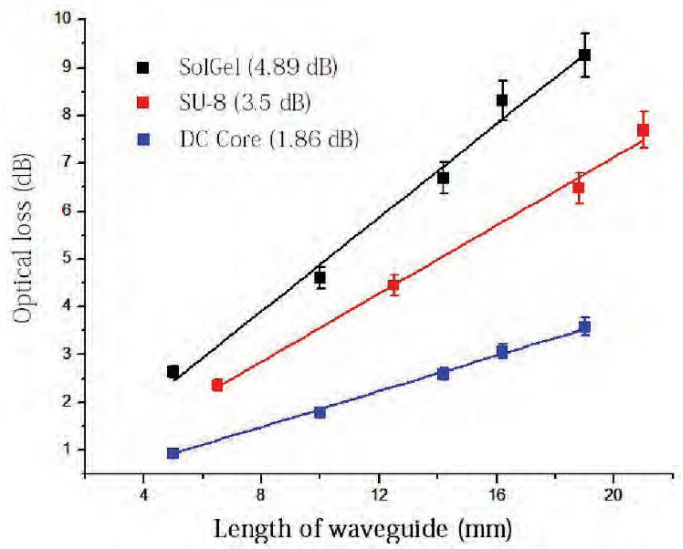

Figure 8. Optical loss measurements.

Conclusions

Software was developed for a Direct Laser Write system for microfabrication of optical waveguides. Visual programming techniques were applied using the LabVIEW graphical programming environment. Additionally, specific interfaces for a motional controller, a laser, and laser shutter were implemented. Future work includes measuring transmission loss for fabricated waveguides as a function of the system parameters including writing speed and laser power intensity. Further work will be needed in fabrication and testing of optical couplers and Mach-Zehnder Interferometers. To improve adhesion of the SU-8 to the glass substrate, processing with an adhesion promoter needs to be optimized.

References

1. ESP 301 Motion controller/driver user manual
   http://www.newport.com/images/webDocuments-EN/images/14294.pdf

2. Labview 2009 Programming concepts
   http://www.ni.com/pdf/manuals/371361f.zip

3. Thorlabs T-Cube solenoid controller
   http://www.thorlabs.us/Thorcat/15700/15791-D01.pdf

4. Microchem SU-8 data sheet
   http://www.microchem.com/products/pdf/SU-82000DataSheet2000_5thru2015Ver4.pdf

5. Teem Photonics UV Laser
   http://www.teemphotonics.com/assets/files/PDF/Microchip/MicroChip_SxV.pdf

Acknowledgments

The author would like to thank Dr. Ram Voorakaranam for his guidance and mentoring, Dr. Robert A. Norwood for hosting the research and also for his guidance and mentoring and Dr. Arkady Bablumian for building the DLW system. Funds for this research were provided by the Center on Materials and Devices for Information Technology Research (CMDITR), an NSF Science and Technology Center No. DMR 0120967.

VICTOR ROBLES will graduate with a Bachelor of Science in Electrical Engineering at Arizona State University. He will further pursue his PhD in Electrical Engineering with an emphasis on Signal Processing and Communications to work on Radar Systems.

Open Circuit Voltage Dependence on Bandgap in Bulk Heterojunction Solar Cells

JULIA RUTHERFORD, Pacific Lutheran Univeristy
Elisabeth Strein, David Ginger, University of Washington

Introduction

To determine whether open circuit voltage of bulk heterojunction (BHJ) organic solar cells is dependent on the bandgap of semiconductor quantum dots (QDs) when used in these cells, several steps were taken. Various sizes of cadmium selenide (CdSe) QDs were synthesized and used as electron acceptors in the active layers of BHJ OPV devices.

QDs are semiconductor nanocrystals whose radii are smaller than the Bohr radius of an exciton. Quantum confinement in these nanocrystals has many implications. In this particular study, the most interesting property of these particles is their size tunable bandgaps.

Organic solar cells are thin, transparent, and flexible. They can be made from conductive polymers and small molecules which absorb light.[1] OPV cells are cheaper than silicon solar cells, but have lower efficiencies resulting in a higher cost/watt. While this remains a problem, they will continue to be a less competitive alternative. The solar cells made here are BHJ devices made using a CdSe QDs and poly(3-hexylthiophene) (P3HT) blend as the active layer.

In a bulk heterojunction, active layer components are combined to maximize interfacial area and reduce recombination while maintaining thickness required for sufficient light absorption. In this type of heterojunction, each layer has many long extensions into the other, allowing for enhanced charge transfer.

Open circuit voltage (V_{OC}) is the voltage of a device at zero net current. A voltage must be applied for the current to be zero as it would in an open circuit. The dark current in one direction must overcome the photocurrent in the opposite direction.

Importantly, power is defined as the product of voltage and current. The larger these values can be made, the higher the power of the device will be and the better the power conversion efficiency.[2,3] An increase in V_{OC}, given a constant short circuit current (J_{SC}), will result in a more efficient cell.

Previous results have suggested that VOC may be dependent upon bandgap.[1,4,5] QDs have bandgaps which can be manipulated by size change, allowing this to be explored. By testing organic solar cells made using CdSe QDs over a large size range, a trend may be visible. Device fabrication required development of consistent syntheses for large and small CdSe QDs with comparable surface chemistry.

Experimental

To synthesize CdSe QDs, 0.0765 g cadmium oxide (99.99+%, Aldrich) and 0.65 g oleic acid (90%, Aldrich) in 2 g of 1-octadecene (ODE, >95%, Fluka) were reacted in a 3-neck round bottom flask with a stir bar, heating mantle, and J-Kem thermocouple at 220 °C under nitrogen gas to form cadmium oleate. The solution was then cooled and ligands added.

Ligands used were 0.5 g trioctylphosphine oxide (TOPO, 90%, Aldrich) and 1 g octadecylamine (ODA, 98%, Aldrich). Oxygen was removed under vacuum for 1 hour between 20 and 50 millitorr. The solutions were returned to a nitrogen atmosphere and heated to the desired injection temperature. The higher the temperature at injection, the larger the QDs. This worked best over a range from approximately 210-300 °C.

A solution premade in a glovebox of 0.239 g selenium (99.99%, Aldrich) dissolved in 0.655 g of tri-n-butylphosphine (99%, STREM chemicals) at room temperature was rapidly injected into this mixture. For smaller QDs, this solution was diluted with 2.1 g of ODE to promote nucleation over growth in the reaction. After completion of desired growth, excess ligand was removed by a methanol and hexane extraction.

One or more of the ligands which are ideal for synthesis such as TOPO, ODA, and oleic acid which prevent aggregation while allowing for growth also result in insulated product. These were then exchanged for pyridine (99.0%, EMD) on the surface on the QDs to allow for carrier mobility. Very large and very small QDs required alterations on this synthetic method.

To produce QDs much larger than ones which are possible from the above procedure, excess of each precursor, Se:TBP and the cadmium oleate mixture were mixed together. This solution was then dripped into a post synthesis reaction mixture at 180 °C to allow growth with minimal nucleation. For blue QDs, batch size was doubled to increase yield, injection temperature was reduced to between 210 and 220 °C, and quenching of the reaction occurred near 20 seconds after injection. The Se precursor for this was diluted with 4.2 g of ODE (90%, Aldrich).

Devices were made by spin coating first PEDOT and then the active layer onto ITO coated glass slides and evaporating electrodes into place under a nitrogen atmosphere.

IV curves were taken under AM 1.5 illumination under dynamic vacuum. Absorption spectra were taken using an Agilent 8453 UV-vis in solution in hexane.

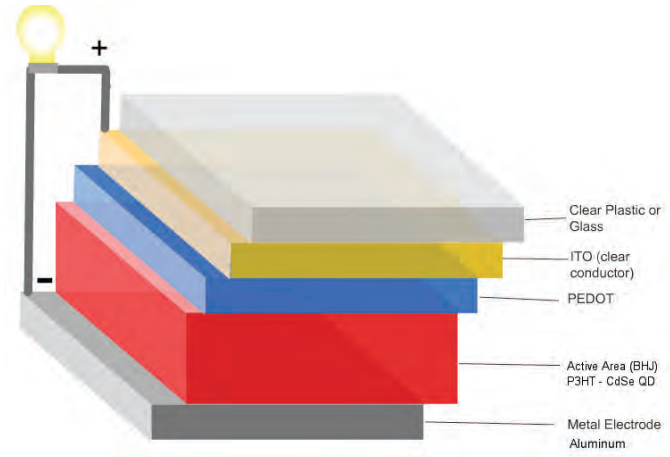

Figure 1. General structure of an organic solar cell.

Results and Discussion

In the method in which excess precursor was dripped into a reaction solution to create red shifted QDs, size increased to around 595 nm max absorbtion for the first exciton peak before polydispersity developed.

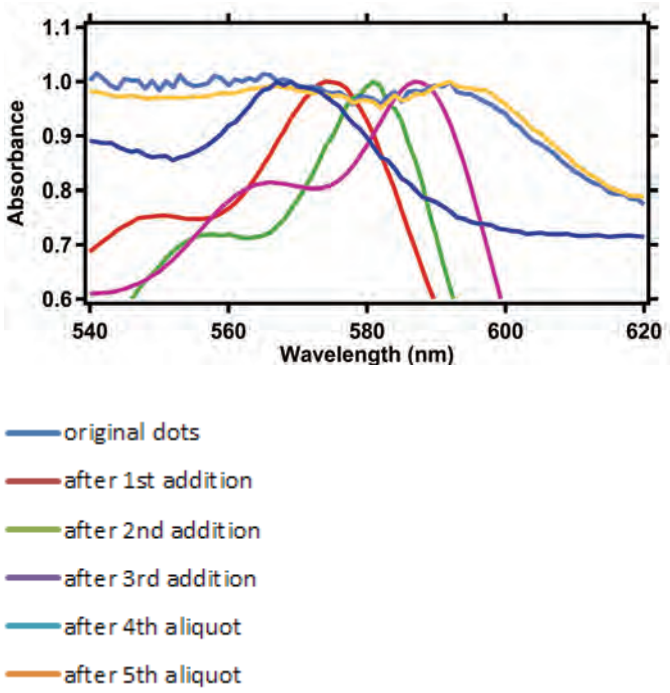

Figure 2. UV-Vis spectroscopy of aliquots from QD growth method.

The blue shifted QDs showed absorption maxima consistently in a range from about 470- 490 nm with very low yields due to rapid quenching of the reaction. Multiple reactions were required to create masses of QDs sufficient for device fabrication, leading to some polydispersity in devices using these QDs.

Concerning V_{OC}, preliminary data from a limited sample size using devices of CdSe-P3HT and Lead Sulfide (PbS)-poly(2,3-didecyl-quinoxaline-5,8-diyl-alt-N-octyldithieno[3,2-b:2',3'-d]pyrrole) (PDTPQx) shows variation between the two types of devices.

It has been assumed that the relationship between V_{OC} and bandgap will be independent of the compositional changes; however data comparing them shows an increase in V_{OC} for the larger bandgap material, suggesting the bandgap change as a possible reason for the V_{OC} increase.

IV curves for devices made using blends of P3HT/CdSe and PDTPQx/PbS show different V_{OC} measurements in Figure 3.

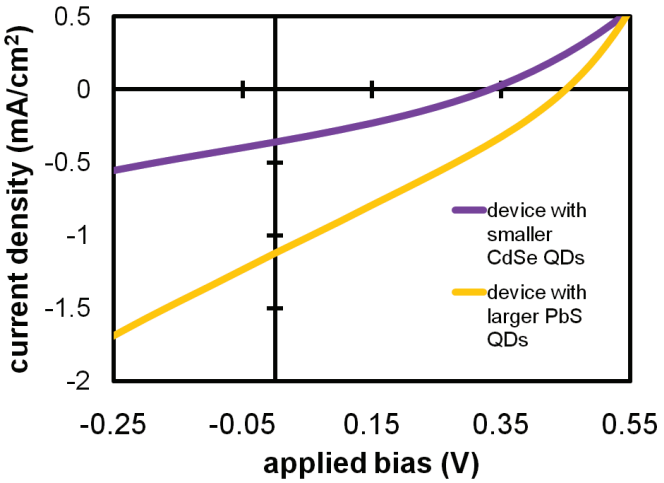

Figure 3. V_{OC} measurements shown here are significantly different between CdSe and PbS devices.

In other preliminary data, a trend between V_{OC} and bandgap between devices of the same composition was not readily apparent as shown in Figure 4.

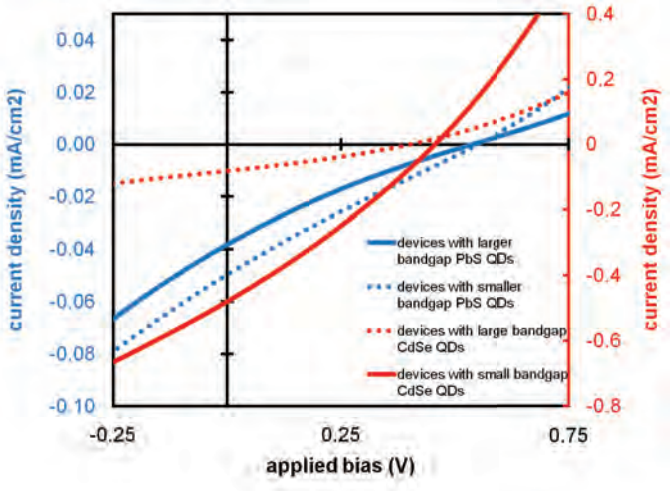

Figure 4. IV curves showing no difference between slightly differed sizes of QDs with the same composition.

Sets of QDs synthesized with larger bandgap differences between them described earlier are currently being made into devices and tested.

Devices made using red shifted QDs at 597 nm were successfully tested. Insufficient trials have been conducted to show that these measurements of V_{OC} are different from measurements of intermediate sizes of CdSe QDs shown in Figure 4. More data may be able to show agreement with or disprove the idea that bandgap is capable of increasing V_{OC}.

Ligand exchange on 494 nm CdSe QDs failed, leading to non-functioning devices. Reasons for this may include under cleaning of the QDs before ligand exchange or some difference in the behavior of the QDs due to their size. It may also be possible that some aspect of this altered synthesis leads to QDs with different ligand binding capabilities and preferences. IV curves and other measurements from these devices will likely be useful data in determining the possibility of controlling V_{OC} and some actual measurement of a relationship should one exist.

Conclusions

Devices continue to be made and tested, currently using the quantum dots described earlier. More data is required to make a positive statement on the relationship between bandgap and open circuit voltage. It is impossible from the trials discussed here to determine if there is any significant dependence.

There are many possibilities remaining. It may be that no measurable correlation exists and that other factors dominate determination of V_{OC}. It is also possible that the lack of correlation in some devices is due to undetermined differences in those devices which have a larger role in determining current flow than QD bandgap. In the second case, that knowledge may lead to further studies.

The hope here is that by using QDs of the same composition with larger bandgap differences between them, devices will show a significant change in V_{OC} suggesting that is the source of the relationship seen in Figure 3. This is supported by the most recent data using large sized CdSe QDs.

After testing a large number of devices, it would be ideal for many data points to show a relationship that can be described mathematically. This could then be used more easily as a method of determining at which QD size the greatest advantage to solar cell efficiency lies. Ultimately; any result is useful and pertinent which allows for the ability to control V_{OC} and may lead toward higher efficiency solar cells.

References

1. C. J. Brabec, A. Cravino, D. Meissner, N. S. Sariciftci, T. Fromherz, M. T. Rispens, L. Sanchez, J. C. Hummelen, Origin of the Open Circuit Voltage of Plastic Solar Cells, Adv. Funct. Mater. 2001, 11, 374-380.

2. H.-Y. Chen, J. Hou, S. Zhang, Y. Liang, G. Yang, Y. Yang, L. Yu, Y. Wu & G. Li, Polymer Solar Cells with Enhanced Open-Circuit Voltage and Efficiency Nature Photonics 2009, 3, 649-653.

3. C. Deibel, and V. Dyakonov. Polymer–Fullerene Bulk Heterojunction Solar Cells, Rep. Prog. Phys. 2010, 73

4. A. Gadisa, M. Svensson, M. R. Andersson, and O. Inganas, Correlation Between Oxidation Potential and Open-Circuit Voltage of Composite Solar Cells Based on Blends of Polythiophenes/ Fullerene Derivative Appl. Phys. Lett. 2004, 84 1609

5. J. Cremer, P. Bäuerle, M. M. Wienk, and R. A. J. Janssen, High Open-Circuit Voltage Poly(ethynylene bithienylene): Fullerene Solar Cells, Chem. Mater. 2006, 18, 5832-5834.

Acknowledgments

Funds for this research were provided by the Center on Materials and Devices for Information Technology Research (CMDITR), an NSF Science and Technology Center No. DMR 0120967. The author would also like to thank the Ginger research group at the University of Washington including mentor Elisabeth Strein for use of their lab space and expertise, and members of the Dalton group at the University of Washington, especially Meghana Rawal for help on various sections of the project.

JULIA RUTHERFORD is hoping to complete her undergraduate degree at Pacific Lutheran University and pursue graduate studies in the sciences.

CdSe Quantum Dot Synthesis and Ligand Exchange for Use in Hybrid Solar Cells

OSCAR ERIC SANDOVAL, California State Polytechnic University
Katherine Mazzio, Christine Luscombe, University of Washington

Introduction

Traditional photovoltaics (PVs) can be highly efficient; converting over 30% of the sun's light into electricity.[1] They are also attractive due to their high charge mobilities and long life times. Although traditional photovoltaics possess these important characteristics they are also expensive to make due to the need of high temperatures and vacuum processes.[2] One alternative to traditional solar cells is the organic solar cell, which has a short lifespan, low charge mobility, and a short exciton diffusion length, but is solution processable and potentially cheaper to make than its counterpart. The exciton is a bound entity made up of an electron and hole pair. In order to promote exciton disassociation into charge carriers, the dimensions of the polymer should be on the order of the exciton diffusion length. In the case of organic solar cells this is about 3-15 nm.[3] Once the exciton has diffused the charge carriers must be collected by the electrodes before recombination occurs. One problem is that in bulk heterojunction PV cells, cells whose donor and acceptor phases have been tightly blended together, the large interfacial area between the acceptor-donor interface makes it easy for recombination to occur.[3] The HOMO and LUMO levels cause another setback. The band gap is the energy difference between the HOMO, highest occupied molecular orbital, and the LUMO, lowest unoccupied molecular orbital as can be seen in Figure 1.

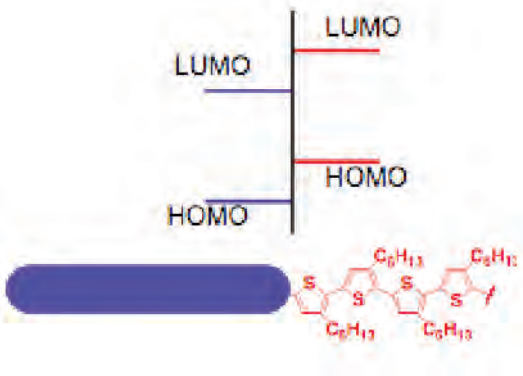

Figure 1. Energy level diagram, the blue rod is the inorganic material.

In order to effectively dissociate excitons, a certain offset between the HOMO and LUMO levels must be achieved. The optimum LUMO offset needs to 0.3 eV. Until the LUMO level offset of the donor and acceptor can be optimized the bulk heterojunction PV's efficiency will be reduced.[4] One solution may be to create a hybrid PV, one that possesses the low cost, solution processability of the organic PV and the high charge mobility of the inorganic PV. The ideal configuration for the hybrid PV is a blended interface in which the acceptor and donor material are mixed. This configuration may allow for the ideal disassociation to occur.[5]

We will be working with a hybrid PV with an organic polymer poly-(3-hexylthiophene) that acts as the donor phase, or P-type organic semiconductor and a quantum dot, CdSe, as the acceptor phase, or N-type inorganic semiconductor. The quantum dots are ideal for use in hybrid solar cells because of their low cost solution processability and ability to control their band gaps by controlling their size.[3] The shape of the quantum dot we will be seeking to implement is the nanorod shape. The nanorod is useful because it allows for charge transfer with less interparticle hops.[5] Nanorods have the tendency to lie flat on the plane of the film, which is not ideal for charge transfer. If this proves to be a problem, we may investigate CdSe tetrapods, as their shape prevents them from lying flat. PVs incorporating CdSe tetrapods have shown to have efficiencies of up to 2.8%. [6]

Objectives

My objective for the summer was to determine how to change the size of the quantum dots and the execution of ligand exchanges. I experimented with the quantum dots to change their dimension in order to accommodate these needs in the future of this research. In order for the objective to be met I learned how to synthesize CdSe, which was done by working with the Ginger group in the Chemistry department at the University of Washington. According to Sand-Hyun Choi, et al, varying the concentration of Cd and the Se precursor can change the dimension of the quantum dots.[2] In order to produce nanorods as opposed to spherical quantum dots, the precursor is injected multiple times instead of just once.[3] To perform the ligand exchange a substance is added that will form a stronger bond than the ligand already attached. This will make the quantum dots attach to the ligand that will form the stronger bond.

Experimental

CdSe Synthesis

Materials used to perform the CdSe quantum dot synthesis include Selenium (Se), tri-n-butylphosphine (TBP), 90% octadecene (ODE), Cadmium oxide (CdO), 90% oleic acid, and octadecene (ODE). The ligands used in the synthesis were 90% tri-n-octylphosphine oxide and 95% octadecylamine (ODA). The tri-n-butylphosphine was purchased from Strem Chemicals and used as received. All other

materials were purchased from Aldrich and used as received.

CdSe quantum dots were synthesized according to the CdO/amine-route synthesis. Se-TBP stock solutions were prepared in inert atmosphere at room temperature. 1.4 g Se and 3.84 g TBP were combined and allowed to stir over night until all of the Se was dissolved. 12.33 g ODE was then added and mixed well.

In a typical CdSe synthesis, 0.077 g CdO, 2.0 g ODE, and 0.68 g oleic acid are heated to 220 °C under N_2. While heating, this mixture turns from brown to clear due to the CdO reacting with the oleic acid to form Cd-oleate. Once all of the CdO has reacted, the solution is allowed to cool to room temperature at which point the ligands, 0.5g TOPO and 1.5 g ODA, are added and stirred until well mixed. This solution is then put under vacuum for at least an hour and heated to 110 °C. After an hour, the solution is heated to 260 °C under N_2. Once the injection temperature is reached, 3.0 g of the Se-TBP stock solution is swiftly injected with an N_2 purged needle. The quantum dots are grown at this temperature until the desired size is reached. The solution is then quenched with a water bath and allowed to cool to room temperature. The quantum dots may be extracted with methanol and hexanes. The methanol will dissolve the ligands and the hexanes will dissolve the quantum dots, the use of as little hexanes as possible is best.

Ligand Exchange

A preliminary ligand exchange was performed on the quantum dots. Only about 10 mL of quantum dots were used in the ligand exchange. 15 mL of pyridine was added to the 10 mL of quantum dots and this mixture was refluxed under nitrogen for 24 h. Excess hexane was added to the pyridine quantum dot solution and then centrifuged to facilitate separation. The supernatant solution was discarded. The pyridine and phosphonic acid form a salt; to remove this, toluene was added to the precipitate. This solution was centrifuged at 3000 rpm for 5 min, and 2 mL of a pyridine/chloroform solution was added. The solution was super sonicated for five minutes then centrifuged for 60 minutes at 3300 rpm.[9]

Characterization

A Perkin Elmer Lambda 9 UV/Vis spectrophotometer was used to characterize the optical properties of the quantum dots and estimate their sizes. An FEI Tecnai F-20 TEM was used for particle morphology and dimension verification. It was operated with a 120 kV accelerating voltage.

Results and Discussion

From the absorbance spectra provided by UV-vis in Figure 2 we were expecting the size of the quantum dots to be in the range of 2 to 8 nm because of the data in Figure 3.[7] We were interested in the absorbance spectra of the quantum dots that were run through UV-vis 17 h after synthesis, because our quantum dots were run through UV-vis a long time after they were first synthesized. As can be seen in Figure 2, the first absorbance peak is seen at 563 nm. This is close to the first absorbance peak of 560 nm seen in Figure 3.

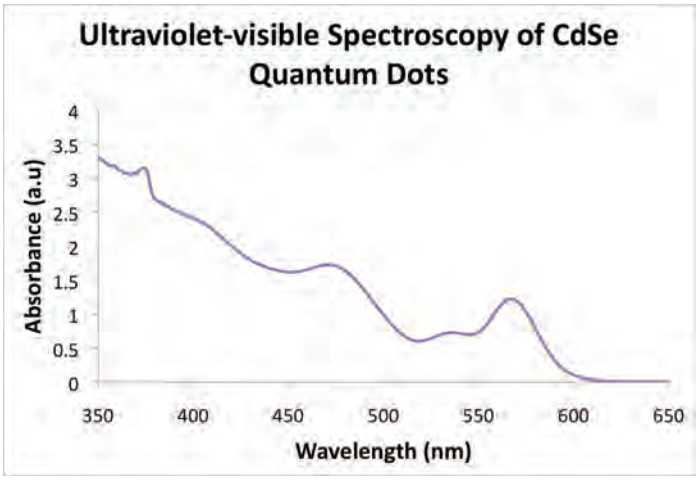

Figure 2. Absorption measurements of QDs first batch.

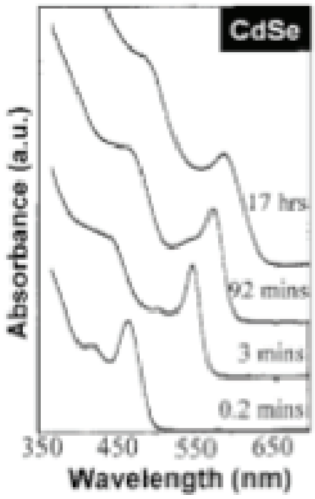

Figure 3. Absorbance spectra of quantum dots at varying times after synthesis.[7]

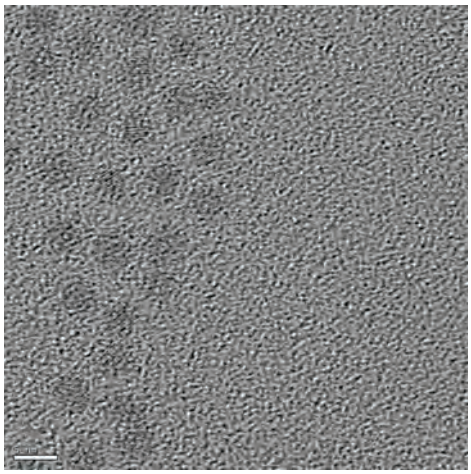

Figure 4. TEM imagery of quantum dots 4 nm in size.

TEM imagery in Figure 4 shows that the quantum dots were 4 nm in diameter, within our range of expectation. The quantum dots can be seen to be uniform in shape. The second TEM image, Figure 5, shows the quantum dots 6 nm in size and uniform in shape. The size difference can be associated with the difference in the amount of Se-TBP solution that was injected during the synthesis. For the quantum dots 4 nm in size the amount of Se-TBP injected was 4.5 g. For the quantum dots 6 nm in size 9 g of the Se-TBP solution was injected.

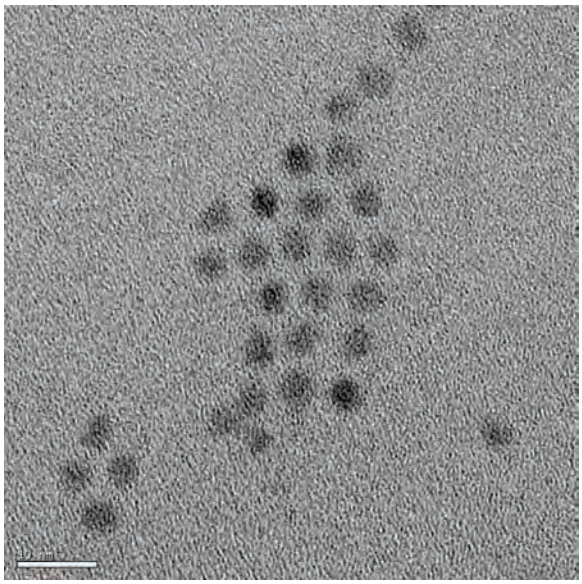

Figure 5. TEM imagery of quantum dots 6 nm in size.

The ligand exchange performed was a preliminary study that will lead to a systematic ligand exchange as seen in Figure 6.

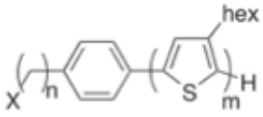

Figure 6. Systematic ligand exchange that is to be performed to CdSe quantum dots. X= SH, SeH, NH_2, PO_3H, CS^-_2. n= 0, 1, 4, 6, 8, 10.

The ligand the quantum dots are capped with when they are first synthesized is TOPO; this is a long molecule that stabilizes the nanoparticle and allows for the formation of the quantum dot. By performing the ligand exchange we believe this will allow for better performance when the quantum dots are used in devices. If we vary n we are varying the length of the chain, and by doing so we can strike a balance between the amount of charge dissociation and recombination.

Conclusion

CdSe quantum dots of varying size and uniform in shape using TOPO as the ligand were fabricated. The dimension of the quantum dots changed as the amount of Se-TBP stock solution increased. The research performed has laid out the groundwork to synthesize nanorods. Nanorods are wanted for the manufacturing of devices because they require less interparticle hops for charge transfer. Nanorod synthesis was attempted but proved unsuccessful. We believe the problem lies in the heating of the solution while synthesizing. If too much heat is applied to the solution, the quantum dots will tend to form spheres rather than nanorods.[8]

References

1. Sung, B., et al., Vertically Segregated Hybrid Blends for Photovoltaic Devices with Improved Efficiency, J. Appl. Phys. 2005, 97.

2. Choi, S. H., et al., Synthesis of Size controlled CdSe Quantum Dots and Characterization of CdSe-conjugated Polymer Blends for Hybrid Solar Cells, J. Photochem. Photobio. A 2006, 179, 135.

3. Goh, C.; Scully, S. R.; McGehee, M. D., Effects of Molecular Interface Modification in Hybrid Organic-inorganic Photovoltaic Cells. J. Appl. Phys. 2007, 101.

4. Gilles, M.; Scharber, M. C.; Brabec, C. J., Polymer-Fullerene Bulk-Heterojunction Solar Cells, Adv. Mater. 2009, 21, 1323.

5. Sun, B.; Marx, E.; Greenham. N. C., Photovoltaic Devices Using Blends of Branched CdSe Nanoparticles and Conjugated Polymers, Nano Letters 2007, 3.7, 961.

6. Dubois, F., et al., A Versatile Strategy for Quantum Dot Ligand Exchange, J. Am. Chem. Soc. 2007, 129, 483.

7. Peng A. Z.; Peng X., Formation of High-Quality CdTe, CdSe, and CdS Nanocrystals Using CdO as Precursor, J. Am. Chem. Soc. 2001, 123, 184.

8. Shieh, F.; Saunders E. A.; Korgel A. B., General shape control of Colloidial CdS, CdSe, CdTe, Quantum Rods and Quantum Rod Heterostructures, J. Phys. Chem. B, 2005, 109, 8542

Acknowledgements

Funding for this research was provided by the Center on Materials and Devices for Information Technology Research (CMDITR), an NSF Science and Technology Center No. DMR 0120967. Part of this work was conducted at the University of Washington Nano Tech User Facility, a member of the NSF National Nanotechnology Infrastructure Network (NNIN). Thanks to Elisabeth Strein for her help and guidance through the synthesis. Thanks also go to everyone in the Luscombe group for allowing me to work alongside them especially Natasha Doubina and Shane Boyd. A special thanks goes to my mentor Katherine Mazzio for her help, her guidance, and her support. And everyone in the Hooked on Photonics program for being so friendly and welcoming, especially April Wilkinson.

OSCAR ERIC SANDOVAL is an electrical engineering major at the California State Polytechnic University, Pomona. He plans on attending graduate school and pursuing a doctorate in electrical engineering to further work on alternative energy.

Acceptor-Donor-Acceptor N-channel Organic Semiconducting Materials Utilizing Naphthalene-Diimide

BRIAN SEIFRIED, Georgia Institute of Technology
Lauren Hayden, Seth R. Marder, Georgia Institute of Technology

Introduction

Organic field effect transistors (OFETs) are exciting alternatives to inorganic transistors, having applications in electronic paper,[1, 2, 3] sensors,[4, 5] and memory devices such as radio frequency identification cards (RFIDs).[6, 7] The performance of OFETs may not be able to compete with that of crystalline silicon field effect transistors (FETs), but OFETs offer the possibility of replacing amorphous silicon FETs by possessing unique advantages such as being lightweight and flexible, as well as having a potentially lower production cost and a lowerfabrication temperature.[8]

Developments in n-channel OFETs lag behind those of p-channel OFETs for a variety of reasons. The LUMO level of organic materials is typically around 2-3 eV. This creates an extremely high injection barrier towards common (e.g. gold and platinum) electrodes. Metals with appropriately low work functions, such as calcium or magnesium, are not environmentally stable. On top of all of those problems is the issue that organic radical anions are susceptible to being oxidized by oxygen and water. The motivation for developing n-channel FETs, despite the number of difficulties, is to create logic elements that go beyond single transistors, e.g., inverters. Inverters consist of interconnected p-channel and n-channel transistors that are wired in such a way that when in a steady logic state one transistor is on and the other is off. This reduces current flow to a minimum, thus greatly reducing power consumption when compared to other circuit architectures.[10] The strategy chosen, in an attempt to remedy some of the problems with n-channel OFETs, is to synthesize molecules with lower LUMO levels. Ideally, a lower LUMO would address several issues, such as, establishing lower energy barriers for charge injection into stable electrodes like gold and being less susceptible to electron trapping impurities.[9] The primary electron trapping reactions are oxidation by H_2O ($2H_2O + 2e^- \rightarrow H_2 (g) + 2OH^-$) and O_2 ($O_2 + 4H^+ + 4e^- \rightarrow 2H_2O$) in the air; to avoid oxidation by H_2O, it is believed that a reduction potential more positive than -0.66 V vs. SCE is required, whereas a potential greater than +0.57 V vs. SCE is necessary to avoid oxidation by O_2. It has been suggested that the large over-potential observed for oxidation by O_2 helps prevent ambient trapping in materials with reduction potentials less than +0.57 V vs. SCE.[10] To lower the LUMO of the semiconducting materials, two strategies were implemented: the use of acceptor-donor-acceptor, and electron acceptor interactions. The acceptor-donor-acceptor approach is typically used to decrease the band gap through the hybridization of the energy levels of electron donating and electron accepting portions, whereas, the incorporation of electron withdrawing groups serves to lower orbital energies of the molecule by increasing the electron affinity.[10, 11]

Naphthalene diimide (NDI) was chosen as the initial building block towards the synthesis of electron transport materials for OFETs due to its robust nature, flexible molecular orbital energetics, tailorable charge transport properties,[10] and possession of a reduction potential high enough to avoid oxidation by H_2O.[12] The series of target molecules involve two NDI molecules connected by a bridge, with the goal of the bridge being to allow the orbitals of the two NDIs to interact through the bridge, thus further lowering the LUMO of the molecule.

Experimental

Synthesis of 4-bromo-2,7-dialkylbenzo[lmn][3,8]phenanthroline-1,3,6,8(2H,7H)-tetraone

Naphthalene 1,2:5,6-tetracarboxylic dianhydride (NDA) (20.0706 g, 74.8400 mmol) was dissolved in oleum (390 mL) and heated to 55 °C. Potassium 1,5-dibromo-4,6-dioxo-1,4,5,6-tetrahydro-1,3,5-triazin-2-olate (DBI) (19.5 g, 60.0 mmol) was dissolved separately in oleum (250 mL). The DBI solution was added to the NDA solution and heated to 85 °C for 24 h. The resulting solution was quenched in ice water and filtered by vacuum filtration washing with methanol (3 x 25 mL). A solution of the crude product and n-alkylamine (0.570 mol) in glacial acetic acid (600 mL) was refluxed under nitrogen for 20 min. After cooling, the solution was precipitated in methanol and collected by vacuum filtration. The crude product was dissolved in dichloromethane, filtered to remove solids, and purified by flash chromatography (silica gel, dichloromethane). The solvent was removed under reduced pressure. The product was collected as a yellow solid (4.23 g, 8.25 mmol, 11.5%). A sample of the product was further purified by vacuum sublimation (39.7 mg, 0.0775 mmol, 36.4 % recovery). ^{13}C NMR (400 MHz, $CDCl_3$) δ 162.40, 161.78, 161.66, 160.97, 138.36, 131.61, 130.66, 128.60, 128.53, 126.78, 125.98, 125.91, 125.64, 123.85, 41.47, 41.09, 31.46, 31.42, 27.93, 27.87, 26.75, 26.66, 22.54, 22.49, 14.01.

Synthesis of 4,4'-(thieno[3,2-b]thiophene-2,5-diyl)bis(2,7-dialkylbenzo[lmn][3,8]phenanthroline-1,3,6,8(2H,7H)-tetraone)

A solution of 4-bromo-2,7-dialkylbenzo[lmn][3,8] phenanthroline-1,3,6,8(2H,7H)-tetraone (NDI-Br) (1.00 g, 1.96 mmol), copper iodide (0.022 g, 0.117 mmol), 2,5-bis(tributylstannyl)thieno[3,2-b] thiophene (0.683 g, 0.951 mmol) in anhydrous toluene (20 mL) was heated to 90 °C under N_2. Tetrakis (triphenylphosphine) palladium ($Pd(PPh_3)_4$) (0.584 g, 0.506 mmol) was added to the solution. The solution was refluxed for 18 h. After cooling the reaction mixture was diluted with dichloromethane and filtered through celite. The filtrate was concentrated through rotary evaporation. The crude product was purified by flash chromatography (silica gel, 10:2 chloroform: ethyl acetate). The product was precipitated from iso-propanol and

collected as a purple solid (0.257 g, 0.256 mmol, 26.9 %). ^{13}C NMR (400 MHz, $CDCl_3$) δ 162.69, 162.38, 162.36, 161.87, 143.22, 140.91, 140.10, 136.08, 131.51, 130.82, 127.83, 126.87, 126.57, 126.35, 125.30, 123.63, 120.60, 41.22, 41.02, 31.48, 31.46, 28.00, 26.75, 26.70, 22.55, 22.51, 14.00.

Results and Synthetic Progress

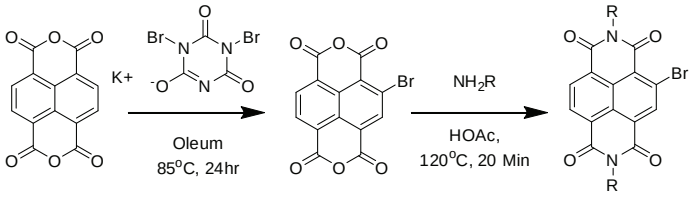

Scheme 1. Synthesis of NDI-Br.

Several conditions for the synthesis of 4-bromo-2,7-dialkylbenzo[lmn][3,8] phenanthroline-1,3,6,8(2H,7H)-tetraone (NDI-Br) were investigated. Originally various equivalents of bromine with catalytic amounts of iodine were used as the brominating agent, but the yields of those syntheses were comparably low. Potassium 1,5-dibromo-4,6-dioxo-1,4,5,6-tetrahydro-1,3,5-triazin-2-olate (DBI) was substituted as the brominating agent and resulted in better yields. A 20 g scale synthesis of NDI-Br was performed, and 4.23 g of slightly impure NDI-Br was obtained. There still are significant quantities of material requiring purification. The NDI-Br was characterized by ^{1}H NMR, ^{13}C NMR, and high-resolution mass spectrometry (HRMS). A sample of NDI-Br (0.109 g sent, 39.7 mg, 36.4 % recovery) was further purified by vacuum sublimation and sent for elemental analysis (EA).

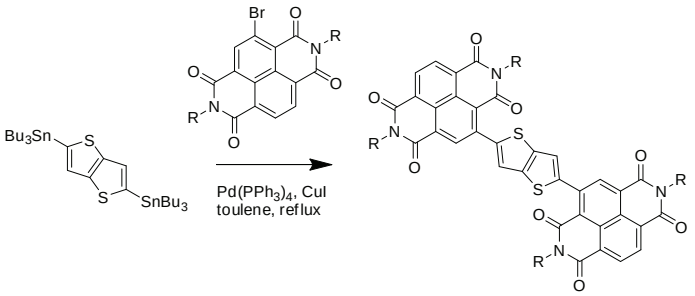

Scheme 2. Synthesis of NDI-Thienothiophene oligomer.

4,4'-(thieno[3,2-b]thiophene-2,5-diyl)bis(2,7-dialkyllbenzo[lmn][3,8] phenanthroline-1,3,6,8(2H,7H)-tetraone) (NDI-TT-NDI) was synthesized by a Stille Coupling reaction. The 2,5-bis(tributylstannyl) thieno[3,2-b]thiophene was synthesized by Qing Zhang and a sample was used for this synthesis. The product of the reaction was purified by column chromatography: first by chloroform on silica gel, then in 2% ethyl acetate in chloroform solution on silica gel. The product was then precipitated from iso-propanol. The synthesis resulted in 0.257 g of NDI-TT-NDI. The product has been characterized by ^{1}H NMR and ^{13}C NMR, and is being characterized by HRMS and EA.

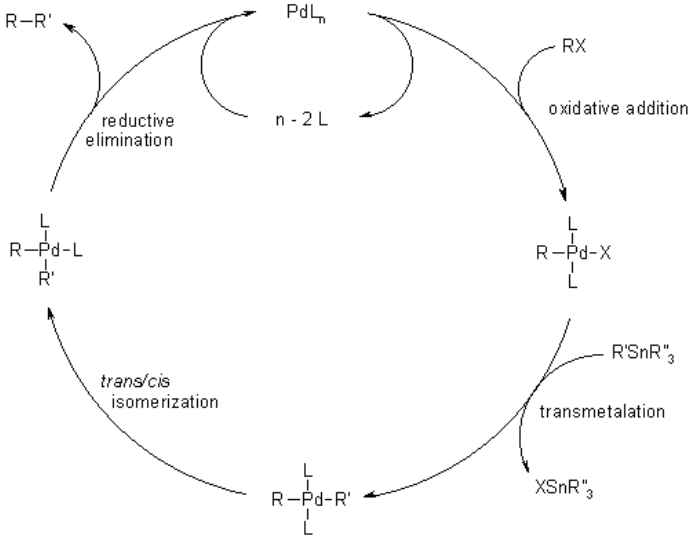

Figure 1. Generic Catalytic Cycle for Stille Coupling Reactions.[13]

Discussion

NDI-Br is a challenging material to synthesize because it is difficult to stop the brominating agent from performing multiple brominations on the NDI core. There were three main products formed when attempting to synthesize NDI-Br: NDI-Br, the desired product; NDI-Br_2, the dibromonated compound; and NDI, the non-brominated compound. None of the attempts using bromine with catalytic amounts of iodine as the brominating agent resulted in NDI-Br as the major product. DBI was chosen because in literature it had been shown as a successful brominating agent for NDA.[14] The synthesis utilizing DBI resulted in NDI-Br as the major product when utilizing 0.80 equivalents of brominating agent.

It was difficult to isolate the NDI-Br from the reaction mixture. The NDI-Br_2 is much less soluble in most solvents than NDI-Br, making a recrystallization to isolate the product unfeasible. When the reaction mixture was purified by column chromatography the NDI-Br_2 had a tendency to precipitate out of solution and subsequently redissolve, causing trace impurities in all of the fractions. The amount of NDI-Br_2 put on the column was minimized by filtering the reaction mixture after it had been partially dissolved in dichloromethane. Vacuum sublimation does not fully remove the NDI-Br_2, as it is still visible in small amounts by ^{1}H NMR. The pure NDI-Br is expected to be a white solid, but a yellow color is observed when trace amounts of NDI-Br_2 are present.

The NDI-TT oligomer reaction mixture was challenging to purify. The reaction mixture's behavior observed by thin layer chromatography (TLC) did not directly correlate to its behavior by column chromatography. The non-reacted NDI-Br was removed from the reaction mixture by flash chromatography in silica gel and chloroform. When eluded by TLC in a 1% methanol in chloroform mixture, three spots were observed (R_f: 0.10, 0.20, 0.30), but the mixture failed to separate when run on the column. This may be due to solubility issues, because the NDI-TT-NDI has very little solubility in methanol. NDI-TT-NDI is relatively soluble in ethyl acetate, and

separated on 2% ethyl acetate in chloroform column. There were still trace impurities by ^{1}H NMR, but those were removed by precipitation from *iso*-propanol.

Conclusion

The synthesis of NDI-Br was investigated and optimized settling on using DBI as a brominating agent with 0.80 equivalents. An NDI-TT-NDI oligomer was synthesized and is being characterized. The NDI-TT oligomer is part of a molecular series examining the effect of the conjugation length of the bridge molecule on physical and electronic properties.

Future Outlook

The NDI-TT-NDI must be fully characterized synthetically then tested for transistor behavior. 4,4'-(thiophene-2,5-diyl)bis(2,7-dialkylbenzo[lmn][3,8] phenanthroline-1,3,6,8(2H,7H)-tetraone) (NDI-T-NDI) will be synthesized to continue the molecular series.

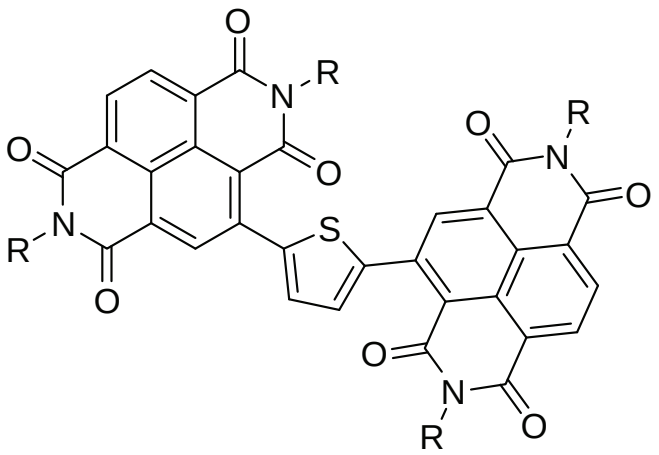

Figure 2. NDI-T-NDI.

References

1. Rogers, J. A.; et al.; Proc. Nat. Acad. Sci. USA 2001, 98, 4835.
2. Gelinck, G. H.; et al.; Nat. Mater. 2004, 3, 106.
3. Sheraw,C. D.; et al., Appl. Phys. Lett. 2002, 80, 1088.
4. Zhu, Z.-T.; et al.; Appl. Phys. Lett. 2002, 81, 4643.
5. Crone, B. K.; et al.; J. Appl. Phys. 2002, 91, 10140.
6. Voss, D.; Nature 2000, 407, 442.
7. Baude, P. F.; et al.; Appl. Phys. Lett. 2003, 82, 3964.
8. Di, C.; Yu, G.; Liu, Y.; Zhu D.; J. Phys. Chem. B 2007, 111, 14083-14096.
9. Sirringhaus, H.; Adv. Mater. 2005, 17, 2411-2425.
10. Jones, B.A.; Facchetti, A.; Wasielewski, M.R.; Marks, T. J.; J. AM. Chem. Soc. 2007, 129, 15259-15278.
11. Mullekom, H. A. M; et al.; Mater. Sci. Eng., 2001, 32, 1-40.
12. Katz, H. E.; Johnson, J.; Lovinger, A. J.; Wenjie, L.; J. Am. Chem. Soc. 2000, 122, 7787-7792.
13. Organic Chemistry Portal Stille Coupling. http://www.organic-chemistry.org/namedreactions/stille-coupling.shtm (accessed July 9, 2010).
14. Chen, Z.; Zheng Y.; Yan H.; Facchetti A.; J. Am. Chem. Soc. 2009, 131, 8-9.

Acknowledgments

This research was made possible by the mentorship of Lauren Hayden as well as Seth Marder and the Marder research group. Funds for this research were provided by the Center on Materials and Devices for Information Technology Research (CMDITR), an NSF Science and Technology Center No. DMR 0120967.

BRIAN SEIFRIED is currently a rising second year student at Georgia Institute of Technology working towards a bachelors degree in Chemical and Biomolecular Engineering. He plans on pursuing an advanced degree in graduate school.

Linewidth Narrowing of Sodium Guidestar Semiconductor Laser

NATHANIAL SHEEHAN, University of California, Santa Barbara
Chris Hessenius, Mahmoud Fallahi, University of Arizona

Abstract

We report on the characterization and linewidth narrowing of the fundamental wavelength of an infrared VECSEL. The VECSEL is shown to emit multi-watt CW laser light, and the addition of intra-cavity birefringence filters (BFs) reduces the linewidth significantly. A linewidth of 95 MHz was achieved with a 20T BF.

Introduction

We report on the characterization and linewidth narrowing of a high power tunable infrared laser, which can be modified to become a yellow-orange laser. The laser has been designed to cover the wavelength range of 1147 nm to 1197 nm. A yellow-orange laser (~589 nm) is desired for applications in adaptive optics as a sodium guidestar laser. This modification from infrared to optical wavelengths is based on intra-cavity frequency doubling of the widely-tunable, highly-strained InGaAs/GaAs vertical-external-cavity surface-emitting laser (VECSEL) operating near 1175 nm. Development of a semiconductor-based yellow laser is very attractive for their high-gain, large volume production and low-cost.[1] Linewidth narrowing is important because it is more efficient for the power from our laser to be at the specific wavelength at which sodium fluoresces. A linewidth of less than 100 MHz is targeted.

In general, optically pumped vertical-external-cavity surface-emitting lasers (VECSELs) using multi-quantum well semiconductors are very attractive as low-cost high-power high-brightness sources.[2,3] In addition, by having easy access to the intra-cavity, several attractive features such as wavelength tuning and frequency doubling for visible generation can be achieved. Intra-cavity frequency doubling is used because, due to their limited direct band-gap energy, it is difficult to fabricate a range of visible emission wavelengths. In sum, VECSELs are low cost, high power, easy access to cavity, tunable lasers. Along with applications in adaptive optics such as a sodium guidestar lasers (when frequency doubled), VECSELs have possible applications in the fields of medical technology and communications.[1]

A sodium (Na) guidestar is an artificial reference point used for adaptive optics, made by exciting sodium ions ~90 km above earth's surface with a laser. Adaptive optics is a method of correcting atmospheric wavefront distortions from extraterrestrial light sources, providing higher resolution images of the object. It requires a very bright reference object to be very near the object that one desires to look at. Only 1% of the sky is naturally accessible to adaptive optics, but with a Na guidestar, laser telescopes can make their own bright reference object, opening up 80% of the night sky.[4] Na guidestar lasers for adaptive optics is a relatively new field, and dye lasers were the first to be used. Dye lasers are expensive and large, sometimes being contained in a room at the base of a telescope. Semiconductors are emerging as a source of Na guidestars because they have several attractive characteristics such as simple setup, small size, low cost, and high output power. Our VECSEL is innovative because it can be designed for specific wavelengths, is tunable, and allows for easy cavity access.[1]

Methods

To characterize the fundamental operation of the laser, we focused a fiber-coupled 808 nm pump source on a 480 μm-diameter spot on the chip. A folding concave mirror that is highly reflective at the fundamental (~1175 nm) wavelength is used along with an external flat mirror that is 4% transmissive. The external flat mirror serves as the output coupler.[5] The radius of curvature for both output couplers was 30 cm, and the cavity length was 9 cm.

We characterized the laser chip by measuring the output power and spectrum for each current, at each temperature, with each output coupler. The spectrum is read by an optical spectrum analyzer (OSA). We control the pump power to our VECSEL by changing the current to our diode pump laser. To equate current to pump power requires a few calculations. The net pump power is the pump power minus the pump light that is reflected off the chip (chip reflectivity power). Thus, we can express our results in terms of current or net pump power. The current range was from threshold current, where the VECSEL starts to lase, to 40 A (~24 W net pump power). The temperatures we characterized the VECSEL at were 5, 15, and 25 °C. The output couplers had reflectivities of 96% and 98%. In addition, we measured chip surface photoluminescence.

We characterized the birefringent filters (BFs) by inserting each at Brewster's angle and measuring the output power and spectrum for each one, as we tuned it through the entire tunable range. Then we measured the output power vs. net pump power for the wavelength with the highest P_{out} (found in previous step). For fundamental signals, the functions of the BF are threefold: an extremely low-loss wavelength tuning component, a Brewster window to select polarization, and a filter introducing longitudinal mode discrimination.[2] The linear polarization and narrow linewidth of the fundamental beam are extremely important for the SHG phase-matching condition.[6] The key property for linewidth narrowing is that BFs favor transmitting a certain wavelength that undergoes the least loss.

We characterized the low finesse Fabry-Perot Etalon (FPE) by inserting it into the cavity and measuring the spectrums and output powers we observed. An FPE is an object with a medium between two

highly reflecting surfaces. Once light enters, it will be reflected within the etalon, either constructively or destructively interfering with itself. The key property is that a given FPE will have specific wavelengths that it lets pass because each self-interferes in a manner conducive to transmission for the given FPE width.[7] This helps explain how we will measure linewidths. We then characterized how the laser light was affected when passing through an external (i.e. not in the laser cavity) high finesse FPE by looking at the spectrum and output power after etalon transmission. The finesse of an FPE is the ratio of the free spectral range to the peak width.[8] As finesse increases, the peak narrows, but there is a tradeoff because less power is transmitted.

To measure the linewidth, and what each BF was able to reduce it to, we used a Scanning Fabry-Perot Interferometer (FPI). A scanning FPI is an FPE with variable width, d. A piezoelectric transducer changes the length of the cavity, and thus the wavelength that the FPI will let pass to the photodiode detector with ~100% transmission. Because the width of the cavity is programmed to change over the requisite range, we are able to observe the strength of transmission for every infinitesimal wavelength the laser emits. This is what creates the accurate image of the linewidth displayed on an oscilloscope. Coupling the laser output into the scanning FPI was very difficult, and required fine-tuning of the position and tip-tilt angles of two mirrors and a focusing lens. We set up our scanning FPI so the peak-to-peak distance would be 10 GHz. We then equated the milliseconds displayed on the oscilloscope to MHz, and zoomed in on our linewidth measurement. We introduced BFs into the cavity individually and measured the linewidth for each. Then we tried a combination of one BF and the low finesse FPE.

Results

The threshold current of our VECSEL differed depending on the setup parameters (the current magnitudes have been rounded up for digestibility and to be matched with the translation into net pump power) as shown in Table 1. Increasing either the percent reflectivity of the output coupler or the temperature decreased the threshold pump power. Barring the 98% OC at 25 °C, increasing the reflectivity or temperature by 10 °C decreases the threshold current by 4 A.

Threshold Net Pump Power and Current		
	96% OC	98% OC
5°C	16.8 W (27A)	13.2 W (23A)
15°C	13.1 W (23A)	9.92W (19A)
25°C	9.8 W (19A)	8.3 W (17A)

Table 1. Threshold net pump power and current.

For the 96% OC we are getting watts of continuous wave (CW) power, which is desirable (Figure 1). Slope efficiency (SE) increases as temperature decreases. The highest output power is 2.334 W at 25 °C. For the 98% OC, the threshold pump power to cause lasing is lower than for the 96% OC, but SE and P_{out} are lower, although still over 1 W (Figure 2). The same trend of SE increasing as temperature decreases can be seen. The highest output power is 1.782 W at 25 °C.

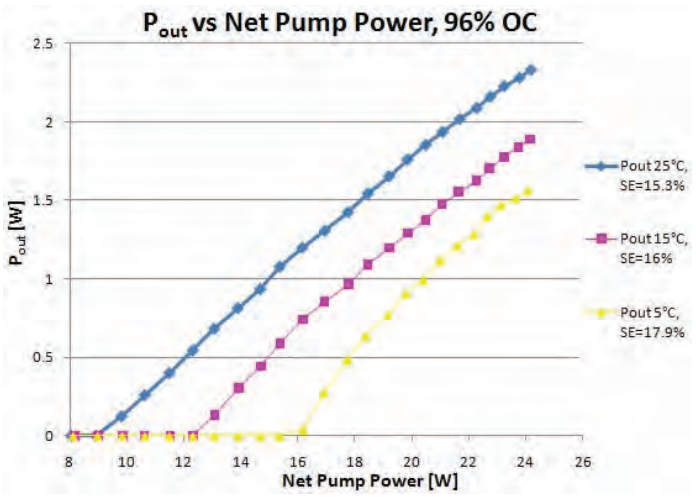

Figure 1. VECSEL fundamental output power vs. net pump power (SE: Slope efficiency).

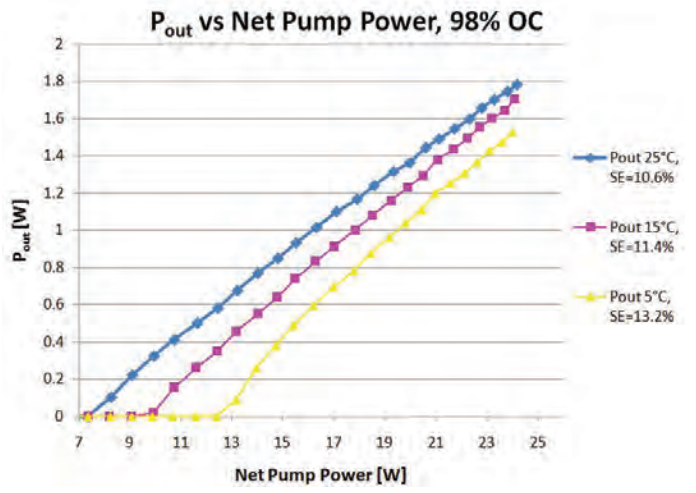

Figure 2. VECSEL fundamental output power vs. net pump power (SE: Slope efficiency).

For the 96% OC at 15°C there is a very visible red shift for emitted wavelengths (Figure 3). As pump power increases, the laser wavelength increases. This is undesirable because, regardless of variations in pump power and temperature, we would like to frequency double our laser and lase at the specific wavelength that causes sodium to fluoresce. Also, the linewidth broadens, which means our power will be spread across wavelengths we do not want to emit at. We show this lasing spectra because we performed linewidth narrowing at these conditions: 96% OC at 15 °C.

BF characterization occurred at 25 °C, although linewidth narrowing occurred at 15 °C. This is not expected to change the linewidths of our results significantly, only the output powers, which were not the focus of this initial study. Tuning curves for all BFs show that P_{out} and the tunable range decreases as BF thickness increases, as expected (Figure 4). This is a point of consideration, because it is expected that thicker BFs will narrow the linewidth more than thinner BFs, but at the cost of a decrease in output power. The curve for the 15T BF is notable because it deviates considerably from the expected shape

of a tuning curve (4T or 20T curve). This was likely due to alignment errors in the setup. The 2T and 6T curves both show a deviation from the expected curve shape at ~1181.5 nm. These deviations do not affect our results, but suggest re-measurement and further study of the tuning curves. Output powers for all BFs show that P_{out} decreases as BF thickness increases, as expected (Figure 5). The threshold pump power increased for all BFs by ~1.5 to 7 W. The slope efficiency appeared to increase for the 2T BF, and decreased for the four other BFs by 1.7 to 6.3%. This apparent increase is believed to be caused by slight cavity variations caused by moving the output coupler to take chip surface photoluminescence measurements.

The empty cavity P_{out} of our setup at 40 A pump current was 2.148 W. Inserting a BF into the cavity causes a loss of 0.28 to 1.41 W at 40 A (~13-66% decrease). Figure 6 shows two peaks found by inserting a low finesse FPE into the linear cavity. The separation and wavelengths shown here were the typical values. The output power of our empty cavity laser is 1.38 W at 35 A. The P_{out} with the low finesse FPE was 1.15 W, a decrease of 0.23 W (17%).

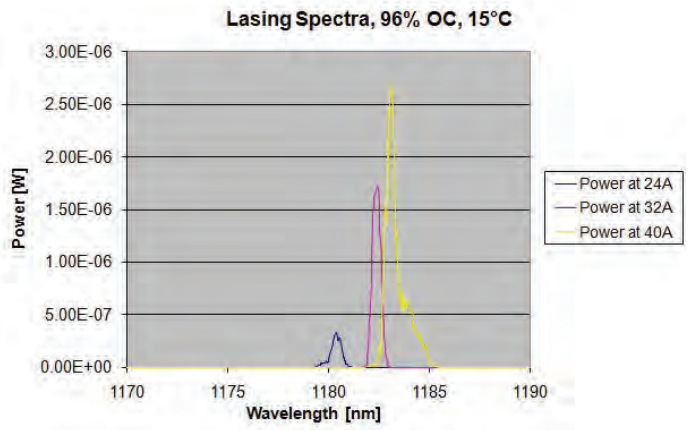

Figure 3. VECSEL power coupled into OSA vs. wavelength at three pump currents.

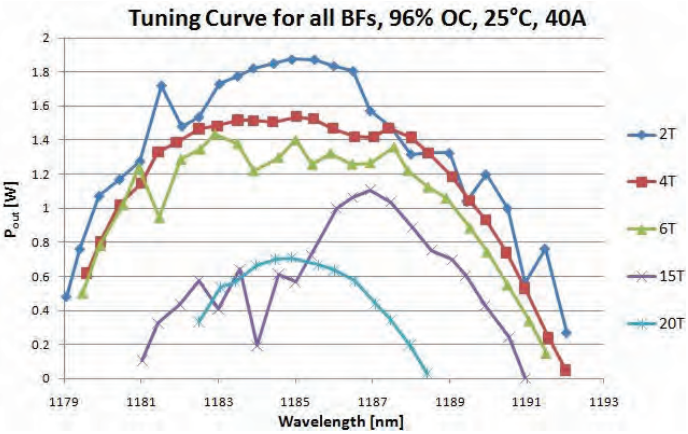

Figure 4. Output power vs. wavelength for all BFs.

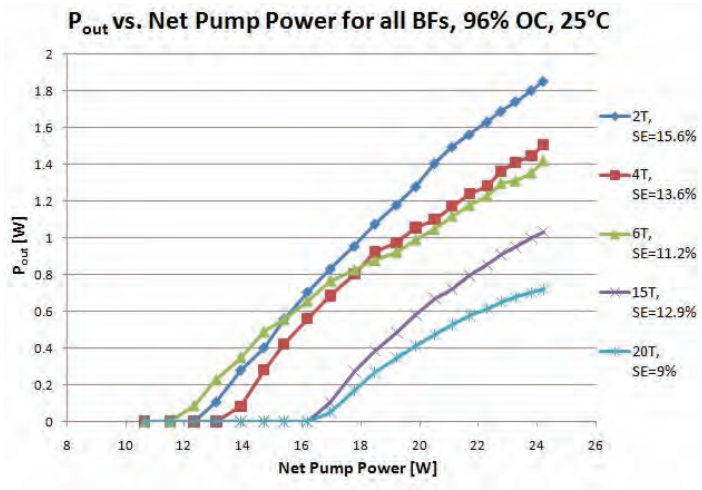

Figure 5. Output power vs. net pump power for all BFs.

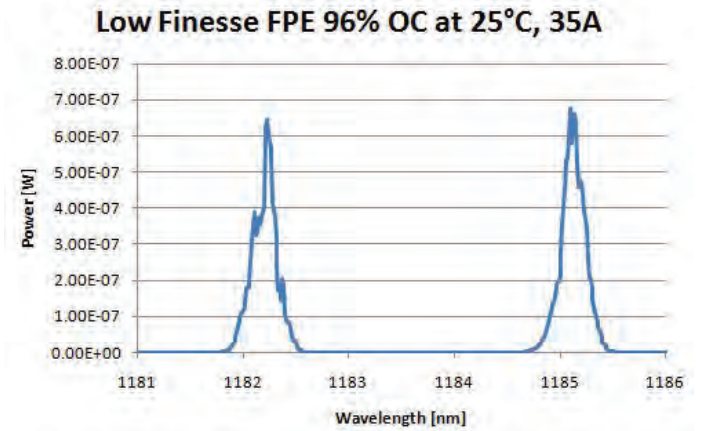

Figure 6. VECSEL power coupled into OSA vs. wavelength with intra-cavity low finesse FPE.

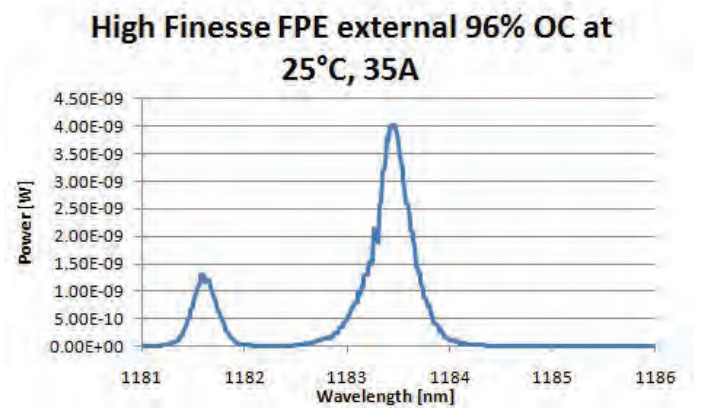

Figure 7. VECSEL power coupled into OSA vs. wavelength with high finesse FPE external to the cavity.

Figure 7 shows two peaks found by placing a high finesse FPE outside of the linear cavity. They show a smaller separation between peak wavelengths than the low finesse FPE, and a broader linewidth. These highly unexpected results merit further investigation. It is believed that this is due to the low finesse FPE we used having a

unique nature that prohibits further comment at this time. The P_{out} with the high finesse FPE was 1.2 W, a decrease of 0.18 W (13%).

Linewidth narrowing results using intra-cavity BFs, and one combination of a BF and FPE, are summarized in Table 2. The BF-FPE combination is notable because it immediately reduced the linewidth by 50 MHz (18%) from the 6T BF alone. Figure 8 shows the linewidth vs. T of BF, with a power regression overlaid. The large R^2 value shows that there is a definite trend of linewidth decreasing as T increases, and gives us a model to predict what BF thickness would be needed to reach much smaller linewidths. For example, Figure 9 and Figure 10 show that the linewidth for a 6T BF is 275 MHz, and the linewidth for a 20T BF is 95 MHz, which meets our goal.

Linewidth Achieved With Each BF	
T of BF	Linewidth (MHz)
2	1000
6	275
6T and low finesse FPE	225
15	210
20	95

Table 2. Linewidth achieved with each BF.

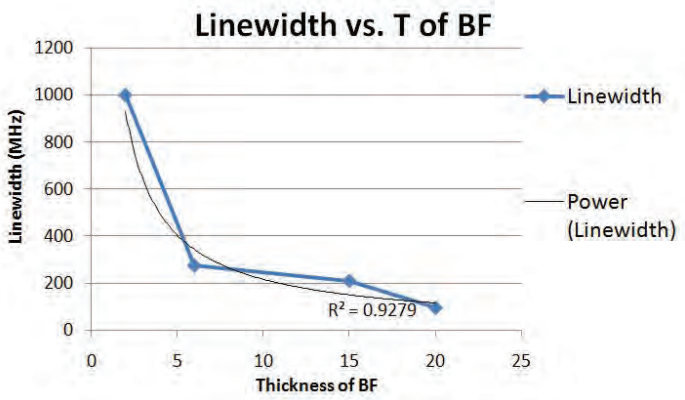

Figure 8. Linewidth vs. thickness of BF.

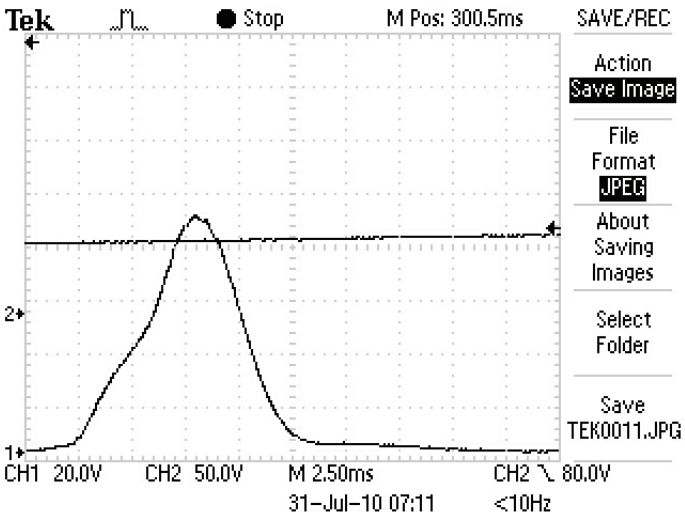

Figure 9. Linewidth for the 6T BF.

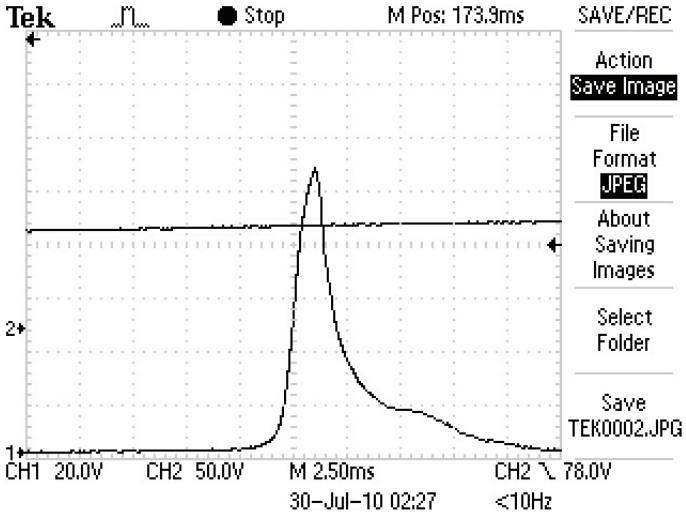

Figure 10. Linewidth for the 20T BF.

Conclusion

We have shown that our VECSEL emits multi-watt CW laser light, but that the linewidth broadens as pump power increases. Our chosen solution, adding intra-cavity BFs, reduces the linewidth significantly. Thicker BFs reduce linewidth more than thin BFs, but have more loss and decreased tunability. We reached the goal of <100 MHz linewidth (~95 MHz) with the 20T BF, and also saw the linewidth could be reduced further by combining the low finesse FPE with a BF. The spectrum of the low finesse FPE is notable for unexpectedly having two peaks, and merits further study.

For future work, we would need a higher resolution scanning FPI, because we reached the resolution limit of our scanning FPI. The next step will be to test additional intra-cavity combinations of the low finesse FPE with BFs thicker than 6T. Because of the length of our cavity and the size of thicker BFs, this might require a different way of inserting the BFs into the cavity, or lengthening the cavity without sacrificing the characteristics for which we chose the length.

References

1. Fallahi, M.; Fan, L.; Kaneda, Y.; Hessenius, C.; Hader, J.; Li, H.; Moloney, J. V.; Kunert, B.; Stolz, W.; Koch, S.; Murray, J.; Bedford, R. 5 W Yellow Laser by Intra-Cavity Frequency Doubling of High-Power Vertical External-Cavity Surface-Emitting Laser. IEEE Photon. Technol. Lett. 2008, 20, 1700-1702.
2. Fan, L.; Fallahi, M.; Murray, J. T.; Bedford, R.; Kaneda, Y.; Zakharian, A. R.; Hader, J.; Moloney, J. V.; Stolz, W.; Koch, S. W. Tunable high-power high-brightness linearly polarized vertical-external-cavity surface-emitting lasers. Appl. Phys. Lett., 2006, 88, 021105.
3. Hader, J.; Moloney, J. V.; Fan, L.; Fallahi, M.; Koch, S. W. Closed-Loop design of a semiconductor laser. Optics Letters, 2006, 31, 3300-3302.
4. W.M. Keck Observatory. LASER GUIDE STAR AVAILABLE FOR ADAPTIVE OPTICS | W. M. Keck Observatory. http://keckobservatory.org/index.php/news/laser_guide_star_available_for_adaptive_optics/ (accessed July 29, 2010).
5. Fallahi, M.; Hessenius, C.; Kaneda, Y.; Hader, J.; Moloney, J.V.; Kunert, B.; Stolz, W.; Koch, S. Novel semiconductor lasers attractive for UV-visible applications. SPIE Newsroom [Online], Feb. 13, 2009, DOI: 10.1117/2.1200901.1473, http://spie.org/x33567.xml?highlight=x2422&ArticleID=x33567 (accessed June 1, 2010).
6. Fan, L.; Hsu, T.; Fallahi, M.; Murray, J. T.; Bedford, R.; Kaneda, Y.; Hader, J.; Zakharian, A.R.; Moloney, J. V.; Koch, S. W.; Stolz, W. Tunable watt-level blue-green vertical-external-cavity surface-emitting lasers by intracavity frequency doubling, Appl. Phys. Lett., 2006, 88, 251117.
7. Milonni, P., Eberly, J. Laser Physics; Wiley: New Jersey, 2010.
8. TecOptics. TecOptics Etalons >> Fabry-Perot Etalon Theory. http://www.tecoptics.com/etalons/theory.htm (accessed August 5, 2010).

Acknowledgements

NSF sponsored Science and Technology Center on Materials and Devices for Information Technology Research, No. DMR-0120967

Pierre-Yves Guinet

Kimberly Sierra-Cajas

Hooked on Photonics REU

College of Optical Sciences

University of Arizona

US Air Force, AFOSR-MRI program

NATHANIAL SHEEHAN is pursuing a Bachelor's degree in Electrical Engineering at the University of California, Santa Barbara. Upon completion, his goal is to attend graduate school and receive a PhD in Electrical Engineering. Eventually, he would like to become a professor.

Mid-infrared Waveguiding on Silicon-and-Sapphire

ALEXANDER SPOTT, University of Washington
Michael Hochberg, University of Washington

Introduction

Waveguides on silicon can be used to construct all of the components of data transmission systems on a single chip.[1,2] Photonic integrated circuits can be constructed by integrating waveguides with CMOS electronics.[3] Ring resonator devices have been used at these wavelengths for a number of applications including modulation, biosensing, and wavelength conversion. To date, however, the majority of experiments with silicon waveguides have been at wavelengths in the near-infrared, between 1.1-2 μm.

Longer wavelengths, however, have applications not realizable in the NIR regime. Examples include astronomy,[4] and thermal imaging[5] both of which require the detection of mid-infrared (MIR) wavelengths, defined as between 2 and 20 μm. Chemical bond spectroscopy[6] is also an application that benefits from a very long range of wavelengths, including both the NIR and MIR spectra.

We recently demonstrated the first waveguides for MIR wavelengths at 4.5 μm.[7] We constructed our waveguides on a silicon-on-sapphire (SOS) substrate. Sapphire avoids the issue of increased losses at MIR wavelengths, while also maintaining the additional benefit of avoiding electrical substrate leakage, making it possible to work with electrically modulated MIR waveguides.

Over the course of this summer, we also tested waveguides with a new laser and test setup in an effort to demonstrate waveguiding at even longer wavelengths as well as show working ring resonators for the MIR.

Results and Discussion

The devices tested were fabricated with electron-beam lithography on an SOS substrate. Ridge waveguides constructed were 1.8 x 0.6 μm. The primary reported ring resonator was 40 μm in radius with an edge-to-edge spacing of 0.25 μm between the resonator and the added waveguide. A second waveguide was also placed in close proximity to the ring resonator in order to match the input coupling and achieve critical coupling.

Devices were tested with a 5.5 μm mode-hop free, tunable, continuous wave quantum cascade laser from Daylight Solutions. The test setup can be seen in Figure 1. The beam was roughly 1.5 mm wide and 1 mm tall, and was narrowed down to a spot size near 60 μm wide to facilitate edge coupling. A lock-in amplifier was synchronized to a mechanical chopper, cutting the beam at 6 kHz in order to improve the signal-to-noise ratio. A dynamic range near 85 dB was achieved.

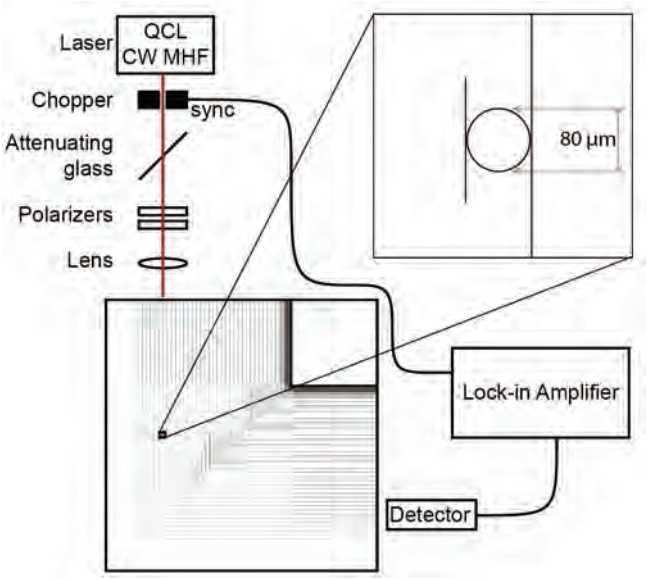

Figure 1. A diagram of the test setup and the layout of the chip, also showing the resonators that were tested.

A linear correlation of guide length vs. transmission (as seen in Figure 2) was used to determine propagation loss. Losses of 4.0 dB/cm at 5.5 μm were determined. As simulations suggested, only the TE mode guided, while light seen from TM radiation was either weakly confined or lost due to scattering.

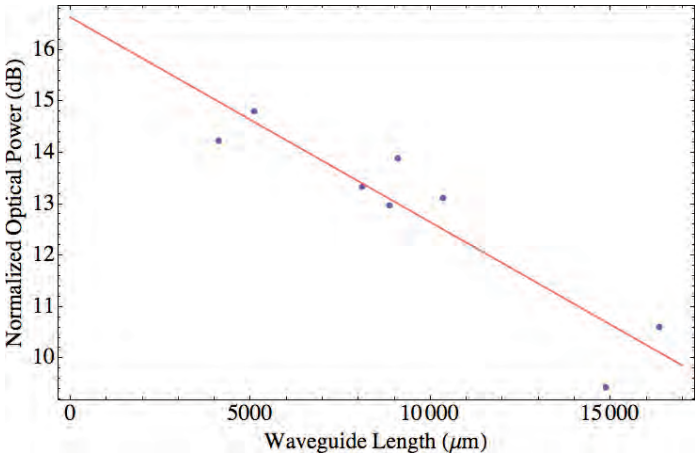

Figure 2. Transmitted optical power vs. waveguide length. A propagation loss of 4.0 ± 0.7 dB/cm is seen.

Ring resonator devices were tested by sweeping the wavelength of the laser. As seen in Figure 3, one particular ring shows peaks with a free spectral range (FSR) near 29.7 nm, very close to the theoretical value of 29.2 nm. Ring quality factors of up to 3.0 k were seen for this particular ring.

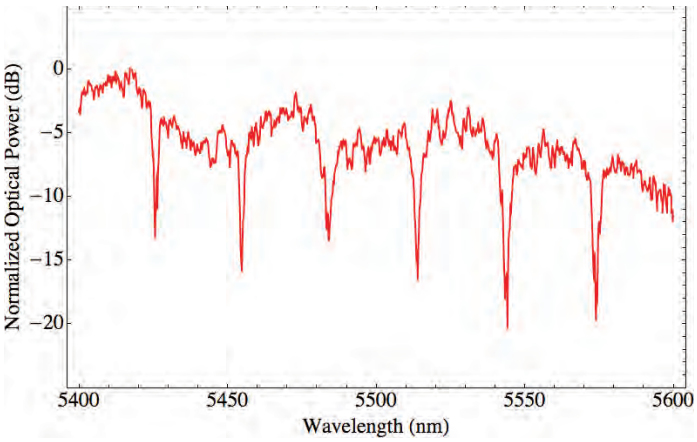

Figure 3. Wavelength sweep for a ring with a radius of 40 μm and an edge-to-edge spacing of 0.25 μm. An average FSR near 29.7 nm is seen, as well a Q-value of 3.0 k.

Conclusions

In conclusion, we were able to demonstrate working waveguides and ring resonators at wavelengths near 5.5 μm. This is the first successful demonstration of ring resonators in the mid-infrared. We found waveguides with losses of 4.0 ± 0.7 dB/cm and Q-values up to 3.0 k. As theoretical Q-values for losses of 4.0 dB/cm are near 25 k, we believe it will be possible to improve our designs and fabrication techniques in order to greatly improve both waveguide loss and Q-values.

With working ring resonators, it will be possible to explore a variety of applications and optical devices at MIR wavelengths including biosensing, and OPOs.

References

1. Liu, A.; Liao, L.; Rubin, D.; Basak, J.; Chetrit, Y.; Nguyen, H.; Cohen, R.; Izhaky, N.; and Paniccia, M.. Semicond. Sci. Technol. 2008, 23(6), 064001.

2. Chen, L.; and Lipson, M. Opt. Express 2009, 17(10), 7901–7906.

3. Huang, A.; Gunn, C.; Li, G.-L.; Liang, Y.; Mirsaidi, S.; Narasimha, A.; and Pinguet T. International Solid-State Circuits Conference (IEEE, 2006), 24–25.

4. Labadie, L.; and Wallner, O. Optics Express 2009, 17, 1947-1962.

5. Holst, G. C.; and McHugh, S. W., Proceedings of SPIE (SPIE 1992), 78-84.

6. Gray, H. B. Chemical Bonds: An Introduction to Atomic and Molecular Structure (University Science Books, 1994).

7. Baehr-Jones, T.; Spott, A.; Ilic, R.; Spott, A.; Penkov, B.; Asher, W.; and Hochberg, M., Opt. Express 2010, 18, 12127-12135.

Acknowledgments

Funds for this research were provided by the Center on Materials and Devices for Information Technology Research (CMDITR), an NSF Science and Technology Center No. DMR 0120967. The authors would like to thank Gernot Pomrenke, of the Air Force Office of Scientific Research, for his support through AFOSR YIP and PECASE awards, and would like to acknowledge support from the Washington Research Foundation, the Mary Gates Endowment, and the Washington NASA Space Grant Consortium.

ALEXANDER SPOTT is an undergraduate student at the University of Washington in the process of obtaining a dual major in physics and applied and computational mathematical sciences (ACMS). He intends to continue to grad school in pursuit of a Ph.D. in physics.

Geometric and Electronic Structures of Alternative Electron Transport Materials for Bulk-Heterojunction Solar Cells

EMILY TEETER, University of West Georgia
Chad Risko, Stephen Lee, Jean-Luc Brédas, Georgia Institute of Technology

Introduction

As there is a need for increased energy production that can be generated in a clean and sustainable manner, research in both industry and academia has turned to photovoltaics for the conversion of solar energy to electricity. Current solar photovoltaic applications typically use inorganic semiconductors (e.g., silicon) to transform sunlight into electricity. Unfortunately the inorganic materials used are often fragile, heavy, and expensive to produce. Considerable research is being done to use organic semiconductors as alternatives to inorganic semiconductors. Organic-based electronic devices can be flexible, lightweight, and cheaper to produce versus their inorganic counterparts.[1-4]

The efficiency of typical inorganic materials is decent, with conventional silicon-based solar cells having efficiencies of about 20%.[4] Unfortunately, the organic materials studied to date do not lead to devices with the same efficiency as inorganic devices. Research is being done to find organic materials with the electronic, optical, and charge transport properties to increase efficiency. This research can also lead to advances in other organic-based electronic devices, including light emitting diodes and thin-film transistors.

With an eye towards improving the performance of organic solar cells that employ the bulk-heterojunction structure, new electron transport materials that are of interest to replace phenyl-C_{61}-butyric acid methyl ester (PCBM) in the active layer have been synthesized. This work aims to understand how chemical substitution along the base molecular structure influences the geometric and electronic structures, electrostatic properties, and solid-state packing arrangements for a series of substituted triisopropyl-silylethynyl (TIPS)-pentacene derivatives (see Figure 1). This information will be used to not only understand how the materials perform in an organic-based solar cell, but also used to assist in the design of new materials.

Methodology

Density functional theory (DFT) methods are used to evaluate the electronic (i.e., ionization potential, electron affinity) and charge transport (i.e., electronic coupling, reorganization energy) properties of the new molecular crystal materials of interest. A series of unsubstituted acenes, triisobutyl-silylethynyl (TIBS)-pentacene, TIPS-substituted acenes, and TIPS-pentacene derivatives with electron withdrawing groups are studied herein. Geometry optimizations were performed using the B3LYP functional, where Becke's three-parameter hybrid exchange functional is combined with the Lee-Yang-Parr correlation functional,[5-7] and a 6-31G** split valence plus polarization basis set. DFT calculations were carried out using the GAUSSIAN09 suite of programs.[8] Single point calculations were also carried out to find the reorganization energies.

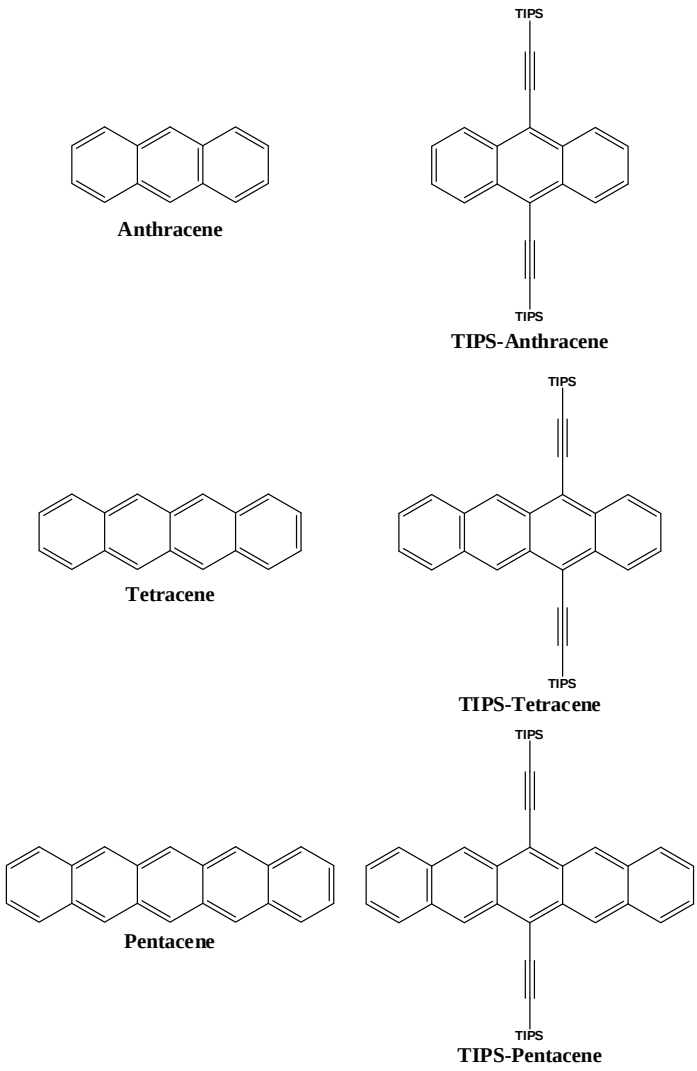

Figure 1. Chemical structure of acene series. TIPS= triisopropyl-silylethynyl. TIBS= triisobutyl-silylethynyl. X=H, Cl, CN, CF_3.

Results and Discussion

A. Geometric and Reduction-Oxidation Properties

The neutral, anionic, and cationic electronic configurations of each molecule were optimized, and information pertaining to the bond lengths was gathered. Table 1 shows the evolution of the bond lengths going from the neutral to anion and cation states in the unsubstituted acenes; see Figure 2 for bond numbering scheme.

		Anthracene			Tetracene			Pentacene		
		Neutral	Anion	Cation	Neutral	Anion	Cation	Neutral	Anion	Cation
Bonds (Å)	1	1.43	1.40	1.41	1.43	1.41	1.41	1.43	1.42	1.42
	2	1.37	1.39	1.39	1.37	1.39	1.38	1.37	1.38	1.38
	3	1.43	1.42	1.41	1.43	1.42	1.42	1.44	1.43	1.42
	4	1.40	1.41	1.41	1.39	1.41	1.41	1.39	1.40	1.40
	5	1.40	1.41	1.41	1.41	1.41	1.41	1.41	1.41	1.41
	6	1.43	1.42	1.41	1.41	1.41	1.41	1.40	1.41	1.41
	7	1.37	1.39	1.39	1.39	1.41	1.41	1.40	1.41	1.41
	8				1.43	1.42	1.42	1.41	1.41	1.41
	9				1.37	1.39	1.38	1.39	1.40	1.40
	10							1.44	1.43	1.42
	11							1.37	1.38	1.38

Table 1. Bond lengths (Å) of anthracene, tetracene, and pentacene in the neutral, anion, and cation states as determined at the B3LYP/6-31G** level of theory.

In anthracene, with the shortest conjugation path, there is a substantial change in bond length between the neutral and anion/cation states. As the conjugation path gets longer, the changes in bond length are much less noticeable. In the neutral state the single bonds are longer than the double bonds. As we look at the anion and cation states we can see that the bond lengths begin to look more similar and the differences between single and double bonds become much less. To form an anion or cation you are adding or taking away an electron. This causes the charge to then want to distribute itself throughout the molecule. In the shorter molecules, this charge has limited space with which to distribute, while the longer the molecules provide more space.

As the charges distribute, the bonds shift and change the bond length alteration pattern.

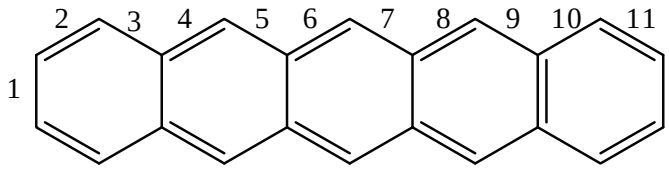

Figure 2. Bond numbering scheme used for geometric analysis.

From the energies of these optimized states, the ionization potential and electron affinities were calculated, along with the intramolecular reorganization energy (see Table 2). From these tables we can compare the energies and see which molecular structures are optimal for use in the active layer. As the conjugation paths get longer, the energy it takes to add and/or remove electrons gets smaller. The lower the IP energy, the easier it is to remove an electron. The lower the EA energy, the easier it is to add an electron onto the molecule. The electronegative substituents make it significantly easier to add an electron to the molecules, while also making it easier to remove an electron.

The reorganization energies show the energy it takes for the molecule to reorganize itself after losing or receiving an electron. We look for molecules with lower reorganization energies so energy is not wasted when electrons are added or removed. The longer that the molecules get, the lower the reorganization energies get.

B. Electronic structure

We gathered the highest occupied molecular orbital (HOMO) and the lowest unoccupied molecular orbital (LUMO) energies for each molecule. Images of the HOMO and LUMO wavefunctions are shown in Figure 3. We look at these energies to understand more about the electronic structure of the molecules and see how adding a particular substituent changes these energies. The energies are shown in Table 3. The HOMO and LUMO energies follow what the IP and EA energies suggest. The HOMO and LUMO pictures show that the distributions are not significantly affected by the substitutions on pentacene. However, Table 3 shows that the HOMO and LUMO energies are significantly impacted by the presence of the substituents.

	HOMO	LUMO
Anthracene	-5.24	-1.65
Tetracene	-4.87	-2.09
Pentacene	-4.61	-2.40
TIPS-Anthracene	-5.14	-2.25
TIPS-Tetracene	-4.86	-2.51
TIPS-Pentacene	-4.63	-2.73
TIPS-Pentacene Cl	-4.76	-2.86
TIPS-Pentacene CN	-4.93	-3.06
TIPS-Pentacene CF_3	-4.83	-1.93
TIBS-Pentacene	-4.62	-2.73

Table 3. HOMO and LUMO energies (eV) as determined at the B3LYP/6-31G** level of theory.

		IP	λ_{1e}	λ_{2e}	λ_{te}	EA	λ_{1a}	λ_{2a}	λ_{ta}
Un-substituted	Anthracene	6.82	0.07	0.07	0.14	-0.12	0.10	0.10	0.20
	Tetracene	6.28	0.06	0.05	0.11	-0.71	0.09	0.08	0.17
	Pentacene	5.90	0.05	0.05	0.10	-1.14	0.07	0.07	0.14
TIPS	Anthracene	6.28	0.11	0.11	0.22	-1.16	0.16	0.17	0.33
	Tetracene	5.91	0.04	0.14	0.18	-1.45	0.13	0.13	0.26
	Pentacene	5.63	0.04	0.11	0.15	-1.73	0.11	0.11	0.22
	Pentacene Cl	5.78	0.08	0.08	0.16	-1.83	0.15	0.06	0.21
	Pentacene CN	5.95	0.08	0.07	0.15	-2.07	0.10	0.10	0.20
	Pentacene CF_3	5.85	0.09	0.08	0.17	-1.93	0.11	0.11	0.22
TIBS	Pentacene	5.64	0.08	0.08	0.16	-1.75	0.11	0.11	0.22

Table 2. Ionization potentials (IP), electron affinities (EA), and reorganization energies (λ) as determined at the B3LYP/6-31G** level of theory.

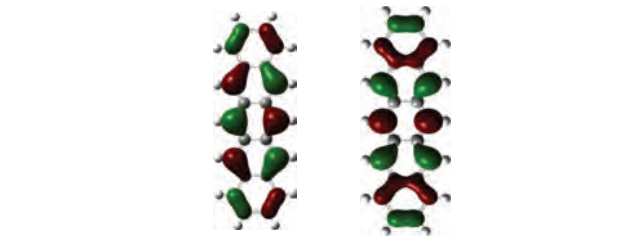

HOMO and LUMO for Pentacene.

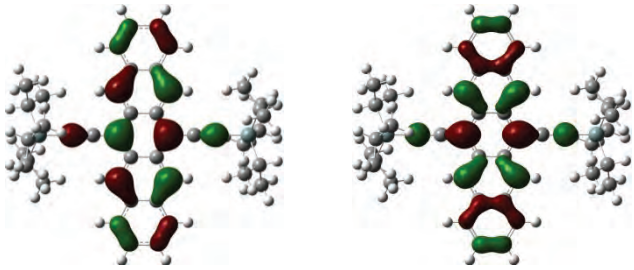

HOMO and LUMO for TIPS-Pentacene.

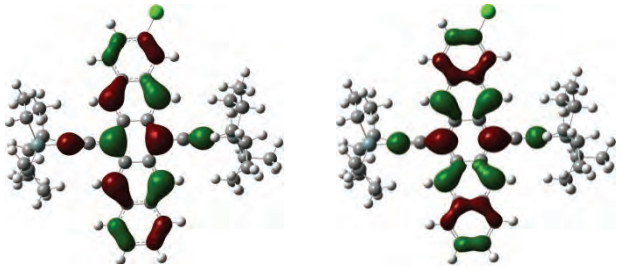

HOMO and LUMO for TIPS-Pentacene Cl.

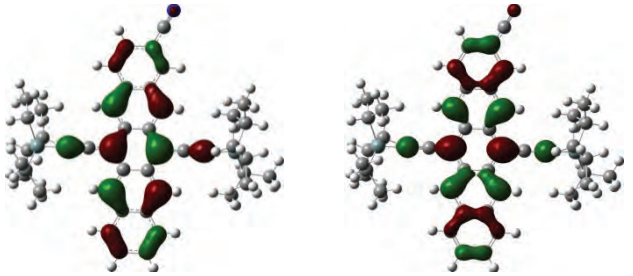

HOMO and LUMO for TIPS-Pentacene CN.

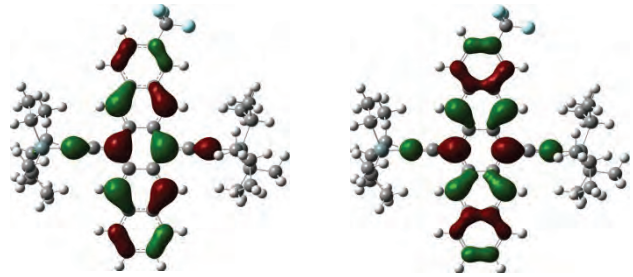

HOMO and LUMO for TIPS-Pentacene CF_3.

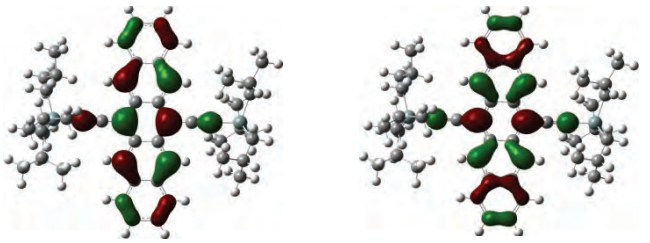

HOMO and LUMO for TIBS-Pentacene.

Figure 3. Images of the HOMO and LUMO interaction for the molecules of interest.

Conclusions

The different energies (IP, EA, HOMO, LUMO, and reorganization energies) show that adding molecular substitutions to the basic molecular structure increases its potential to be used as an electron transport layer in the active component in bulk-heterojunction solar cells. The TIPS-pentacene derivatives with electron withdrawing groups show potential to be possible replacement materials for PCBM in the active layer. This data will be used for further research on these molecules. Further research will examine the excited state energies and oscillator strengths, as well as serve as the basis for molecular mechanics and dynamics simulations of solid-state models.

References

1. Thompson, B. C.; Fréchet, J. M., J. Angew. Chem. Int. Ed. 2008, 47, 58-77.
2. Bredas, J. L.; Norton, J. E.; Cornil, J.; Coropceanu, V., Acc. Chem. Res. 2009, 42, 1691-1699.
3. Kippelen, B.; Bredas, J. L., Energ. Environ. Sci. 2009, 2, 251-261.
4. Venkataraman, D.; Yurt, S.; Venkatraman, B. H.; Gavvalapalli, N. J. Phys. Chem. Lett. 2010, 1, 947-958.
5. Becke, A. D. Phys. Rev. A: At. Mol. Opt. Phys. 1988, 38, 3098-3100.
6. Becke, A. D., J. Chem. Phys. 1993, 98, 1372-1377.
7. Lee, C.; Yang, W.; Parr, R. G. Phys. Rev. B: Condens. Matter Mater. Phys. 1988, 37, 785-789.
8. Frisch, M. J.; et al, Gaussian09, Revision A.02; Gaussian, Incorporated: Wallingford, CT, 2009.

Acknowledgments

The Center on Materials and Devices for Information Technology Research (CMDITR), an NSF Science and Technology Center No. DMR 0120967 provided funds for this research.

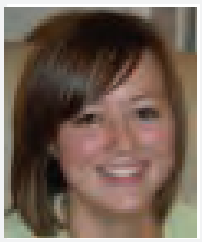

EMILY TEETER is currently pursuing degrees in physics and engineering. She hopes to finish her physics degree soon at the University of West Georgia and transfer to the Georgia Institute of Technology to work towards a degree in engineering.

Thermogalvanic Cells with Nanostructured Carbon Electrodes

KYARRA THOMPSON, Clark Atlanta University
Sameer Rao, Baratunde A. Cola, Georgia Institute of Technology

Introduction

This work describes an experimental study to understand the effect of different nanostructured carbon electrodes on the current generation capacity of thermogalvanic cells. Two electrode types were investigated: carbon nanotube forest, and carbon nanotube sheets. Electrodes that provide increased current density were to improve the efficiency of waste thermal energy to electrical energy conversion using thermogalvanic cells.

Thermocells are used for low grade (temperature below 130°C) thermal energy harvesting by converting waste thermal energy into electrical energy. Thermogalvanic cells (or thermocells, galvanic thermopiles, thermal electrochemical cells), stirling engines, and thermophotovoltaics are different technologies that are used for converting waste heat to electricity. Stirling engines are heat engines that operate by a cyclic compression and expansion of air or other gas, the working fluid, at different temperature levels such that there is a net conversion of heat energy to mechanical work[3]. Thermophotovoltaics are the direct conversion processes from heat differentials to electricity via photons.

By contact with the appropriate reservoirs, any desired gradient or difference in temperature may be induced and maintained within the system[1] of a thermocell. If the substances constituting the system are able to move independently from one region of the temperature to another they will in general do so until a condition of equilibrium, accompanied by no further net transfer of material, is reached.[1] However, a temperature difference must be created to effectively promote ionic mobility. To understand how thermogalvanic cells work, it is important to describe the Soret effect and the Seebeck effect. The Soret effect is the process of a temperature gradient producing a concentration gradient. The solutions of binary electrolytes are really to be regarded in the present connection as systems of three components.[2] These parts are associated with free energy change, due to a concentration gradient which is due to the electrical gradient.[2] Moreover, this follows because of the partially independent distribution of the ions in the temperature gradient which manifests itself in the accompanying potential gradient in the solution.[2] The Seebeck effect is the process of a temperature difference leading to a voltage gradient. The Seebeck coefficient is defined by the voltage gradient divided by the temperature gradient $\Delta V/\Delta T$.

The thermocells that were investigated in the NanoEngineered Systems Laboratory at Georgia Institute of Technology were in the geometry of button cells (Figure 1) which are stainless steel coin cells used for lithium batteries.

Figure 1. Photo of a button cell.

Button cells are currently used as batteries to power small electronic devices such as hearing aids, and wrist watch. The reason for the particular study of thermogalvanic button cells are because they are inexpensive to make, easy to characterize, and have a favorable device geometry for commercialization.

For thermogalvanic cells, there are two reactions, and one reaction cannot happen without the other. The cause is creating a thermal difference. The effect is the chemical process known as a reduction/oxidation (redox) reaction which is also considered the electrolyte. An electrolyte is any substance containing free ions that make the substance electrically conductive. In the experiment that was performed, the electrolyte made for use in a thermogalvanic button cell was an aqueous solution. In the aqueous solution, the temperature range of the button cell was not to go below 0 °C or to exceed 100 °C because of the freezing and boiling points of water. The electrolyte that was investigated was the redox couple potassium ferri/ferro cyanide. Below is the following solid-state redox reactions:

Reduction (cathodic reaction):

$$-Fe^{III}(CN)_6 + e^- \rightarrow Fe^{II}(CN)_6$$

Oxidation (anodic reaction):

$$Fe^{II}(CN)_6 - e^- \rightarrow -Fe^{III}(CN)_6$$

This implies that the $-Fe^{III}(CN)_6$ migrated near the anode and $Fe^{II}(CN)_6$ near the cathode region when the temperature gradient was produced. The more negative ion migrated to the hot side and the less negative ion migrated towards the cold side.

The factors effecting thermogalvanic cells are: the efficiency of

electrodes, the type of electrolytes, and thermal and electrical properties such as boiling and freezing points of the electrolyte, the density of the electrodes, energy dissipation and energy storage of the thermocell. For traditional electrodes, the electrode reaction involves mass transport of the electroactive species from the bulk solution to the electrode surface and an electron transfer step at the electrode surface. The electrolyte is the redox pair responsible for the chemical reaction which happens on the site of the electrodes. The thermal conductivity of the electrolyte determines the temperature gradient across the cell. The rate of ion transport through the electrolyte and the efficiency of electron collection at the electrodes determine the cell current (Figure 2).

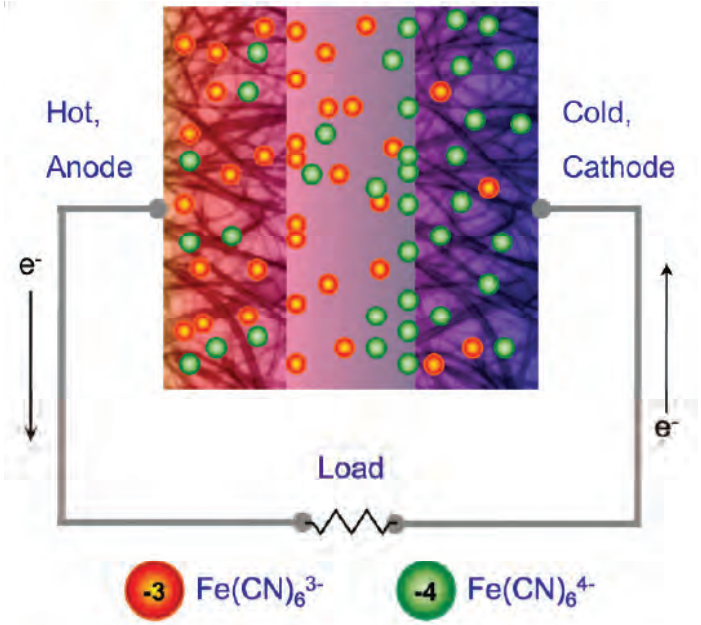

Figure 2. Schematic of a thermocell with nanostructured electrodes showing concentration gradients of the ferri-ferrocyanide redox ions during power generation[6].

The motivation for this study was derived from the study of converting waste heat into electricity. This application is a combination of concepts between electrochemistry, thermodynamics, and engineering.

The purpose of this research experiment consisted of studying the previously mentioned material by studying thermal and electrical properties. Also, by creating a low cost, high efficiency thermogalvanic cell to harvest waste heat into electricity using nanostructured electrodes, carbon nanotube sheets. This is because porous carbon electrodes are expected to offer improved performance because of their large surface area. Different electrode materials were explored such as carbon nanotube sheets and carbon nanotube forest growth. The carbon nanotube forest growth electrode was expected to have an improved resistance over carbon nanotube sheets.

Experimental/Computational Method

The experiments of previous literature concerning the production of the button cells were replicated. The machine to seal the button cells is called a crimper (Figure 3).

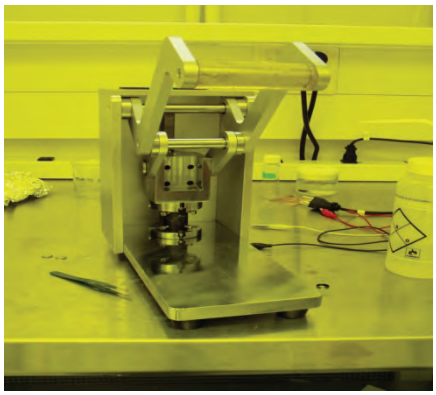

Figure 3. Machinery used to crimp button cells.

The crimper compressed the top and bottom cell that held the electrode, electrolyte, and the separator. Once crimped properly, the button cell was tested. The button cell tester contained two copper blocks to create thermal contact, and hot and cold reservoir to create a temperature gradient. Also, a digital multimeter was used to characterize the open circuit voltage, the short circuit current, and the resistance of the button cell (Figure 4).

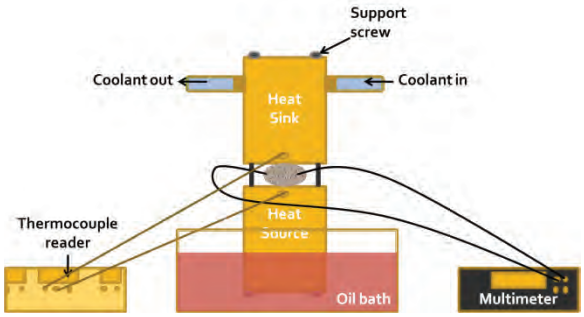

Figure 4. Experimental setup for button cells

Procedure

The production of button cells included parameters such as the bonding of carbon nanotube sheets using silver paste, and carbon nanotube forest growth on the direct surface of the button cell, porous separators and electrolyte. Being able to produce a carbon nanotube forest directly onto the cell was a vital objective of the experiment. The forests were grown by a chemical vapor deposition technique using resources in the Georgia Institute of Technology clean room. The cells were assembled sandwiched around a separator. The separator prevents contact between the anode and cathode, and helps promote ionic mobility. When the ionic flux became dominant, any current flow in the sandwiched assembly required the redox reactions to occur at both sandwich forming electrodes.[6] More specifically, nail polish was used as an insulator by coating the polish on the top and bottom cells leaving just enough room in the middle of the cells for the CNT electrodes. The CNT electrodes were cut into 0.5cm x 0.5cm squre to fit into the top and bottom parts of the button cell. The electrodes were bonded on the cells using silver paste. The paste from the cell dried. The separator was soaked in electrolyte

and then placed in the prepared bottom part of the button cell. The bottom of button cell was placed on the bottom dye of the crimper. The button cell was then filled with electrolyte (liquid mixture of equal 0.4M concentration of the redox pair ferri/ferro Cyanide until a convex meniscus was formed. The top of the button cell was centered onto the bottom filled with the electrolyte. The button cell was crimped 3-5 times until properly sealed.

Results and Discussion

After replicating previous literature on producing thermogalvanic cells, different separators were investigated. Three separators that were investigated were thin separators which were cloth material and a nomex separator (Graphs 1, and 2). Also, the efficiency of CNT electrodes was investigated with current and voltage generation and their relation, which are fundamental thermocell performance characteristics (Graph 3).

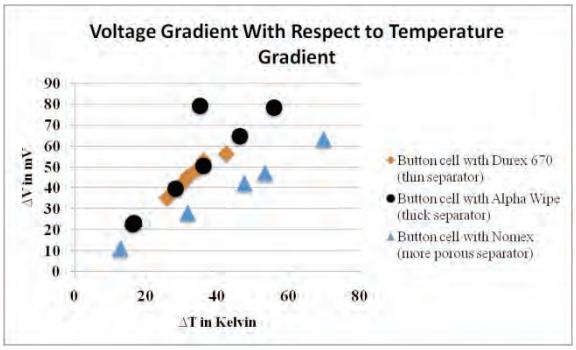

Graph 1. Data analysis measuring the voltage gradient with respect to the temperature gradient.

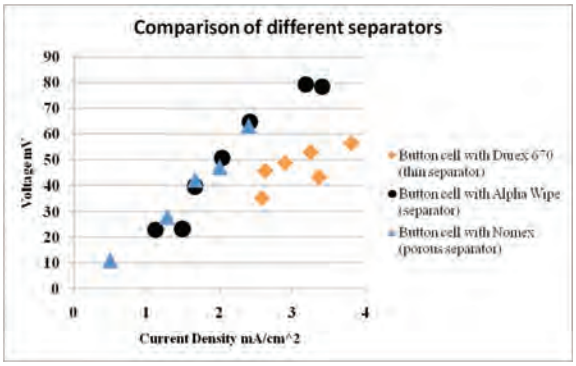

Graph 2. Data Analysis measuring the voltage output and current density.

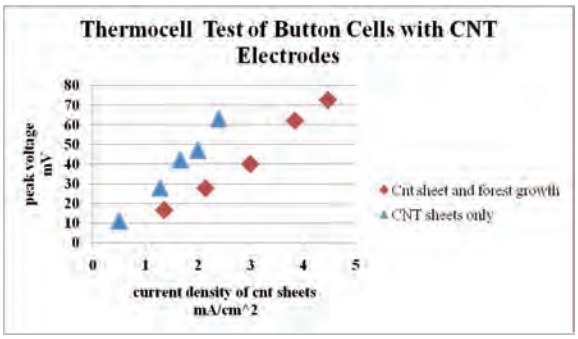

Graph 3. Data Analysis measuring current and voltage generation and their relation to CNT electrodes.

The purpose in investigating the separators was to measure the current flow. In Graph 1, a linear relationship existed between the voltage gradient and the temperature gradient because the seebeck coefficient is 1.4 mV/K. For Graph 2, the current density was enhanced using a thinner text wipe material because its porosity is bigger, and a better absorbent. Also, the higher the current flow, the higher the ionic mobility. For Graph 3, the current density of the CNT forest growth was higher than in the CNT sheets.

Conclusion

The more porous the separator was in thermogalvanic cells, the higher the current flow. When the thermogalvanic cells were created, it was important to have a systematic method of crimping the button cell. Too much pressure applied on the small device resulted in a shortage of the cell. An issue that occurred was that there were not enough electrolytes in some of the button cells produced resulting in a low current flow. It has been proven that carbon nanotube forest growth performed more efficiently than carbon nanotube sheets due to their highly density and large surface area. Overall, creating a device to convert wasted heat into electrical heat was very proficient. Although more studies need to be performed and observed, the production and improved efficiency is promising. Ultimately in the future, a high grade thermogalvanic cell with non-aqueaous electrolyte solution will be created. Also, the production of a polymer film is necessary, which will be used to help to promote increased electron/ion transport in the thermocells.

References

1. Eastman, E.D. American Chemical Society 1926, 48, 1428.
2. Eastman, E.D. American Chemical Society 1928, 50, 285.
3. G. Walker. Stirling Engines Clarenden Press 1980 Oxford, page 1.
4. Inzelt, G. A New Era in Electrochemistry 2008, 2, 282.
5. Kulesza, Pawel; Galus, Zbigniew. J. Electroanal Chem., 1992, 323, 261-274
6. Hu, Renchong; Cola, Baratunde. Nano Letters 2010.

Acknowledgements

Funds for this research were provided by the Center on Materials and Devices for Information Technology Research (CMDITR), the NSF Science and Technology Center No. DMR 0120967. Research performed was conducted in the NanoEngineered Systems and Transport (NEST) Lab.

KYARRA THOMPSON's educational goals consist of earning a Bachelor of Science Degree in Chemistry with a mathematics minor, and a Ph.D. in Organic Chemistry. She also plans to earn a Medical Degree in the field of Anesthesiology.

Combinatorial Search for Electro-Optical Intercalating Dyes

ZACHARY H. WATANABE, The Northwest School
Lewis E. Johnson, Bruce H. Robinson, University of Washington

Introduction

Research and development of non-linear optical (NLO) devices attempts to address the growing demand for information technology with lower costs, lower energy consumption, and increased bandwidth.[1] Inorganic electro-optical (EO) materials are currently used industrially but have reached the peak of their physical capacity.[2] One possible solution to these limits involves thin films containing organic dyes. Thin films are used as an environment for dyes that exhibit electro-optical activity; also known as chromophores. Non-linear optical chomophores react to an electric field by changing the phase of light that passes through the material. This is called the electro-optical effect (Pockels effect) and is used to create either constructive or destructive interference with the original beam of light. Electro-optical modulators use the Pockels effect to translate electrical input into an optical signal that can be used in computers and telecommunications.

Modulators using organic NLO materials are currently limited by low chromophore order. The strength of the electro-optical effect (quantified by the EO coefficient r_{33}) is related to the vector sum of the effect of individual chromophores, which depends on the molecular first hyperpolarizability (β). The dipole moment is the first term and the hyperpolarizability is the third term (quadratic in **E**) in the equation describing polarization in response to an electric field.

$$p_i = p_{0,i} + \alpha_{ij}E_j + \frac{1}{2}\beta_{ijk}E_jE_k + \frac{1}{6}\gamma_{ijkl}E_jE_kE_l + \ldots$$

Therefore, the effect is greatest when all of the chromophores are aligned such that their dipole moments are parallel. An electric poling field applied to NLO materials, just below the glass transition temperature of the material, causes chromophores to orient themselves in the direction of the electric field.[3] While this method increases chromophore order, its effectiveness is limited by dipole-dipole interactions, dielectric breakdown, phase separation, and operating temperatures. Physically constraining the number of ways in which a chromophore can orient itself, also known as reducing dimensionality,[4] is one strategy to overcome these deficiencies. DNA's molecular structure could potentially reduce dimensionality by allowing a chromophore to intercalate between its base pairs.[5] Several chromophores, such as Ethidium Bromide, have been demonstrated to intercalate into DNA but none of them exhibit strong non-linear optical activity.[6] Intercalating a chromophore with non-linear optical activity in to DNA will reduce the dimensions in which a chromophore can align itself, thus creating conditions for a higher non-linear optical effect.

There are two sets of criteria to consider when designing an intercalating NLO dye. In order for dye to intercalate, it must be positively charged, fit within the size restriction, and have an aromatic, fused ring core structure.[7] A dipolar NLO dye must also have an electron acceptor, electron donor, and a bridge to connect the two. The positive charge can act as an acceptor but can also delocalize such that the dye no longer has a donor-bridge-acceptor arrangement. Here, opposing hyperpolarizability vectors are created within each molecule and negate each other. This results in low hyperpolarizability along the dipole axis (β_{zzz}). However, the rotationally-averaged hyperpolarizability obtained from Hyper-Rayleigh scattering experiments (β_{HRS}) vector should not be greatly affected. In order to design an intercalating electro-optic chromophore, analysis of the characteristics of charge chromophores must be completed first in order to yield some insight into better designs.

Computational Methods

Several theoretical calculation methods were integrated to produce accurate values at low computational expense for the desired combinatorial sets. First, the computational chemistry software Spartan was used to perform initial geometry optimization using a semi empirical PM3 method. Then the computational software Gaussian was used to fine-tune molecular geometry and calculate hyperpolarizability using density functional theory (DFT) with a B3LYP functional and a 6-31G* basis set. The results from these calculations were verified by repeating the procedure using a M026X functional and 6-31G* basis set. All of the calculations were run in vacuo and only static hyperpolarizabilities were calculated.

The non-linear optical chromophore DAST (see Figure 1) was used as a control for these calculations because its derivatives have the potential to meet all of structural criteria of both intercalating and NLO dyes.[8] DAST has a dipole moment (μ) of 6.7 D, a β_{HRS} of 60 x 10^{-30} esu, a β_{zzz} of -147 x 10^{-30} esu, and a bandgap of 2.67 eV. It also had a minimalist donor, bridge and acceptor design which made it easy to isolate the three components. The clear distinction between components allowed them to be easily optimized.

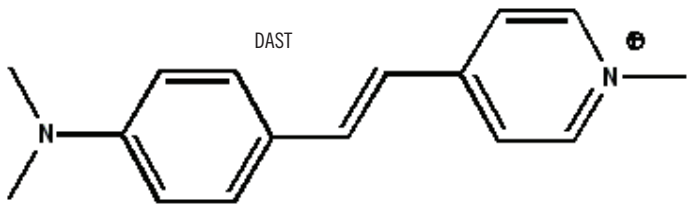

Figure 1. Molecular structure of DAST.

Additionally the benchmark of the CLD-1 chromophore was used because it is standard for non-charged electro optic dyes.[9] CLD-1 has a dipole of 19.4 D, a β_{HRS} of 347 x 10^{-30} esu, and a β_{zzz} of 643 x 10^{-30} esu calculated at the B3LYP/6-31G* level of theory.

The combinatorial search for a chromophore that met the criteria for both intercalation and electro-optic activity was subdivided into several calculation sets. Specifically, the categories for the sets are: non-heterocyclic bridges, non-heterocyclic six membered acceptors, heterocyclic six membered acceptors, and heterocyclic five membered acceptors. All of the calculations involved a methylated pyridinium or pyrrolinium. The heterocyclic atoms used in this study were sp2 nitrogen, sp2 carbon, oxygen, and sulfur. Preliminary calculations suggested that placing a heterocyclic atom adjacent to the charge yields low β_{zzz} values. Candidates with this characteristic were excluded from combinatorial screening. The number of heterocyclic atoms was limited to one out of concern for chemical stability. However, in the heterocyclic six membered acceptors calculation set, a second sp3 orbital atom needed to be added in to order satisfy the octet rule. For this purpose, a malanonitrile, a carbonyl, or an sp3 carbon was used. In the remaining positions on the acceptor, a cyano group, an nitro group, or a sp2 carbon was selected to occupy that position.

This combinatorial study systematically optimized charged acceptors under the aforementioned parameters. The charge and the heterocyclic atom were rotated around the different positions to ensure that no possible configuration was skipped. However an axis of symmetry was assumed along an extended vector of the bond connecting the acceptor to the bridge to eliminate conformers from the combinatorial search.

Selected molecules that did not fit the trends in the relationships between β_{zzz}, β_{HRS}, μ, and bandgap were tested using the higher basis of M026X to better understand the discrepancies. In particular, the calculations which exhibited significant variation in the trend between β_{HRS} and β_{zzz} were selected for additional calculations.

Results and Discussion

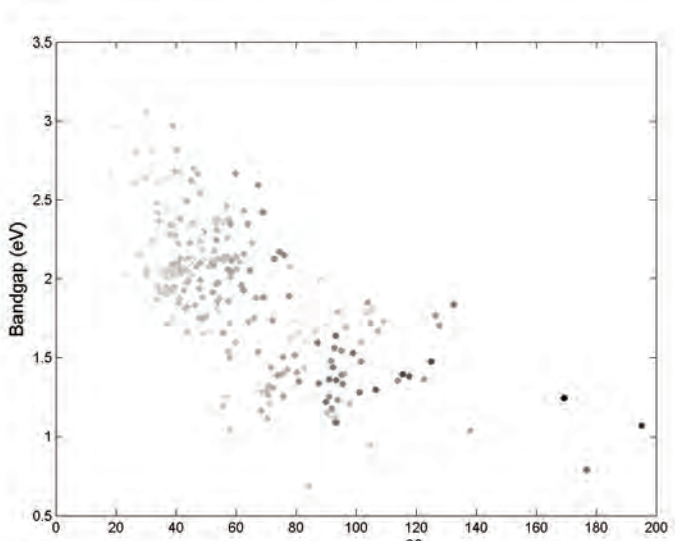

Figure 2. Distribution of β_{zzz} values in relation to both β_{HRS} and bandgap.

Figure 2 models the relationship between bandgap and β_{HRS} based on calculated values from all molecules within the acceptor optimization combinatorial sets. The shade of each data point correlates to a β_{zzz} value, darker shades denoting higher values of β_{zzz}.

Figure 2 suggests that a definitive range of β_{HRS} can exist for a given band gap. This range widens as the band gap approaches zero, resulting in a horizontal asymptote as β_{HRS} approaches infinity. Within the given range, β_{zzz} are expected be proportional to $\beta_{HRS}$and inversely proportional to bandgap as predicted by the two state model.[10] Therefore the large number of low β_{zzz} values above the bandgap of 2 eV and/or with aβ_{HRS} below 60 are considered normal. Dyes with low β_{zzz} values but high β_{HRS} values are likely to be octupolar. The pockets of these values further indicate there may be other measurable characteristics to measure the degree octupolarity of a dye.

Figure 3 shows the relationship between β_{zzz} and β_{HRS} for all chromophores screened in the acceptor optimization combinatorial set.

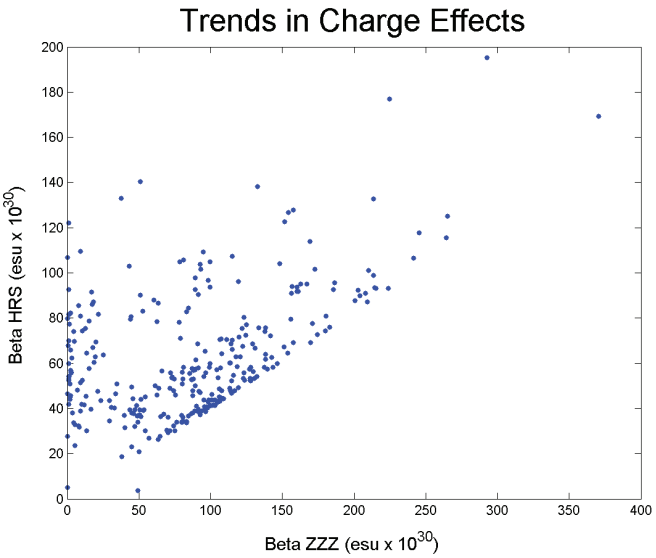

Figure 3. Trends in charge localization on charged chromophores via β_{zzz}/β_{HRS} ratio.

The data points along the y axis represent octupolar dyes which have inherently low β_{zzz}. However, if a dye has low β_{HRS} values and close proximity to the y axis, then these characteristic are not an indication of an octupolar dye. Figure 2 also suggests that a limit of the ratio of β_{zzz}/β_{HRS} exists at approximately 2.5. In addition, many of the chromophores with the largest β_{zzz}values are along this limit. This limit occurs because a maximum amount of β_{HRS} is contributed by β_{zzz}. When examining charged dyes, charge localization becomes a large factor in achieving higher β_{zzz} values. Delocalized charge will spread over a large region and weaken the hyperpolarizability along any individual vector. This means that charge delocalization will adversely affect β_{zzz} but not necessarily β_{HRS}. The ratio of β_{zzz}/β_{HRS} then allows us to measure the relative magnitude of charge delocalization.

Figure 4 illustrates the relationship between the dipole and hyperpolarizability of chromophores screened in the acceptor optimization combinatorial set.

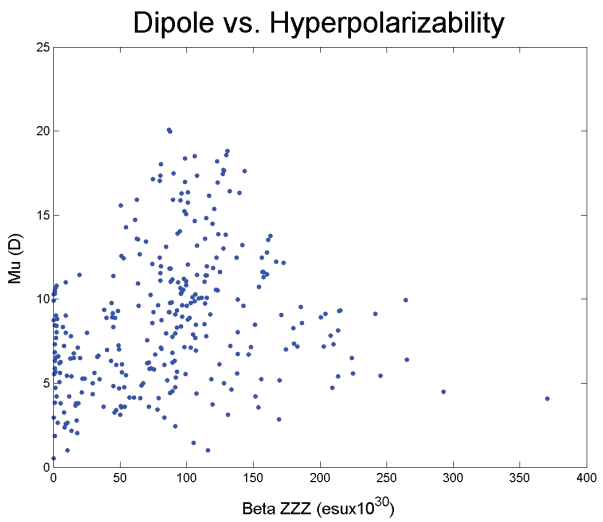

Figure 4. Magnitude of dipole moment in relation to the hyperpolarizability along the dipole vector.

There is very little correlation between the dipole moment and the β_{zzz} value. However, many of the chromophores with high β_{zzz} values have unusually low dipole moments when compared to traditional, uncharged chromophores. This could mean that these chromophores will order to a higher degree than chromophores with larger dipoles because while large dipole molecules order better in an electric poling field by μ, dipole-dipole interactions reduce acentric order by μ^2. However, the DNA will shield the intercalated dyes from dipole-dipole interaction meaning that larger dipoles could be beneficial.

Through the combinatorial screening process, several promising chromophore acceptors were discovered. The higher preforming acceptor was a five membered ring with a methylated pyridinium with a (see Figure 5) heterocyclic oxygen meta to the charge and a nitro group in between. It was observed that the charge localizes onto the nitro group which contributes to to increase in β_{zzz}. The optimized chromophore has a dipole of 4.0 D, a (β_{HRS}) of 169 x 10^{-30} esu, a β_{zzz} of 370 x 10^{-30} esu, and a bandgap of 1.24 eV. This is a 2.5 fold improvement in β_{zzz} over DAST. However, the ratio of β_{zzz}/ β_{HRS} decreased from 2.48 to 2.19, suggesting that there is still room to improve charge localization. The β_{zzz} of the optimized chromophore was only 58% of the CLD-1's β_{zzz}. The combinatorial search needs to be extended in order to achieve a β_{zzz} competitive with traditional chromophores such as CLD-1.

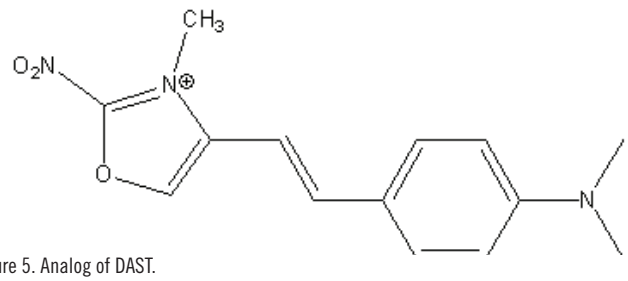

Figure 5. Analog of DAST.

Conclusions

In order to achieve an EO-active intercalating dye that is competitive with current materials, it is necessary to optimize a chromophore for both intercalation and high NLO activity. Large amounts of charge delocalization and octupolar character in a chromophore can be easily spotted but lesser degrees of octupolar characteristics cannot. A β_{zzz}/β_{HRS} ratio of approximately 2.5 is an indicator of minimal charge delocalization and correlates highly with chromophores with large β_{zzz} values. Some charged chromophores also have unusually small dipole moments which may increase acentric order. In addition, a chromophores acceptor with 2.5 fold increase over the β_{zzz} of DAST was discovered. Future work on this project will include finishing optimization on the acceptor and bridge components of a chromophore, synthesizing the highest performing chromophore yielded from the combinatorial screening, and creating a thin film to test the properties of the chromophore experimentally.

References

1. Dalton Research Group http://depts.washington.edu/eooptic/research/index.html.
2. SPIE. http://spiedigitallibrary.org/ebooks/spie/press_monographs/pm194/pm194_ch16 (accessed July 8, 2010).
3. Sullivan P. A.; Dalton L. R. Theory-Inspired Development of Organic Electro-Optic Materials. ACR Online 2008, Vol. 30, A-I.
4. Benight, S. et al. Reduced Dimensionality in Organic Electro-Optic Materials: Theory and Defined Order. J. Phys. Chem. B., 2010, ASAP article.
5. Bigelow, Nicholas. "Ethidium-DNA Binding Analysis Using Experimental Data and Computer Simulation Methods." Senior Thesis. 25 May 2008. University of Washington Department of Chemistry.
6. Robinson Research Group. "Use of DNA to Create a Host Environment." REU summer research project description. University of Washington Department of Chemistry, 2009.
7. Del Castillo, P; Horobin, R. W.; Blázquez-Castro, A; Stockert, J. C.; Binding of Cationic Dyes to DNA: Distinguishing Intercalation and Groove Binding Using Simple Experiments and Numerical Models. Biotech Histochem, 2010, Early Online.
8. Gunter, Peter et al; Organic Thin Film crystal growth for nonlinear Optics: Present Methods and Exploratory Developments. C. R. Physique 3, 2002, 449-462.
9. Zhang, C.; Dalton, L.; Low $V\pi$ Electrooptic Modulators from CLD-1: Chromophore Design and Synthesis, Material Processing, and Characterization. ACS, 2001,3043-3050.
10. Oudar, J. L.; Chemla, D. S.; Hyperpolarizabilities of the Nitroanilines and Their Relations to the Excited State Dipole Moment. J. Chem. Phys. 66, 6, 1977.

Acknowledgments

Funds for this research were provided by the Center on Materials and Devices for Information Technology Research (CMDITR), an NSF Science and Technology Center No. DMR 0120967. Additional funding was provided by UTC Air Force Grant FA8650-06-D-5401/0005, Task Order 0014. I would also like to thank the following people and company for the advice, assistance, and support that they gave me: Lewis Johnson, Prof. Bruce Robinson, Chris Moss, Dr. Bruce Eigenger, Meghana Rawal, Ilya Kosilkin, and Rainbow Photonics.

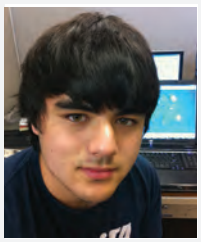

ZACHARY H. WATANABE is currently pursuing a high school diploma at the Northwest School. He plans on continuing his education by going to college and pursuing research opportunities.

Crystallography of New Non-Linear Optical Compounds

JOEL A. ZAZUETA, New Mexico Highlands University
Werner Kaminsky, University of Washington

Introduction

In Dr. Kaminsky's group we dealt with i-butyl-N-(4-x-phenyl) thiocarbamates with x = H, F^- Cl^-, Br, I^-, NO_2^- which represents a family of new compounds where we were looking for patterns of feature changes in relation to the functional group x (see Scheme 1).

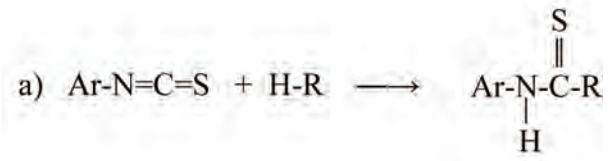

Compound, formula		Ar	H-R
1	$C_9H_{10}ClNOS$	3-chlorophenyl	Ethanol
2	$C_9H_{10}ClNOS$	4-chlorophenyl	Ethanol
3	$C_9H_{10}BrNOS$	4-bromophenyl	Ethanol
4	$C_{11}H_{14}FNOS$	4-fluorophenyl	2-butanol
5	$C_{11}H_{14}ClNOS$	4-chlorophenyl	2-butanol
6	$C_{11}H_{14}BrNOS$	4-bromophenyl	2-butanol
7	$C_{11}H_{14}N_2O_3S$	4-nitrophenyl	2-butanol
8	$C_{11}H_{14}ClNOS$	4-chlorophenyl	(S)-(+)-2-butanol
9	$C_{11}H_{14}N_2O_3S$	4-nitrophenyl	(S)-(+)-2-butanol
10	$C_{15}H_{15}ClN_2S$	4-chlorophenyl	α-MBA
11	$C_{15}H_{15}BrN_2S$	4-bromophenyl	α-MBA
12	$C_{15}H_{15}N_3O_2S$	4-nitrophenyl	α-MBA

Scheme 1. The structures studied in this report as synthesized by previous REU students and members of the Kaminsky research group.

We are especially interested in morphological as well as optical features that include refraction coefficients, second harmonic generation, electro-optical effects and chiro-optical properties like optical rotation. Optical rotation is often used to characterize materials in solutions, where the measured value represents the isotropic average of the rotation tensor. When dealing with optical rotation in crystals more details become visible from the anisotropy of the optical rotation tensors which are coupled to the orientation of chiral molecules in the crystal lattices. When comparing calculated features with experimental evidence, this project aims at contributing to the understanding of how to predict crystalline features from molecular coordinates obtained in X-ray diffraction studies of crystals.

This series promises to be well suited especially for providing molecular geometries from X-ray structure experiments due to heavy elements in the molecules such as sulfur, which scatters X-rays well. The presence of a nitro group and other halogens may serve as electron donors and enhance optical features.

The second portion of the project also aims to conduct Second Harmonic Generation (SHG) testing on the non-centrosymmetric crystals. The data from these tests will be compared to a known standard, KH_2PO_4.

This choice of thiocarbamates is known to build hydrogen bonds, forming thioamide dimers to further promote crystal growth (see Figure 1).[1] The dimer formation is key for eliminating a static dipole of the molecules.

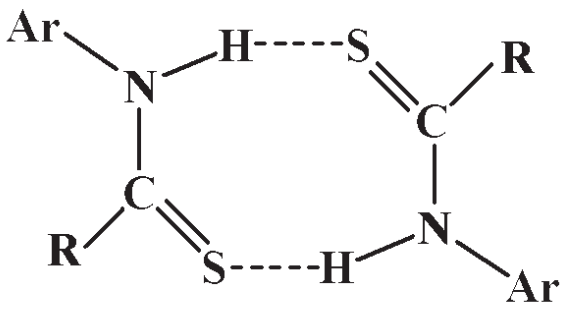

Figure 1. $\{\ldots H\text{-}N\text{-}C{=}S\}_2$ dimer. R = i-butyl alcohol. Ar = (4-x-phenyl) with x = H, F^- Cl^-, Br, I^-, NO_2^-.

If the molecules can exist in a left- and right-handed form, the dimer formation introduces a center of symmetry. However, if the thiocarbamates are synthesized from Isothiocyanates (ITCs) and enantiopure i-butyl alcohol, only one hand of molecules exists, which does not permit the existence of centro-symmetry. In this case a molecular dipole may not completely be quenched and crystallization of these compounds is likely to be more difficult.

It has to be mentioned that the enantiopure compounds are potentially of medical interest,[2] however this is beyond the scope of this project. Related compounds to those of this study are published elsewhere.[3]

Optical features depend on the crystal symmetry, i.e. the linear electro-optic effect, second harmonic generation and optical rotation require the absence of a center of symmetry.[4] Similarly, the structural differences between enantiopure and racemic compounds will affect the morphology of the new compounds (see Figure 2).

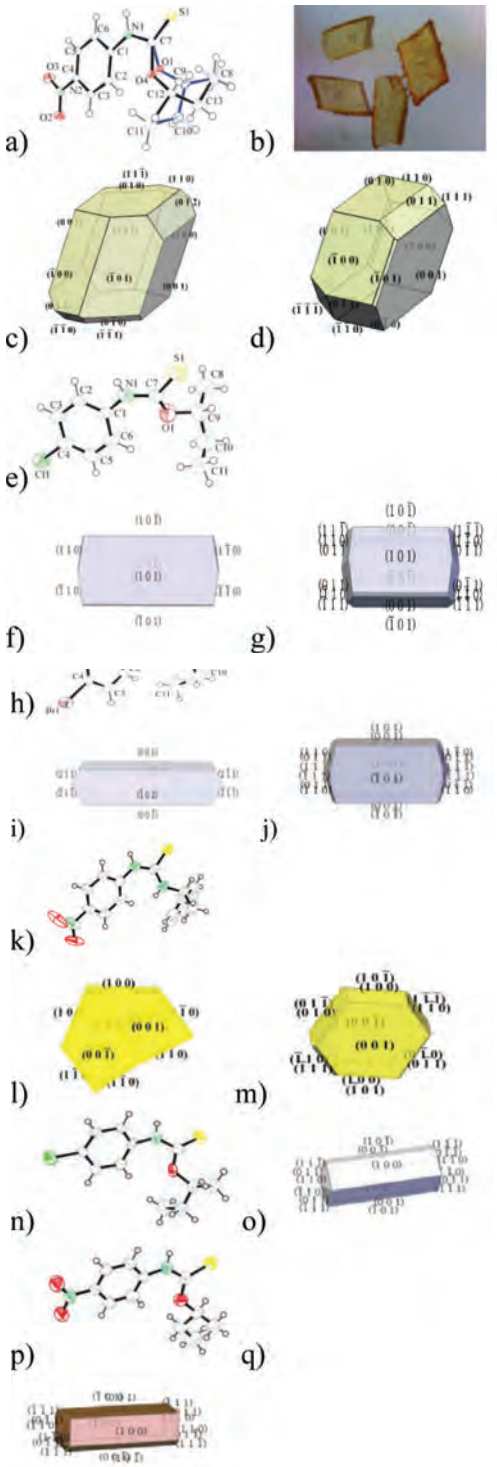

Figure 2. a) i-butyl-N-(4-nitrophenyl) thiocarbamate (compound **7**), The racemic mixture of the alcohol is evident in the disorder as well as space group symmetry of the compound, b) crystals of this compound. The size of the crystals is ca. 1-2 mm across. c) indexed morphology and d) in same orientation calculated morphology. The following compound is 4-chloro 2-Butanol racemic compound and has a chemical formula of e) $C_{11}H_{14}NOClS$ (compound **5**), and f) calculated morphology of the same formula. Provided for this compound also calculated g) Bravais, Friedel, Donnay, Harker (BFDH) model shape. The following compound is a racemic version of 4-bromo 2-butanol (compound **6**) and has an empirical formula of h) $C_{11}H_{14}NOBrS$ and the i) calculated morphology, followed by the j) BFDH model. A related compound (**12**) is k) $C_{15}H_{15}N_3O_2S$ where 2-butyl is replaced by methylbenzylamine and has the l) indexed twin morphology and m) BFDH model. n) Here we have the enantiopure compound of 4-chloro 2-S-butanol compound **8** with o) the BFDH model and finally we have p) compound **9** $C_{11}H_{14}N_2O_3S$, which is the enantiopure version of **7** as well as q) the calculated morphology.

Within the series of already synthesized thiocarbamates is a possibility of polymorphism where the same molecules crystallize in different symmetries. The thiocarbamates are split into two different groups with closely related symmetries (P 2_1/c and P 2_1 versus P$\bar{1}$ and P 1) but we have yet to crystallize a polymorph for a given composition.

We studied these Isothiocyanates through X-ray diffraction to find the morphology of the newly synthesized compounds, most of which were already at hand resulting from the work of previous REU students. Morphologies will be compared to those calculated via the Bravais-Friedel, Donnay-Harker model from within the WinXmorph software package.[5]

From X-ray structures we studied the crystal packing employing Hirshfeld surface calculations[6] to understand the predicted morphologies which may be affected by residual dipoles and hydrogen bonds, and calculate optical properties with the OPTACTS/DES software packages.[7]

Discussion and Results

i) Morphologies

Once the crystals were obtained and good samples available, the winxmorph program came in handy when calculating the morphologies of both racemic and enantiopure compounds listed in Figure 2. The BFDH models were also predicted using the winxmorph program. As evident in Figure 3, the intermolecular bonding scheme shows significant differences between racemic compounds **7** and enantiopure **9** although they are identical in chemical composition.

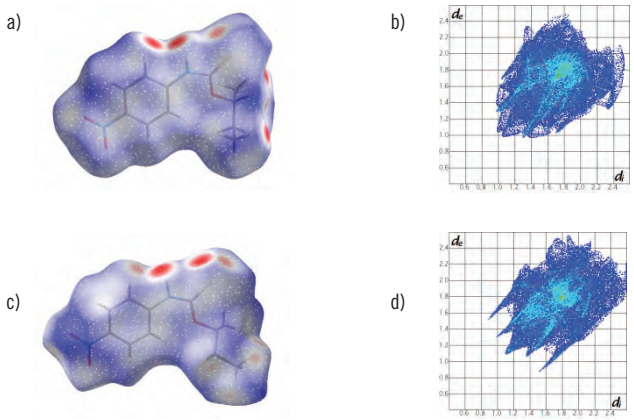

Figure 3. a) Hirshfeld surface and b) fingerprint plots for racemic compound **7**. c), d) surface and fingerprint for enantiopure compound **9** of identical composition. Hirshfeld surfaces are designed to smoothly enclose almost all available space around a molecule. Points **r** on a HS are found where the sum of all spherically approximated electron densities of a molecule at **r** is twice the contribution of all atoms in the unit cell at **r**. The surface than can be color-coded relative to the distances from points **r** to the nearest atoms. When choosing a color scheme where red indicates short distances and blue large ones, hydrogen bonds or other close contacts of a molecule to a neighboring one are easily spotted.

Because **7** exhibits more expressed hydrogen bonds and the bonding is less directional, the BFDH model compares better with the indexed morphology than for compound **9** where not well expressed long thin needles which did not even allow proper face indexing were

significantly different to the calculated morphology which in turn also differs strongly from the more prismatic indexed and calculated models of the racemic equivalent (**7**).

ii) Second harmonic generation

The second portion of the experiment involved the second harmonic generation testing. The compounds tested were the enantiopure compounds **9** and **12**. Some other previously synthesized crystals, 4-chloro isothiocyanates (ITC) methyl benzyl amine (MBA) and 4-bromo ITC MBA will be part of future work for the SHG portion of the project.

For SHG testing we used an SHG microscope. The sample powder was placed in oil on a slide and bombarded at 3.55 MW pulses and a wavelength of 860 nm (+/-) 5 nm. The light passed through a 430 nm, (+/-) 5 nm band pass filter. 10 x 10 µm across micrographs recorded from the experiment in Figure 4 showed dark to bright spots with brighter spots in compound **12** indicating higher SHG efficiency than the reference sample (KH_2PO_4).

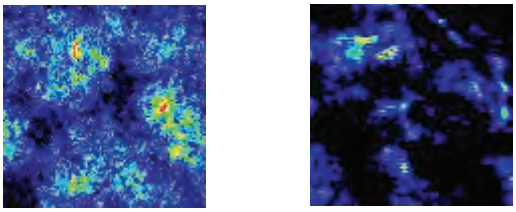

Figure 4. SHG micrographs 10 x 10 µm of compounds a) 4-nitrophenyl isothiocyanate (ITC) methyl benzyl amine (MBA) (**12**) and b) KH_2PO_4.

In a further experiment (see Figure 5) integrated SHG intensities were recorded against the input intensity showing that compound **12** has three times more SHG efficiency than KH_2PO_4. This proves that there are in fact useful properties involved in this new family of compounds.

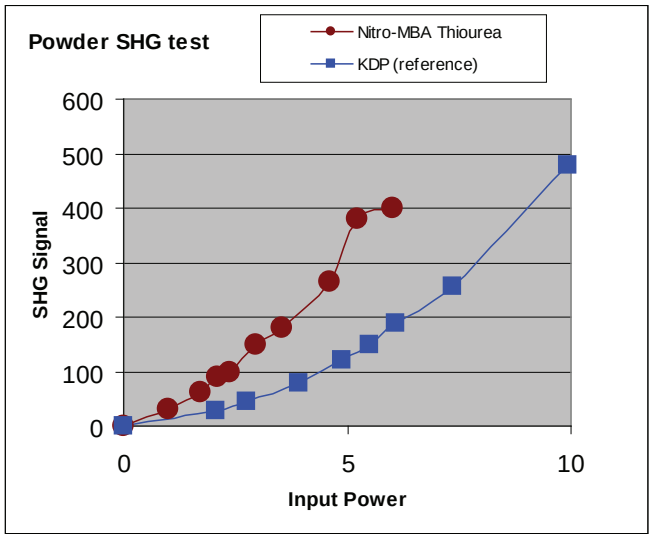

Figure 5. Comparison of SHG efficiency between compound **12** (red dots) and KH_2PO_4 (squares). Evident is the expected (non-linear) quadratic dependency of SHG signal on input intensity (arbitrary units).

iii) Tensor calculations

Calculation of SHG efficiencies were performed via the OPTACT/DES theory. With the dipole-dipole interaction model it is possible to calculate refractive indices from given atom coordinates and symmetry of a crystal. Input variables are here the electronic polarizabilities of atoms.

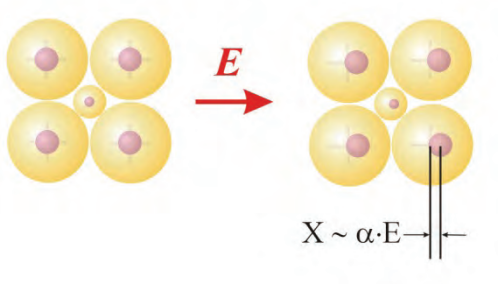

Figure 6. Change x of atomic position due to an external electric field E in proportion to the electronic polarizabilities of individual atoms.

Recalculating the refractive indices for structures under the influence of an electric field then yields electro-optic tensors coefficients and with rescaling of the polarizabilities for the SHG input wave length it is possible to obtain SHG coefficients. A set of suitable polarizabilities which reproduced experimental refractive indices for compound **12** was also used for compound **9**. Both compounds contain a nitro group as electron donor. The resulting tensors in Figure 7 show similar scale but distinct differences in shape indicating the different roles of α-methylbenzylamine and 2-S-butanol in these compounds which otherwise are of identical composition.

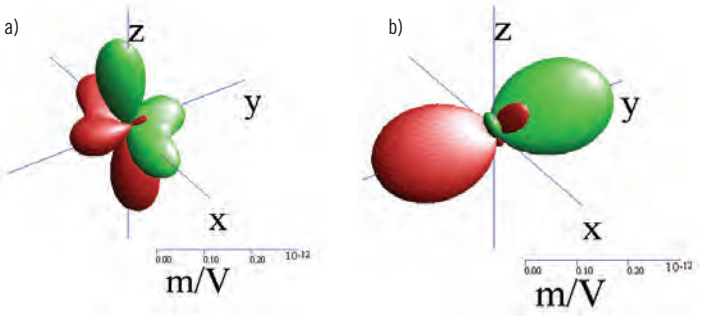

Figure 7. Calculated SHG tensors for compounds a) **12** and b) **9**. Electronic polarizabilities are (Å³) C, H, N, O, S = 0.09, 0.7, 0.005, 2.5, 5.3, respectively. Input wavelength 1064nm.

The SHG calculations are best used to find correlations between closely related compounds. A theoretical comparison with other compounds or KH_2PO_4 for that matter is not reliable. The experimental SHG efficiency in 12 is 3 times that of KH_2PO_4 thus we can expect that **9** would also have similarly large effects. Direct testing revealed unfortunately that **9** does not endure SHG testing conditions.

Conclusion

The face indexing was compared to calculated morphologies from the Bravais, Friedel; Donnay, Harker (BFDH) model utilizing the winxmorph program. Different intermolecular bonding schemes are revealed in differences of the observed and estimated morphologies.

SHG tests for 4-Nitrophenyl ITC MBA showed promising 3 times larger signals than that found in reference material KH_2PO_4.

More enantiopure compounds will be tested for SHG efficiency.

If technically promising optical properties are predicted, we will then synthesize more material to grow larger crystals for testing any possible practical applications.

References

1. Ho, S. Y.; Bettens, R. P. A.; Dakternieks, D.; Duthie, A.; Tiekink, E.R.T. Prevalence of the thioamide {…H–N–CLS}2 synthon—solid-state (X-ray crystallography), solution (NMR) and gas-phase (theoretical) structures of O-methyl-N-aryl-thiocarbamides. Cryst. Eng. Comm. 2005, 7, 682–689.

2. a) Humeres, E.; Zucco, C.; Nunes, M.; Debacher, N.; Nunes, R. Hydrolysis of N-aryl thioncarbamate esters. Modified Marcus equation for reactions with asymmetric intrinsic barriers J. Phys. Org. Chem. 2002, 15, 570-575. b) Fowke, J.; Chung, F.; Jin, F.; Qi, D.; Cai, Q.; Conaway, C.; Cheng, J.; Shu, X.; Gao, Y.; Zheng, W. Urinary isothiocyanate levels, brassica, and human breast cancer. Cancer Res. 2003, 63, 3980-3986. c) These thiocarbamates are typical of the structures often used (or found) in high-throughput screens and often have multiple activities. Something this small is often a fragment or part of the overall pharmacophore. It may have low (µmol to µmol) affinity for part of the receptor binding epitope and will eventually be complemented by a second fragment of approximately the same size that occupies the other part of the binding epitope. As far as for specific activity these compounds are not part of a predictable class of biologically active compounds. Activity studies would require unbiased high throughput screens and fragment approaches.

3. a) Taylor, R.; Tiekink, E. R. T. Crystal and molecular-structure of O-ethyl-N-phenylthiocarbamate, Z. Kristallogr. 1994, 209, 64-67. b) Benson, R. E.; Broker, G. A.; Daniels, L. M.; Tiekink, E. R. T.; Wardell, J. L. Young, D. J. (E)-O-Ethyl N-(4-nitrophenyl) thiocarbamate, Acta Cryst. 2006, E62, 4106–4108. c) Ellis, C. A.; Miller, M. A.; Spencer, J.; Zukerman-Schpector, J.; Tiekink, E. R. T. Co-crystallization experiments of thiocarbamides with bipyridine-type molecules, Cryst. Eng. Comm. 2009, 11, 1352–1361. d) Jian, F. F.; Yu, H. Q.; Qiao, Y. B.; Liang, T. L. O-Isobutyl N-phenylthiocarbamate, Acta Cryst. 2006, E62, 3416-3417. e) Ho, S. Y.; Lai, C. S.; Tiekink, E. R. T. O-Methyl N-phenylthiocarbamate, Acta Cryst. 2003, E59, 1155-1156. f) Kuan, F. S.; Mohr, F.; Tadbuppa, P. P.; Tiekink, E. R. T. Principles of crystal packing in O-isopropyl-N-aryl-thiocarbamides: iPrOC(LS)N(H)C6H4-4-Y: Y 5 H, Cl, and Me, Cryst. Eng. Comm. 2007, 9, 574–581. g) Kaminsky, W.; Goldberg, K.I .; West D. X. Synthesis and structures of two N,N'-bis(2-pyridinyl)thioureas and N-(2-pyridinyl)-N'-(benzoyl)thiourea, J. Mol. Struct. 2002, 605, 9-15. h) Hermetet, A. K.; Ackerman, L. J.; Eilts, K. K.; Johnson, T. K.; Swearingen, J. K.; Giesen, J. M.; Goldberg, K. I.; Kaminsky, W.; West, D. X. Structural, spectral and thermal studies of N-2-(4,6-lutidyl)-N'-chlorophenylthioureas, J. Mol. Struct. 2002, 605, 214-247. i) Valdes-Martinez, J.; Henandez-Ortega, S.; Espinosa-Perez, G.; Presto, C. A.; Hermetet, A. K.; Haslow, K. D.; Ackerman, L. J.; Szczepura, L. F.; Goldberg, K. I.; Kaminsky, W.; West, D. X. Structural, spectral and thermal studies of substituted N-(2-pyridyl)-N'-phenylthioureas, J. Mol. Struct. 2002, 608, 77-87. j) Szczepura, L. F.; Kelman, D. R.; Hermetet, A. K.; Ackerman, L. J.; Goldberg, K. I.; Claborn, K. A.; Kaminsky, W.; West, D. X. Structural, spectral and thermal studies of N-2-(picolyl)-N'-4-chlorophenylthioureas, J. Mol. Struct. 2002, 608, 245-251. k) Giesen, J. M.; Claborn, K. A.; Goldberg, K. I.; Kaminsky, W.; West, D. X. Structural, thermal and spectral studies of N-2-pyridyl-, N-2-picolyl- and N-2-(4,6-lutidyl)-N'-(3-methoxyphenyl)thioureas, J. Mol. Struct. 2003, 613, 223-233. l) Kaminsky, W.; Kelman, D. R.; Giesen, J. M.; Goldberg, K. I.; Claborn, K. A.; Szczepura, L. F.; West, D. X. Structural and spectral studies of N-2-(pyridyl)-, N-2-(3-, 4-, 5-, and 6-picolyl)- and N-2-(4,6-lutidyl)-N'-2-thiomethoxyphenylthioureas, J Mol. Struct. 2002, 616, 79-89. m) Kelman, D. R.; Claborn, K. A.; Kaminsky, W.; Goldberg, K. I.; West, D. X. Structural, spectral and thermal studies of N-2-(pyridyl)- and N-2-(picolyl)-N'-(3-chlorophenyl)thioureas, J Mol. Struct. 2002, 642, 119-127. n) Kelman, D. R.; Claborn, K. A.; Kaminsky, W.; Goldberg, K. I.; Li, D. T.; West, D. X. Structural studies of N-2-(6-aminopyridine)-N'-arylthioureas, J. Mol. Struct. 2003, 654, 145-152. o) Valdes-Martınez, J.; Hernandez-Ortega, S.; Rubio, S. M.; Li, D. T.; Swearingen, J. K.; Kaminsky, W.; Kelman, D. R.; West, D. X. Study of the sulfur atom as hydrogen bond acceptorin N(2)-pyridylmethyl-N'-arylthioureas, J. Chem. Crystallogr. 2004, 34, 533-540. p) Valdes-Martınez, J.; Hernandez-Ortega, S.; Hermetet, A. K.; Ackerman, L. J.; Presto, C. A.; Swearingen, J. K.; Kelman, D. R.; Goldberg, K. I.; Kaminsky, W.; and Douglas X.; West, D. X. Structural studies of N-2-(3-picolyl)- and N-2-(4-picolyl)-N'-tolylthioureas, J. Chem. Crystallogr. 2002, 32, 431-438. q) Hermetet, A. K.; Ackerman, L. J.; Swearingen, J. K.; Presto, C. A.; Kelman, D. R.; Giesen, J. M.; Goldberg, K. I.; Kaminsky, W.; West, D. X. Structural studies of N-2-(6-picolyl)-N'-tolylthioureas, J. Chem. Crystallogr. 2002, 32, 17-25. r) Allen, F. H.; Motherwell, W. D. S.; Raithby, P. R.; Shields G. P.; Taylor, R. Systematic analysis of the probabilities of formation of bimolecular hydrogen-bonded ring motifs in organic crystal structures, New J. Chem. 1999, 23, 25-34.

4. The following review is only one of many examples: Kaminsky, W. Experimental and phenomenological aspects of circular birefringence and related properties in transparent crystals. Rep. Prog. Phys. 2000, 63, 1575-1640.

5. a) Kaminsky, W. From *.cif to virtual morphology: new aspects of predicting crystal shapes as part of the WinXMorph program. J. Appl. Cryst. 2007, 40, 382-385. b) Kaminsky, W. WinXMorph: a computer program to draw crystal morphology, growth sectors and cross-sections with export files in VRML V2.0 utf8-virtual reality format. J. Appl. Crystallogr. 2005, 38, 566-567. c) Bravais, A., du Cristal Considere Comme un Simple Assemblage de Points, Etude Cristallographiques; Gauthier-Villars: Paris, France, 1866. d) Friedel, G. Studies on the law of Bravais, Bull. Soc. Franc. Mineral 1907, 22, 326-455. e) Donnay, J. D. H.; D. Harker, D. A new law of crystal morphology extending the law of Bravais, Am. Mineral. 1937, 22, 446-467.

6. a) McKinnon, J. J.; Mitchell, A. S; Spackman, M. A. Hirshfeld Surfaces: A New Tool for Visualising and Exploring Molecular Crystals, Chem. Eur. J. 1998, 11, 2136–2141. b) McKinnon, J. J.; Spackman, M. A.; Mitchell, A. S. Novel tools for visualizing and exploring intermolecular interactions in molecular crystals, Acta Crystallogr. Sect. B 2004, 60, 627–668. c) Spackman, M.; McKinnon, J. J. Fingerprinting intermolecular interactions in molecular crystals, Cryst. Eng. Comm 2002, 4, 378–392. d) McKinnon, J. J.; Spackman, M. A.; Mitchell, A. S. Novel tools for visualizing and exploring intermolecular interactions in molecular crystals, Acta Crystallogr. Sect. B 2004, 60, 627–668.

7. a) Devarajan, V.; Glazer, A. M. Theory and computation of optical-rotatory power in inorganic crystals Acta Crystallogr, Sect. A 1986, 42, 560. b) Kaminsky, W.; Glazer, A. M.; Comparison of experimental optical properties of TGS with calculations using the DES model, Phase Transit. 1997, 66, 1–21. c) Kaminsky, W.; Glazer, A. M. Crystal optics of Mannitol, C6H14O6: Crystal growth, structure, basic physical properties, birefringence, optical activity, Faraday effect, electro-optic related effects and model calculations, Z. Kristallogr. 1997, 212, 283-296.

JOEL A. ZAZUETA is a senior in chemistry at New Mexico Highlands University. After graduation, Joel plans to earn a Doctor of Pharmacy.

Study of Surface Morphology of Organic Photovoltaic by Atomic Force Microscopy

SHUTONG ZHAN, Duke University
Ben Wunsch, Jassem Abdallah, Seth Marder, Georgia Institute of Technology

Introduction

Organic photovoltaics (OPVs) have been studied since the discovery of photo-induced charge transfer in composites of conjugated polymers and fullerenes a decade ago.[1] The materials used in OPVs generally have a delocalized π-electron system that can absorb sunlight and transport charges. In order to use such materials in a solar cell device, they are generally processed into a thin film with a thickness between 100 to 500 nm. OPVs have shown promising potential due to their flexibility on large surfaces, low cost and easy manufacturing compared to inorganic solar cells. The main disadvantages associated with OPVs are low efficiency and low stability compared to inorganic solar cells. The efficiencies of polymer photovoltaic (PV) cells improved with the introduction of the bulk hetero-junction (BHJ) concept, which consists of an interpenetrating network of electron donor and acceptor materials as shown in Figure 1.[2] The difference in electron affinity between the acceptor and donor materials generates an electric field at their interface. The local electric potential helps to generate charges from excitons, which are bound states of an electron-hole pair generated by light. From experiment and simulation, the ideal spacing between two material domains is estimated at 10-20 nm, in order to match the exciton's diffusion length.[3]

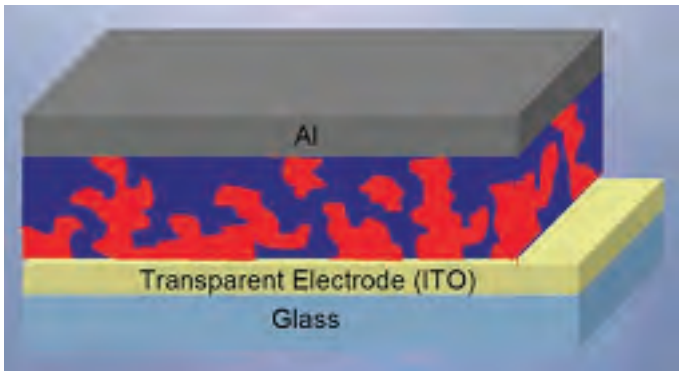

Figure 1. A schematic of a BHJ solar cell.[4]

The domains (concentration of certain phase of materials) should have an "optimum" morphology of bi-continuous columns or paths so that charges can transverse to their corresponding electrodes.[5] The importance of the BHJ structure highlights the perceived, essential morphological requirements for OPV systems. Currently, BHJs composed of regioregular poly(3-hexyl thiophene) or RR-P3HT as the donor and [6,6]-phenyl-C_{61}-butyric acid methyl ester or PCBM as the acceptor have been extensively studied. Researchers have obtained power conversion efficiencies as high as 5% using the P3HT:PCBM system.[6] While morphological research on the P3HT: PCBM system is relatively mature, other conjugated materials, including electron acceptor polymers and small molecule donors, remain largely uncharacterized. It is unclear how to generate or control BHJ morphology for most OPV blends; therefore fundamental studies of OPV blend morphology are essential to improve overall device performance.

One starting point to decipher the morphology of OPV films is to link the blend's thermodynamic property with its morphological properties. This requires mapping phase changes in the OPV blend with the corresponding morphology changes in the thin film. Towards this goal, previous work in the Marder Group has established the macro phase changes of an OPV blend made of a novel oligomeric donor, a benzothiadiazole-dithienopyrrole – BTD-DTP (LEH-II-105),[7] and alternating co-polymer acceptor, napthalenediimide-dithiophene – NDI-2T (TS-II-248).[8]

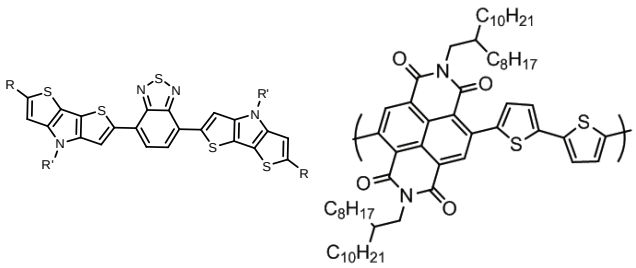

Figure 2. (left) LEH-II-105 (the oligomer donor); (right) TS-II-248 (the polymer acceptor).

The Phase diagram of LEH-II-105 and TS-II-248 based on differential scanning calorimetry data indicates major physical transitions of the two materials as shown in Figure 3.[9] The polymer has a suspected melting transition at 282 °C. The oligomer has two major transitions: first one at 51 °C suspected as a crystal polymorphism, followed by a melting transition at 134 °C. The shift of the polymer melting point with increasing oligomer content suggests some degree of miscibility of the two materials.

The goal of this research is to characterize and map this oligomer/polymer blend's morphology evolution at the thin film (mesoscopic) level by Scanning Probe Microscopy. Specifically, Atomic Force Microscopy (AFM) is used in this study to scan the topography of the sample surface at thermodynamic equilibrium at increasing temperatures, following the form of the phase diagram. The samples are studied with AFM both *in situ* and *ex situ*. The *in situ* AFM study

gives the ability to scan the sample during annealing.[10] The *in situ* method is ideal for this study; however, due to limited equipment, the *ex situ* study is also performed to complete the study. The *ex situ* scans the surface morphology at room temperature after temperature quenching from annealing, which preserves the surface morphology at annealing temperature. The morphology evolution result will be further compared to the macro scale thermodynamic phase change.

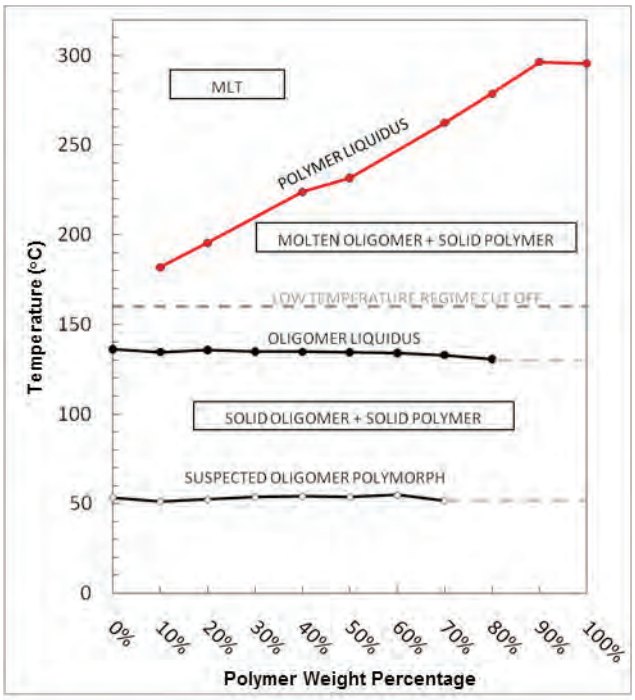

Figure. 3 Phase diagram of LEH-II-105 and TS-II-248 created based on DSC data.[9]

Experimental

Materials and Sample

Films were prepared by spin-coating on ITO coated glass substrates successive layers of PEDOT: PSS (~60 nm) and polymer/oligomer blend (~80-100 nm). Stock solutions of 1.2 – 1.4% PEDOT:PSS (H.C. Starck, Clevios ™ P) in distilled water and 15 mg/mL OPV blend in chloroform were used. Stock solutions were allowed to stir for >12 h and filtered with a 0.2 µm PTFE syringe filter (Whatman) prior to use. ITO substrates were cleaned with acetone and modified by oxygen plasma prior to spincasting. The films are named by their weight percentage in the blends.

In situ AFM

The 50 wt% polymer sample is imaged under *in situ* AFM study. The sample is first scanned under ambient conditions at 25 °C. Then the sample is heated on a hot stage (Agilent 5500 LS) at 2 °C/min ramping rate to 35 °C in air. After reaching the desired temperature, the sample remains on the heating stage for 10 min while the temperature equilibrates. The heating regime is shown in Figure 4. Next the AFM is engaged onto the surface and scanned at 1, 5, 10, and 20 µm x µm to capture as much breadth of scale as possible. This procedure is repeated for successive temperatures up to 200 °C. Smaller temperature increments (e.g. 10 °C) were chosen around 55 °C and 130 °C, which correspond to the major macrophase transitions in the oligomer, to obtain better resolution. The total scanning time at each temperature is roughly 20 min.

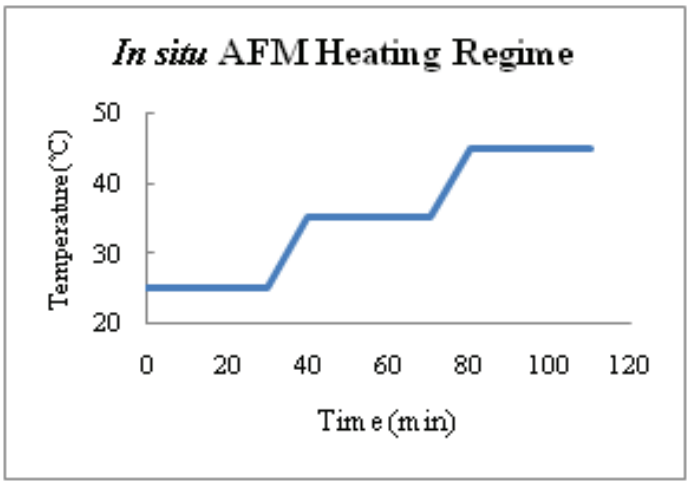

Figure 4. Heating regime for the *in situ* AFM study.

The *in situ* AFM study is carried out at the following temperatures: 25 °C, 35 °C, 45 °C, 55 °C, 65 °C, 80 °C, 100 °C, 120 °C, 130° C, 140 °C, 170 °C and 200 °C.

Ex Situ AFM

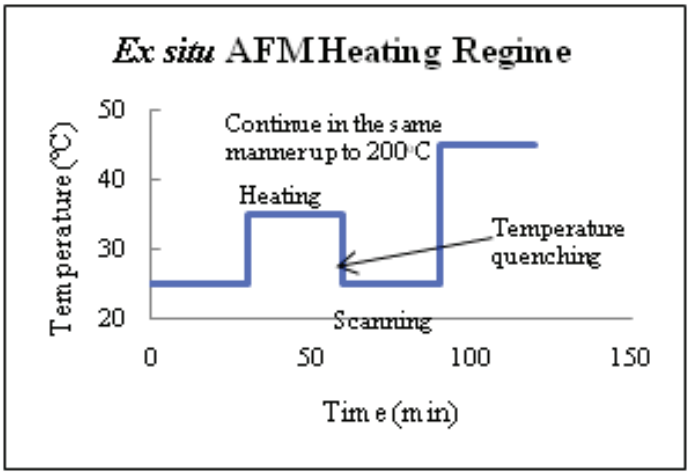

Figure 5. Heating regime for the ex situ AFM study.

For the *ex situ* AFM, 20, 50 and 80 wt% polymer samples were scanned for comparative study to distinguish how each material affects the film morphology. They are all studied at the same temperatures where the *in situ* study takes place with an additional 90 °C heating regime. Samples are first heated on a hotplate (Dataplate 720) at the desired temperature for 30 minutes in a nitrogen environment. After heating, the samples are quenched by placing rapidly onto a large metal plate at room temperature in order to capture the morphology of the sample at the annealing temperature. This can be represented

by the *ex situ* heating regime in Figure 5. They are left on the metal plate for 30 min to ensure cooling to room temperature. After cooling, the sample surfaces are scanned in AFM under ambient conditions.

The *in situ* AFM was carried out with an Agilent 5600LS. The *ex situ* AFM is first carried out with Agilent 5600LS and then with Vecco Dimension 3100, using Mikromasch, Ultrasharp NSC35/no Al (k = 7.5 N/m) probes. The temperature of the heating stage and the hotplate were calibrated with Extect Surface Probe (K type).

All AFM data are processed and analyzed by Gwyddion 2.19. The topography images are mainly leveled by removing second degree polynomial background and lines corrected by matching height median. Root mean square (RMS) measurement of the surface background texture is used to quantify the roughness of the sample. Some large high droplet features are masked in order to level the background texture of the image and measure the surface background texture roughness.

Results and Discussion

1. *In situ* AFM results

In the low temperature regime (25-45 ºC) it is observed that the RMS roughness decreases from 3.12 nm to about 2 nm shown in Figure 6, indicating a progressive smoothing of the surface. The major textures at different temperatures are shown in Figure 7. Starting at 65 ºC, a grain-like texture with average widths of 200-300 nm develops on the surface. At 100 ºC, a complete new texture separates from the surface in a manner similar in appearance to spinodal dewetting. The dewetting texture obtains widths around 200 nm to 600 nm.

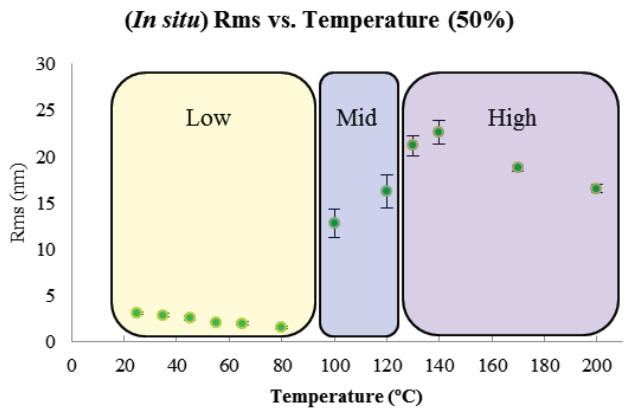

Figure 6. The roughness evolution of the *in situ* 50 wt% polymer sample.

After 100 ºC, the dewetted texture starts to aggregate and forms larger, more circular particulates indicated by data shown in Figure 8.

Concurrently micro-sized droplets start to form on the film surface, which can be viewed under the AFM's optical camera. This unexpected structure was first noticed at 170 ºC; however, the exact onset temperature is unknown. After cooling to 25 ºC, both the mesoscale particulates and micron-sized droplets remain on the surface.

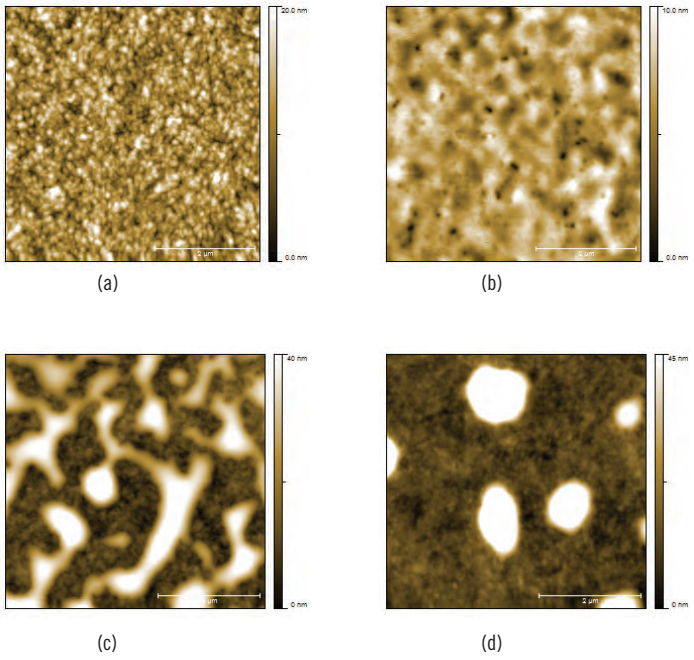

Figure 7. The topography images of the *in situ* 50 wt% polymer sample at (a) 25 ºC, (b) 80 ºC, (c) 100 ºC, (d) 200 ºC.

Since the experiment is conducted under the assumption that the sample surface is at morphological equilibrium, it is important to confirm it with experimental evidence.

	130 ºC	140 ºC	170 ºC	200 ºC
Average Width (nm)	540	570	600	770

Figure 8. The average short axis width of the mesoscale particulates forming on the *in situ* 50 wt% polymer sample at different temperature.

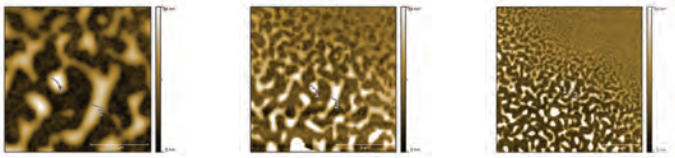

	5 µm scan	10 µm scan	20 µm scan
Length of Mark 1 (µm)	0.76	0.71	0.73
Length of Mark 2 (µm)	0.59	0.62	0.56

(d)

Figure 9. Evidence of equilibration of the sample for *in situ* study at 100 ºC: (a) 5 µm scan, (b) 10 µm scan, (c) 20 µm scan, (d) the average length of the two marks.

First, the same feature is scanned at different sizes during *in situ* study and they do not show major variation during the scanning time (roughly 5 minutes per scan) shown in Figure 9. The same feature does not appear to change during the 20 minutes scanning time. Compared to the major texture change during the 10 minutes temperature ramping, which indicates a fast kinetic process, it suggests that the sample is at thermodynamic equilibrium.

2. *Ex situ* AFM result

The 20 wt% polymer sample:

Analysis of the RMS roughness shows three distinct temperature regimes that correlate to changes in the surface morphology, as shown in Figure 10. Major textures are shown in Figure 11. The surface has a plate like texture at ambient temperature. At low temperatures (25-100 ºC), the plate-like texture starts coarsening, as indicated by a gradual increase in roughness. Starting at 120 ºC, micron-sized droplets (Figure 12a) along with small particulates form on the surface. These textures develop up to 130 ºC where more small particulates form on the surface. Starting at 140 ºC, the small particulates aggregate into larger globules, clearing from the surface to reveal a fibril-like texture in the background. The average width of the background fibrils is 29 ± 6 nm at 200 ºC.

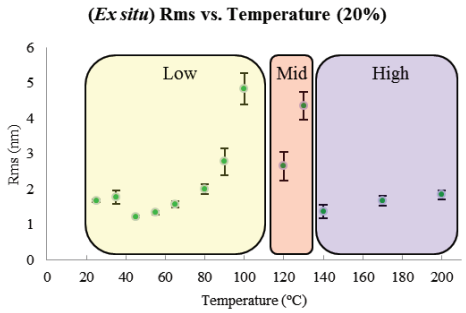

Figure 10. The roughness evolution of the *ex situ* 20 wt% polymer sample.

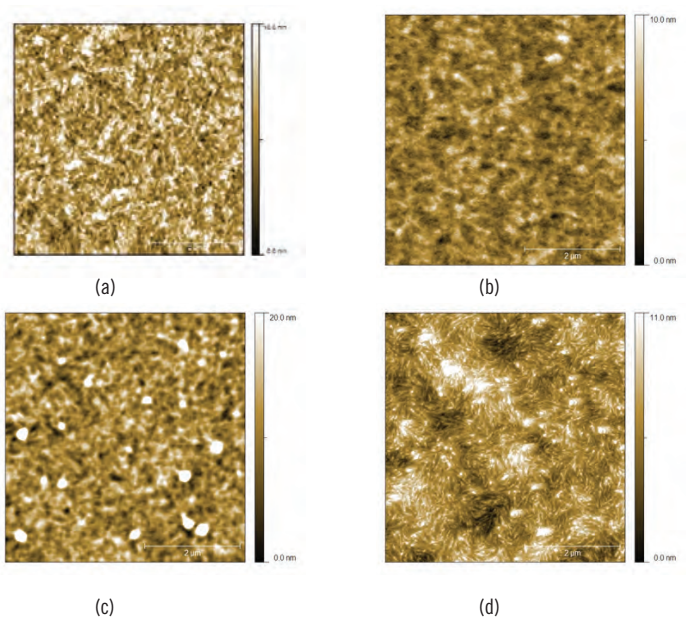

Figure 11. The topography images of the *ex situ* 20 wt% polymer sample at (a) 25 ºC, (b) 55 ºC, (c) 130 ºC, (d) 200 ºC.

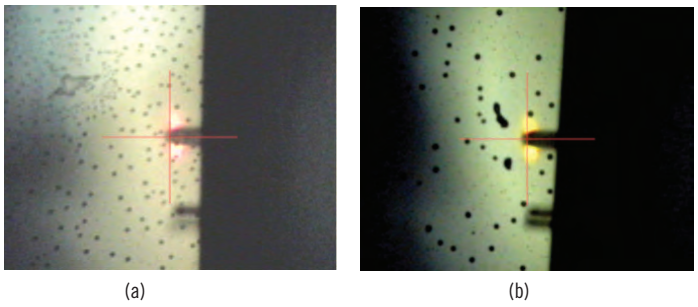

Figure 12. Images taken under AFM optical camera scanning *ex situ* 20 wt% polymer sample annealed at (a) 120 ºC, (b) 170 ºC.

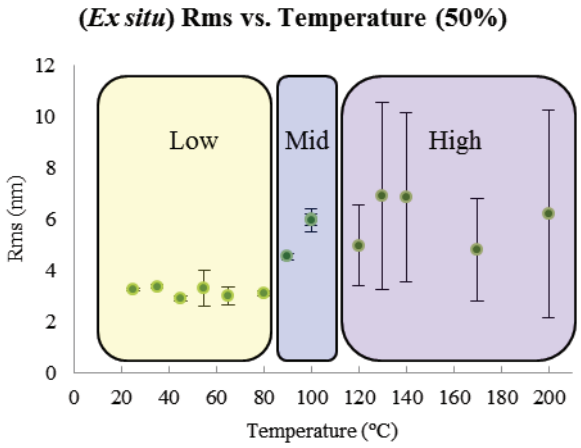

Figure 13. The roughness evolution of the *ex situ* 50 wt% polymer sample.

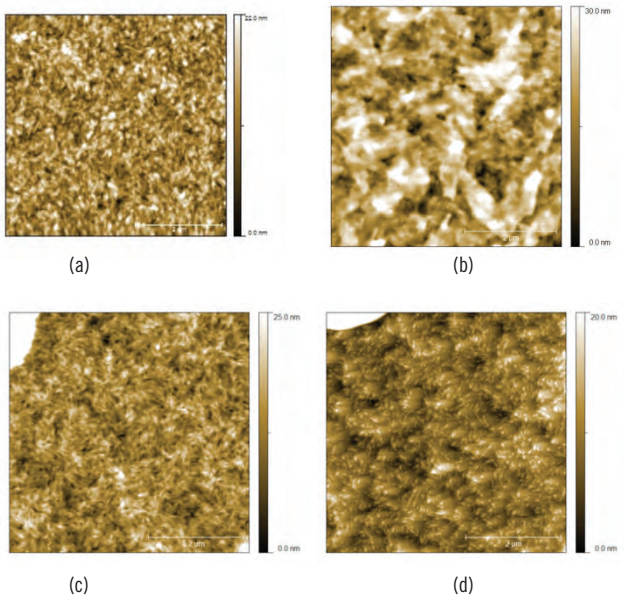

Figure 14. The topography images of the *ex situ* 50 wt% polymer sample at (a) 25 ºC, (b) 100 ºC, (c) 120 ºC, (d) 200 ºC.

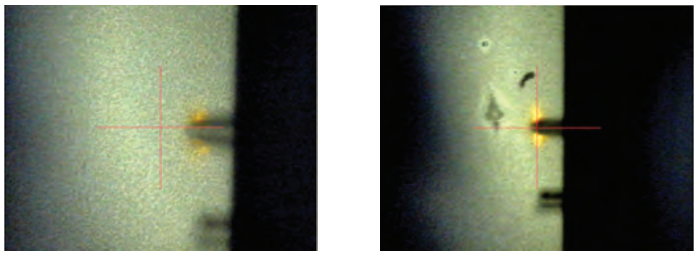

(a) (b)

Figure 15. Images taken under AFM optical camera scanning *ex situ* 50 wt% polymer sample annealed at (a) 120 ºC, (b) 140 ºC.

	120 °C	170 °C	200 °C
Average Width (nm)	67 ± 16	53 ± 8	45 ± 7

Figure 16. The average width of the fibril texture forming on the *ex situ* 50% wt% polymer sample decreases as temperature increases.

The 50 wt% polymer sample:

Based on the RMS roughness measurement (Figure 13) and major texture change from the images (Figure 14), the 50 wt% polymer sample also displays three distinctive temperature regimes in the surface morphology. At low temperatures (25 – 80 ºC), the texture does not change significantly up to 80 ºC, as indicated by image texture and a stableness of the roughness. Starting at 90 ºC, some crystal like textures form on the surface. The new texture becomes highly distinctive at 100 ºC, which causes the increase in roughness. As the sample enters the high temperature regime from 120 ºC, micron-sized droplets (Figure 15) form and leave fibril-like texture on the background. The average width of the background fibrils ranges from 67 nm at 120 ºC to 47 nm at 200 ºC indicated by Figure 16.

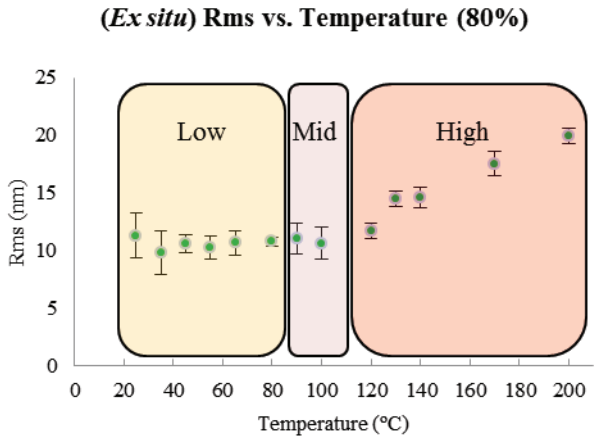

Figure 17. The roughness evolution of the *ex situ* 80 wt% polymer sample.

The 80 wt% polymer sample:

Analysis of the RMS roughness (Figure 17) and visible surface texture change (Figure 18) show three distinctive temperature regimes also. At ambient temperature, the 80 wt% polymer sample displays a fibril-like texture, which is different from the 20 and 50 wt% polymer sample at ambient condition. This texture has a width between 70 nm to 100 nm and does not change noticeably up to 80 ºC where tiny particulates start to form between the fibrils. At 120 ºC, the surface shows some aggregation of the particulates. As temperature increases, the particulates aggregate into larger circular particulates on the surface, which explains the increase in roughness of the surface. Also, the background evolves from fibril-like to grain-like texture. However, no micron-sized droplets are visible under the optical camera. The background exhibits clusters of mesoscale droplets that do not merge with each other up to 200 ºC.

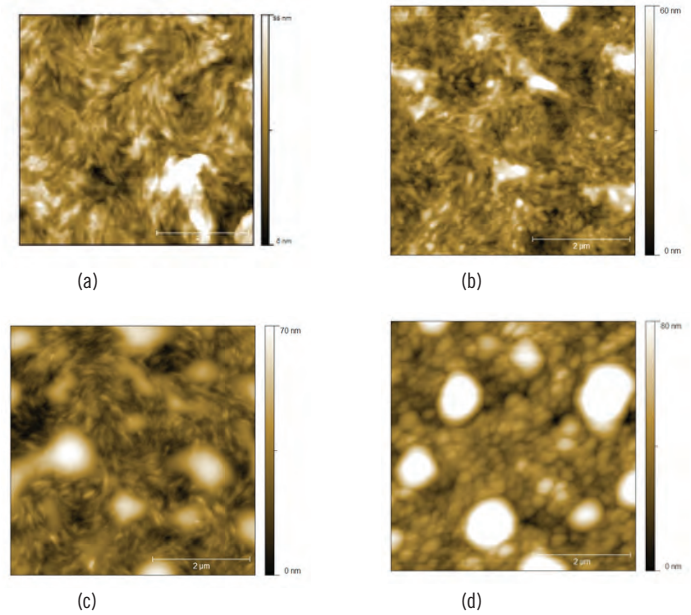

(a) (b) (c) (d)

Figure 18. The topography images of the *ex situ* 80 wt% polymer sample at (a) 25 ºC, (b) 80 ºC, (c) 120 ºC, (d) 200 ºC.

Overview of *ex situ* study

First, in order confirm the samples are at thermodynamic equilibrium, the 50 wt% polymer sample in *ex situ* study is annealed twice at 100 ºC for 30 min each time. Two results from both annealing processes show stable crystal like texture shown in Figure 19. This indicates the texture of the sample is at equilibrium after annealing for 30 min. The sizes of the crystal texture increase, which might be caused by more crystallization events around the existing crystal textures.

Second, the data shows a complete dewetting event happening between 100 ºC and 120 ºC. The fact that the samples with more oligomer content (20 and 50 wt%) show larger aggregation of the dewetting texture suggests that it is an oligomer rich phase. This is further supported by the background fibril-like texture left after dewetting in the 20 and 50 wt% polymer samples, which is associated polymer texture[9] shown in Figure 20 (left). The pure oligomer surface[9] shown in Figure 20 (right) demonstrates an aggregating texture akin to the droplet formation. Thus, the dewetting event suggests stratification of the oligomer rich phase form on the film.

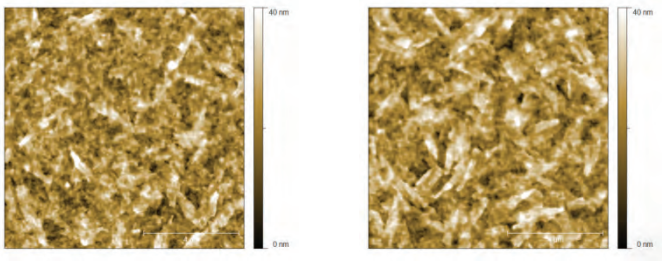

Figure 19. Evidence of equilibration of the 100 ºC annealed 50 wt% polymer sample for *ex situ* study: Surface topography of the *ex situ* 50 wt% polymer sample annealed at 100 ºC after (left) 1st time, (right) 2nd time.

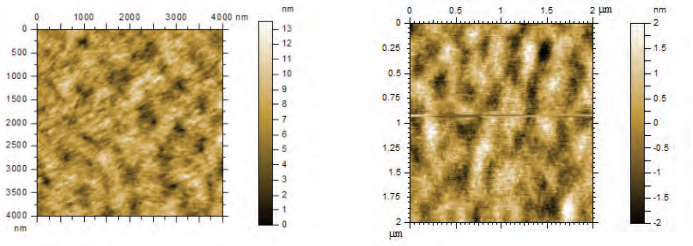

Figure 20. (left) surface topography of pure polymer TS-II-248; (right) surface topography of pure oligomer LEH-II-105.

Third, at high temperature, the 20 wt% polymer sample at 200 ºC has a thinner fibril texture than the 50 wt% does. This suggests the background is not only polymer rich, but consists of different polymer/oligomer ratios. Since the texture of the grains/fibril like texture is in the tenth of nanometers (~exciton diffusion length) it would be interesting for further study.

Fourth, the amount and the size of droplet formation suggests that the oligomer has a higher mass mobility in the 20 wt% relative to the 80 wt% polymer sample. The 20 wt% polymer sample droplets appear to merge with each other through successive temperature increases. The mesoscale particulates formed at 120 ºC disappear from the background as temperature, increases suggesting that the particulates either form individually then merge later, or are the leftovers from the droplet aggregation process. In contrast, the droplets in the 80 wt% polymer sample at higher temperatures (120 – 200 ºC) never merge into larger micron-sized droplets. More interestingly, the background clusters in the 80 wt% polymer sample. This could be caused by differences in surface energy, or changes in oligomer mobility as the polymer/oligomer ratios differ in each sample.

Last, small crystal-like texture appears at low temperature in the 20 wt% polymer sample, while the 50 wt% polymer sample at 100 ºC forms larger crystals but none shows up in the 80 wt% polymer sample at any temperature. It is possible that in the 20 wt% polymer sample, the polymer is diffusely embedded in the oligomer at low temperature such that it interrupts the crystal formation. On the other hand, there might not be sufficient oligomer connected with each other to form the crystal structure in the polymer rich film. Another possible explanation is related to nucleation of the oligomer. An oligomer rich phase could be reasoned to have a higher probability to produce nuclei for crystal growth. However, more nuclei mean they compete for surrounding material for crystallization, which could lead to a large population of smaller crystals. In contrast, the 50 wt% polymer sample has lower probability to produce nuclei, which allows enough surrounding materials to nucleate into crystals. From the same reasoning, the polymer rich sample might not possess enough oligomer to form appreciable nuclei populations.

In comparing the macro-phase and micro-phase transitions, the bulk transition around 50 ºC in the OPV phase diagram is not seen in the mesoscale mapping. The dewetting between 100 ºC and 120 ºC could represent the oligomer melting taking place earlier than 130 ºC as found in the macro phase. This effect could be due to effects of the surface interface or nano-scale confinement of the thin film. Another possible explanation is that the oligomer rich content is able to gain enough mobility in the thin film to dewet from the surface, which would not be represented in a macro thermodynamic phase transition.

3. Comparison between *in situ* and *ex situ* AFM study (50 wt%)

Overall, the *in situ* and *ex situ* studies on the 50 wt% polymer samples agree with each other on the dewetting event of the oligomer rich domain. However, the two events take place at a slight different temperature. The dewetting from *in situ* study starts between 80 ºC and 100 ºC in a form of a spinodal-like dewetting and forms individual droplet textures between 120 ºC and 130 ºC. The dewetting in *ex situ* starts between 80 ºC and 90 ºC as a crystal-like texture formation that then complete dewets from the underlying film between 100 ºC and 120 ºC.

The crystal-like texture formation in the *ex situ* 50 wt% polymer sample might be caused by the temperature quenching, whereas the *in situ* study never cools down between scanning temperatures. The differences in the transformation onset temperatures could be a kinetic effect caused by the two, different temperature heating regimes.

4. Laser Effect

During the *in situ* AFM study, there was an unexpected laser effect shown on the surface at the end of the 200 ºC heating regime (Figure 21). The pattern shown on the surface corresponds to the sharp of the laser. More aggregation of the micron-sized droplet texture take place at the edge of the laser mark and nearly no micron-sized droplets appear at the center.

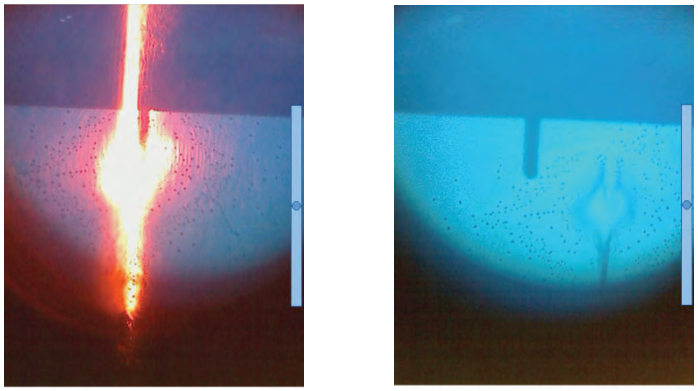

Figure 21. (left) the AFM (Agilent 5600LS) optical camera image of the laser shape at 200 ºC; (right) the AFM (Agilent 5600LS) optical camera image of the laser mark on the sample with scanning tip offsite.

During *ex situ* study, this effect once again shows up for the 20 and 50 wt% polymer sample. Example of the 20 wt% polymer sample is shown in Figure 22. First, the laser will create a "bleach" mark on the sample that has the same shape as the laser shadow. Then after annealing to the next desired temperature, there are the micron-sized droplets aggregating along the edge of the mark and no droplets in the center area. The effect is first noticed for 120 ºC annealed 20 and 50 wt% polymer samples. However, at that stage there are already multiple laser marks shown on the surface. Based on the number of laser marks and the number of scanning sites of the sample, this laser effect is predicted taking place around 55 ºC or 65 ºC. However, further testing should be carried out for the exact onsite time.

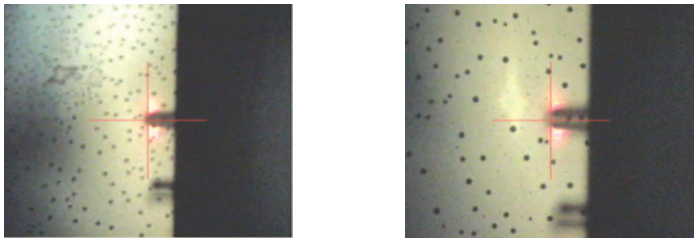

Figure 22. (left) the AFM (Veeco Dimension 3100) optical image before scanning 120ºC annealed 20% wt% polymer sample; (right) the AFM (Veeco Dimension 3100) optical image after scanning 120ºC annealed 20% wt% polymer sample.

Several factors might be responsible for this effect: laser, heating, temperature, air, and the tip. The tip factor is first eliminated by a laser test. A test sample is placed both at ambient temperature and 200 ºC under laser without a scanning tip for about 3 hours. The sample at room temperature does not show any change and the heated sample shows the same laser effect. The *ex situ* studied samples are annealed under inert atmosphere in the absence of laser. This means the laser does not directly affect the surface and instead modifies the surface under atmosphere condition permanently, which cause aggregation event of the oligomer rich domain behaves differently at the affected area.

Possible reasons that can cause this effect: (1) the sample reacts chemically with air or itself under laser; (2) the sample contents rearrange physically under laser. One piece of information worth mentioning is that the oligomer's excitation wavelength matches the wavelength of the laser used during imaging. This might be another reason causing this effect, which requires further testing.

For the *in situ* study, there is the possibility that the scanned surface has been damaged by the laser effect, which requires further testing. The result from *ex situ* study should still be valid, since a new site is scanned every time, unless the material is reacting with air under ambient temperature. Future tests necessary to understand the origin of this effect include focusing a laser on the surface in inert atmosphere both at ambient temperature and heated conditions to determine the influence of atmospheric oxygen and water, and to use a laser with a wavelength off the absorbance bands of the OPVs.

Conclusions

The mesoscale morphology of oligomeric donor and polymeric accepter OPV thin films was mapped using scanning probe microscopy. Its morphology evolution shows variations compared to its macro scale phase diagram. Overall, this study establishes a method to map surface morphology of OPV films, which can be applied to more OPV systems. This method provides information on mesoscale morphology of the OPV film, which is essential to understanding OPV structure formation and performance.

Future work should be conducted to map morphological evolution with AFM *in situ* under inert atmosphere to exclude possible reactions with oxygen and water. The Photoconductive AFM method could be used to measure the photocurrent of the thin film morphology, allowing the possible correlation of photocurrent to meso-scale structure. Furthermore, the obtained textures must now be mapped chemically to establish composition in order to understand the movement of individual species during development of morphology.

References

1. Sariciftci, N. S.; Smilowitz, L.; Heeger, A. J.; Wudl, F., Photoinduced Electron-Transfer from a Conducting Polymer to Buckminsterfullerene. Science 1992, 258 (5087), 1474-1476.
2. Yu, G.; Gao, J.; Hummelen, J. C.; Wudl, F.; Heeger, A. J., Polymer Photovoltaic Cells - Enhanced Efficiencies Via a Network of Internal Donor-Acceptor Heterojunctions. Science 1995, 270 (5243), 1789-1791.
3. Haugeneder, A.; Neges, M.; Kallinger, C.; Spirkl, W.; Lemmer, U.; Feldmann, J.; Scherf, U.; Harth, E.; Gügel, A.; Müllen, K., Exciton diffusion and dissociation in conjugated polymer/fullerene blends and heterostructures. Physical Review B 1999, 59 (23), 15346.
4. Thompson, B. C.; Fréchet, J. M. J., Polymer-Fullerene Composite Solar Cells. Angewandte Chemie International Edition 2008, 47 (1), 58-77.
5. (a) Campbell, A. R.; Hodgkiss, J. M.; Westenhoff, S.; Howard, I. A.; Marsh, R. A.; McNeill, C. R.; Friend, R. H.; Greenham, N. C., Low-Temperature Control of Nanoscale Morphology for High Performance Polymer Photovoltaics. Nano Lett 2008, 8 (11), 3942-3947; (b) Kimber, R. G. E.; Walker, A. B.; Schroder-Turk, G. E.; Cleaver, D. J., Bicontinuous minimal surface nanostructures for polymer blend solar cells. Phys Chem Chem Phys 2010, 12 (4), 844-851; (c) Moon, J. S.; Lee, J. K.; Cho, S. N.; Byun, J. Y.; Heeger, A. J., "Columnlike" Structure of the Cross-Sectional Morphology of Bulk Heterojunction Materials. Nano Lett 2009, 9 (1), 230-234.
6. Thompson, B. C.; Frechet, J. M. J., Organic photovoltaics - Polymer-fullerene composite solar cells. Angew Chem Int Edit 2008, 47 (1), 58-77.
7. Synthesised by Lauren Hayden of the Mader group.
8. a) Yan, H.; Chen, Z.; Zheng, Y.; Newman, C.; Quinn, J. R.; Dotz, F.; Kastler, M.; Facchetti, A., A high-mobility electron-transporting polymer for printed transistors. Nature 2009, 457 (7230), 679-686; (b) Synthesised by Tissa Sajoto of the Mader group.
9. Data was obtained from mentor, Ben Wunsch.
10. (a) Ivanov, D. A. D., R.; Magonov, S.N. . Exploring the High-Temperature AFM and Its Use for Studies of Polymers. Application Note Published by Digital Instruments/Vecco metrology Group (2001). URL: http://www.veeco.com/pdfs/appnotes/an45_hightempheater_090104_reva1_19.pdf [Online]; (b) Oulevey, F.; Gremaud, G.; Semoroz, A.; Kulik, A. J.; Burnham, N. A.; Dupas, E.; Gourdon, D., Local mechanical spectroscopy with nanometer-scale lateral resolution. Review of Scientific Instruments 1998, 69 (5), 2085-2094; (c) Schönherr, H.; Bailey, L. E.; Frank, C. W., Analyzing the Surface Temperature Depression in Hot Stage Atomic Force Microscopy with Unheated Cantilevers: Application to the Crystallization of Poly(ethylene oxide). Langmuir 2001, 18 (2), 490-498.

Acknowledgments

This research was made possible by the help and guidance of Ben Wunsch, Jassem Abdallah as well as Seth Marder and the Marder Research Group at Georgia Institute of Technology. Funds for this research were provided by the Center on Materials and Devices for Information Technology Research (CMDITR), an NSF Science and Technology Center No. DMR 0120967.

SHUTONG ZHAN is a sophomore at Duke University in Durham, North Carolina. She is a double major in chemistry and mathematics and plans to continue on with her education in graduate school or medical school.